CORA Cork Open Research Archive
Cartlann Taighde Oscailte Chorcaí

Title	Experimental analysis of novel telecom source materials and devices
Authors	Harnedy, Patrick
Publication date	2015
Original Citation	Harnedy, P. 2016. Experimental analysis of novel telecom source materials and devices. PhD Thesis, University College Cork.
Type of publication	Doctoral thesis
Rights	© 2015, Patrick Harnedy. - http://creativecommons.org/licenses/by-nc-nd/3.0/
Download date	2026-11-06 12:27:43
Item downloaded from	https://hdl.handle.net/10468/2710



UCC
University College Cork, Ireland
Coláiste na hOllscoile Corcaigh

Experimental analysis of novel telecom source materials and devices

Patrick Harnedy
BSc.



NATIONAL UNIVERSITY OF IRELAND, CORK

Faculty of Science
Department of Physics

Thesis submitted for the degree of Doctor of Philosophy

January 2015

Supervisors: Prof. Eoin P. O Reilly
Dr. Simon Osborne
and Dr Robert Manning
Head of Department/School: Prof John G. McInerney

Research supported by BIANCHO FP7

Contents

List of Figures v
List of Tables ix
Acknowledgements xi
Abstract xii
Publications xiii
0.1 Journal papers xiii
0.2 Conference talks xiii
0.3 Posters xiii

1 Introduction **1**
1.1 Thesis structure 2

2 Background theory **4**
2.1 Introduction 4
2.2 Lasers 5
2.3 Semiconductor diode lasers 6
2.3.1 A brief history of diode lasers 7
2.3.2 Materials for diode lasers 10
2.3.3 Device geometry 16
2.3.4 Carrier generation and recombination in active regions . 18
2.3.5 Matrix elements 22
2.3.6 Auger recombination 24
2.3.6.1 Removal of CHSH Auger recombination through bandstructure engineering 25
2.4 Summary 26

3 Research methodologies **27**
3.1 Introduction 27
3.2 Laboratory equipment 28
3.2.1 Cryostat 28
3.2.2 8 GHz oscilloscope 29
3.2.3 Lock-in amplifier 29
3.2.4 Spectrograph 30
3.2.5 InGaAs Femtowatt detector 30
3.2.6 Pulsed current source 31
3.3 Measurement techniques 31
3.3.1 Spectrally resolved spontaneous emission measurements . 32
3.3.2 Temperature dependent facet and spontaneous emission measurements 34
3.3.3 Temperature dependent fibre coupled facet emission measurements 37
3.3.4 Temperature dependent photoluminescence spectroscopy 40
3.3.5 Photovoltage spectroscopy 42
3.3.5.1 Polarisation resolved photo-voltage 44
3.3.5.2 Spectral corrections 44

3.3.5.3 Extraction of transition energies 46
3.3.5.4 Device mount 47
3.4 Summary 48

4 Experimental analysis and rate equation modelling of an InP based quantum dash laser showing bistable threshold 49
4.1 Introduction 49
4.2 Materials studied 51
4.3 Experimental analysis 52
4.4 Theoretical interpretation of measurements 55
4.5 Model 56
4.6 Results 60
4.7 Summary 64

5 Experimental study of bismuth-induced broadening in $GaAs_{1-x}Bi_x$ quantum well laser structures 66
5.1 Introduction 66
5.2 Materials studied 68
5.3 Experimental analysis 69
5.4 Theoretical interpretation of results 73
5.4.1 Lasing characteristics of 2.2 % GaBiAs QW structure . . 78
5.5 Calculations by Christopher A. Broderick 80
5.6 Summary 82

6 Experimental determination of the $GaAs_{1-x}Bi_x$/GaAs band offset, and k · p paramterisation 83
6.1 Introduction 83
6.2 Materials studied 87
6.3 Experimental measurements 88
6.4 Determination of the bulk $GaBi_xAs_{1-x}$/GaAs band offset 91
6.5 Results 94
6.5.1 Parameterisation of the 12-band model: samples 1 & 2 . 95
6.5.2 Verification of parameterised model: samples 3 – 6 . . . 101
6.6 Summary 103

7 Experimental investigation of optical lifetimes in $GaAs_{1-x}Bi_x$ quantum wells using TRPL 105
7.1 Introduction 105
7.2 Materials studied 106
7.3 Experimental method 106
7.4 Results 107
7.5 Summary 111

8 Conclusions 112
8.1 Summary 112
8.1.1 Experimental analysis and rate equation modelling of an InP based quantum dash laser showing bistable threshold 112

8.1.2 Experimental study of bismuth-induced broadening in $GaAs_{1-x}Bi_x$ quantum well laser structures 112
8.1.3 Experimental determination of the $GaBi_xAs_{1-x}$/GaAs band offset, and $\mathbf{k} \cdot \mathbf{p}$ parameterisation 113
8.1.4 Experimental investigation of optical lifetimes in $GaAs_{1-x}Bi_x$ quantum wells using TRPL 114
8.2 Conclusions 115
8.2.1 Future work 116

A Bistable Q-Dash laser **117**

B Determination of GaAs/GaBiAs band offsets **123**

C Spontaneous emission measurements **138**

I, Patrick Harnedy, certify that this thesis is my own work and I have not obtained a degree in this university or elsewhere on the basis of the work submitted in this thesis.

Patrick Harnedy

List of Figures

2.1 Spectral attenuation of optical signals travelling in silica fibres [76]. 6
2.2 Real space representation of the bandstructure of a homojunction laser (top), a double heterostructure laser (middle), and a separate confinement heterostructure laser (bottom). Note the increasing confinement for carriers and photons going from top to bottom [45]. 8
2.3 Energy gap versus lattice constant for ternary compounds defined by curved lines connecting the binary end point alloys [17]. . . . 11
2.4 Representation of the density of states for bulk, quantum well, quantum wire and quantum dot respectively working from left to right [75]. 14
2.5 Three different processing options for diode lasers. Broad area (oxide stripe) (top), ridge waveguide (middle), and buried heterostructure (bottom) [45]. 16
2.6 Schematic illustration of the three possible outcomes of light-matter interaction. Spontaneous emission (top), absorption (middle), and stimulated emission (bottom) [51]. 19
2.7 Reservoir analogy for the competing processes at play when trying to reach threshold in a diode laser [26]. 20
2.8 Example laser light-current characteristic showing different processes above and below threshold [26]. 21
2.9 Representation of the atomistic potential, u(**r**), and the accompanying envelope function F(**r**) in a periodic crystal structure [26]. 23
2.10 Schematic representation of the predicted CHSH Auger recombination suppression due to bandstructure engineering. 25

3.1 Schematic of the ARS cryostat [95] 29
3.2 Schematic of the SE measurement mount. Figure modified from [45]. 33
3.3 Injection level dependent SE spectra of a GaBiAs QW laser . . 34
3.4 Facet L-I characteristic seen in blue with SE characteristic L-I in red. A clear threshold-like behaviour is present in both. 35
3.5 Temperature dependent ASE (black) and lasing (red) spectra with the FP mode structure resolved. 38
3.6 Bistable threshold current timetrace seen at 190 K. 39
3.7 Set-up for PL experiment. Figure modified from [45]. 40
3.8 PL spectrum of GaBiAs QW at 13 K. 42
3.9 Set-up for PV experiment. Figure modified from [45]. 43
3.10 spectra measured on a GaBiAs QW laser structure. 45
3.11 Left: PV mount in horizontal orientation. Right: PV mount in vertical orientation. 47

4.1 Flat band approximation showing schematically the variation of conduction band edge energy with position for the two DWELL structures considered, one with high barrier (dashed), and the other with a lower barrier. 51
4.2 Temperature dependence of threshold (black) and radiative (red) currents for DW_L (filled circles) and DW_H (crosses). DW_H has a bistable threshold below 220 K. 52
4.3 300 overlayed light-current measurements of the high barrier laser at 190 K, clearly showing an abrupt switch to lasing at 37.5mA and an equally abrupt switch from lasing at 33.3mA. 53
4.4 Left y-axis plot shows the temperature dependence of the experimentally determined threshold current including switch on/off points in the bistable region. Right y-axis plot shows the temperature dependence of the size of the bistability, which is seen to grow in size from 50 K to about 200 K, above which it drops quickly to zero with increasing temperature. 54
4.5 Amplified spontaneous emission (at 80 % of I_{th}) and lasing spectra at 190 K (right) and 300 K (left). Note that the lasing transition is at the high energy side of the gain peak in the bistable region and at the low energy side at 300 K. 55
4.6 Flow diagram of the rate equation system showing how diffusion time, capture time, escape time and recombination time influence carrier distribution through the system. 58
4.7 Calculated escape times for the CB and VB confinement energies 59
4.8 Top panels show calculated light-current characteristics for two different escape times, representing the stable and bistable regimes. Bottom panels show calculated carrier densities for each confined region(well1=black; well2=blue, dashed; well3=red), for the same escape times as the top panels. 60
4.9 Calculated temperature dependence of threshold current (left panel) and the measured temperature dependence of threshold current (right panel). Switch on points red and switch off points black in bistable regime. 61
4.10 Effect of Auger recombination inclusion on the total threshold current, represented by the total carrier density cubed. Switch on threshold in red and switch off threshold in black. 62
4.11 Temperature dependent threshold carrier density normalised to transparency carrier density for each of the three wells modelled, triangles indicate switch on points and dashed lines switch off points. 63

5.1 An example SCH device stack from Philipps-Universität Marburg 68
5.2 Measured TE and TM polarised (blue and red lines respectively) room temperature photovoltage spectra of $GaAs_{1-x}Bi_x$/(Al)GaAs single quantum well laser structures. For each structure the nominal Bi composition x and quantum well thickness are indicated on the plots. 70

5.3 Real-space illustration of transitions between bound-to-bound (1 & 2) and bound to continuum (3) states in quantum well structures 71
5.4 Measured spontaneous emission (blue lines) and photoluminescence (red dashed lines) spectra, for temperatures ranging from 100 to 350 K. The spontaneous emission measurements were performed under electrical injection at the lasing threshold, while the photoluminescence spectra were measured with 70 mW continuous-wave pump power at a wavelength of 640 nm. PL has been offset in the y-direction for clarity. 72
5.5 Illustration of different carrier localisation mechanisms discussed. Bi pair and cluster localised states lying above the band edge shown by green dashed lines and represented by 1. The inhomogeneously broadened VB edge is represented by 2 & 3. 74
5.6 Measured temperature dependent spontaneous emission (crosses) and photoluminescence (filled circles) peak emission energies, as well as the broadening of the spontaneous emission spectra (filled triangles) 76
5.7 Measured injection level dependent spontaneous emission measurements up to threshold carrier density at 250 K, the peaks of each spectrum is indicated by a closed circle 77
5.8 Variation of threshold current density (closed blue circles), J_{th}, and its radiative component (closed red circles), J_{th}^{rad}, with temperature, and the variation of z (closed yellow circles), the power of the carrier density, with temperature 79
5.9 Comparison of measured and calculated SE for the 2.2 % $GaAs_{1-x}Bi_x$ QW laser structure of Ref. [66]. The calculated spectra at 300 K and 350 K have undergone a red shift of 12 nm to compare the shape of the band edge transition. 81

6.1 Black (Grey) solid line: Measured (Simulated) high-resolution x-ray diffraction pattern about the GaAs (004) reflection, for sample 4 of Table 6.1. 88
6.2 Schematic illustration of the calculation of the bulk $GaBi_xAs_{1-x}$/GaAs band offsets for the lowest conduction band (CB), light- and heavy-hole (LH and HH) bands, and the spin-split-off (SO) band in the presence of biaxial strain. The full details of each step in the calculation are outlined in Section 6.4. 94
6.3 Measured polarisation-resolved photovoltage spectra of samples 1 – 6 of Table 6.1. Blue lines: TE polarised photovoltage. Red lines: TM-polarised photovoltage. Blue (Red) arrows denote transition energies extracted from TE (TM) polarised photovoltage spectra. Blue arrows are also used to denote the transition energies for polarisation-insensitive features, which are extracted from both the TE and TM polarised spectra. Black arrows: Transition energies calculated using either an 8-band $\mathbf{k}\cdot\mathbf{p}$ model (for sample 1) or a 12-band $\mathbf{k}\cdot\mathbf{p}$ model (for samples 2 – 6). 96

6.4 First derivative with respect to energy of the product of the photon energy and the measured polarisation-resolved photovoltage for samples 1 – 6 of Table 6.1. Blue (Red) lines denote the derivatives obtained from the TE (TM) polarised spectra. Blue (Red) arrows denote transition energies extracted from the TE (TM) polarised photovoltage spectra. Blue arrows are also used to denote the transition energies for polarisation-insensitive features, which are extracted from both the TE- and TM-polarised spectra. Black arrows: Transition energies calculated using 8- and 12-band $\mathbf{k} \cdot \mathbf{p}$ models for sample 1 and samples 2 – 6 respectively. 97
6.5 Real-space schematic of type-I band offset for $GaBi_xAs_{1-x}$/GaAs bulk interfaces illustrating the use of samples 1 (red) & 2 (blue) for offset determination. Note the almost identical barrier material in both samples. 100

7.1 Device stack from Philipps-Universität Marburg 106
7.2 Schematic of the TRPL setup used 107
7.3 TRPL streak camera image showing the energy and temporal character of the emission from both the GaAs and $GaAs_{1-x}Bi_x$ layers. Red represents strong emission and blue represents zero emission. 108
7.4 Temporal decay of the TRPL streak image integrated at a range of wavelengths. Note the two component decay clearly visible in some of the plots in the region of the GaAs peak. 109
7.5 Integrated PL just after excitation shown in blue with extracted lifetimes plotted in green (line with circles). 109

List of Tables

4.1 Parameters used for modelling of bistable threshold current. . . 59

5.1 Transition energies and broadening extracted from the room temperature photovoltage spectra of samples 1, 2, 3 and 4 shown in Fig. 5.2. 73

6.1 Structural parameters for the $GaBi_xAs_{1-x}$/(Al)GaAs QW structures investigated including nominal well thicknesses and well and barrier material compositions, as well as the expected growth uncertainties in these quantities. The QWs in sample 4 are separated by barriers of thickness 29 nm. The values in brackets are the best fit values used in the theoretical calculations of Section 6.5. . . . 89

6.2 Bi-related parameters for the 12-band $\mathbf{k} \cdot \mathbf{p}$ Hamiltonian of Refs. [20, 21]. The parameters α and β were determined as the best fit to the measured transition energies in sample 2, with the remaining parameters determined by detailed tight-binding supercell calculations. 100

6.3 Details of the measured and calculated transition energies in the QW samples investigated. Transitions labelled as “insensitive" are those for which the measured energies were equal (to within 5 meV) in the TE and TM polarised PV spectra. The associated designations were assigned based on the energies obtained from the 8 and 12-band $\mathbf{k}\cdot\mathbf{p}$ calculations, as well as symmetry considerations based on the character of the measured PV spectra. The structural parameters used as input to the theoretical calculations for each sample are given in parentheses in Table 6.1. The abbreviation BCB (BVB) denotes the barrier conduction (valence) band. . . 102

Time You Enjoy Wasting is Not Wasted Time
Marthe Troly-Curtin

Acknowledgements

I would like to begin by thanking Prof. Eoin O' Reilly for the opportunity to carry out a Ph.D. in an interesting and challenging area, as well as the opportunity of being involved in a European research project. At this point I would like to acknowledge financial support of the BIANCHO (Bismide And Nitride Components for High temperature Operation) 7^{th} framework European project as well as Science Foundation Ireland. Thank you also to my original laboratory supervisor, whose direction and support in the early days was excellent, Dr. Simon Osborne, for his time, feedback and friendship. I would also like to thank my second experimental supervisor who filled the vacuum left by Simon's departure, Dr. Bob Manning, for excellent direction and input in the final year of my PhD. I would like to acknowledge the help and support of my colleague, Dr. Christopher Broderick, with whom it was a pleasure to collaborate. Thank you to Dr. Francois Lelarge and Dr. Siddharth Joshi at Alcatel-Thales III-V joint lab: Bell Labs and Thales Research and Technology, Prof. Kerstin Volz and Dr. Peter Ludewig at Phillips Universität Marburg, Prof. Arunas Krotkus and FTMC in Vilnuis for providing most of the samples used in this research and Dr. Tomasz Ochalski and Prof. Guillaume Huyet for the use of their time resolvd PL measurement equipment. I would also like to thank a number of colleagues and former colleagues from the Tyndall National Institute: Finbarr O'Callaghan, David O'Shea, Anna Hauber, Gerard Duffy, Barry Huchenson and Siobhan O'Halloran. I would like to thank my friends and family, especially my parents, Kathleen and Pat Harnedy, my siblings, Deirdre, James, and Eoghan for their encouragement, love and support. Last, but most assuredly not least, to my girlfriend, Niamh McCarthy, I dedicate this work to you, for having the strength to endure my nonsense for the last three years, you deserve it.

Abstract

Incumbent telecommunication lasers emitting at 1.5 μm are fabricated on InP substrates and consist of multiple strained quantum well layers of the ternary alloy InGaAs, with barriers of InGaAsP or InGaAlAs. These lasers have been seen to exhibit very strong temperature dependence of the threshold current. This strong temperature dependence leads to a situation where external cooling equipment is required to stabilise the optical output power of these lasers. This results in a significant increase in the energy bill associated with telecommunications, as well as a large increase in equipment budgets. If the exponential growth trend of end user bandwidth demand associated with the internet continues, these inefficient lasers could see the telecommunications industry become the dominant consumer of world energy.

For this reason there is strong interest in developing new, much more efficient telecommunication lasers. One avenue being investigated is the development of quantum dot lasers on InP. The confinement experienced in these low dimensional structures leads to a strong perturbation of the density of states at the band edge, and has been predicted to result in reduced temperature dependence of the threshold current in these devices. The growth of these structures is difficult due to the large lattice mismatch between InP and InAs; however, recently quantum dots elongated in one dimension, known as quantum dashes, have been demonstrated. Chapter 4 of this thesis provides an experimental analysis of one of these quantum dash lasers emitting at 1.5 μm along with a numerical investigation of threshold dynamics present in this device.

Another avenue being explored to increase the efficiency of telecommunications lasers is bandstructure engineering of GaAs-based materials to emit at 1.5 μm. The cause of the strong temperature sensitivity in InP-based quantum well structures has been shown to be CHSH Auger recombination. Calculations have shown and experiments have verified that the addition of bismuth to GaAs strongly reduces the bandgap and increases the spin orbit splitting energy of the alloy $GaAs_{1-x}Bi_x$. This leads to a bandstructure condition at x = 10 % where not only is 1.5 μm emission achieved on GaAs-based material, but also the bandstructure of the material can naturally suppress the costly CHSH Auger recombination which plagues InP-based quantum-well-based material. It has been predicted that telecommunications lasers based on this material system should operate in the absence of external cooling equipment and offer electrical and optical benefits over the incumbent lasers. Chapters 5, 6 and 7 provide a first analysis of several aspects of this material system relevant to the development of high bismuth content telecommunication lasers.

Publications

0.1 Journal papers

- P. E. Harnedy, S Osborne, F. Lelarge, S. Joshi, and E. P. O' Reilly. Bistability of threshold in quantum dash-in-a-well lasers, IET Optoelectronics. DOI:10.1049/iet-opt.2013.0083

- Christopher A. Broderick, Patrick E. Harnedy, Peter Ludewig, Zoe L. Bushell, Robert J. Manning, Kerstin Volz, and Eoin P. O'Reilly. Determination of type-1 band offsets in $GaBi_xAs_{1-x}$ quantum wells using polarization-resolved photovoltage spectroscopy and 12-band $\mathbf{k} \cdot \mathbf{p}$ calculations, submitted to Semiconductor Science and Technology.

- Patrick E. Harnedy, Christopher A. Broderick, Robert J. Manning, Peter Ludewig, Kerstin Volz, and Eoin P. O'Reilly. Experimental study of bismuth-induced broadening in $GaAs_{1-x}Bi_x$ quantum well laser structures. In Preparation, Applied Physics Letters.

- Christopher A. Broderick, Patrick E. Harnedy, Robert J. Manning, Peter Ludewig, Kerstin Volz, and Eoin P. O'Reilly. Theory of the electronic and optical properties of dilute bismide quantum well lasers, in Preparation, invited paper, IEEE Selected Topics in Quantum Electronics.

0.2 Conference talks

- P. E. Harnedy, S Osborne, F. Lelarge, S. Joshi, and E. P. O' Reilly. Semiconductor and Integrated Optoelectronics conference (SIOE), Cardiff, 9-11 April 2013: Bistability of threshold in quantum dash-in-a-well lasers.

- Patrick E. Harnedy, C. A. Broderick, Robert J. Manning, Peter Ludewig, Kerstin Volz, and Eoin P. O'Reilly. Semiconductor and Integrated Optoelectronics conference (SIOE), Cardiff, 29 April - 1 May 2014: Experimental analysis of electrical injection $GaBi_xAs_{1-x}/GaAl_xAs_{1-x}$ single quantum well laser

- Patrick E. Harnedy, C. A. Broderick, Robert J. Manning, Peter Ludewig, Kerstin Volz, and Eoin P. O'Reilly. International Bismide Workshop, Cork, July 2014: Experimental study of bismuth-induced broadening in $GaAs_{1-x}Bi_x$ quantum well laser structures.

0.3 Posters

- P. E. Harnedy, S Osborne, F. Lelarge, S. Joshi, and E. P. O' Reilly. Tyndall internal conference, June 2013, Cork: Bistability of threshold in quantum dash-in-a-well lasers.

- P. E. Harnedy, S Osborne, F. Lelarge, S. Joshi, and E. P. O' Reilly. Photonics Ireland, September 2013, Belfast: Bistability of threshold in quantum dash-in-a-well lasers.

Chapter 1

Introduction

To sustain the recent growth in the internet, telecommunications has turned to optical interconnects. These interconnects consist of silica-based optical fibres with telecommunication lasers to transmit optical data, and receivers to decode the optical data. Due to the structural properties of silica fibres, there are two favourable wavelength windows for optical transmission. The first window at 1.3 μm corresponds to a local minimum in the attenuation experienced by an optical pulse travelling in the fibre, but more importantly, 1.3 μm optical signals in silica fibre experience zero dispersion. This is very important for achieving high bit-rate transmission, and so this wavelength is utilised for high speed, short haul interconnects. The second transmission window is at 1.5 μm and corresponds to the minimum attenuation experienced by optical pulses in silica fibre. This wavelength window is used for long haul communication links where the achievable distance between optical repeaters is as critical as bit-rate. This thesis focuses on the development of optical sources for the low loss 1.5 μm transmission window.

The incumbent telecommunication lasers emitting at 1.5 μm are fabricated on InP substrates and consist of multiple strained quantum well layers of the ternary alloy InGaAs, with barriers of InGaAsP or InGaAlAs. These lasers have been seen to exhibit very strong temperature dependence of the threshold current. This strong temperature dependence leads to a situation where external cooling equipment is required to stabilise the optical output power of these lasers. This results in a significant increase in the energy bill associated with telecommunications, as well as a large increase in equipment budgets. If the exponential growth trend of end user bandwidth demand associated with the internet continues, these inefficient lasers could see the telecommunications industry become the dominant consumer of the world's energy.

For this reason there is strong interest in developing new, much more efficient

telecommunication lasers. One avenue being investigated is the development of quantum dot lasers on InP. The confinement experienced in these low dimensional structures leads to a strong perturbation of the density of states at the band edge, and has been predicted to result in reduced temperature dependence of the threshold current in these devices. The growth of these structures is difficult due to the large lattice mismatch between InP and InAs; however, recently quantum dots elongated in one dimension, known as quantum dashes, have been demonstrated. Chapter 4 of this thesis provides an experimental analysis of one of these quantum dash lasers emitting at 1.5 μm along with a numerical investigation of the threshold dynamics of the device. This incremental approach to using InP based materials for telecommunication lasers is reaching saturation as it becomes apparent that the problem is a material property issue with InP.

Another avenue being explored to increase the efficiency of telecommunications lasers is bandstructure engineering of GaAs based materials to emit at 1.5 μm. The cause of the strong temperature sensitivity in InP based quantum well structures has been shown to be Auger recombination as discussed in detail in Chapter 2. Calculations have shown and experiments have verified that the addition of bismuth to GaAs strongly reduces the bandgap and increases the spin orbit splitting energy of the alloy $GaAs_{1-x}Bi_x$. This leads to a bandstructure condition close to x = 10 % where not only is 1.5 μm emission achieved on GaAs based material, but also the bandstructure of the material naturally suppresses the dominant CHSH Auger recombination which plagues InP based quantum well based material. It has been predicted that telecommunications lasers based on this material system should operate in the absence of external cooling equipment and offer electrical and optical benefits over the incumbent lasers. Chapters 5, 6 and 7 offer an in depth analysis of the development of this material system towards the milestone x > 10 % highly efficient telecommunication laser.

1.1 Thesis structure

The remainder of this thesis is laid out as follows. Chapter 2 provides some background and an overview the basic theoretical constructs relevant to the following work. In chapter 3 an in depth description of the experimental methods employed in this body of work is presented. In chapter 4, a temperature dependent analysis of an InP based quantum dash laser emitting at 1.5 μm is presented. A bistability of the threshold current is uncovered in this device. A theoretical understanding of the behaviour is gained, and a rate equation model which achieves excellent

qualitative agreement with the measured data is presented. Chapter 5 provides an experimental investigation of the causes and effects of the bismuth related broadening present in alloys of $GaAs_{1-x}Bi_x$. The first measurement and analysis of spontaneous emission from this material is presented in this chapter. Chapter 6 details a collaborative piece of work undertaken with Christopher A. Broderick, in which experimental polarisation resolved photovoltage measurements, and an 8- and 12-band $\mathbf{k}\cdot\mathbf{p}$ model are used to provide the first ever determination of band offsets for the $GaAs/GaAs_{1-x}Bi_x$ heterointerface. In chapter 7 some of the first ever time resolved, band edge photo luminescence is presented. This is achieved by strong excitation of the $GaAs_{1-x}Bi_x$ to saturate the bismuth pair and cluster related localised states which exist within the bandgap of the material. This is the first time resoled measurement of band edge emission from this material. Finally, in chapter 8, a summary of the work undertaken in this thesis is presented.

Chapter 2

Background theory

2.1 Introduction

The purpose of this chapter is to provide some backgound theory and context for the chapters to come. This is achieved with a brief description in section 2.2 of what a laser is and a brief comparison of semiconductor, gas, and solid state lasers. Following this, considering that this thesis is concerned with measurements made on semiconductor diode lasers, an overview of the attributes of diode lasers is presented in section 2.3. Section 2.3 is split into subsections in which each deals with a feature of diode lasers. In section 2.3.1 a brief history of the diode laser is provided, from the original bulk homojunction lasers to quantum well, wire, and dot separate confinement heterostructure lasers. Section 2.3.2 discusses materials used in modern diode laser active regions, including strained quantum well materials and a description of how the density of states changes when going from bulk material to quantum confinement. In section 2.3.3 a description of three different processing approaches for edge emitting lasers is presented. Section 2.3.4 discusses different carrier recombination mechanisms and how the interplay of these affect the threshold condition for lasing. In section 2.3.5 the selection rules for allowed transitions in quantum confined materials are discussed before a discussion of non radiative recombination mechanisms. Section 2.3.6 discusses Auger recombination and its role in incumbent InP based telecommunications lasers, and how bandstructure engineering can be employed to remove this costly loss mechanism. In section 2.4 the chapter is summed up.

2.2 Lasers

A laser is a light emitting device, where the emission of a coherent beam of photons is achieved through a process of optical amplification based on stimulated emission of electromagnetic radiation and feedback within an optical cavity. The term laser originated as an acronym for **L**ight **A**mplification by **S**timulated **E**mission of **R**adiation[26]. A laser differs from more common light sources in that it emits a coherent beam of photons, enabling applications such as laser cutting and lithography and allows a beam to be collimated, as seen in laser pointers.

Lasers have many important applications. They are used in common devices such as optical disk drives (cd, dvd, blue-ray), laser printers, and barcode scanners. They are used in medicine for laser surgery and various skin treatments, and in industry for cutting and welding materials. They are used in military devices for marking targets and measuring distance and speed. Laser lighting displays use laser light as an entertainment medium. Lasers also have many important applications in research, and as will be seen in this thesis, lasers have a large role to play in modern telecommunications.

There are three broad laser classes: gas, solid state, and semiconductor. Semiconductor lasers will be the focus of the remainder of this chapter and so a brief description of gas and solid state lasers will be given at this point to distinguish them from semiconductor lasers. Helium-Neon and Nd-doped YAG (yttrium-aluminium-garnet) are popular gas and solid state laser sources. Diode lasers are distinguished from these other classes by their ability to be directly electrically pumped, which results in a much better conversion efficiency from electrical to optical power. It is not uncommon for a diode laser to have a 50 % wallplug efficiency, whereas the corresponding efficiency for a gas or solid state laser would be closer to 1 %. These gas and solid state lasers are typically pumped via plasma-pumping or via incoherent optical flashlamps. Size is another differentiating factor between semiconductor and the other laser classes. Gas and solid state lasers are generally thousands of millimetres in length compared to semiconductor lasers where in a lot of cases a 1 millimetre cavity would be considered quite long. This longer cavity, coupled with the narrow gain bandwidth associated with atomic energy levels in solid state and gas lasers, give rise to a generally more coherent optical output than simple semiconductor lasers, whose linewidths lie in the low megahertz range. Semiconductor diode lasers with very narrow linewidths are achievable but are more complex than the basic edge emitting devices discussed here.

2.3 Semiconductor diode lasers

This thesis is interested in its entirety in measurements and analysis of semiconductor diode lasers. Not just any diode lasers, but a very specific subset of diode lasers called telecommunication lasers. All high bit rate telecommunication networks are now based on optical interconnects. Optical fibre communication was proposed in the mid-1960s and by the mid-1970s two windows in the infrared had been identified for telecommunication applications [90]. Optical telecommunication networks are comprised of silica-based optical fibres and semiconductor optical emitters and receivers. The absorption properties of the optical fibres leads to two common telecommunication wavelength transmission windows. These two windows correspond to the wavelengths within the optical fibre where the optical mode undergoes zero dispersion and low loss, 1.3 μm, and minimal loss due to absorption and scattering, 1.55 μm, as seen in Fig. 2.1. Long haul telecommunications relies on the 1.55 μm window as the losses are lowest in this spectral region; however, lasers operating at this wavelength are based on InP and are

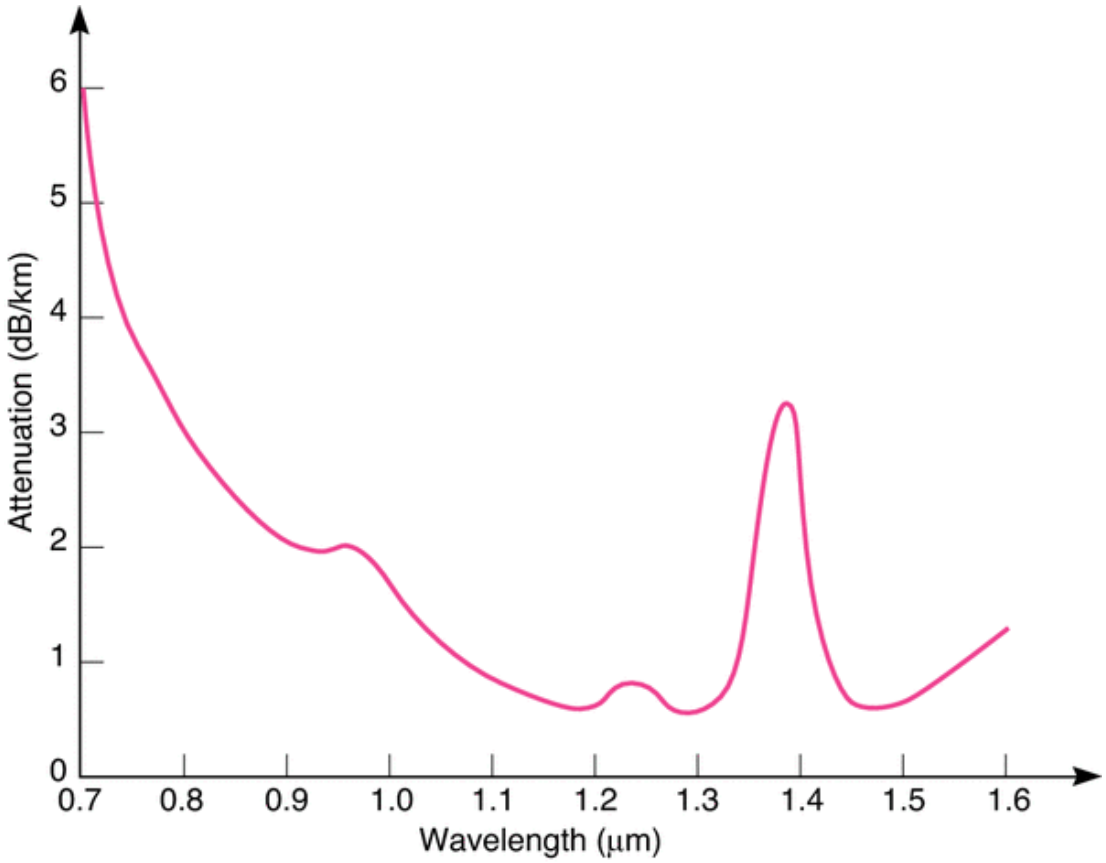


Figure 2.1: Spectral attenuation of optical signals travelling in silica fibres [76].

more expensive to produce and more costly to operate than 1.3 μm lasers based on InP or GaAs. Also the fibre can support a higher bit-rate with lower dispersion at 1.3 μm, provided the higher loss is not an issue. For this reason most short interconnects are based on 1.3 μm technology. In this thesis the topic of 1.55 μm emission is addressed both in terms of an analysis of a quantum dash laser operating at 1.55 μm, and the development of novel materials and devices to extend emission on GaAs to the second telecommunication window at 1.55 μm.

2.3.1 A brief history of diode lasers

A number of books and papers give an account of the history of semiconductor diode lasers [90, 27, 41, 4, 9]. The first electrically pumped semiconductor lasers were based on electron-hole radiative annihilation at a homojunction based on p and n doped bulk semiconductor material, and operated at cryogenic temperatures, and only pulsed. Continuous wave lasing was not possible with these lasers. The real-space band structure of these homojunction lasers, is seen in the top panel of Fig. 2.2. These homojunction lasers had threshold current densities of 10 - 100 kA cm^{-2}, owing at least in part to the absence of both optical and carrier confinement. Carrier and optical confinement were improved in the growth direction by the additional growing of a double heterostructure, which was proposed by Kroemer in 1963 [26], with real space band structure shown in the middle panel of Fig. 2.2. This design proposed an active region which was sandwiched between two doped cladding layers with larger energy gap and smaller refractive index. The two additional cladding layers in this laser design act as an optical waveguide for photons, and also provide a level of carrier confinement to ensure that most of the carriers recombine at the required energy and are not lost through leakage from the laser active region. The first material system proposed to make use of this new double heterostructure laser design, was bulk AlGaAs grown on bulk GaAs, due to the very similar lattice constants of these two materials, often referred to as being lattice-matched. Pulsed and continuous wave lasing were demonstrated at room temperature in 1970 [40, 8, 7], which was a considerable improvement on the cryogenic temperature pulsed operation of the previous homojunction design. Further improvements in diode laser characteristics were seen from the beginning of the 1970s, as the development of molecular beam epitaxy (MBE) and metal organic vapour phase epitaxy (MOVPE) gained traction and growth of semiconductor material for lasers moved from liquid phase epitaxy (LPE) to these new and improved growth methodologies. Some of the advantages accompanying the move to these new growth processes were accu-

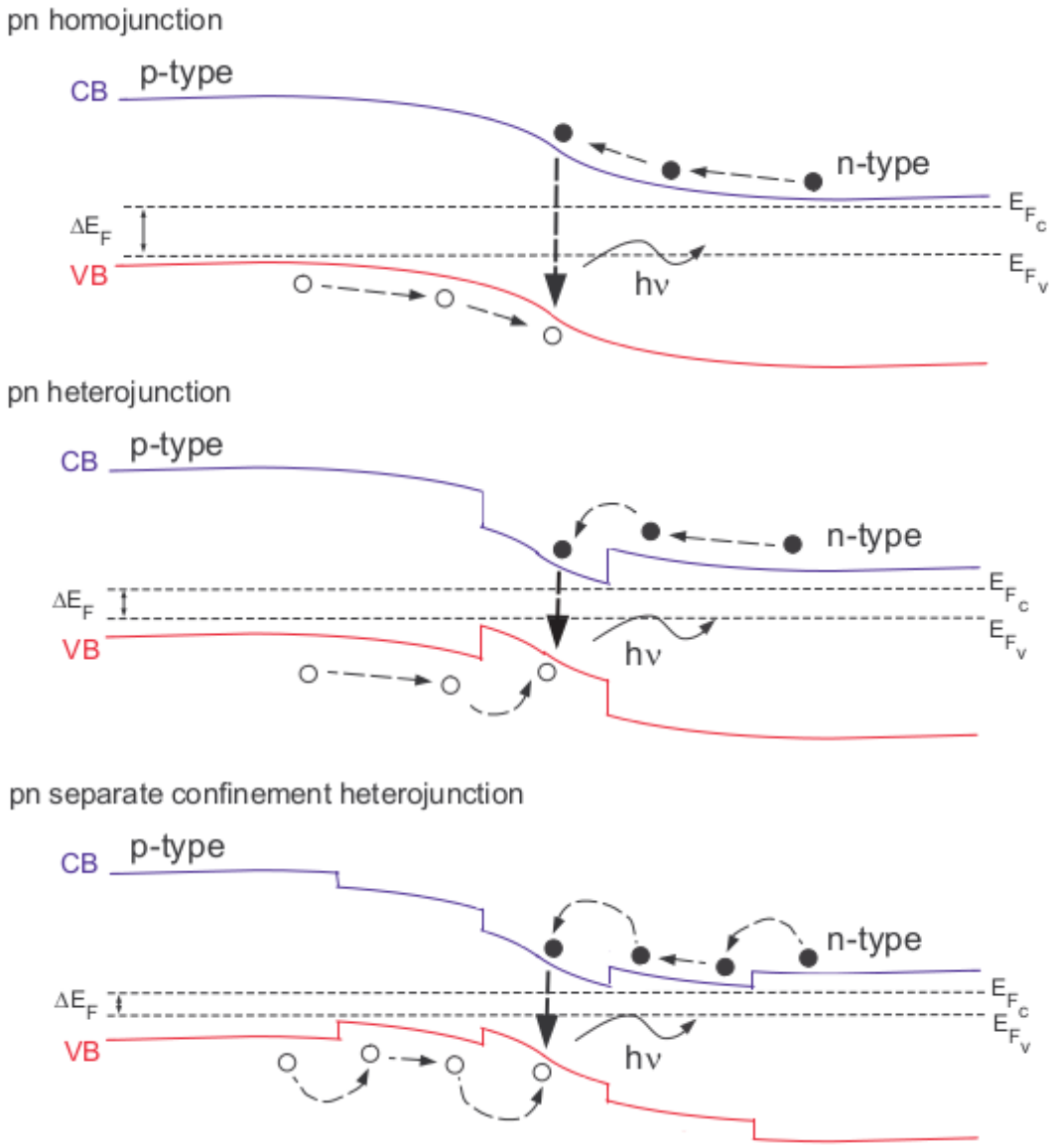


Figure 2.2: Real space representation of the bandstructure of a homojunction laser (top), a double heterostructure laser (middle), and a separate confinement heterostructure laser (bottom). Note the increasing confinement for carriers and photons going from top to bottom [45].

rate, real-time, monitoring of the thickness, composition and planarity of each layer during the growth process. Laser characteristics took another step forward with the development of separate confinement heterostructure lasers, whose real space bandstructure is seen in the bottom panel of Fig. 2.2. These separate confinement regions, as is suggested by the name, provide separate confinement for the carriers and the photons within the structure. This allowed the optimisation of carrier confinement within the structure, and tuning of the waveguide to suit the emission energy separately. After the demonstration of room temperature continuous wave lasing, semiconductor laser diodes found application in many areas, including printing, medicine, data storage and as sources for optical fibre-based telecommunication, as mentioned earlier. The rapid growth in the internet would not have been possible without the roll out of fibre-based optical telecommunication systems where InP-based lasers have played a central role. The growth of quantum wells, which were proposed and demonstrated in the early and mid-1970s [101], was initially challenging even for the new MBE and MOVPE processes. In 1982 the quantum well laser finally outperformed its bulk counterparts [98]. Also in that year Arakawa and Sakaki [11] made the prediction that quantum wire and quantum dot lasers should have reduced threshold current with improved temperature stability compared to quantum well lasers. As with quantum wells, it remained challenging throughout the 1980s and 1990s to grow quantum wires and dots. The first quantum dot laser based on GaAs was demonstrated in 1994 [55] and six years later the first 1.3 μm GaAs-based quantum dot laser with a very low threshold current was reported [81]. GaAs, however, is very difficult to extend to the second telecommunication wavelength window at 1.55 μm. The InP material system is the generally accepted material of choice for this wavelength range, and devices fabricated using this material system are usually comprised of muliple quantum well layers. There are however many inherent problems with this material system. Lasers based on InP have a high temperature dependence of the threshold current and thus require external cooling to stabilise the emitted optical power. The cause of this temperature dependence has been shown to be CHSH Auger recombination [94, 22, 92, 93], which will be discussed in detail further on in this chapter. This recombination mechanism provides for up to 80 % of input electrical power to be converted to heat. Because of this there has been interest in extending GaAs emission to the second telecommunications emission window. There have, however, been issues extending GaAs-based quantum well and quantum dot materials to the second telecommunication window at 1.55 μm, due to the large lattice mismatch between

GaAs and InAs.

Two approaches have been investigated to extend GaAs-based lasers to longer wavelengths. The first involves adding a small amount of N and/or Sb to GaInAs to further reduce the GaAs bandgap [56]. Quantum well lasers have been demonstrated based on this material system [13, 107], but there remain issues related to defects in the active region, and concerns about device reliability. The second approach involves reducing the lattice mismatch between GaAs and InAs by growing a metamorphic buffer layer [59, 109]. Lasing at 1.55 μm has been measured in quantum well and quantum dot lasers with a metamorphic layer [96, 53], but the temperature performance is quite poor. There are also issues of defects in the active region and device reliability in lasers which contain a metamorphic layer.

More recently, and the focus of chapters 5, 6 and 7, came the idea that the addition of bismuth to GaAs can reduce the bandgap of GaAs and offer improved electrical, optical and thermal properties for laser operation at the second telecommunication window and beyond into the mid infrared [94, 22, 92, 93]. The bandstructure engineering of GaAs is discussed in depth within this thesis.

The growth of quantum dots on an InP-substrate is more challenging than on GaAs due to the reduced lattice mismatch. Recently advances have been made in growing quantum dots on the commercially favoured (001)-InP substrate orientation. Using this substrate orientation enables the use of the same fabrication processes as for bulk and quantum well lasers [84, 60]. In chapter 4 in this thesis an experimental analysis of a quantum dash laser based on InP operating at 1.55 μm is presented along with some numerical analysis of threshold dynamics seen in this particular device.

2.3.2 Materials for diode lasers

The successful fabrication and operation of a diode laser is heavily dependent upon the properties of the materials used in the fabrication processes. The available semiconductor materials which possess the relevant qualities to produce a good diode laser are very limited. For double heterostructures, at least two materials must be found which are compatible with each other and have varying bandgaps to produce cladding and active regions. In the more complex separate confinement heterostructure geometries, as many as four of these materials may be required to make up the desired device stack. The underlying requirement for all of these materials is that they have the same crystal structure and very similar lattice constants [26]. The combination of these two requirements allows

the epitaxial growth of defect-free single crystal layers of material. If the layer is of poor quality, it will have a lot of defects. Defects generally act as non-radiative recombination centres and thus reduce efficiency and increase threshold current, as well as reducing device reliability and overall lifetime. In Fig. 2.3, a plot of

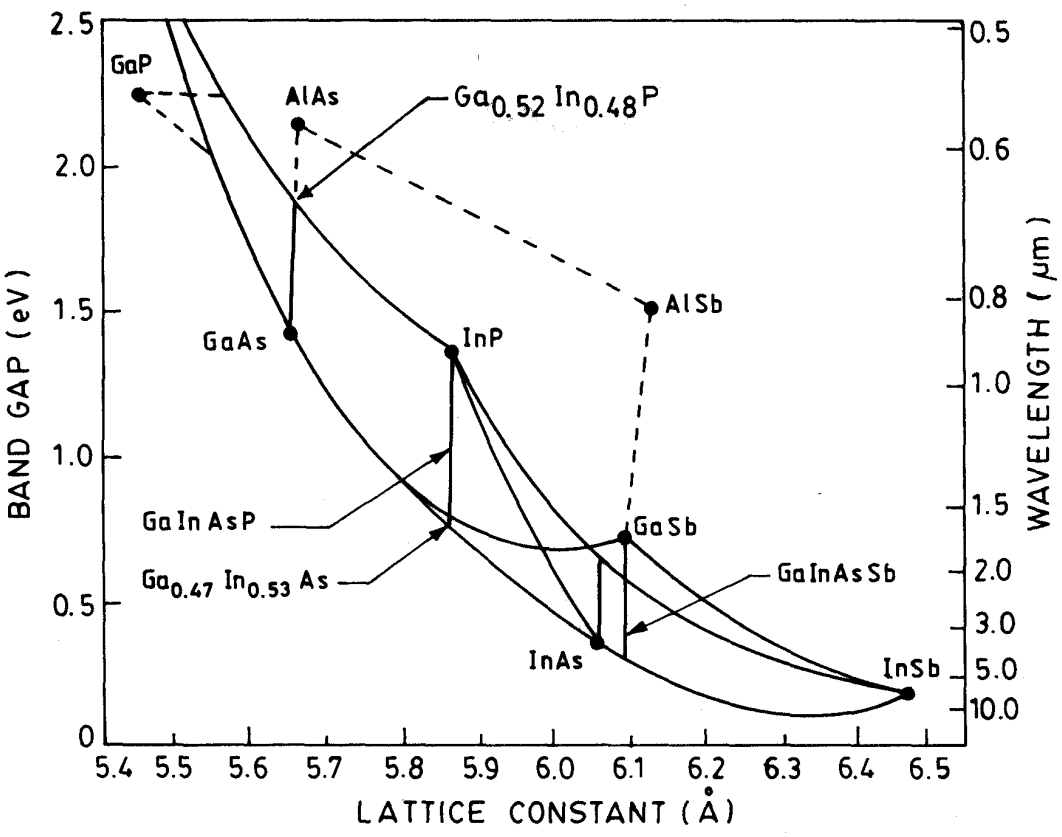


Figure 2.3: Energy gap versus lattice constant for ternary compounds defined by curved lines connecting the binary end point alloys [17].

bandgap versus lattice constant is seen for the most common III-V semconductors. These materials have emerged as the dominant materials for construction of semiconductor lasers. Most of these materials have a direct energy gap, that is, in E-k space the maximum of the valence band and the minimum of the conduction band occur at the same value of k. This means that optical recombination is favoured in these materials due to conservation of momentum due to annihilation of the equal and opposite momenta of the electron and hole [26].

The lines drawn in Fig. 2.3 represent ternary compounds, alloys of the binary compounds labelled at the end points of the lines. The triangular areas enclosed by lines between three binaries illustrate quaternaries, whose energy gap can be adjusted easily without changing the lattice constant by a large amount due to

the large number of degrees of freedom. The dashed lines in the figure represent indirect bandgap alloys and materials, where different k-vectors are associated with the highest valence and lowest conduction band states. These are not ideal optical emitters as optical recombination must be phonon assisted to conserve momentum.

GaAs and $Al_xGa_{1-x}As$ are a special case in alloying III-V's, as is evidenced by the line joining GaAs and AlAs in Fig. 2.3. This line is very close to vertical, meaning that virtually any alloy of the ternary alloy $Al_xGa_{1-x}As$ can be grown epitaxially on GaAs. This gives a large technological advantage to the GaAs material system because devices such as Bragg mirror stacks are quite easy to grow given the available refractive index contrast and lattice-matched growth.

The most popular materials for the 1.55 μm telecommunications window are InGaAsP quaternary alloys grown lattice matched on InP substrates. The quaternary compound is specified as $In_{1-x}Ga_xAs_yP_{1-y}$. It has been found that setting $x \approx 0.46y$ [26] results in lattice matching on InP. Once this ratio is adhered to, the bandgap of the material can be changed by varying x and y, while the material remains lattice matched on InP.

Lattice matching is necessary to avoid defects which degrade the laser characteristics and performance. It is, however, well known that a small lattice mismatch of $\frac{\Delta a}{a} \approx 1\%$ can be tolerated up to a certain critical thickness, ≈ 20 nm, without the introduction of defects into the material. This is of particular interest in quantum well lasers, where the active region is of the order of tens of nm thick. In this case if the lattice matching condition is not met, the lattice constant of the thin quantum well layer has the ability to either stretch, resulting in tensile strain, or shrink, resulting in compressive strain. This strain is compensated in the z direction. A compressively strained well will slightly increase in thickness whereas a tensile strained well will reduce slightly in thickness when compared to their unstrained counterparts. It was generally believed for a considerable period that strain within lasers was not a good thing and that all possible efforts should be made to remove it. However, it has been shown that the introduction of strain, either compressive or tensile, has many positive effects on the characteristics of quantum well diode lasers [3, 78], and a Rank prize has recently been awarded for the work carried out in this area. The introduction of strain into quantum well lasers results in an increase in the energy splitting between the highest heavy-hole and light-hole valence band states, whose degeneracy has already been lifted due to the breaking of the crystal symmetry within the quantum well layer. This has the effect of lowering the density of states at the optical band edge, at the thresh-

old for laisng, and so reducing the carrier and current density required to reach the transparency condition, that the Fermi level separation equals the bandgap [106]. This comes about directly from the fact that either the heavy or light hole subbands (depending upon the compressive or tensile nature of the strain) are no longer at the optical band edge energy, and so the Fermi level separation can equal the bandgap without the need to fill the states associated with one of the bands. This reduction in threshold carrier density is accompanied by a reduction in the threshold current density, as the threshold current density is dominated by Auger recombination, whose magnitude varies in the Boltzmann approximation as n^3, where n is the carrier density. This does not guarantee a reduced temperature dependence of the threshold current density, but should lead to a reduced threshold current density. There are also improvements in efficiency which are gained as a result of changes in the dispersion of the valence bands. Improvements can also be gained in terms of reliability as a result of strain relaxation at the facets. This relaxation inceases very slightly the bandgap at the facet resuting in lower absorption at the facet and less chance of the facet heating resulting in failure of the device.

As the width of the active region decreases from the case of the double heterostructure bulk laser, to a quantum well laser, the carriers begin to become confined along the growth direction. This confinement is increased until the layer thickness is comparable to the De Broglie wavelength for an electron, and so electrons begin to act as a two dimensional gas with momentum quantised in the confined dimension. This brings about some interesting effects not least of which is the change in the density of states within the material. When studying the optical and electronic properties of materials, the density of states close to the band edge is very important. Following this the effect of imposing quantum confinement on the carriers and extending this confinement from 1-D (quantum well) to 2-D (quantum wire) to 3-D (quantum dot) on the density of states will be discussed. As can be seen in Fig. 2.4, there are drastic modifications to the density of states as confinement is increased.

If the case of bulk material is considered, the states are uniformly distributed in k-space and the distance between allowed k values is very small. The number of states, δN, in the interval from k to k + δk is

$$\delta N = D(k)\delta k = D(E)\delta E \tag{2.1}$$

where D(E) is the density of states per unit energy. A parabolic dispersion relation

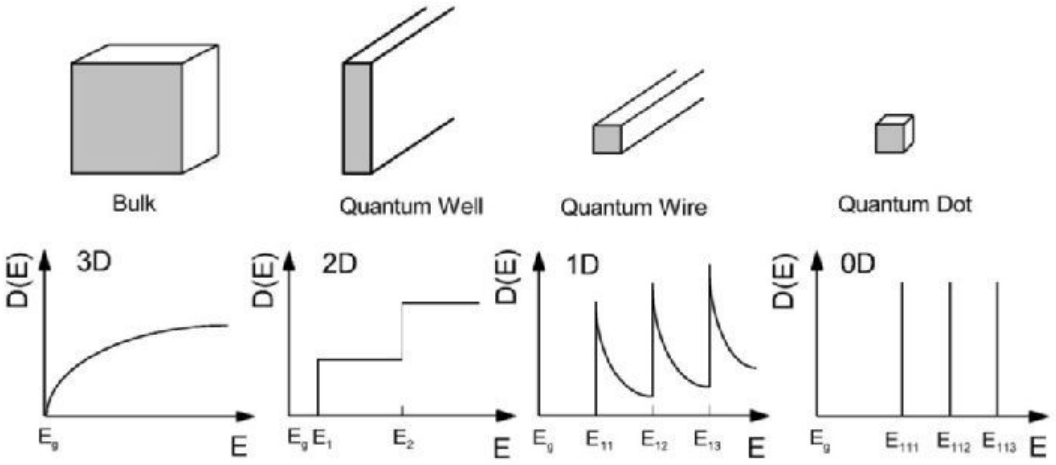


Figure 2.4: Representation of the density of states for bulk, quantum well, quantum wire and quantum dot respectively working from left to right [75].

is assumed

$$E = \frac{\hbar^2 k^2}{2m^*} \tag{2.2}$$

along with a volume V, and δN as the volume of a shell of radius k with thickness δk, $4\pi \mathrm{k}^2 \delta \mathrm{k}$, divided by the volume of a single state, $\frac{8\pi^3}{V}$. A factor of 2 is included to account for the spin.

$$\delta N = D(k)\delta k = 2\left(\frac{Vk^2\delta k}{2\pi^2}\right) \tag{2.3}$$

Writing D(E) by the use of equation 2.1 and using δN from equation 2.3 the expression below is obtained.

$$D(E) = \frac{2V}{4\pi^2}\left(\frac{2m^*}{\hbar^2}\right)^{\frac{3}{2}}\sqrt{E} \tag{2.4}$$

This expression has units of inverse energy. If D(E) is divided by the volume V, the density of states per unit volume, ρ_{3D}(E), is obtained.

$$\rho_{3D}(E) = \frac{1}{2\pi^2}\left(\frac{2m^*}{\hbar^2}\right)^{\frac{3}{2}}\sqrt{E} \tag{2.5}$$

This quantity is illustrated on the left in Fig. 2.4. If one of the bulk dimensions is reduced to the order of a few nm thick then the density of states gets strongly perturbed. If the z direction is reduced than carriers are not free to move in this direction, but only in the x - y plane. By this imposition carrier momentum is

quantized along k_z, and subbands are formed. Considering the density of states as a function of k , D(k), as in equation 2.1 for an area, $A = L_x L_y$, it is seen that the number of states, δN, between k and k + δ k $\propto 2\pi k \delta k$. Following a similar treatment as the bulk case, the density of states for a single subband is found to be

$$\rho_{2D}^{1sub}(E) = \frac{m^*}{\pi\hbar^2} \tag{2.6}$$

To obtain ρ_{2D}(E), as seen in Fig. 2.4 second from the left for 3 subbands, the Heaviside function $H(x - x_0)$ is utilised, where

$$H(x - x_0) = 0 \tag{2.7}$$

if x <0, and

$$H(x - x_0) = 1 \tag{2.8}$$

if $x \geq 0$. It is now possible to write

$$\rho_{2D}(E) = \frac{m^*}{\pi\hbar^2} \sum_{n=1}^{N} H(E - E_n) \tag{2.9}$$

for E $\geq$ E_n, where E_n is the energy of the n^{th} confined state within the quantum well.

The carrier momentum can also be restricted to a single dimension, along y, by the reduction of x and z, to obtain a quantum wire. This situation is illustrated in Fig. 2.4 to the right of the quantum well case. In this case the electron momentum is quantised along x and z and the density of states can be derived as a function of unit length. Following the same analysis as for the bulk case, the density of states per unit length per unit energy for a single subband is

$$\rho_{1D}^{1sub}(E) = 2\frac{\hbar^2}{m^*}\sqrt{\frac{2m^*}{\hbar^2}}\frac{1}{\sqrt{(E - E_{nx} - E_{nz})}} \tag{2.10}$$

for E >(E_{nx} + E_{nz}). As with the quantum well case, the Heaviside function is utilised when a number of subbands are taken into consideration.

$$\rho_{1D}(E) = 2\frac{\hbar^2}{m^*}\sqrt{\frac{2m^*}{\hbar^2}}\sum_{nx,ny=1}^{M,N}\frac{H(E - E_{nx} - E_{nz})}{\sqrt{(E - E_{nx} - E_{nz})}} \tag{2.11}$$

Reducing all 3 dimensions to form a quantum dot, where electron momentum is quantised an all three dimensions, results in a discrete, atomistic-like, density of states as seen on the extreme right of Fig. 2.4.

As well as the discussed changes to the density of states arising from increasing the number of dimensions of confinement, it is also quite clear from Fig. 2.4 that increasing the number of confinement dimensions increases the energy of the first bound state. This has to be taken into account when considering to engineer the bandstructure of semiconductors for laser applications, as the bound state may sit in the barrier instead of the quantum well / wire / dot in some extreme cases.

2.3.3 Device geometry

The previous sections discussed carrier and photon confinement in and about the active region. The discussion mostly focused on confinement in the growth direction. In this section three differing processing methodologies will be discussed and compared for their ability to laterally confine carriers and photons.

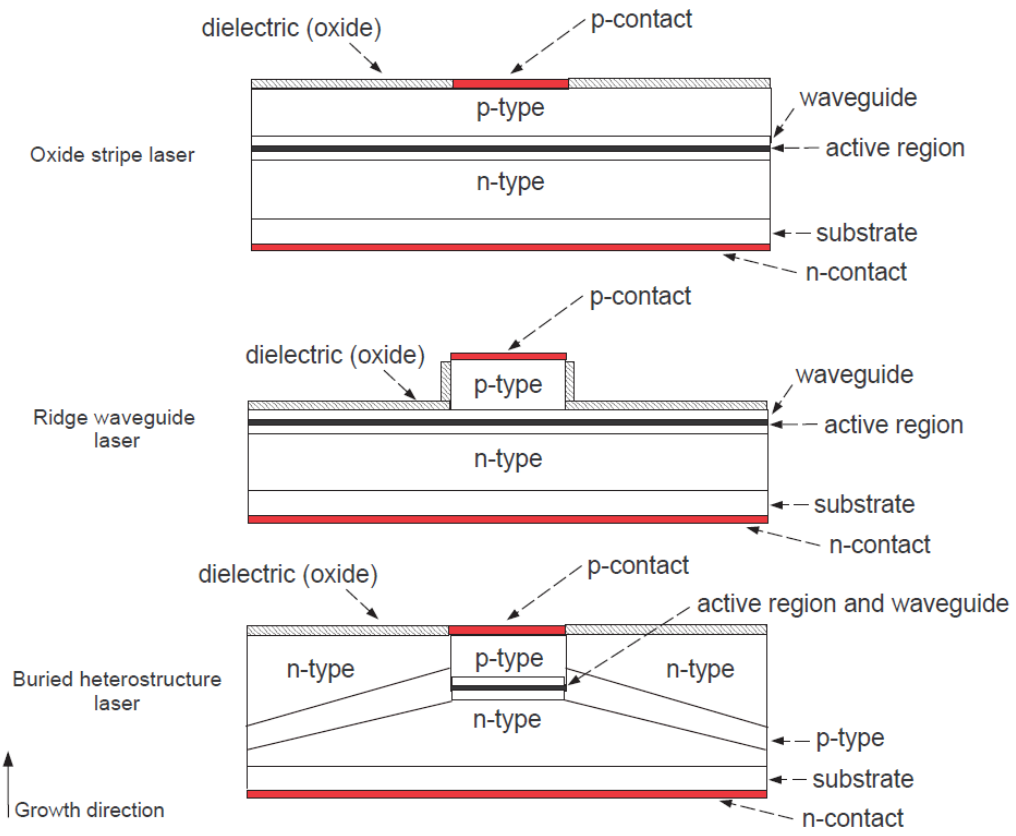


Figure 2.5: Three different processing options for diode lasers. Broad area (oxide stripe) (top), ridge waveguide (middle), and buried heterostructure (bottom) [45].

The three types of processing which will be discussed are shown in Fig. 2.5.

The first, and simplest form of laser structure is called a broad-area, or oxide stripe laser. In this case the epitaxially grown material has a thin dielectric film deposited on the surface of the p doped surface of the wafer. This dielectric film is covered with a photosensitive film onto which windows which define a stripe width are opened through the photosensitive and dielectric layers by selective chemical etching. The wafer is metallised and a lift-off etch removes the unwanted metal from the dielectric layer, but the metal contacts which were deposited on the wafer through the etched windows remain. After this step, the p side of the wafer has a series of stripes, which provide electrical contact to the wafer, separated by regions of non-conducting oxide. The n side of the wafer is completely metallised, leading to electrical contact being achievable on the n-side also. The wafer is cleaved into laser bars perpendicular to the metal stripes on the surface of the p side. Each bar may contain as many as 15 -20 lasers. In this type of laser device, lateral photon confinement is achieved by the slight material refractive index change caused by electrical injection and so devices processed in this manner are regarded as gain guided, and the carriers are not confined laterally and so spread out underneath the contact stripe. This spreading causes degradation of the laser characteristics. The stripe width of these oxide confined lasers is of the order of 20 - 100 μm, which supports the propagation of more than one transverse mode in the cavity; this also degrades the device performance. These lasers are commonly operated using a pulsed drive current, as the heat dissipation properties of the material would not be sufficient to stop the device heating given the large applied currents required to drive such a large pumped area to threshold.

The second laser device considered is the ridge waveguide laser. The processing of this type of device is similar to the broad area device and so will not be repeated in detail. The processing is, however, slightly more difficult. In these devices, as seen in Fig. 2.5, the metal in the ridge waveguide is raised above the surface, this is the ridge. This comes about as a result of most of the top cladding layer being etched away around the ridge allowing a layer of lower refractive index oxide material be deposited on the sides of the ridge. This provides both carrier and photon confinement. Carriers are confined as they cannot spread out in the material before they get to the active region, requiring all of the carriers to excite states in the area defined by the ridge; photons are confined by the high reflectivity created by the large refractive index contrast at the sides of the ridge. This is however only at the p side of the device and so devices processed in this manner are regarded as being weakly index guided. Along with these benefits, these ridges are generally of the order of 0.5 - 5 μm wide, usually allowing only

one transverse cavity mode. The ridge waveguide laser is superior to the broad area laser and results in enhanced lasing characteristics.

The third laser device design considered here is the buried heterostructure laser. This is the most complex design in terms of processing, but also the best in terms of lateral optical and electronic confinement. The buried heterostructure laser can be seen in Fig. 2.5. The processing steps for this laser are the same with the exception that once the ridge is defined lithographically, the etch is continued all through the active region and into the n doped cladding layer. Regrowth is then performed with a lower refractive index material, with a doping profile opposite that of the originally grown wafer. In this way the active region is bounded both parallel and perpendicular by a material of lower refractive index making the carriers and optical mode highly confined. These laser devices are referred to as being fully or strongly index guided. Due to the superior characteristics of this design, these lasers are widely implemented even though they are much more difficult to process.

2.3.4 Carrier generation and recombination in active regions

When light and matter interact, such as in the active region of a diode laser, there are three possible processes which take place. These processes are illustrated in fig. 2.6. The first process is known as spontaneous emission. This is shown in the top panel of fig. 2.6. This occurs in the case where an electron is excited from the lower state (valence band) of energy E_1, to the upper state (conduction band) of energy E_2. The electron is not stable in this excited state and so after a short period of time decays back to the original lower state via the emission of a photon of energy E_2 - E_1. This is the dominant processes in a diode laser when the drive current is less than the threshold current.

The second process in fig. 2.6 is absorption. This is depicted in the middle panel of fig. 2.6. If a photon is travelling in the material, with an energy of E_2 - E_1, this photon can cause the excitation of an electron from the lower energy E_1 to the upper E_2 state by absorption. This excited electron can then behave as described above, decaying back to the lower energy state by spontaneous emission, or by stimulated emission which will be discussed next.

Stimulated emission is the process by which lasing occurs and is shown schematically in the bottom panel of fig. 2.6. This process becomes more favoured than absorption at high drive current levels, close to threshold current, where there is a population inversion (more electrons in the upper state than the lower

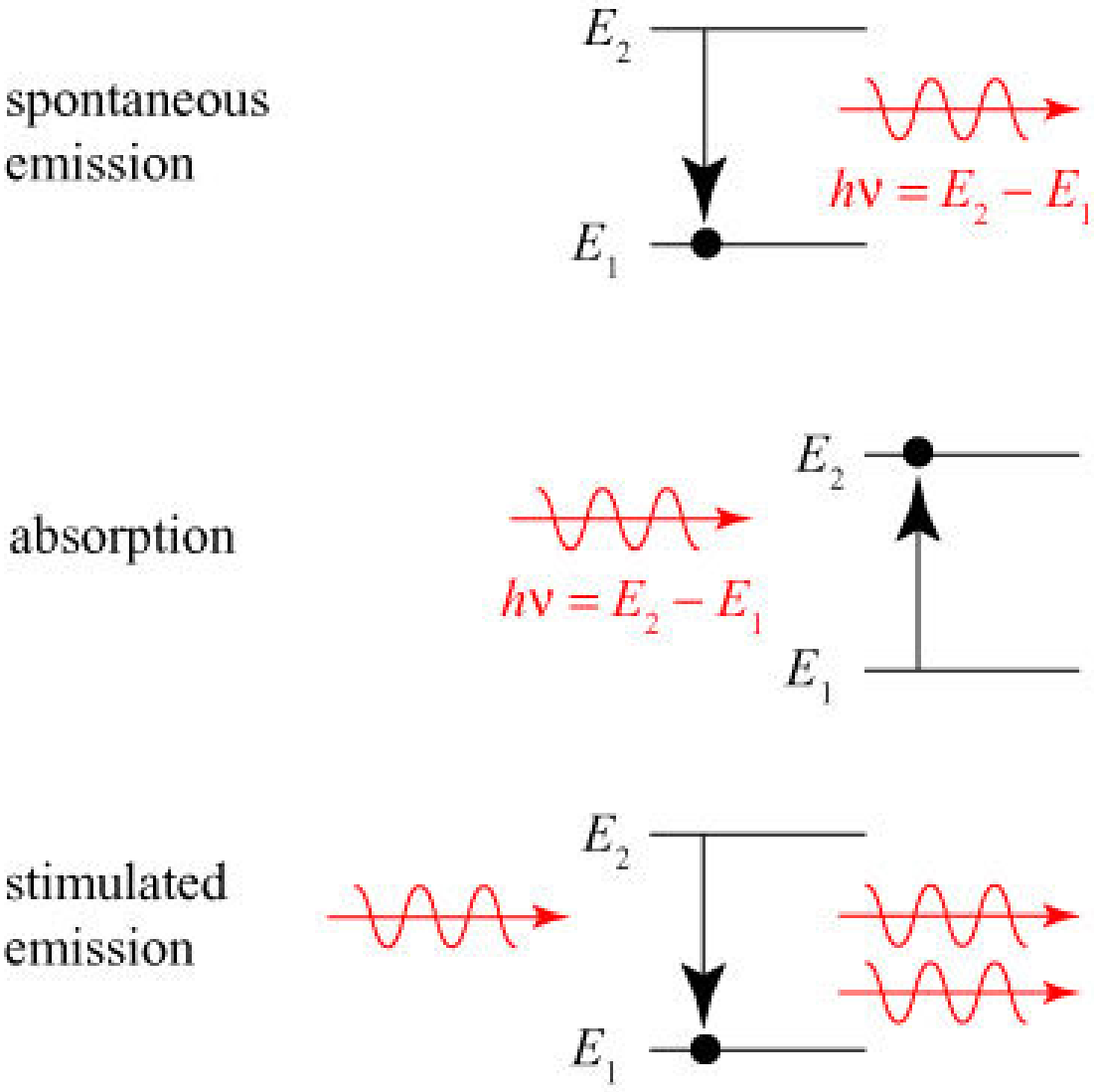


Figure 2.6: Schematic illustration of the three possible outcomes of light-matter interaction. Spontaneous emission (top), absorption (middle), and stimulated emission (bottom) [51].

state). This inversion results in net material gain, which in turn renders the material transparent to a photon of energy E_2 - E_1 travelling through it. As this photon interacts with the excited states, it induces the emission of more photons of the same phase, amplitude and direction, resulting in generation of coherent light. Carrier lifetime is a quantity which describes the amount of time an electronic charge carrier is stable in the excited state. This is a very important parameter for laser materials as if the lifetime is too short achieving population inversion becomes very difficult, whereas if the lifetime is too long (stable) the state may not interact strongly with the optical mode. If a material which achieves inver-

sion is placed within an optical cavity then optical feedback provides the last key ingredient to achieve lasing. Sources which reach the transparency condition but do not have sufficient feedback to produce lasing are known as superluminescent. Stimulated emission dominates laser output above threshold and any additional carriers injected above the threshold carrier density result in an increase in the optical power output.

These processes can be thought of in terms of an analogy with a water reservoir. An illustration of this analogy is seen in Fig. 2.7. In this picture the large

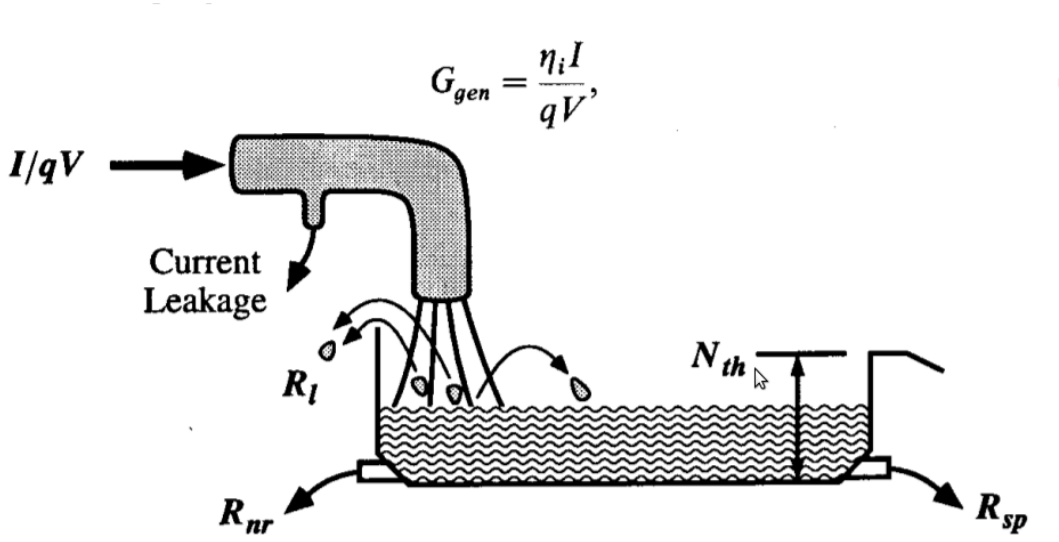


Figure 2.7: Reservoir analogy for the competing processes at play when trying to reach threshold in a diode laser [26].

pipe supplying the water is equivalent to the electrical pumping source which would commonly be used for a diode laser. The amount of carriers per volume per second which reach the active region, G_{gen}, is described by the injected current, I, times an injection efficiency, η_i (typically ≈ 80 %), which takes account of carrier loss mechanisms including injection leakage, divided by the charge on the electron, q, and by V, the volume of the active region. Once the carriers get to the active region, they start to fill the reservoir. Three processes, two optical and a leakage term try in turn to deplete the reservoir of carriers. The first process is, R_l, this describes carriers which gain enough thermal energy to pass the potential barrier of the active region. In a well designed laser this quantity should be small. R_{nr} is the non-radiative recombination rate and is highly dependent upon carrier density. R_{sp} is the spontaneous emission rate and is also highly dependent upon carrier density. N_{th} is the threshold carrier density. As can be deduced from Fig.

2.7, once G_{gen} is larger than $R_{nr} + R_{sp}$ (assuming R_l is negligible) at a particular flow rate, the level of water in the reservoir will rise, and so for a diode laser, the carrier density will rise. If this condition is satisfied up to the line at N_{th}, than the laser has reached threshold. Any additional carriers introduced to the active region will result in stimulated emission but no increase in carrier density. As seen in Fig. 2.7 any additional water will flow away over the spillaway, resulting in no additional rise in level. Because of this carrier density pinning at threshold, the spontaneous emission rate and gain are also pinned, as these are heavily dependent on carrier density. Any additional carriers result in stimulated emission from the active region, and so, lasing. This explains the discontinuity seen in the laser light-current characteristic in Fig. 2.8. For lasing action to occur, the round

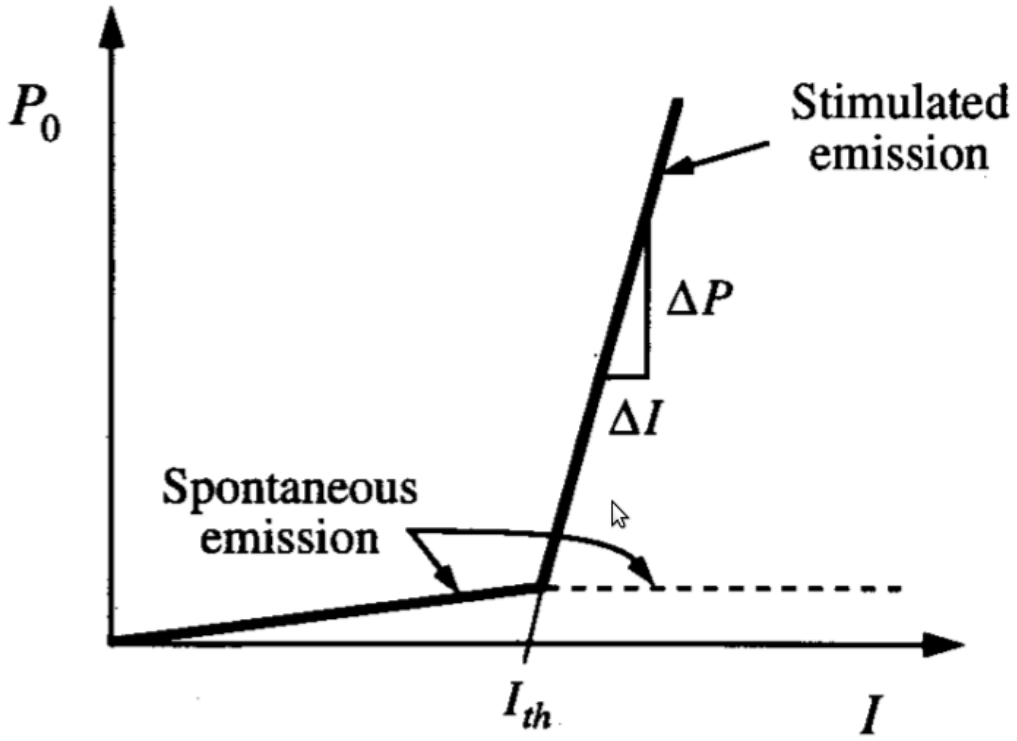


Figure 2.8: Example laser light-current characteristic showing different processes above and below threshold [26].

trip gain of the laser cavity must equal the propagation and transmission losses. This can be written as

$$\Gamma g_{th} = \alpha_i + \frac{1}{L} \ln\left(\frac{1}{R}\right) \tag{2.12}$$

where Γg_{th} is the normalised threshold gain, α_i represents internal losses within the laser cavity and the $\frac{1}{L}\ln\left(\frac{1}{R}\right)$ term describes the cavity mirror losses.

2.3.5 Matrix elements

The transition rate of an electron in a state 2 to a continuum of final states 1 in the presence of a harmonic perturbation, such as an electromagnetic field, is given by Fermi's Golden Rule [26], and is proportional to

$$\frac{2\pi}{\hbar}|H_{21}^{'}|^2 \tag{2.13}$$

where $|H_{21}^{'}|^2$ is the square of the matrix element evaluated at E_{21}, which determines the strength of the interaction between the initial and final states and the optical field. The matrix element H_{21}, is given by

$$|H_{21}^{'}| = \int_V \psi_2^* H_r^{'} \psi_1 d^3r \tag{2.14}$$

where ψ_1 and ψ_2 are the wavefuntions of the isolated electron in states 1 and 2, while $H_r^{'}$ is the Hamiltonian characterising the electronic state and its interaction with the electromagnetic field. In a quantum well, ψ_1 and ψ_2 can be decoupled into a slowly varying envelope function, $F(\mathbf{r})$, which satisfies Schrödinger's equation at a macroscopic level, and a complex Bloch function, $u(\mathbf{r})$, which repeats itself over each unit cell and satisfies Schrödinger's equation at an atomic level. The difference between $F(\mathbf{r})$ and $u(\mathbf{r})$ can be seen schematically in Fig. 2.9. The valence and conduction band wavefunctions can be written

$$\psi_1 = F_v(\mathbf{r})U_v(\mathbf{r}) \tag{2.15}$$

$$\psi_2 = F_c(\mathbf{r})U_c(\mathbf{r}) \tag{2.16}$$

H_r is related to the vector potential $A(r)$ and can be written as [32]

$$H_r^{'} = \frac{qA(\mathbf{r})}{2m_0}(\mathbf{e}\cdot\mathbf{p}) \tag{2.17}$$

where the unit vector $\mathbf{e}$ gives the polarisation direction and $\mathbf{p}$ is the momentum operator. If we substitute equations 2.15, 2.16, and 2.17 into equation 2.14 and assuming that the vector potential is a plane wave with magnitude A_0 and no

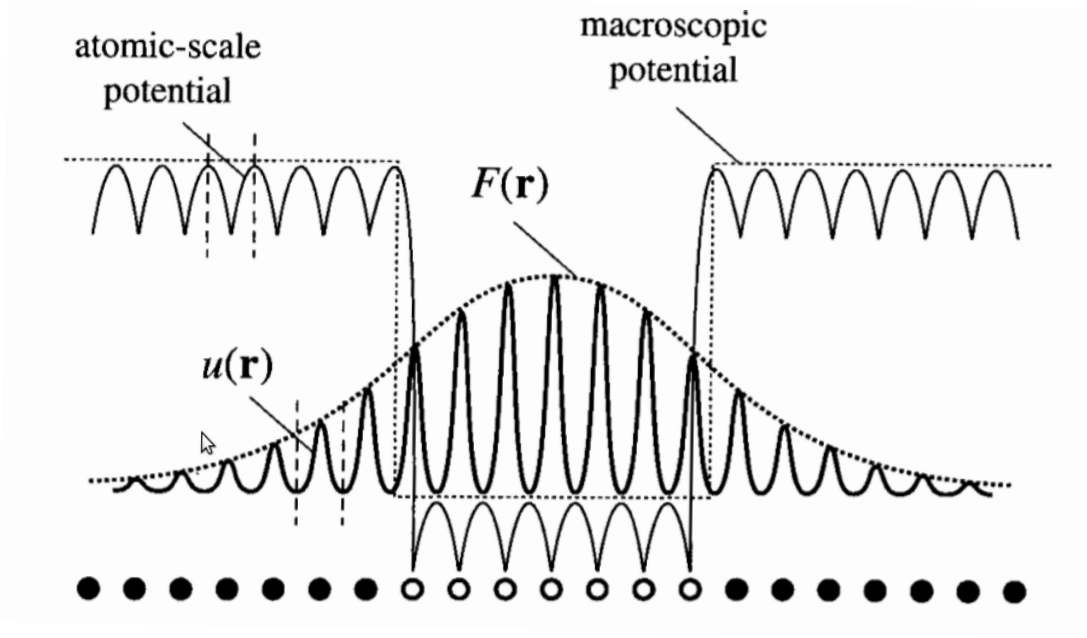


Figure 2.9: Representation of the atomistic potential, u(**r**), and the accompanying envelope function F(**r**) in a periodic crystal structure [26].

spatial dependence, we obtain

$$H'_{21} = \frac{qA_0}{2m_0}|M_T| \tag{2.18}$$

where $|M_T|$ is the transition matrix element and is equal to the product of the overlap integral, $< F_v(\mathbf{r})|F_c(\mathbf{r}) >$, and the momentum matrix element, $|M| = < U_c(\mathbf{r})|\ \mathbf{e}\cdot\mathbf{p}\ |U_v(\mathbf{r}) >$, which gives the polarisation dependence of the interaction. We substitute equation 2.18 into equation 2.13 and can write $|M|^2 = S_x|M|^2 + S_y|M|^2 + S_z|M|^2$, where S_i is the relative transition strength at the band edge along the i^{th} direction. The polarisation dependence of $|M|^2$ does not reveal itself in bulk due to a uniform distribution of electron momentum. However when a quantum well is grown, the degeneracy of the heavy-hole (HH) and light-hole (LH) levels is lifted, with the HH states lying above the LH states in unstrained and compressively strained quantum wells. When light is emitted (absorbed) by recombination into (from) a pure HH state in a quantum well, the emitted (absorbed) photon is polarized in the x − y plane with $S_x = S_y = \frac{1}{2}$ and $S_z = 0$, giving what is referred to as TE-polarized emission (absorption). By contrast, $S_z = \frac{2}{3}$ and $S_x = S_y = \frac{1}{6}$ for a pure LH state, so that transitions involving LH states are predominantly TM -polarized, with the electric field pointing along the z-direction [26].

Non-radiative transitions in diode lasers are, as the name suggests, transitions between electrons and holes which do not produce photons. These transitions are not favourable to good laser characteristics as they produce waste heat in many circumstances, reduce laser efficiency, and increase threshold currents.

Carrier leakage, as discussed earlier, occurs when carriers within the active region are not adequately confined and gain enough thermal energy to escape to the barrier and cladding layers. These carriers can then recombine either radiatively or non-radiatively in these barrier/cladding regions. This process reduces the differential efficiency of the laser and increases the threshold current.

Monomolecular defect-related recombination is a process whereby carriers can recombine in defect states within the bandgap of a semiconductor crystal. These states can be associated with vacancies, dislocations or impurities within the crystal created during the growth process. The defect-related recombination rate is proportional to the carrier density.

Auger recombination is a process whereby an electron and hole recombine, but instead of the generation of a photon, a carrier is promoted in the conduction band or in the valence band. There are three main types of Auger recombination, with the names given to the different Auger processes reflecting the types of carrier involved in that process. Due to Auger recombination being a three carrier process, the Auger recombination current is proportional to the cube of the carrier density. This means that for typical carrier densities of diode lasers, Auger recombination is often the dominant factor in the determination of the threshold current. The resultant excited carrier from this process scatters off the lattice on its way back to the band maximum or minimum and produces waste heat. The specific type of Auger recombination which effects 1.55 μm InP based telecommunication lasers will be discussed in the next section.

2.3.6 Auger recombination

Auger recombination is highly reliant upon a suitable bandstructure in which the required three carrier process can conserve energy and momentum. In incumbent InP based telecommunications lasers, CHSH Auger recombination has been shown to be the dominant loss mechanism [82, 93, 88]. This type of Auger recombination occurs where an electron near the conduction band minimum and a hole near the valence band maximum recombine, giving up their energy to another hole and thus promoting it to the spin split-off-band. This hole then relaxes back to the valence band maximum producing waste heat, and contributing to a highly temperature sensitive threshold current. This temperature sensitivity introduces

the requirement for external cooling equipment with these telecommunication laser chips, to allow operational stability, at a very large energy and equipment cost.

2.3.6.1 Removal of CHSH Auger recombination through bandstructure engineering

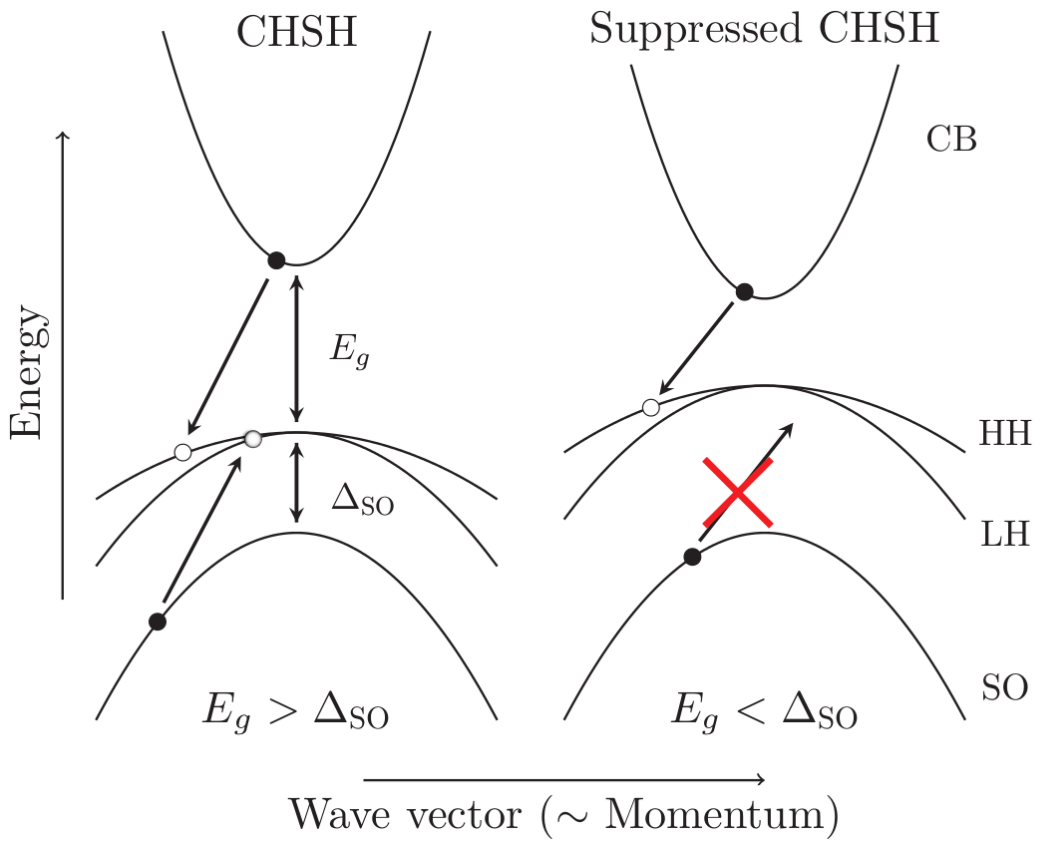


Figure 2.10: Schematic representation of the predicted CHSH Auger recombination suppression due to bandstructure engineering.

It has recently been suggested that this non-radiative recombination pathway can be removed from telecommunications lasers using a bandstructure engineering approach. The addition of bismuth to GaAs to form the alloy $GaAs_{1-x}Bi_x$ results in a rapid decrease in the band gap energy, E_g, and superlinear increase in the spin orbit splitting energy, Δ_{so} [94, 22, 92, 93]. It is predicted that at x ≈ 10%, along with reaching the milestone 1.55 μm emission on GaAs, the Auger suppressing bandstructure illustrated in Fig. 2.10 will be achieved with $\Delta_{so} > E_g$ and this non radiative recombination process then being suppressed due to the requirement for

conservation of energy and momentum. Chapters 5, 6, and 7 provide an in depth discussion of this topic.

2.4 Summary

In this chapter some backgound information and context for the chapters to come has been provided. This was achieved with a brief description in section 2.2 of laser action and a comparison of semiconductor, gas, and solid state lasers. Following this an overview of the properties of diode lasers was presented in section 2.3. Section 2.3 was split into subsections each of which dealt with a feature of diode lasers. In section 2.3.1 a brief history of the diode laser was given, from bulk homojunction to quantum well, wire, and dot separate confinement heterostructures. Section 2.3.2 discused materials used in modern diode laser active regions, including strained quantum well materials and a description of how the density of states changes when going from bulk material to quantum confinement. In section 2.3.3 a description of 3 different processing approaches for edge emitting lasers was described. Section 2.3.4 discussed different carrier recombination mechanisms and how the interplay of these affect the threshold condition. In section 2.3.5 the selection rules for allowed transitions in quantum confined materials were given, followed by a discussion of non radiative recombination mechanisms. Section 2.3.6 discussed Auger recombination and its role in incumbent InP based telecommunications lasers, and how bandstructure engineering can be employed to remove this costly loss mechanism.

Chapter 3

Research methodologies

3.1 Introduction

As has been outlined in chapter 1, this thesis is concerned primarily with temperature dependent optical emission and absorption measurements. These measurements are designed to further our understanding of the bandstructure of materials composed of highly mismatched alloys of GaBiAs, and InP/InAs quantum dashes, and to show how the bandstructure of these materials change with temperature and composition. Measurements are also made on processed laser devices to determine operating properties and efficiencies and to determine the radiative and non-radiative processes at play.

This chapter will be split into two sections. In section 3.2, the main laboratory equipment used in the experimental procedures will be described. Section 3.2.1 discusses the cryostat set-up which is required for all of the temperature dependent measurements, and in sections 3.2.2 - 3.2.6, the rest of the equipment used to construct the various experiments is introduced.

In section 3.3, a detailed description of the various arrangements of the equipment appropriate to each of the experimental techniques is given. This will be followed in each case by an outline of how the results obtained using the measurement technique are helpful for our understanding of the associated material properties. The measurement of pure un-amplified spontaneous emission (SE) is problematic in edge emitting laser structures due to the geometry of the active region and waveguide. Section 3.3.1 explains how spectrally resolved SE spectra of edge emitting laser structures are measured. In section 3.3.2, the technique for measuring temperature dependent SE and facet emission is explored. This technique allows investigation of the variation of I^{th}_{total} and I^{th}_{rad} with temperature and is a valuable device characterisation tool. Section 3.3.3 details the

method employed for temperature dependent optical time trace capture, used to characterise threshold dynamics. In section 3.3.4, the temperature dependent photoluminescence (PL) method used in this work is described. PL spectroscopy is a characterisation tool for direct band semiconductors and yields bandstructure information. Finally in section 3.3.5 the method for collection of photovoltage spectra is presented. PV spectroscopy is the method which has the widest application in this thesis, and the technique utilised allows investigation of the lifting of the degeneracy at the VB edge of QW materials, and further details of the bandstructure.

3.2 Laboratory equipment

In the following section a description of the most frequently used equipment used in the laboratory will be given.

3.2.1 Cryostat

The cryostat used in this work is an Advanced Research Systems (ARS) closed cycle liquid helium cryostat. It is capable of of achieving temperatures as low as 8 K, and up to 400 K, with temperature stability of 0.01 K. This allows measurements over a very broad temperature range. The cryostat operates under a pneumatically driven Gifford-McMahon refrigeration cycle [95] where high pressure helium from the compressor undergoes a pressure drop in the cold head of the cryostat, expands, and in so doing removes heat. This low pressure helium travels back to the compressor where the pressure is once again increased. The heat removed from the cryostat cold head is transferred to cooling water in the compressor and then dumped. The schematic representation of this system is shown in Fig. 3.1. The cryostat is only capable of cooling once the compressor is switched on. The refrigeration cycle works to drive the temperature of the cold head to 8 K. Temperature variation is achieved through a heating coil located at the end of the cryostat cold finger, and a temperature controller. The temperature controller monitors the temperature by measuring the voltage of a calibrated precision silicon diode located on the sample holder. It implements a proportional, integral and derivative (PID) control algorithm to adjust the current flow to the heating coil to reach the desired temperature set by the user, or LabView routine. This cryostat was used for all of the temperature dependent experiments discussed. Numerous mounts for the cold finger of this cryostat

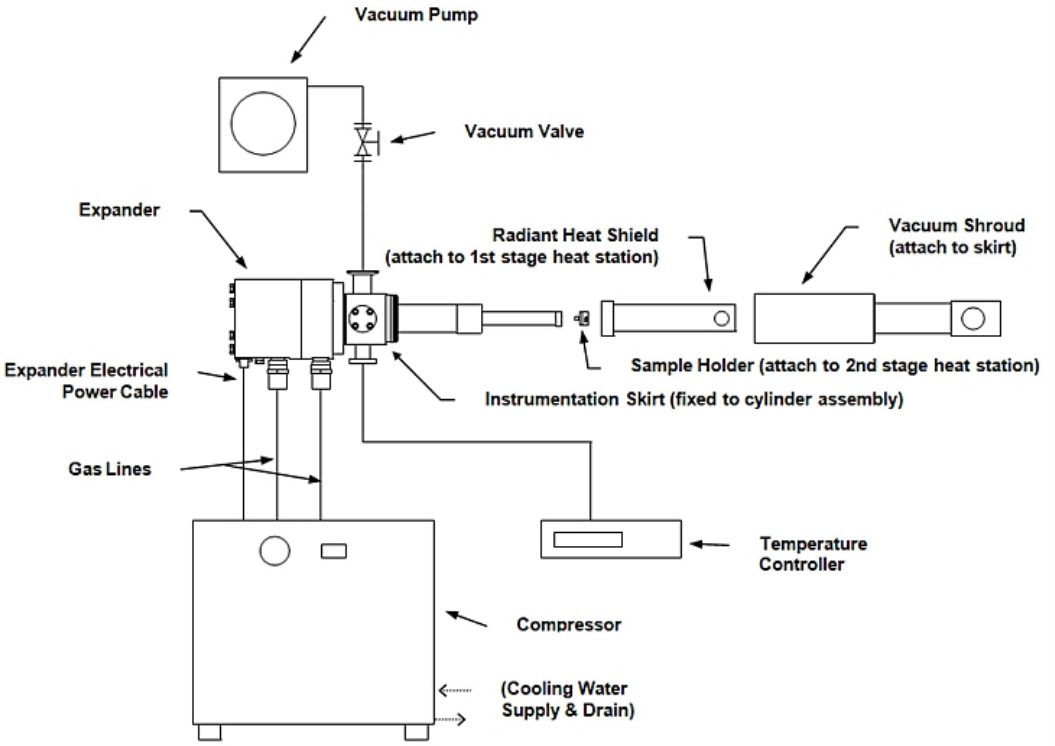


Figure 3.1: Schematic of the ARS cryostat [95]

were developed for the different measurements; these will be discussed with their accompanying measurement technique in the following section.

3.2.2 8 GHz oscilloscope

The oscilloscope used in this work is an Agilent Infinium 8 GHz oscilloscope. The shortest pulse measurable by this oscilloscope is 0.1 ns, due to bandwidth limitations. This oscilloscope is used to measure laser optical time traces. Any dynamics slower than the ns regime that are present in the optical signal can be measured. For dynamics happening on a quicker timescale than this, an autocorrelation measurement is required.

3.2.3 Lock-in amplifier

The lock-in amplifier used is an EG&G DSP 7260. A lock-in amplifier is an instrument used for signal recovery of poor quality signals with low signal-to-noise ratio (SNR) [83]. Signal recovery is achieved through phase sensitive techniques [1]. In this work, this instrument is generally used where measurement of an optically induced voltage, either from a detector or laser structure is required. These

voltages can be very small and noisy. The incident light is chopped at a reference frequency with a 50 % duty cycle which is known to the lock in amplifier. The amplifier then integrates the measured signal, using a phase sensitive detector. When the optical signal is blocked by the chopping wheel, the measured signal contains only noise. When the optical signal is allowed to pass by the chopping wheel, the measured signal will contain signal and noise mixed together. The lock-in amplifier integrates the measured signal in both regimes, and removes the former from the latter, thus removing a large portion of the noise from the measured signal. There is a time-constant which is set on the lock in amplifier which determines how many of these on-off cycles are averaged before the signal is determined. The more of these cycles that are averaged, the less noise will be contained in the measured signal, but the longer the measurement will take. This introduces a trade-off between time efficiency and measurement quality. The procedure implemented by the lock-in amplifier creates a narrow band pass filter at the chopping frequency, dramatically reducing the noise spectrum.

3.2.4 Spectrograph

A large portion of the work undertaken in this thesis involves spectrally resolving light emitted from a material, or light which is destined to illuminate a material. This spectral resolution is achieved in most cases using a Princeton Instruments Acton SpectraPro 2150i spectrograph. This is an imaging grating spectrometer with a focal length of 0.15 m and a 600 line/mm 1 μm blazed grating. The resolution of the spectrograph is 11nm/mm, where the length measurement in the stated resolution refers to the manually set slit-width. This relation between resolution and slit-width results in a sensitivity and resolution trade-off when using the spectrograph. Light is coupled in and out of the equipment using two sets of f-number matched lenses, one for the input slit and one for the output slit. A calibrated tungsten irradiance standard is used for spectral illumination experiments, while the InGaAs detector which will be discussed in the next section is used to detect light generated in emission measurements.

3.2.5 InGaAs Femtowatt detector

For spectrally resolved emission measurements, and measurements of throughput for measuring instrument response functions, a Bookham New Focus 2133 femtowatt front end optical receiver is used. This contains an InGaAs PIN photodiode which allows optical detection up to 1.6 μm. The detector is designed to

provide excellent sensitivity, dynamic range and gain, as well as having fast gain recovery with 20 kHz bandwidth, to aid detection of modulated optical signals for phase sensitive measurements. This detector is used to measure the spectrally resolved emission from materials due to its superior sensitivity, as the optical signals can be very weak in high resolution spectral measurements.

3.2.6 Pulsed current source

Most of the devices studied in this thesis are broad area 50 μm or 100 μm oxide stripe laser structures. These cannot be CW pumped electrically due to heating effects, and so a pulsed current source is required. An Agilent 8114A pulsed current source is used. This has a current output limit of 2 amps and can source 50 Volts. This is generally used to pump lasers at 10 KHz with a 1 % duty cycle to minimise device heating. The applied current is measured using a current probe and digital oscilloscope due to the fact that these pulse generators infer the current flowing by assuming a 50 Ω load and using the applied voltage.

Interfacing to all of the equipment discussed in this section is carried out using NI LabView and the GPIB (general purpose interface bus) protocol. Once the experiments which will be discussed in the next section are designed, their implementation is achieved by decomposing the experimental technique into the fundamental tasks required of each instrument. LabView routines are then developed to automate the measurement by communicating in turn with each instrument as required and either collecting experimental data or changing the experimental operating conditions, such as the temperature, electrical pump power or optical pump power.

3.3 Measurement techniques

The main experimental methods used in the thesis will be explained in this section. After this in each case the merits of the method will be discussed before an overview is presented of how the method helps further our understanding of the properties of the material/device under test. The methods are discussed in order of their use in the thesis.

3.3.1 Spectrally resolved spontaneous emission measurements

As mentioned in the introduction, SE measurement cannot easily be achieved from the facet of edge emitting laser structures [37]. This is because light which is emitted from the facet has passed through the waveguide and gain region, and thus may have undergone some amplification. Some authors misleadingly refer to this amplified spontaneous emission (ASE) from the facet as SE [38]. This amplification can be circumvented by measuring SE through a transparent window etched in the substrate of the laser structures [82]. Windows can also be made during the processing of the laser devices [46] The nature of a quantum well (QW) structure is that it is extremely thin in the out-of-plane direction. This means that even if there is significant reflection of the SE by the waveguide in the z direction, photons will undergo negligible amplification, due to the very thin nature of the gain region in this direction. The transparent windows are achieved by etching the laser substrates using a technique known as focused ion beam (FIB) milling. A FIB is very similar to an electron microscope in its operation [104]. A beam of highly energetic ($\approx$ 30 keV) gallium ions (Ga+) bombard the substrate and remove some of the substrate material along with the metal of the bottom contact [91, 85]. The spatial resolution of this beam is $\approx$ 10 nm. The window is generally milled along the length of a laser bar, which may contain 6-8 lasers, allowing comparison of results from different devices along the laser bar. Measurements of the laser light-current-voltage (L-I-V) characteristics are made before and after windowing to ensure no damage has been done to the laser electrical characteristics during windowing. The windows are 5 μm wide and 5 μm deep.

Once windowing has been completed the lasers are mounted on a specially designed SE measurement mounting system. This mount is shown schematically in Fig. 3.2. The mount consists of a horizontal brass block with a height adjustable, vertical, cylindrical brass bushing attached on its end. There is an electrically insulated copper spring clip with height adjusting screw to electrically contact devices, which sits over the bushing. The contacting spring clip system has a silver wire as the contact surface to ensure excellent electrical contact characteristics. The centre of the brass bushing has a 100 μm hole in it into which a bare cleaved optic fibre is glued using a temperature stable epoxy glue. The top surface of the bushing is polished to avoid scattering of the light emitted from the window in the laser substrate. The mount has a terminal to connect to the cryostat temperature sensor, and also attaches to the cryostat cold head to provide both room

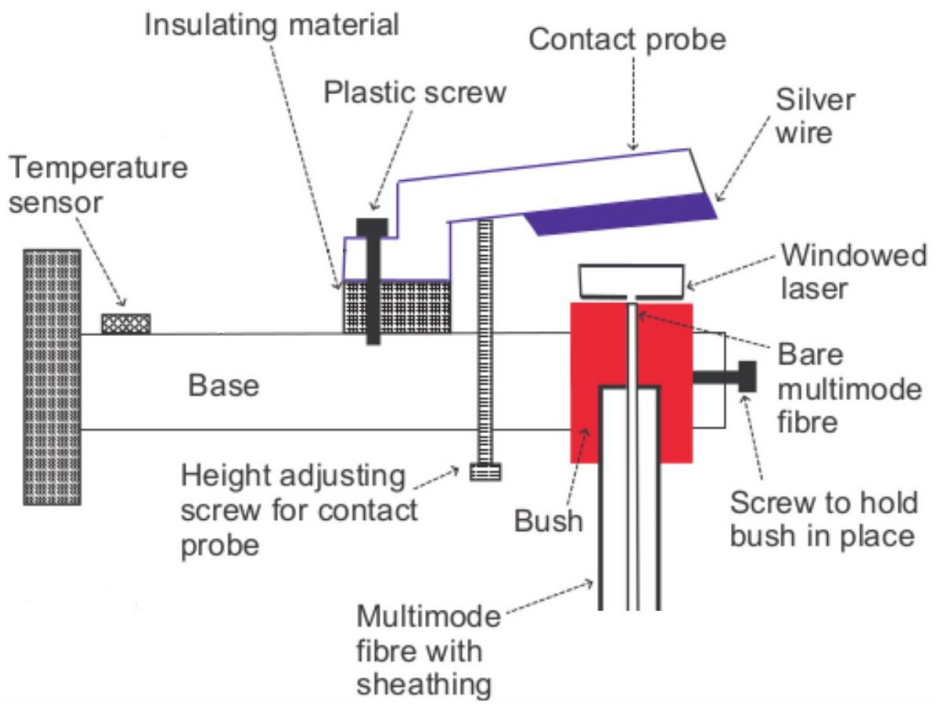


Figure 3.2: Schematic of the SE measurement mount. Figure modified from [45].

temperature and temperature dependent capabilities.

Devices are placed on this mount with the transparent window facing the polished fibre in the brass bushing. The electrical contact clip is lowered to achieve electrical contact to the device, electrical injection is applied (pulsed or CW, device dependent), and the device position is optimised to achieve optimum SE coupling efficiency from the substrate window into the fibre. The light output from the fibre is incident on a fibre coupled detector for optimisation of the signal as the integrated SE is a much easier quantity to measure than the spectrally resolved SE.

To measure the spectrally resolved SE after this set-up work has been completed, the device is forward biased electrically, usually to threshold current, and the SE spectrum is collected using an optical spectrum analyser. The spectrum can be analysed at any drive current; however, using this windowing technique, laser emission is scattered into the SE once threshold current is exceeded and the laser peak is then visible in the SE spectrum, as is clearly seen in Fig. 3.3. This measurement can be made temperature dependent very easily by inserting the mount into the cryostat and varying the temperature between the available limits of 8 K and 400 K. A more thorough discussion of temperature dependent SE measurements will be provided in the next section.

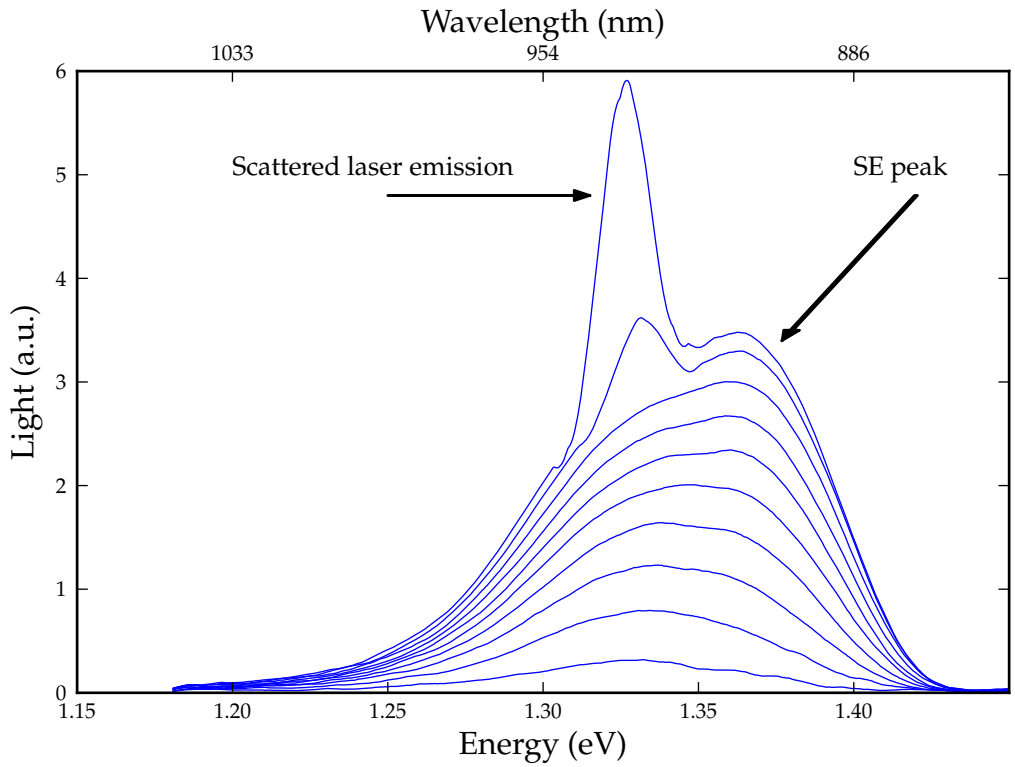


Figure 3.3: Injection level dependent SE spectra of a GaBiAs QW laser

SE measurements give information about the bandstructure and carrier distribution within the device under test [37, 46, 54]. The SE spectrum is, essentially, a visual representation of the distribution of carriers in the semiconductor active region under electrical injection. This carrier distribution, and its energy, are dependent upon the bandstructure of the device. From this measurement we can extract the main band to band transition energy of the material and also the broadening of the optical transition, which is an important parameter in the GaBiAs material system, for assessment of the magnitude of the disorder present in the material.

3.3.2 Temperature dependent facet and spontaneous emission measurements

As has already been mentioned, as well as material bandstructure measurements, measurements are carried out to characterise device performance within this thesis. Temperature dependent facet and SE measurements give information regarding both of these aspects of laser devices. The laser structure we wish to test is mounted and the optical SE signal optimised in the manner discussed in section

3.3.1. The mount is attached to the cold finger of the cryostat, the shroud is put in place and a vacuum of $\approx 10^{-7}$ mBar is applied to the cryostat chamber. The laser facet emission is measured through a sapphire window in the cryostat shroud using a broad area Ando detector. As electrical injection is applied to the device, and the level is increased, the facet emission is measured by the broad area detector, and concurrently the integrated SE is measured by a fibre coupled detector. Example light-current characteristic curves can be seen in Fig. 3.4. Threshold-like behaviour of both (SE and facet emission) traces is clearly seen.

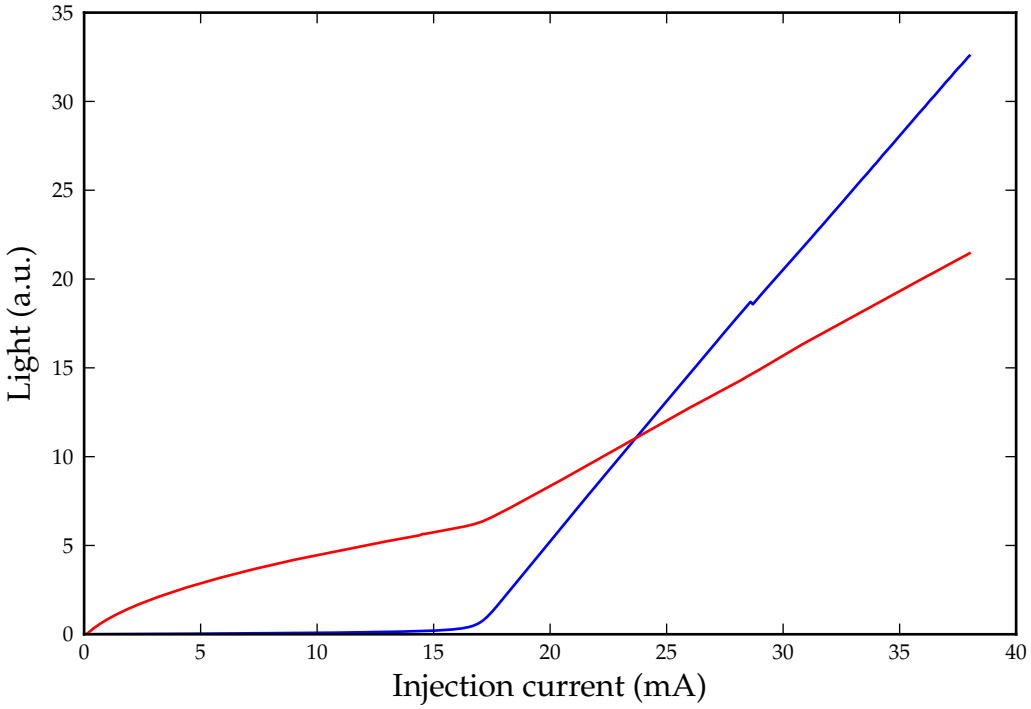


Figure 3.4: Facet L-I characteristic seen in blue with SE characteristic L-I in red. A clear threshold-like behaviour is present in both.

We expect threshold behaviour from the facet emission of a laser, but not the SE. The SE should pin at threshold in an ideal laser, along with carrier density and gain, as the gain counteracts the losses and any extra injected carriers contribute to the laser emission. The threshold-like behaviour of the SE characteristic comes about as a result of laser emission being scattered into the substrate window as mentioned in section 3.3.1. This has been verified by integration of the spectra at each drive current ignoring the laser peak. This analysis shows pinning of the SE at drive currents exceeding threshold. If the integrated SE continued increasing, even after the exclusion of the laser peak, the behaviour would then be indicative

of either a carrier density which is not in thermal equilibrium, or emission from barrier regions at high energy positions in the bandstructure.

A set of curves similar to those seen in Fig. 3.4 are collected for temperatures between 50 K and 350 K. Total threshold current, I^{th}_{total}, is extracted by a systematic derivative analysis of the facet L-I curve. I^{th}_{total} is taken as the peak of the second derivative of the facet L-I curve. This extracted value for the I^{th}_{total} lies on the point of inflection of the first derivative of the L-I curve and consequently half way between the two distinct slopes of the L-I curve. The threshold radiative current, I^{th}_{rad}, is the value of the integrated SE at the extracted total threshold current. It is very important for this experiment that the SE collection efficiency does not change during the course of the measurement, which can take up to four days to complete. This is ensured by beginning the experiment at 350 K, collecting the facet and SE data and then reducing the temperature in 20 K steps. This process is continued until a temperature of 50 K is reached. After the measurement at 50 K is completed, the temperature is increased by 10 K to 60 K, once the measurement at 60 K has finished the temperature is increased in steps of 20 K and the measurement taken at each temperature up to 340 K. By using this technique the static nature of the collection efficiency can be verified by the interleaving nature of the extracted temperature dependent I^{th}_{rad} values. If there is an offset between the data gathered with increasing and decreasing temperature, the collection efficiency has changed; if there is no offset then the measurement is valid.

Using these measurements, the variation of I^{th}_{total} and I^{th}_{rad} with temperature can be investigated. This is an important characteristic for laser performance as the ratio of I^{th}_{rad} to I^{th}_{total} provides a measure of the electrical to optical conversion efficiency, the internal quantum efficiency, η_{int}. The slope of the facet emission L-I curve above threshold provides the external differential quantum efficiency, η^{d}_{ext}.

Using the data gathered in this experiment, another analysis can be applied which yields further information regarding the dominant recombination mechanism at a given temperature [82]. It is assumed that the total current through the device, I_{tot} is given by

$$I_{tot} = qV(An + Bn^2 + Cn^3) + I_{leak} \tag{3.1}$$

where An, Bn^2 and Cn^3 are the contributions from monomolecular, radiative and Auger recombination, respectively. I_{leak} is leakage current, q is the electronic charge and V is the volume of the active region. Assuming negligible leakage,

and for a dominant recombination process, I_{tot} can written as

$$I_{tot} \propto n^z. \tag{3.2}$$

If the device is dominated by defect related monomolecular recombination z≈ 1, radiative recombination z≈ 2, or Auger recombination z≈ 3. Using the fact that $n^2 \propto I_{rad}$, Eq. 3.2 can be rewritten as

$$I_{tot} \propto (\sqrt{I_{rad}})^z \propto \left(\sqrt{L}\right)^z \tag{3.3}$$

In this way z can be extracted as

$$\frac{d \ln I_{tot}}{d \ln (\sqrt{L})} \propto z \tag{3.4}$$

The extracted slope of a graph of log(I) versus log($\sqrt{SE}$) between one third I^{th}_{total} and I^{th}_{total} gives the value of z. This technique allows measurement of the dominant recombination mechanism in lasers, provided one is present.

To estimate η_i, it is assumed that the current is dominated by radiative recombination at low temperatures and so I^{th}_{rad} and I^{th}_{total} are normalised at 50 K. We also note that the SE measured from the bottom contact window is a lower bound measure of the radiative current due to the neglect of the TM polarised spontaneous emission, which cannot be measured with this window orientation, due to the electric field vector of this light pointing in the direction of the window.

The parameters extracted using this measurement technique are important for analysing the temperature dependent operating efficiencies and loss mechanisms in laser devices. Understanding these parameters opens a route to improvements through bandstructure engineering to reduce losses and increase efficiencies.

3.3.3 Temperature dependent fibre coupled facet emission measurements

This experimental technique is, again, related to device performance measurements. It supports measurements of both temperature dependent optical time-traces and spectrally resolved high resolution amplified spontaneous emission (ASE). Fibre coupling the facet emission of a laser involves collimating the facet emission and then focusing this collimated beam into a fibre on an x,y,z fibre launch stage. This is quite a simple proposition on the optical bench and can be achieved quite easily. However, to achieve temperature dependent measurements,

the measurement must be made on a laser in the cryostat. This introduces a difficulty as the focal length of the lenses used in this method are generally quite small, and the distance between the laser and the window in the cryostat vacuum shroud is 55 mm. This results in only a very small portion of the emitted facet emission being collimated using a lens external to the cryostat, and not enough light being collected to support high resolution measurements.

This problem is overcome through the use of a different, specially designed, fibre coupling mount. This mount is very similar to that seen in Fig. 3.2, with the exception that there is no optic fibre for SE measurement. This mount has,

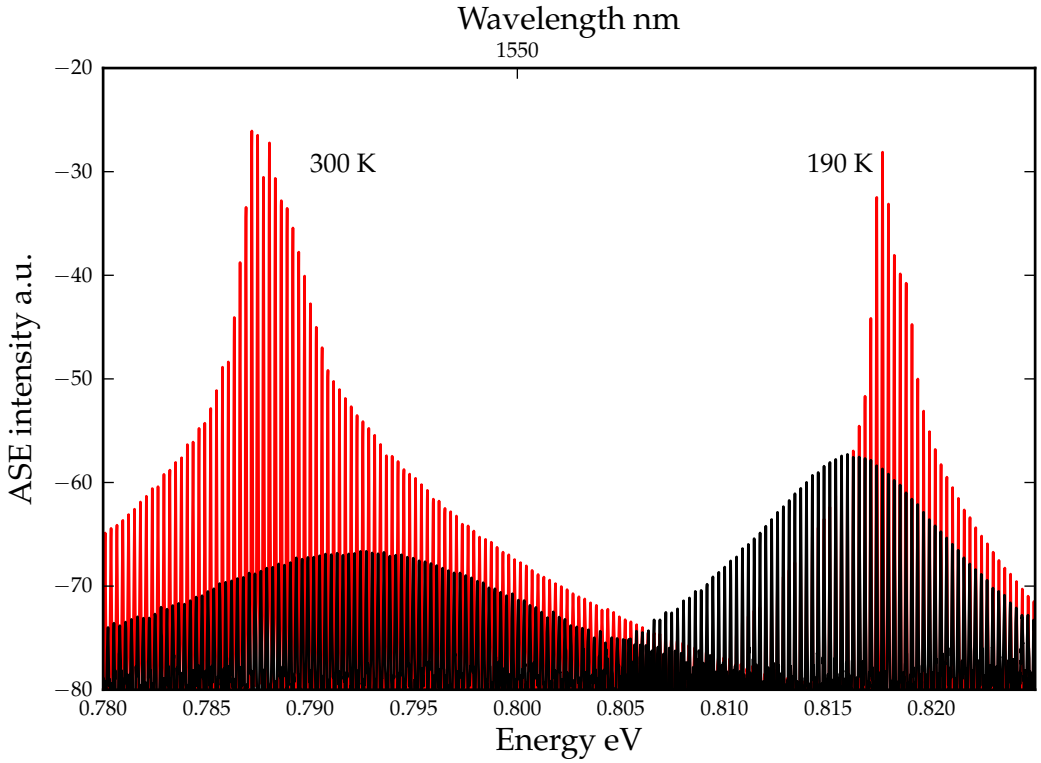


Figure 3.5: Temperature dependent ASE (black) and lasing (red) spectra with the FP mode structure resolved.

however, an adjustable position lens which moves on a brass slide in front of the laser. This allows collimation of the laser beam on the cryostat mount before the shroud is put in place, resulting in a collimated laser beam exiting through the cryostat window when the shroud is in place. For ease of optimization of the signal, a 3-axis adjustable mirror is inserted in the path of the collimated beam to add another degree of freedom to the fibre coupling as the adjustment of the beam at the laser is no longer possible once the shroud is replaced on the cryostat. This measurement is demanding as a very slight misalignment of the beam into the

fibre results in almost complete loss of the measured signal and, once the cryostat is switched on, the cold finger moves with the pneumatic valve changeover in the cold head. For this reason the cryostat is switched on and let cool to its lowest achievable temperature; once this temperature is reached, the cryostat is switched off and the optical signal optimised. Measurements have to be carried out quickly, especially at low temperature, because once the cryostat is off, there is no cooling capacity and the system will begin to warm up. As the system warms up temperature dependent measurements can be made on the laser as with the cryostat turned off there is now no movement of the cold head. The optical signal is measured using the 8 GHz oscilloscope for timetraces or the optical spectrum analyser for spectral measurements. Examples of spectral measurements are seen in Fig. 3.5, and temporal measurements in Fig 3.6. As can be seen in Fig. 3.5

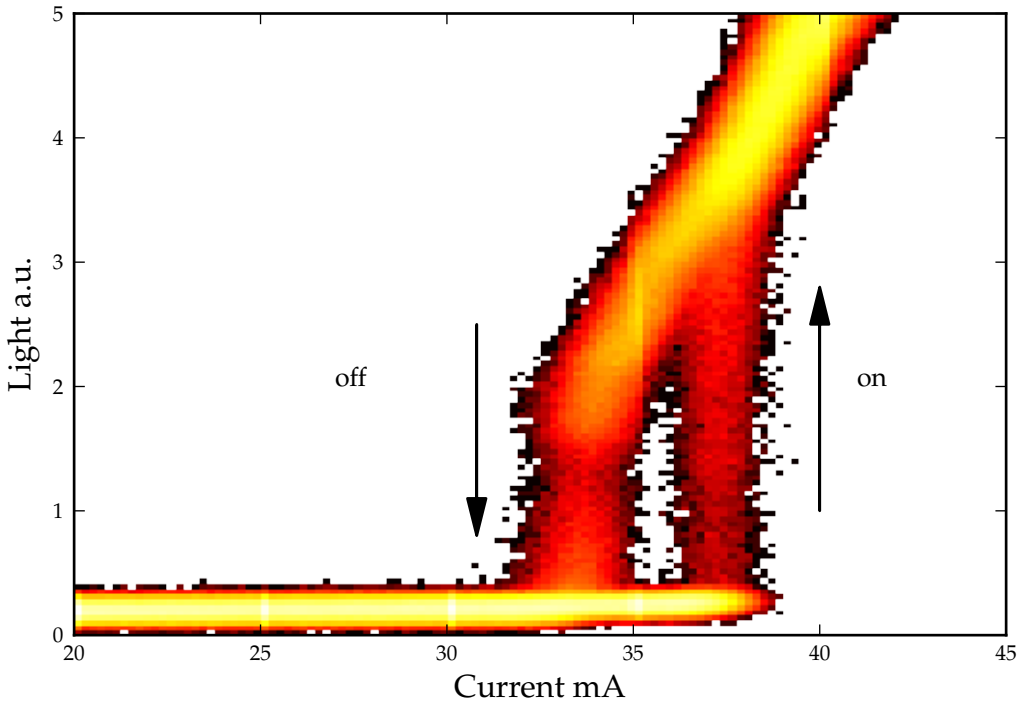


Figure 3.6: Bistable threshold current timetrace seen at 190 K.

we achieve excellent resolution of the ASE spectra using this method. The FP modes are clearly resolved and we can use this method to accurately track the variation of the ASE and lasing peak energies with temperature. This can be used to infer how material losses change with temperature. This method can also be used to make temperature dependent gain measurements from 8 K to 400 K using either the Hakki-Pauli [38] or Cassidy [24] methods. Fig. 3.6 shows multiple

overlaid timtraces captured at 190 K. This timetrace was captured as the injection current was modulated between 0.1 x I^{th}_{total} to 2 x I^{th}_{total}. This clearly shows an on/off intermittency/ hysteresis/ bistability of the light-current characteristics.

As will be seen in chapter 4, the use of this experimental technique (both spectral and temporal) is a valuable tool to further understanding of device behaviour at low temperature, and hence improve devices at operating temperature by input to the device design stage.

3.3.4 Temperature dependent photoluminescence spectroscopy

In contrast to all of the previous techniques discussed, photoluminescence (PL) spectroscopy is a measurement carried out not on a processed laser device, but rather on a bare wafer sample. The PL measurement is carried out by illumi-

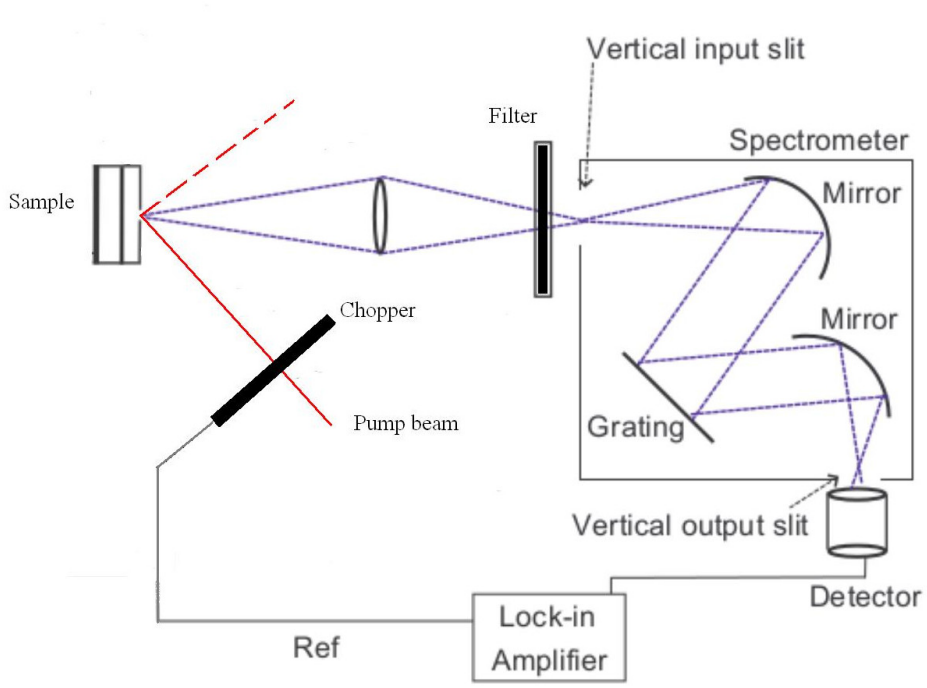


Figure 3.7: Set-up for PL experiment. Figure modified from [45].

nating the bare wafer sample with emission from a 640 nm diode laser. This incident radiation creates electron-hole pairs within the material under test and, because the photons in the 640 nm pump beam are much more energetic than the band-gap of the material which is being investigated, these carriers are promoted to levels high in the conduction band and low in the valence band. From here the

carriers decay towards the conduction and valence band edges, and depending on the radiative lifetimes in each region emit photons or decay to a lower energy state within the bandstructure, where radiative recombination occurs. We measure and spectrally resolve these radiative transitions to gain insight into material bandstructure, and lifetimes at certain temperatures and energies. The experimental set-up used for this experiment can be seen in Fig. 3.7.

The wafer is clamped on a vertical flat mount in the cryostat. The pump beam is chopped with an optical chopping wheel at a frequency of 1 kHz and is directed through the cryostat window at an angle of ≈ 30 degrees to the surface of the wafer. The emission from the wafer resulting from the pump beam will emerge in a symmetric cone with its apex at the illumination point of the pump beam. A collimating lens with focal length equal to the distance between the sample surface and the cryostat window is placed in the path of the emitted radiation. This collimated beam is then passed through a lens which is f-number matched to the spectrometer input slit optics and the beam is passed through an 800 nm high pass optical filter to remove any trace of the pump beam. The beam passes through the spectrometer and is spectrally resolved. The output of the spectrometer is passed through a lens f-number matched to the spectrometer output optics for collimation and focused onto the femtowatt detector. As the energy of the light passing through the spectrometer is varied, the voltage from the femtowatt detector is recovered using lock-in amplification. In this way a PL spectrum is acquired. This process is repeated as temperature is varied and a full temperature dependent PL spectrum can be built up. A PL spectrum of a GaBiAs QW can be seen in Fig. 3.8.

There is, however, some post-processing required on the measured spectra. This is as a result of spectral variation of the transmission of all of the optical components of the experimental set-up. To eliminate this the instrument response function is found and applied to the measured signal. To find the instrument response function, the sample is replaced by a calibrated tungsten source with known spectral response. With the rest of the system unchanged, a spectrum is collected in the same spectral region as the measurement which needs correction, with the tungsten source as input to the spectrometer. This spectrum is corrected by dividing by the known spectral response of the femtowatt detector and the known emission profile of the source, and the resulting spectrum is the instrument response function for the system. All of the measured spectra are then divided by this spectrum to correct for spectral variations in the transmission of the optical components.

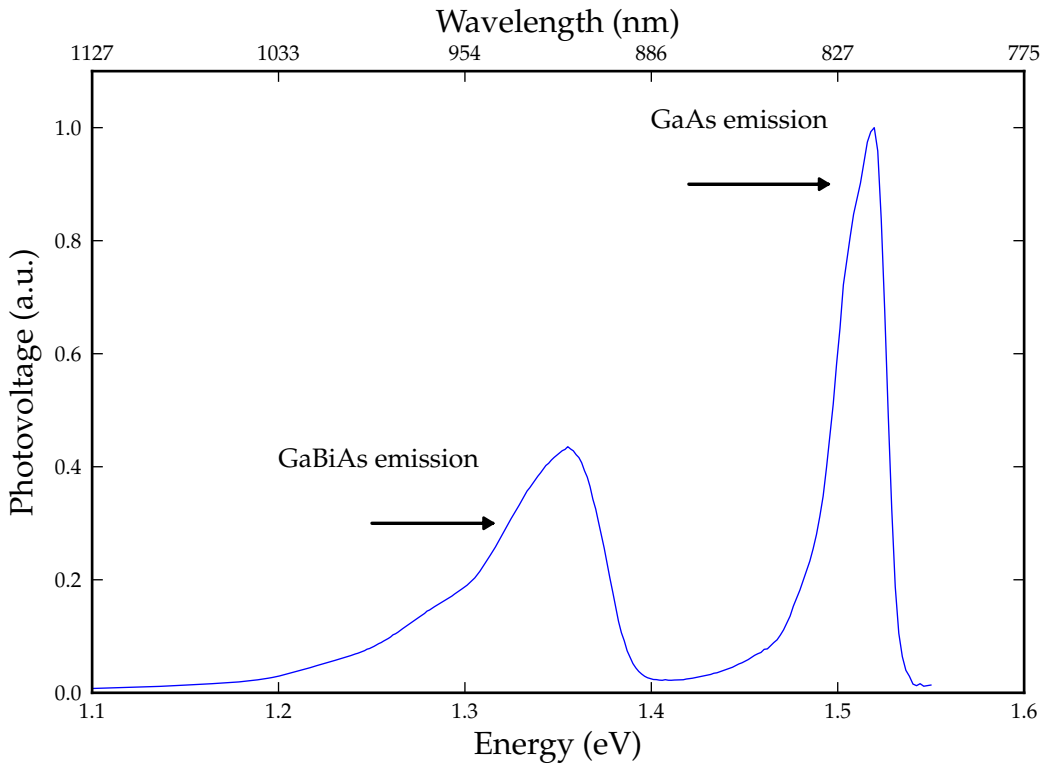


Figure 3.8: PL spectrum of GaBiAs QW at 13 K.

PL is a very useful experimental tool. Similarly to the spectrally resolved SE measurement, it provides bandstructure information, but over a much larger energy range. It is also much easier to measure PL at lower carrier densities than SE, as there is less absorbing material to degrade the optical signal since it is emitted from the wafer. Comparison between PL and SE is useful to determine if any changes have occurred during the processing of the material into laser devices, or to find out if there is any difference between the material response to electrical and to optical injection.

3.3.5 Photovoltage spectroscopy

Similarly to the earlier measurement techniques, this technique is applied to fully processed laser structures. In this method the material bandstructure is probed using the laser as a PIN photodetector [23], while illuminating the facet of the laser with spectrally resolved, chopped light from a calibrated tungsten source, and measuring the voltage response of the laser to the energy of the photons incident on the facet. An order-sorting high pass optical filter is used to ensure that there is no harmonic mixing present in the spectrally resolved light incident

on the laser facet. The experimental set-up seen in Fig. 3.9 is used with the exception of the polariser.

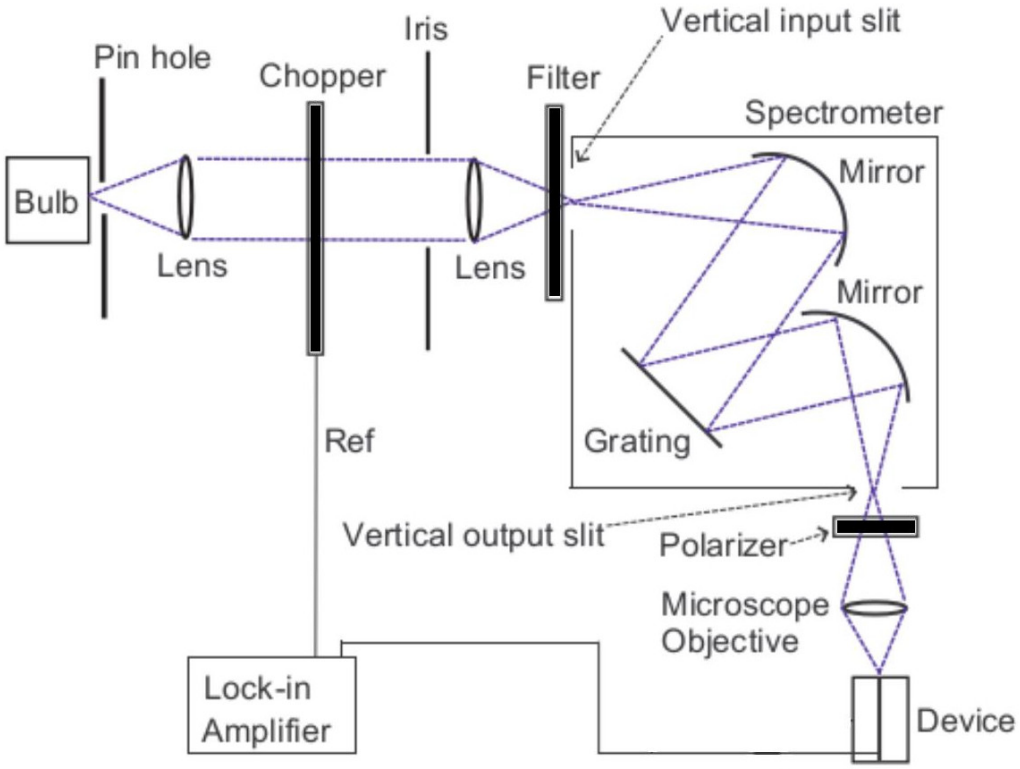


Figure 3.9: Set-up for PV experiment. Figure modified from [45].

Once the energy of the light incident on the facet of the laser exceeds the bandgap energy of the material, the light is absorbed in the intrinsic region of the device. This absorption results in the formation of electron-hole pairs within the material. These photo-generated carriers are swept out of the intrinsic region of the device by the built-in electric field created by the p-n junction. The photo-voltage induced by this photocurrent is measured using phase sensitive detection.

The photovoltage produced at any given incident energy is related to the density of states (DOS) and the recombination lifetime of a state at that energy. PV is used to probe QW bandstructure in this thesis. The DOS of ideal QW structures is step-like and so the PV signal should be step-like in the energy region of the QW. Once energy is increased enough to promote the photo-generated carriers into the continuum states of the barrier region, a large increase in the voltage is seen, related to the DOS of the bulk barrier material of the device. Similarly to the previous section, a spectral correction is required to remove the instrument response from the measured spectra. In this case it is simpler

than the previous section as the device under test is replaced by a detector with known spectral response and a spectrum of the light incident on the laser facet is collected. This is then divided into the measured device spectrum to remove the instrument response.

This is then a useful tool to determine the energy of the lowest lying transition in a material and verifying the QW and the barrier composition. A measure of the broadening present can also be gained by Gaussian fitting to the absorption edge. Much more insight can, however, be gained by exploiting the orthogonal nature of the P-like states at the valence band edge in tetrahedrally bonded QW materials [71, 72, 61, 87].

3.3.5.1 Polarisation resolved photo-voltage

As discussed in chapter 1, TE polarised light incident on the facet of the laser will excite states with mainly heavy-hole (HH) character with a small contribution from states with light-hole (LH) character. TM polarised light incident on the facet of the laser excites states with entirely LH character. Knowing this, a polariser is inserted into the experimental set-up to allow polarisation-resolved measurements. These can then be used to determine separately the energies of the HH and LH valence band edge states, characteristic of QW structures. This is a very useful measurement, since the lowest lying transition energy, the HH - LH splitting, and broadening of each of these states are all measured independently. These are very important parameters in QW lasers as the threshold condition is related directly to the VB edge DOS, the Fermi level separation and the bandgap, with the VB edge DOS strongly dependent on the strain induced HH-LH splitting. As will be seen later in the thesis, the parameters extracted from this experiment feed directly into a continuum modelling code for GaBiAs QW laser devices in order to develop a set of reliable parameters for modelling the material. An example of the polarisation resolved measurement is shown in Fig. 3.10.

3.3.5.2 Spectral corrections

Polarisation resolved spectra require spectral correction in the same manner as the polarisation unresolved measurements, with further corrections also required to ensure that the TE and TM spectra are treated on an equal footing. The experimental set up used is shown in Fig. 3.9. An instrument response function is found for the polariser parallel to, and perpendicular to, the spectrometer slits. Each spectrum is divided by its applicable response function. Due to an intrinsic polarisation dependence of the system, there is a requirement for a polarisation

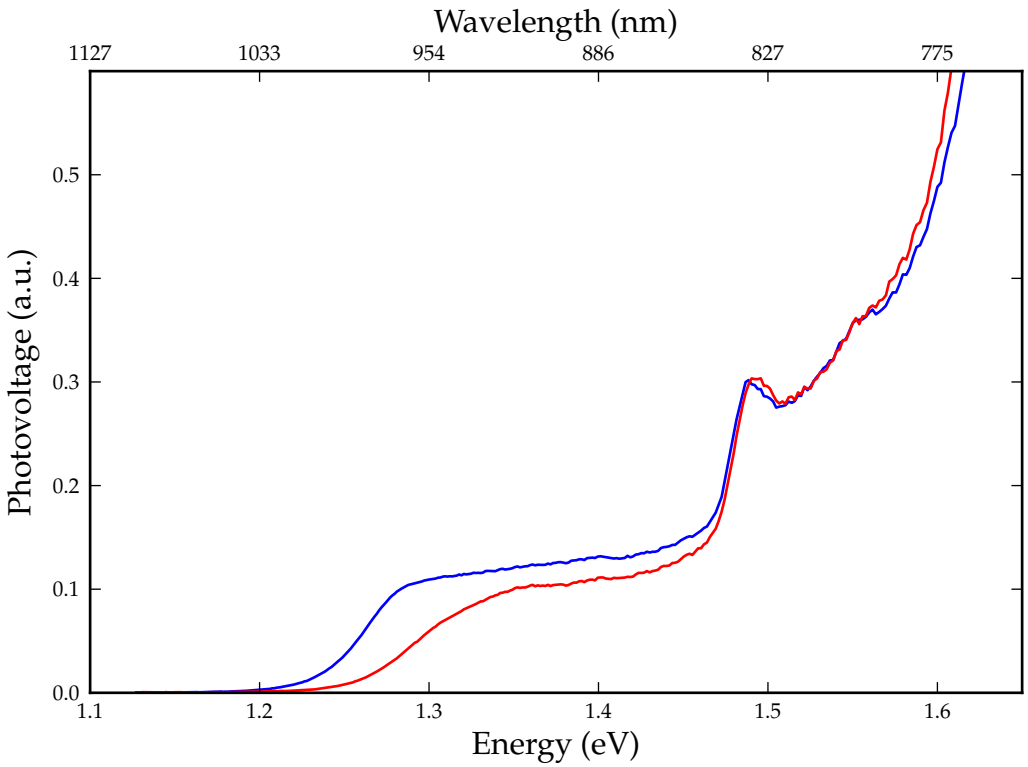


Figure 3.10: spectra measured on a GaBiAs QW laser structure.

correction to these measurements also in order to be able to compare the TE and TM measured spectra. In order to correct for this polarisation dependence, two measurements must be made of the TE spectrum and a further two measurements of the TM spectrum [71]. These measurements are made with the plane of the QW parallel and perpendicular to the spectrometer slits by rotating the device by 90 degrees. The four measured spectra after removal of the system spectral dependence can be written

$$Sp_{para}(\lambda, TE) \propto S(a) \tag{3.5}$$

$$Sp_{perp}(\lambda, TE) \propto S(b) \tag{3.6}$$

$$Sp_{para}(\lambda, TM) \propto S(b) \tag{3.7}$$

$$Sp_{perp}(\lambda, TM) \propto S(a) \tag{3.8}$$

where Sp_{para} and Sp_{perp} represent spectra collected with the QW growth plane parallel to, and perpendicular to the spectrometer slits. The TE and TM excitation is achieved in each orientation by changing the polarisation angle. S(a) and S(b) represent the orientation of the polariser relative to the spectrometer

slits, where S(a) represents the polariser parallel to the slits and S(b) represents the polariser perpendicular to the slits. From this the ratio of the polarisation sensitivity factors S(a)/S(b) can be written

$$\frac{S(a)}{S(b)} = \left(\frac{Sp_{para}TM}{Sp_{perp}TM} \times \frac{Sp_{perp}TE}{Sp_{para}TE} \right)^{\frac{1}{2}} \tag{3.9}$$

By considering Eq. 3.6 and Eq. 3.8 we can write

$$Sp_{perp,corr} = \frac{S(a)}{S(b)} \times Sp_{perp} \tag{3.10}$$

This correction results in the removal of the polarisation dependence of the system, and calibration of $Sp_{perp}TM$ for plotting on the same scale as $Sp_{perp}TE$. Errors which affect the results from this method can arise from generating the photocurrent-induced photovoltage from different areas of the junction in the different orientations. These errors can be minimised by careful alignment of the sample in both orientations.

3.3.5.3 Extraction of transition energies

Transition energies for the observed features in each of the TE- and TM-polarized spectra are extracted by examining the first derivative of the measured PV spectrum multiplied by the photon energy. Transition energies are systematically assigned using the peaks in these first derivatives, which correspond to the points of inflection in the spectra associated with the optical absorption edges. This method for determining the transition energies has been shown [86] to provide results in good agreement with those determined using photo-modulated reflectance, a differential technique which is highly sensitive to critical points in the band structure. [47, 39]

Due to the symmetry present in an (001)-grown QW, the TE-polarized optical transitions involve both HH and LH states, while the TM-polarized transitions involve LH states only. Therefore, in order to accurately determine the energy splitting between the highest LH and HH states in the QW, we correct the measured TE-polarized PV spectra in order to remove the LH contributions and obtain the PV generated by heavy-holes only. For LH states in an ideal QW the TM-polarized optical transition strength is four times that associated with TE-polarized transitions. [25] Assuming that this relationship holds in the QW laser devices studied here, we correct the measured TE-polarized PV spectra at a given photon energy by subtracting one quarter of the TM-polarized PV mea-

sured at that photon energy. Since the LH-related transitions occur at higher energies than those related to HH states in the compressively strained QWs studied in this thesis, this correction has the effect of decreasing the magnitude of the TE- polarized PV signal as the photon energy increases above the band edge. This then leads to a small increase in the measured splitting between the highest energy LH and HH states compared to that obtained using the TE-polarized spectra.

3.3.5.4 Device mount

A device mount designed for this experiment is shown in Fig. 3.11. This mount consists of a brass plate with a similar electrically contacting spring clip set-up to that discussed in section 3.3.1. This mount has the capability to rotate through 90 degrees to allow access to all of the sample-polariser-slit orientations discussed in the previous section. This mount also has a Peltier heater/cooler to allow

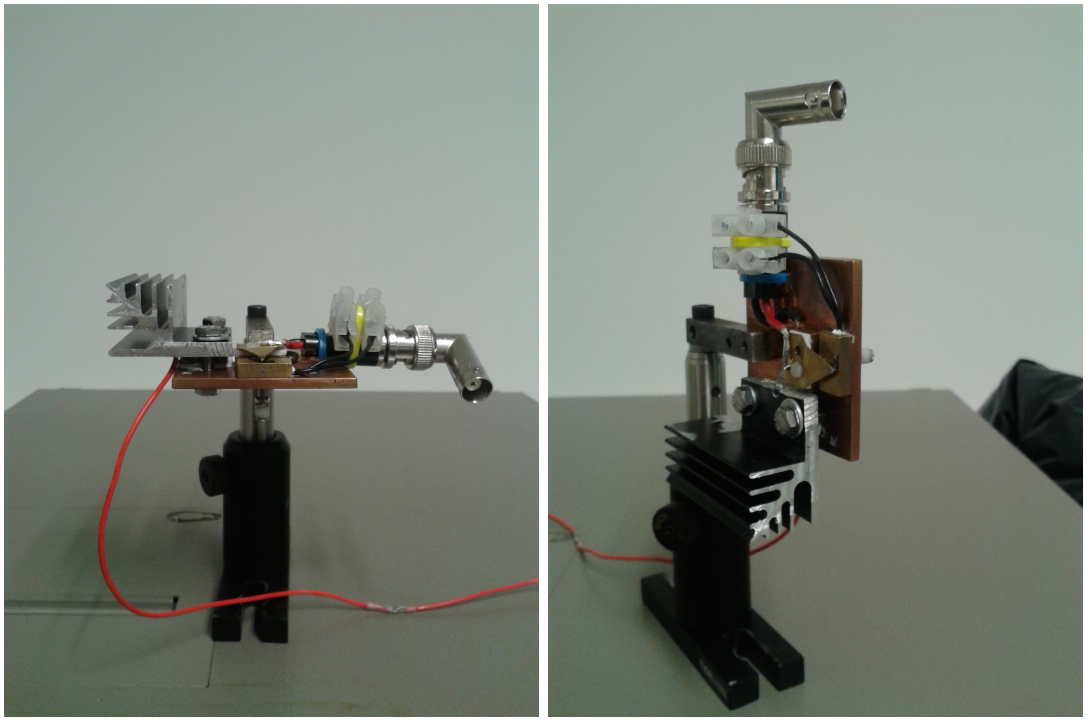


Figure 3.11: Left: PV mount in horizontal orientation. Right: PV mount in vertical orientation.

temperature dependent measurements of PV from room temperature to $\approx$ 350 K.

3.4 Summary

In summary this chapter provides an overview of the main experimental methods used in this work. Firstly a description of the main experimental instruments used is presented. In the next section the experimental methods are explained in detail. Firstly the method for collection of spectrally resolved SE is given. This is followed by a description of the temperature dependent collection of SE and integrated facet emission. Next a description of the method used to fibre couple facet emission from the cryostat is given. This is followed by the technique for measurement of temperature dependent PL. Finally detail is given on the collection of room temperature PV spectra and the how the spectra are corrected for extraction of bandstructure information.

Chapter 4

Experimental analysis and rate equation modelling of an InP based quantum dash laser showing bistable threshold

4.1 Introduction

Semiconductor laser active regions composed of quantum dots or wires have attracted much interest for future optelectronic devices. This interest arose due to impressive predicted attributes of these confinement geometries, where lasers have been predicted with very low, if not zero temperature dependence of the threshold current, and very low values for chirp and linewidth enhancement factor [12, 11]. However, due to growth inhomogeneities among other issues, these materials have never fully delivered on their predicted benefits. Most of the interest in these active region geometries has been in quantum dots on GaAs for the 1.3 μm telecommunication window [16, 62]. It is, however, very difficult to extend emission on GaAs to the 1.5 μm window for telecommunications. InP is the accepted material of choice for this spectral region. InAs grown on the commercially favoured (100) InP substrate orientation can, under appropriate growth conditions, form quantum dots elongated along the (1-10) axis, known as quantum dashes [10]. Quantum dash lasers have shown many impressive attributes including low threshold current, high characteristic temperature, T_0, low chirp and in some cases spontaneous mode-locking [60].

Quantum dash lasers offer improved optical bandwidth over quantum well lasers due to inhomogeneous broadening caused by the dash size distribution.

This offers the possibility of extremely short pulses from these lasers [58]. The InAs/InP quantum dash material system is an exciting prospect for next generation optical networks, due to the high temperature stability and large bit rates which have been associated with it [33].

Quantum dash laser devices are studied in this chapter to investigate the possibilities as well as constraints offered by increasing confinement of the carriers within quantum confined structures. The temperature dependent gain and loss mechanisms of these lasers are investigated.

In this chapter, two quantum dash laser devices emitting at 1.55 μm at room temperature are studied, which are nominally identical except for barrier height. As seen in fig 4.1, these devices have a dash-in-a-well structure. From here on the high barrier device will be referred to as DW_H and the lower barrier device will be called DW_L. Both devices are processed as ridge-waveguide lasers with as cleaved facets. The temperature dependent characteristics of these devices are measured and a temperature dependent bistability of threshold is uncovered in DW_H. A theory based on carrier localisation and impeded interwell transport at lower temperatures is put forward to explain this bistable behaviour and a simple rate equation model is used to test this theory. Very good qualitative agreement is achieved between the measured and calculated data.

Details of the device composition are available in section 4.2. Here it is seen that both devices have very similar electronic structure with the exception of the confining potential of the barrier. In section 4.3 a comparison of experimental measurements which have been made on DW_H and DW_L is shown, including a temperature dependent bistability measured at threshold in DW_H. In this section amplified spontaneous emission (ASE), timetrace and detailed temperature dependent threshold characteristics are presented. Theoretical analysis of the measured data is made in section 4.4. A theoretical framework which accounts for the bistable behaviour is proposed, which is the basis for a numerical model. In section 4.5 the model which is used to simulate the dynamical behaviour of the laser threshold is introduced. The method employed to model the behaviour is described in detail and all model parameters are shown. In section 4.6 the results of the modelling are presented and a comparison of calculated and experimental data is made. Some suggestions are made to improve the quantitative accuracy of the model. Very good qualitative agreement is achieved between the measured and simulated data. The chapter is summarised in section 4.7.

4.2 Materials studied

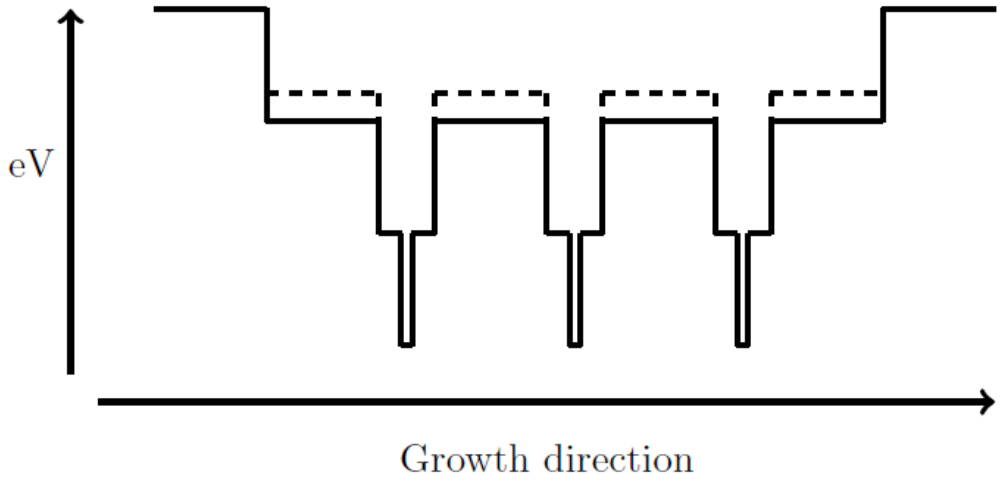


Figure 4.1: Flat band approximation showing schematically the variation of conduction band edge energy with position for the two DWELL structures considered, one with high barrier (dashed), and the other with a lower barrier.

This section includes a description of the two materials studied in this chapter. For each of the two materials studied, 8 lasers were tested from 4 laser bars; these bars were cleaved from one quarter of their respective wafers. Consistent results were found for the different devices from each material. The devices studied in this chapter were grown by gas-source molecular beam epitaxy (GSMBE) at Alcatel - Thales III-V Lab by François Lelarge. The device structure consists of 6 stacks of InAs quantum dashes surrounded by quantum wells of the quaternary alloy $Ga_xIn_{1-x}As_yP_{1-y}$. The wells are bounded by barriers, also of $Ga_xIn_{1-x}As_yP_{1-y}$. This active region is grown in a p-n junction lattice-matched to the InP substrate and to the cladding layers. The growth of these materials is reported in [60]. The thickness of the InAs quantum dash embedded within the QW is slightly larger for DW_H in order to keep the same emission wavelength ($\approx 10\%$ increase). The quantum well region of both devices is of $Ga_{0.36}In_{0.64}As_{0.78}P_{0.22}$ and is 3.5 nm thick each side of the quantum dash layer. Both designs are based on 20 nm-thick barriers with a 140 nm-thick separate confinement heterostructure. The only differentiating factor between the materials is the barrier composition, with DW_L composition $Ga_{0.20}In_{0.80}As_{0.43}P_{0.57}$, and DW_H composition $Ga_{0.15}In_{0.85}As_{0.32}P_{0.68}$, leading to greater confinement for carriers in DW_H.

4.3 Experimental analysis

In this section the results of the experimental methods are presented.

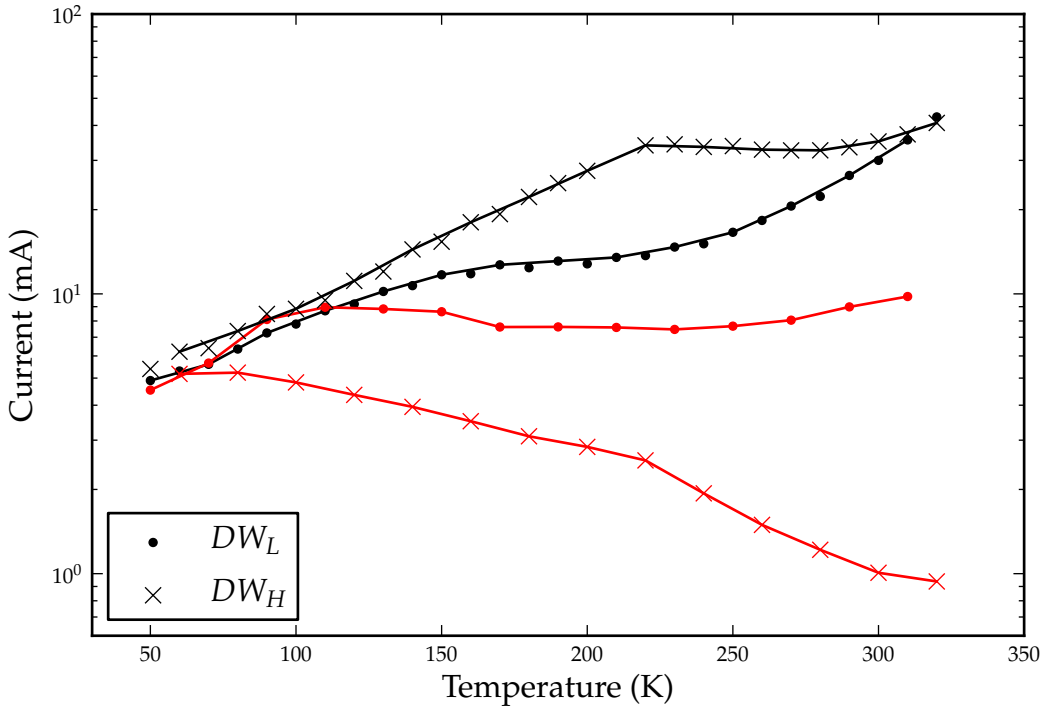


Figure 4.2: Temperature dependence of threshold (black) and radiative (red) currents for DW_L (filled circles) and DW_H (crosses). DW_H has a bistable threshold below 220 K.

The bare laser chips are mounted on the cold finger of a closed cycle helium cryostat and contacted using a clip system as discussed in chapter 3. The temperature dependence of the threshold current of the lasers is measured from the temperature dependent facet light-current curves. Lasing is observed from the quantum dash states at all temperatures. Threshold current is found using the derivative method outlined in chapter 3. The temperature dependence of the radiative current of the lasers is extracted from spontaneous emission measurements made from a window in the laser substrate, as in [82], and normalised to J_{th} at low temperature. As can be seen from Fig. 4.2, the threshold current of DW_L increases exponentially from low temperature to 148 K. This is followed by a region of slightly increased T_0 up to 235 K. This is attributed to the formation of a thermal equilibrium of carriers in the dashes, resulting in a slight decrease in the rate of increase of threshold current. This is then followed by a region of expo-

nentially increasing threshold current, with $T_0 = 61$ K. In this laser the radiative current increases with threshold current up to 150 K and then decreases up to 230 K before recovering and increasing again above this temperature. DW_L exhibits temperature dependent lasing characteristics which are typical of previous quantum dash lasers which have been measured [43].

In DW_H the threshold current at which lasing commences increases exponentially up to 230 K; between 230 K and 310 K there is a reduction in threshold current accompanied by a giant (and negative over a small interval) T_0 value. Above 310 K the threshold current once again increases exponentially. The radiative current of this device is decreasing over the entire temperature range, showing only slight signs of increasing above 320 K. Similar characteristics have previously been observed in 1.3 μm quantum dot in a well lasers [30].

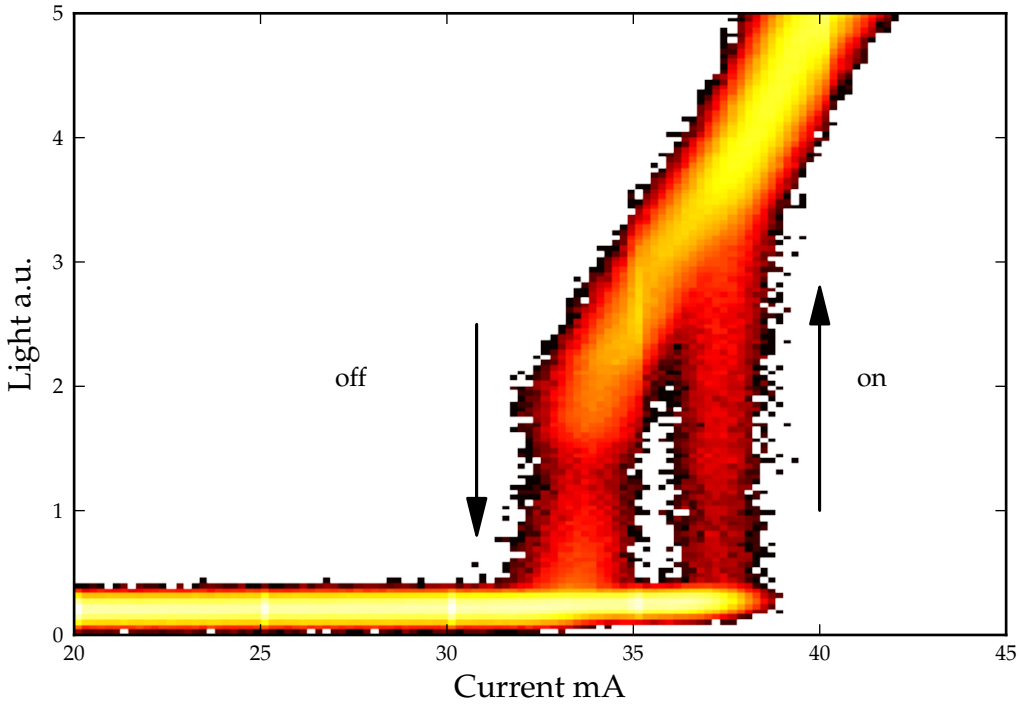


Figure 4.3: 300 overlayed light-current measurements of the high barrier laser at 190 K, clearly showing an abrupt switch to lasing at 37.5mA and an equally abrupt switch from lasing at 33.3mA.

At temperatures lower than 220 K, DW_H shows bistability of threshold, as seen in Fig. 4.3, with lasing switching off at a lower current than it switches on. There is an increased threshold current compared to DW_L and an abrupt switch

to and from lasing seen in DW_H at these temperatures.

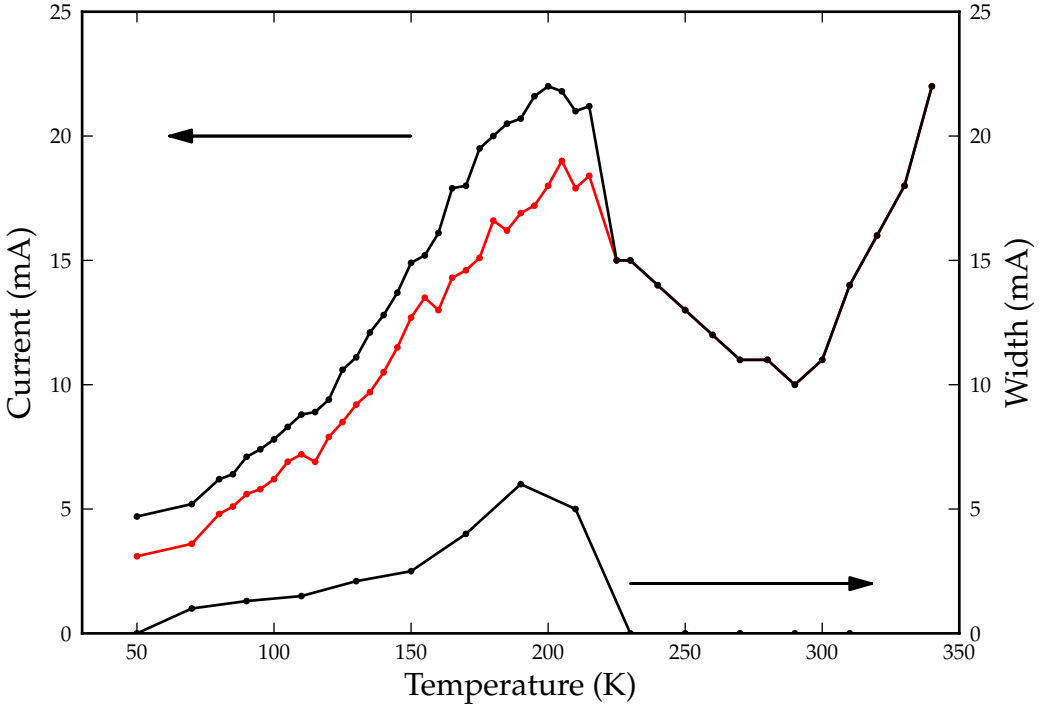


Figure 4.4: Left y-axis plot shows the temperature dependence of the experimentally determined threshold current including switch on/off points in the bistable region. Right y-axis plot shows the temperature dependence of the size of the bistability, which is seen to grow in size from 50 K to about 200 K, above which it drops quickly to zero with increasing temperature.

In Fig. 4.4 the temperature dependence of the measured switch points of the bistability can be seen. It is noted that the width of the bistability in mA grows from low temperature to a maximum size at 190 K and from there diminishes very strongly with increasing temperature, before disappearing by 230 K.

Fig. 4.5 shows ASE spectra above and below threshold at 190 K and 300 K. At room temperature (stable region) the lasing transition occurs on the low energy side of the gain spectrum, as is typical in a semiconductor laser. In the bistable region (190 K) the lasing transition occurs on the high energy side of the the gain spectrum and is considerably narrowed. It is speculated that this high energy lasing is a result of preferential absorption of spontaneous emission at the band edge due to saturable absorption, thus pushing the lasing transition to higher energies than it would otherwise occur. This saturable absorption effect could be achieved if the energy gap of the first well was slightly larger than that of later

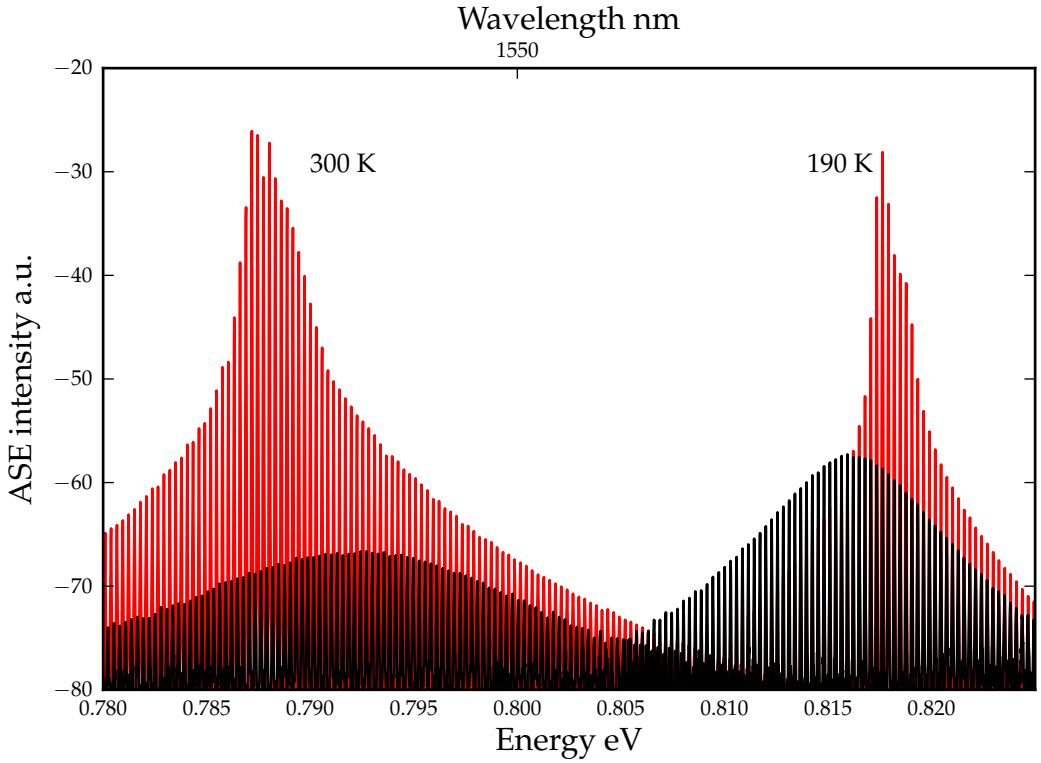


Figure 4.5: Amplified spontaneous emission (at 80 % of I_{th}) and lasing spectra at 190 K (right) and 300 K (left). Note that the lasing transition is at the high energy side of the gain peak in the bistable region and at the low energy side at 300 K.

wells. We do not need to include such a bandgap shift in the theoretical model presented below in order to demonstrate the transition to bistable behaviour at lower temperatures. Overall, the narrowing of the 190 K spectrum is also at least in part a thermal effect, with the carriers being distributed over a decreased energy range at lower temperature, leading to increasing carrier localisation, consistent with the sharp roll off observed at the short wavelength end of the gain spectrum at lower temperature.

4.4 Theoretical interpretation of measurements

In this section a detailed description of the proposed mechanism which accounts for the bistable behaviour is given.

Passive saturable absorption as a result of carrier localisation at low temperature is proposed as the mechanism supporting the bistable behaviour in DW_H.

It is well established that InGaAsP alloys grown on InP have a small conduc-

tion band offset, and that there is a large valence band offset, in particular for unstrained barriers [57, 14, 89] such as are considered here [44]. Because of this and the low hole mobility, the carrier distribution can become localised, and so holes get trapped in the quantum wells near the p-doped side of the device at lower temperatures. This leads to large changes in the carrier density in successive layers, with the holes in particular being preferentially trapped in the upper layers, on the p-doped side. Some layers which are less populated act as absorbers, while others produce gain. This can lead to saturable absorption in the temperature range where the carrier densities vary strongly from layer to layer. Extra gain is then required in the first (p-side) well so that the net gain can equal the cavity and mirror losses plus the extra absorption from the n-side layers in order to achieve lasing. Once enough gain is produced to saturate the absorbing regions, and they become transparent, an abrupt switch to lasing occurs. At this point the absorbing wells should clamp at or near transparency, supported by the formation of a photon-mediated carrier equilibrium. As current is reduced from this state of lasing, stimulated emission keeps this photon-mediated carrier equilibrium active to a current less than the original abrupt switch on, leading to the bistability seen in Fig. 4.3.

As the temperature rises, the escape rate increases for carriers trapped in a given (p-side) well, and so a thermal distribution of carriers begins to form. This leads above 230 K for DW_H to a region of decreasing threshold current and giant T_0 as the losses due to the absorbing layers decrease and as these layers become populated with carriers. Previous analysis has shown that Auger recombination provides an increasingly significant recombination pathway with increasing temperature in 1.5 μm quantum dash lasers [43], consistent with the reduced T_0 then observed at higher temperatures both in DW_H and in DW_L.

Based on the above analysis, it is concluded that the bistable effect is most likely caused by transport issues between the quantum well regions of DW_H at low temperature. In order to test this hypothesis, a simplified quantum well structure is modelled to investigate how transport within the structure influences the light output as temperature changes.

4.5 Model

In this section, the model used to simulate the bistable behaviour is presented. In this model, it is presumed that transport between quantum well layers is the limiting factor at low temperatures. Although the gain in the actual devices is due

to recombination in six quantum dash layers, it is found that the main physical effects can be understood by using a simple system of rate equations incorporating carrier transport effects to model a three quantum well device: [102]:

$$\dot{n}_1^b = \frac{\eta_i I}{qV} - \frac{n_1^b}{\tau_d} + \frac{n_1^{w_u}}{\tau_d} - \frac{n_1^b}{\tau_n} \tag{4.1}$$

$$\dot{n}_i^b = \frac{n_{i-1}^{w_u}}{\tau_d} - \frac{2n_i^b}{\tau_d} + \frac{n_i^{w_u}}{\tau_d} - \frac{n_i^b}{\tau_n} \tag{4.2}$$

$$\dot{n}_4^b = \frac{n_3^{w_u}}{\tau_d} - \frac{n_4^b}{\tau_d} - \frac{n_4^b}{\tau_n} \tag{4.3}$$

$$\dot{n}_i^{w_u} = \frac{n_i^b}{\tau_d} - \frac{2n_i^{w_u}}{\tau_d} + \frac{n_{i+1}^b}{\tau_d} - \frac{n_i^w}{\tau_c} + \frac{n_i^w}{\tau_e} - \frac{n_i^{w_u}}{\tau_n} \tag{4.4}$$

$$\dot{n}_i^w = \frac{n_i^{w_u}}{\tau_c} - \frac{n_2^w}{\tau_e} - \frac{n_i^w}{\tau_n} - G_i S \tag{4.5}$$

$$G_i = G_0 S \ln(\frac{n_i^w}{n_{tr}}) \tag{4.6}$$

$$\dot{S} = \Gamma v_g \sum_{i=0}^{m} G_i S - \frac{S}{\tau_p} + \beta \sum_{i=0}^{m} \frac{n_i^w}{\tau_n} \tag{4.7}$$

For a 3 well device, this model consists of a set of 11 coupled differential equations, as are represented by Eq. 4.1-4.7. Here η_i is the injection efficiency, I is the current, q is the elementary charge, V is the volume of the active region. $\dot{n}_i^b$, $\dot{n}_i^{w_u}$ and $\dot{n}_i^w$ are the rate of change of carrier population in the barriers, the unconfined quantum well regions and the confined quantum well regions, with respect to time. n_{tr} is the transparency carrier density. τ_c, τ_e, τ_d, τ_n, and τ_p are the capture, escape, diffusion, recombination, and photon lifetimes. $\dot{S}$ is the rate of change of photon density with respect to time and G_i is the gain calculated using the logarithmic gain approximation of Eq. 4.6 in each of the quantum wells. Layer indexing starts on the p-side of the device.

The dynamic flow of carriers through the equation system is depicted in fig 4.6. The capture, escape, diffusion and recombination time constants are used to distribute carriers through the system.

All of the carrier lifetimes used in the model are assumed to be independent of temperature and carrier density, except for the carrier escape time. This is justified by τ_e having a much larger temperature dependence than other processes. Inclusion of carrier density dependent lifetimes is possible, but would not qualitatively change the overall behaviour observed. The parameters used for modelling the bistable behaviour are listed in Table 4.1. The parameters used are taken

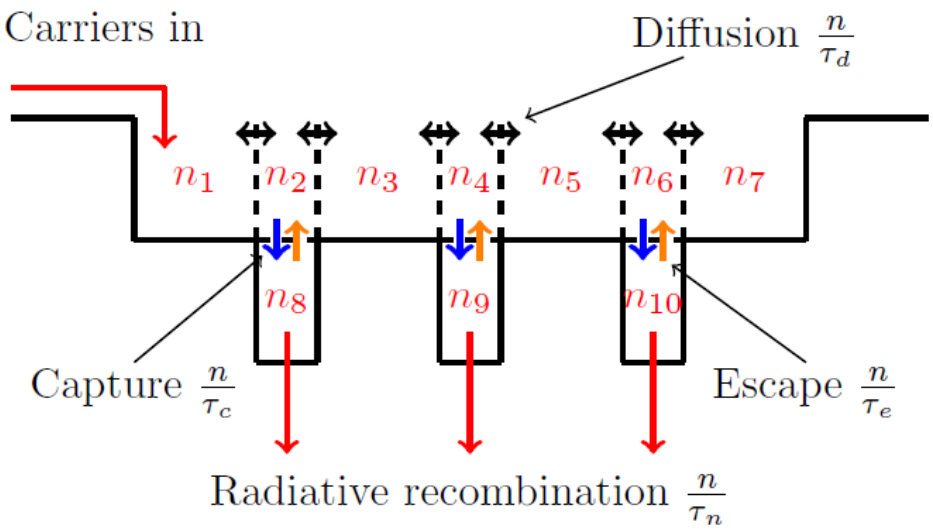


Figure 4.6: Flow diagram of the rate equation system showing how diffusion time, capture time, escape time and recombination time influence carrier distribution through the system.

from Refs. [102] and [74]. We include a temperature dependence for the transparency carrier density, N_{tr}, in order to account for the temperature dependence of the gain in Eq. (6). The escape time is calculated from

$$\tau_e = \tau_c * \exp^{(\frac{E_b}{k_b T})} \tag{4.8}$$

where k_b is the Boltzmann constant, E_b is the energy difference from the band edge of the well to the band edge of the barrier and T is temperature [29]. The escape time calculated from this relation and using the conduction and valence band confining potentials for DW_H can be seen in Fig. 4.7. It can be clearly seen that the escape time for holes is much longer than for electrons, resulting in the localisation of holes at low temperature. The temperature dependence of the transparency carrier density is included through the relation [80]

$$N_{tr}(T) = N_{tr}(300) * \frac{T}{300} \tag{4.9}$$

At low temperatures, the calculated escape time is large enough to result in carriers becoming localised in the upper layers due to the large ratio of capture

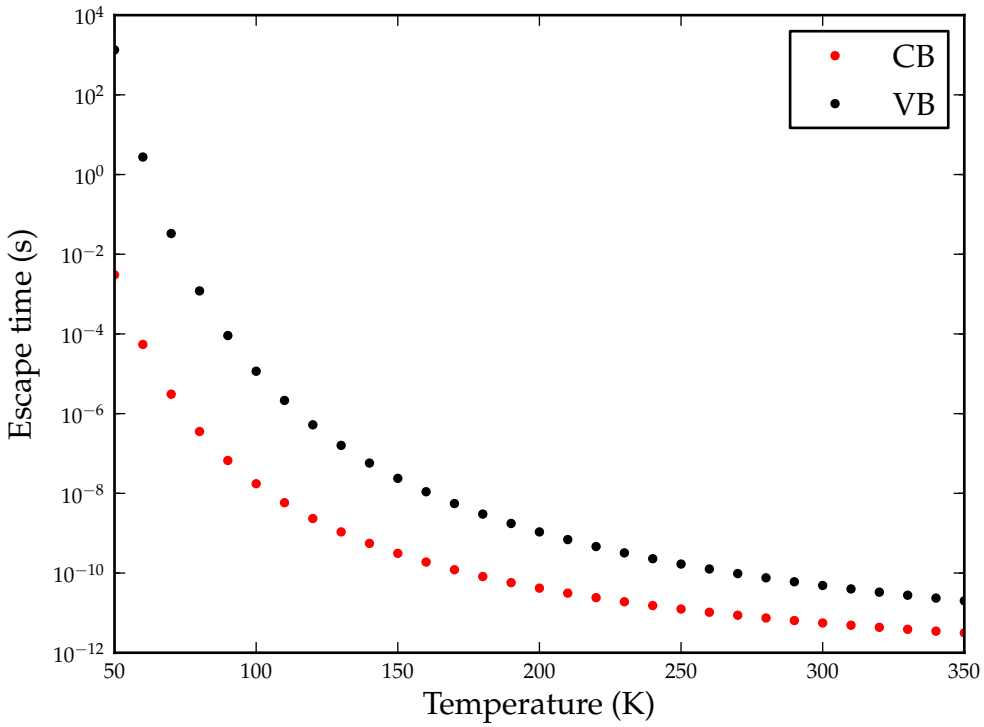


Figure 4.7: Calculated escape times for the CB and VB confinement energies

Table 4.1: Parameters used for modelling of bistable threshold current.

Parameter	Value	Unit
τ_c	0.1 x 10^{-12}	s
τ_n	1.4 x 10^{-9}	s
τ_d	0.3 x 10^{-12}	s
τ_p	1.28 x 10^{-12}	s
N_{tr}	1.8 x 10^{18}	n/a
η_i	0.8	n/a

and escape times; this causes saturable absorption.

As the temperature approaches 230 K, and the ratio of escape time to capture time decreases, a more uniform distribution of carriers across the wells begins to develop, removing the saturable absorption process so that the bistability is eliminated and the threshold current reduces with increasing temperature. At higher temperatures, τ_e approaches τ_c, this represents thermal broadening of the carrier distribution and higher energy states being populated with carriers. This state-filling makes it more difficult to achieve transparency carrier density at the lasing energy, as described by Eq. (4.9), which contributes to the increasing

threshold current with increasing temperature in this temperature region.

4.6 Results

In this section the results of the modeling are presented.

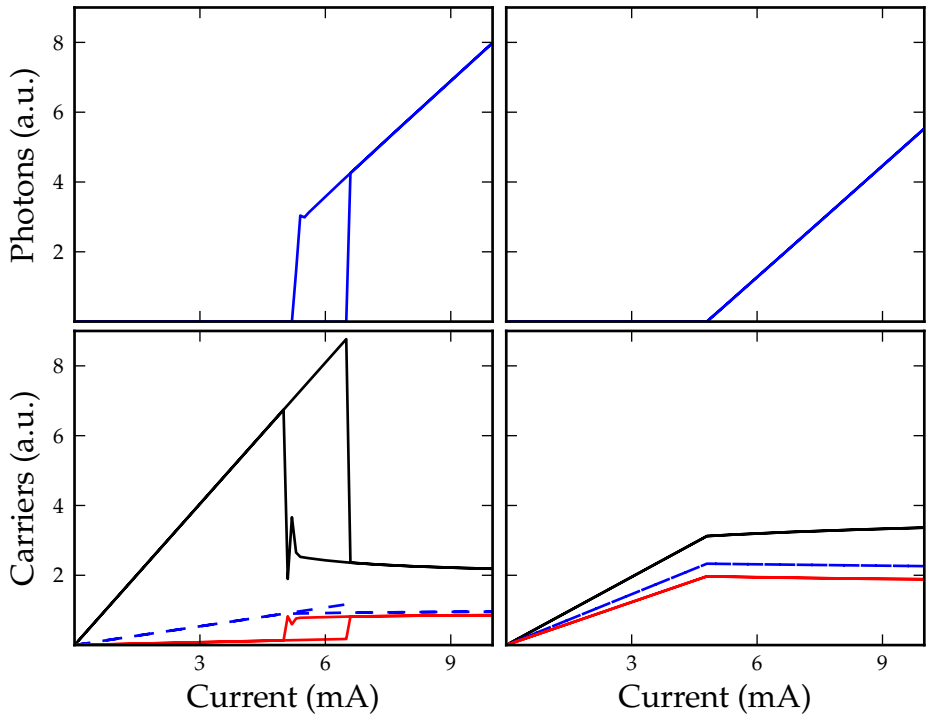


Figure 4.8: Top panels show calculated light-current characteristics for two different escape times, representing the stable and bistable regimes. Bottom panels show calculated carrier densities for each confined region(well1=black; well2=blue, dashed; well3=red), for the same escape times as the top panels.

The 11 dimensional system of equations is integrated using a fourth order Runga-Kutta method to determine the device characteristics as a function of drive current and of temperature. The right panels in Fig. 4.8 show the calculated photon density (top) and carrier density in the quantum wells (bottom) versus applied current for an escape time which corresponds to room temperature. As can be seen the light output shows lasing with no sign of bistability and the carrier densities all clamp at threshold, as expected.

The left panels show the same calculation for an escape time which corresponds to a temperature of 150 K. At 150 K a bistability of the light current

characteristic and of the carrier density can be clearly seen.

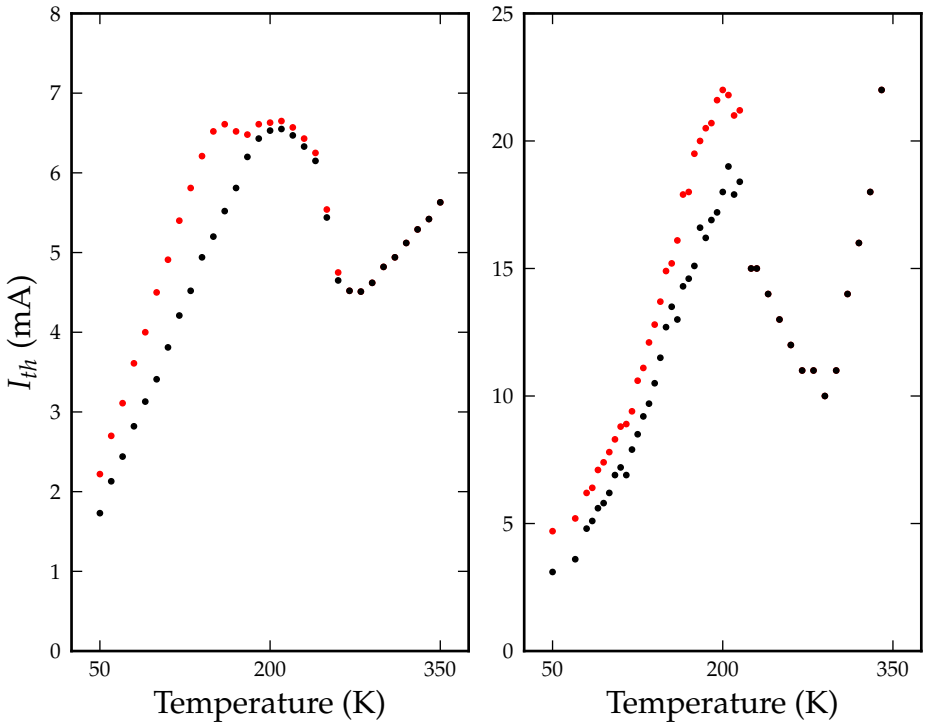


Figure 4.9: Calculated temperature dependence of threshold current (left panel) and the measured temperature dependence of threshold current (right panel). Switch on points red and switch off points black in bistable regime.

The escape time is varied according to Eq. (8) and the transparency carrier density according to Eq. (9) in the temperature range from 50 K to 350 K and the resulting threshold currents are compared to the measured values in fig 4.9.

From 50 K to 230 K in both cases there is a bistable, increasing threshold current. From 230 K to 280 K there is a decreasing threshold current, and giant T_0. Both the measured and calculated values of threshold current begin to increase above 300 K. Despite that the model presented here includes only two temperature dependent parameters; the transparency carrier density N_{tr} and the carrier escape time from the quantum wells, τ_e, it still provides very good qualitative agreement between the measured and calculated threshold currents. Overall, the simple model presented here confirms that carrier localisation and a non-uniform spatial carrier distribution can lead to bistable behaviour of the threshold current at low temperatures in the DW_H device considered here.

To achieve results with stronger quantitative agreement, Auger recombination

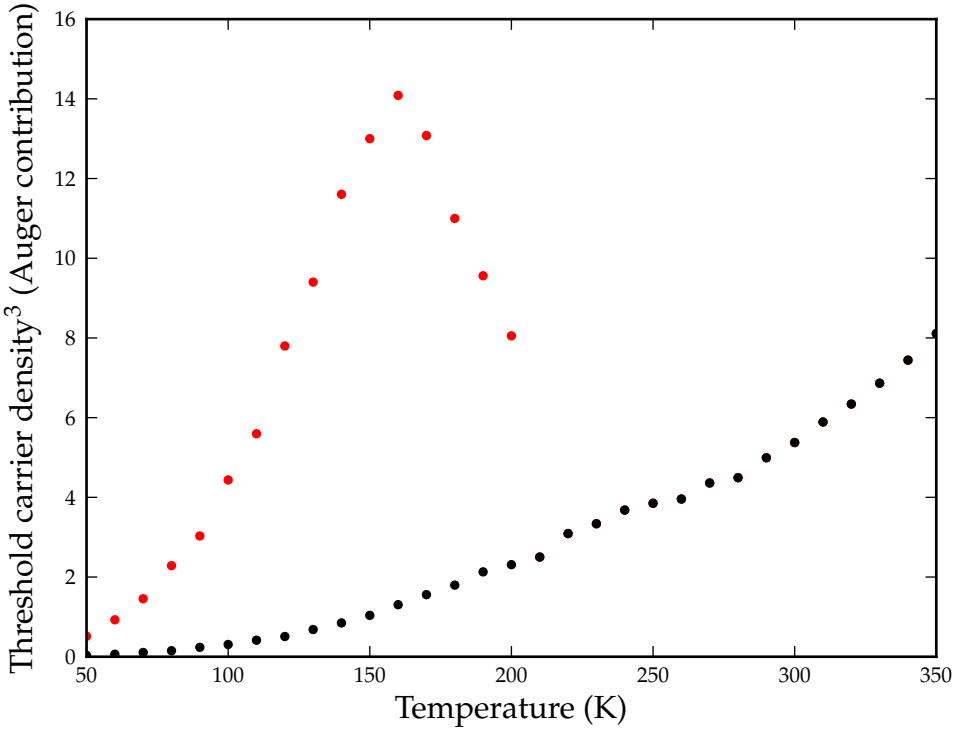


Figure 4.10: Effect of Auger recombination inclusion on the total threshold current, represented by the total carrier density cubed. Switch on threshold in red and switch off threshold in black.

would have to be considered. Auger recombination is a 3 carrier process and so the Auger contribution at threshold is a cubic function of the total carrier density. The effect of this can be seen analytically by summing the threshold carrier density in each of the modelled well regions and plotting the cube of this number as a function of temperature, as shown in Fig. 4.10. This is not a quantitative measure of the Auger contribution, it does, however, provide insight into how Auger recombination will qualitatively effect the model. It is seen in Fig. 4.10 that, overall, the Auger contribution at threshold introduces a larger increase in threshold current with increasing temperature. This effect would serve to bring the calculated data into closer agreement with the measured data by increasing threshold values at higher temperatures. It is also seen in Fig 4.9 that the increase in the size of the bistability with increasing temperature is not as strong in the calculated data as the measured data. The Auger contribution also brings the model and experimental measurements into closer agreement, because the higher total carrier density required to reach switch-on threshold in the bistable regime leads to increased Auger losses for the switch-on threshold when com-

pared to the switch-off threshold. This combined with the temperature dependent transparency carrier density, results in an Auger contribution to threshold in the bistable temperature regime which increases the the size of the bistability with increasing temperature, before it is eliminated due to the formation of a thermal distribution of carriers throughout the structure at elevated temperatures.

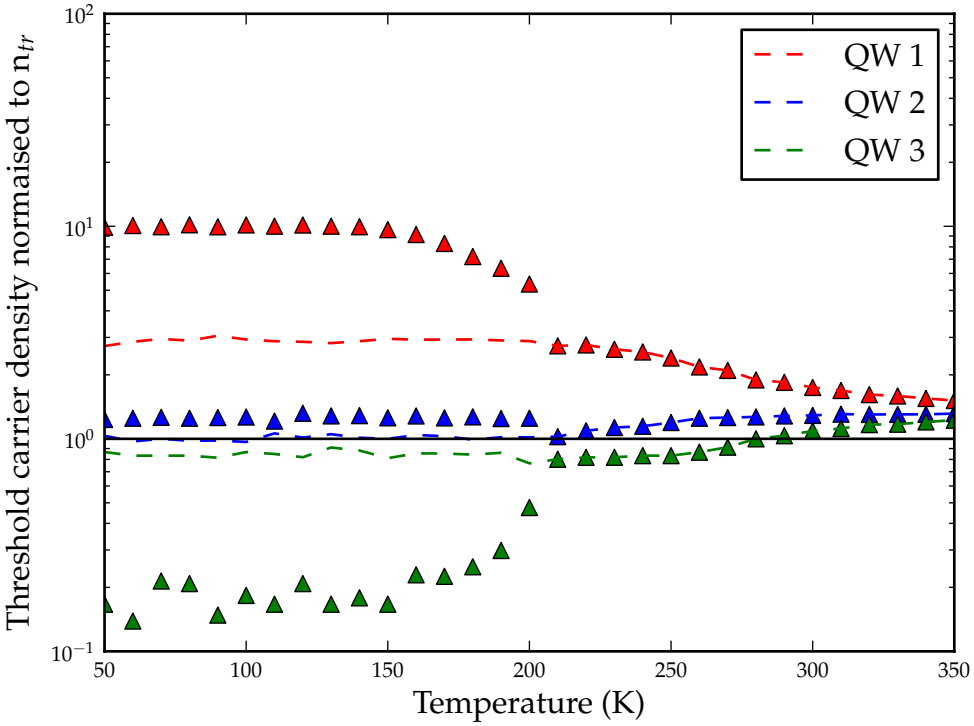


Figure 4.11: Temperature dependent threshold carrier density normalised to transparency carrier density for each of the three wells modelled, triangles indicate switch on points and dashed lines switch off points.

Strong insight into how the behaviour of the carriers in this model results in a bistable threshold current can be gained by studying Fig 4.11. In this figure the temperature dependent carrier density at threshold in each well is plotted with increasing current threshold (switch-on) represented by triangles and decreasing current threshold (switch-off) represented by dashed lines. The carrier density has been normalised to transparency carrier density in this plot for comparison of carrier density in each region without the effect of the temperature dependent gain. At low temperature it is clear that most of the injected carriers populate well 1 (red). Enough carriers escape from well 1 to ensure that well 2 (blue) is electrically pumped to transparency. The carrier density in well 3, however, re-

mains far below transparency and consequently well 3 strongly absorbs. A total carrier density much greater than the minimum of three times transparency is required to achieve lasing as a result of this absorption. Once enough carriers have been injected to produce enough gain in well 1 to achieve lasing, the aforementioned photon mediated carrier equilibrium takes effect, resulting in well 3 remaining at or close to transparency by absorbing photons - well 3 is essentially optically pumped to transparency. As current is reduced, stimulated emission ensures that well 3 remains at transparency to a value of total carrier density much lower than was required for the initial switch on, and so it is seen that the switch off carrier density of well 3 is very close to transparency. As temperature is increased above 150 K, it is seen that the carrier density of well 3 at switch on threshold begins to rise, signifying that carriers have gained enough thermal energy to escape well 1 and 2 and to reach well 3. As temperature is further increased, a thermal distribution of carriers across the structure begins to form, resulting in a near uniform carrier density in each well at higher temperatures.

4.7 Summary

In this chapter a bistability of threshold is discovered in a quantum dash in a well laser at low temperatures. Firstly, in section 4.2 an overview of the studied materials was given. In section 4.3 the experimental methods utelised and the data aquired were examined. Following this, in section 4.4 a proposed mechanism for the bistable behaviour was put forward. In section 4.5 the model developed to describe the bistable behaviour was presented. Finally in section 4.6 the results of theoretical calculations and experimental measurements were compared before a thorough discussion of the results of the model was given.

It was concluded that passive saturable absorption causes a bistability in the higher barrier laser due to impeded interwell transport at low temperature. It was seen that this bistability is followed at higher temperatures by a giant, and sometimes negative, value of T_0. A modified 11 dimensional rate equation model incorporating carrier transport effects was used to qualitatively test the proposed mechanism for bistability and very good qualitative agreement between theory and experiment was found.

This effect has potential to be exploited in several areas. Modelocking, where decoupled carrier states are required to achieve transform limited pulses, and where a wide gain bandwidth provides the possibility of very short pulses, could be achieved by making a two section device from the DW_H material. In addition,

if the composition were varied to achieve a higher barrier, it would offer the possibility of bistable behaviour at room temperature, allowing applications such as passive optical switching using either injected light or current to switch between the two stable output powers.

Chapter 5

Experimental study of bismuth-induced broadening in $GaAs_{1-x}Bi_x$ quantum well laser structures

5.1 Introduction

This chapter is the first in the thesis to focus on the novel semiconductor alloy $GaAs_{1-x}Bi_x$. This material is of interest as an active region for next generation telecommunication sources. The reasons for the interest in this material are threefold. Firstly the addition of bismuth to GaAs introduces the ability to engineer the energy-sapping CHSH Auger recombination pathway out of telecommunication lasers, thus, secondly, allowing the development of lasers whose temperature stability is excellent. Thirdly, the rapid shrinkage of the bandgap with the introduction of bismuth allows 1.55 μm emission from materials grown on technologically favourable GaAs substrates, allowing the possibility for future development of VCSELs and Bragg gratings on this material platform. In this chapter, some initial characterisation and analysis of materials and devices grown within the European FP7 BIANCHO project (www.biancho.org) are presented.

The replacement of a small fraction of the arsenic atoms in GaAs by bismuth (Bi), to form the $GaAs_{1-x}Bi_x$ alloy, results in a rapid decrease in the band gap and increase in the spin-orbit-splitting energy with increasing x. Due to the large chemical and size differences between Bi atoms and the As atoms they replace, Bi acts as an isovalent impurity in GaAs. The observed rapid variation of the band gap and spin-orbit-splitting energy with x in $GaAs_{1-x}Bi_x$ has been attributed to

a band anti-crossing interaction [5, 21] between the extended states of the GaAs valence band (VB) edge, and highly localised Bi-related states which are resonant with the GaAs VB.

It has been predicted theoretically [100] and confirmed experimentally [15] that for $x \gtrsim 10\%$ the spin-orbit-splitting energy exceeds the band gap in $GaAs_{1-x}Bi_x$ alloys. It has also been predicted that this band structure condition should lead to suppression of the CHSH Auger recombination mechanism [94]. This non-radiative recombination pathway accounts for up to 80% of the threshold current at room temperature in InP-based semiconductor quantum well lasers operating at telecommunication wavelengths [82], resulting in a strong decrease in efficiency and increased heating in laser chips, which in turn imposes a requirement for external cooling in order to maintain operational stability.

$GaAs_{1-x}Bi_x$ has gained much exposure over the last number of years as a candidate material system for highly efficient, temperature stable laser operation at telecommunication wavelengths on the commercially favoured and technologically important GaAs substrate. Strong interest in this material system has led recently to the development of the first electrical injection $GaAs_{1-x}Bi_x$ QW laser [66]. However, there remains much to understand regarding the fundamental effects of Bi incorporation on the electronic and optical properties of $GaAs_{1-x}Bi_x$ and related alloys.

This chapter focuses on understanding the Bi-induced broadening of the band edge optical transitions in $GaAs_{1-x}Bi_x$ QW laser structures. The materials studied in this chapter are described in detail in section 5.2. Using photovoltage spectroscopy (PVS) it is shown in section 5.3 that alloy disorder effects cause strong inhomogeneous broadening of the $GaAs_{1-x}Bi_x$ valence band edge, and temperature-dependent photoluminescence (PL) and spontaneous emission (SE) measurements suggest a non-thermal carrier distribution at temperatures below room temperature. In section 5.4 it is shown that the broadening extracted from the PV measurements is confined predominantly to the VB and therefore that the conduction band remains relatively unaffected by the incorporation of Bi, in accordance with the results of previous theoretical analysis [100]. It is suggested that this alloy disorder results in spatial fluctuations of the $GaAs_{1-x}Bi_x$ VB edge within the QWs. Evidence for the formation of Bi-related localised states with transition energies lying below the band edge is also seen. The analysis of the temperature dependent PL and SE measurements demonstrate that both of these factors strongly affect the carrier distribution, and show that localisation of carriers is important in determining the optical properties of $GaAs_{1-x}Bi_x$ alloys below

room temperature. In section 5.4.1 the temperature dependent lasing characteristics of the $GaAs_{0.978}Bi_{.022}$ QW device of Ref. [66] are presented. In section 5.5, calculations of temperature dependent SE carried out by Christopher A. Broderick are shown and discussed, which cast further light on the experimental measurements. In section 5.6 the work undertaken in this chapter is summarised.

5.2 Materials studied

In this section a brief description of the materials studied in this chapter will be given. All of the devices studied in this chapter are broad-area SCH single quantum well laser structures with either 50 μm or 100 μm stripe width, 1 mm long cavities and as-cleaved facets. The standard device structure used in these materials can be seen in Fig. 5.1. PL measurements are carried out on bare wafer samples of the laser structure before metallisation. In this chapter, 5 samples are

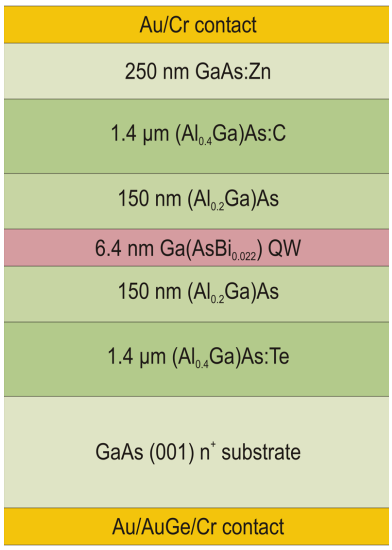


Figure 5.1: An example SCH device stack from Philipps-Universität Marburg

studied. Four of these are studied using PV measurements, while temperature dependent PL, SE and lasing characteristic measurements are undertaken on the fifth sample. Samples 1, 2 and 3 used in the PV work were grown at Philipps-Universität Marburg by Peter Ludewig using metal organic vapour phase epitaxy (MOVPE). Sample 1 and 2 have 20 % nominal AlGaAs barriers and Bi composition of 0.0 % and 1.7 % respectively. Sample 3 has a pure GaAs barrier and 4.4 % Bi in the QW. Sample 4 is called a hybrid growth device, it has a 6.6 % Bi QW. Because the incorporation of Bi into GaAs by MOVPE is technologically very difficult, attaining high composition devices by MOVPE is not currently possi-

ble. It is easier to achieve Bi incorporation by molecular beam epitaxy (MBE). However it is difficult with the MBE chamber at FTMC used in BIANCHO to grow thick cladding layers. For this reason, hybrid laser structures were grown in the BIANCHO project where the bottom cladding layers were grown in Marburg before the material was removed from the reactor and sent to FTMC in Vilnius to Prof. Arunas Krotkus, where the active region was grown by MBE. The material was then returned to Marburg where the top cladding was grown and the wafer was distributed for PL measurement or processed into laser devices. The fifth sample studied is the 2.2 % laser of Ref. [66], which is studied here using PL and SE measurements. The temperature dependent lasing characteristics of this material are also extracted from the measurements.

5.3 Experimental analysis

In this section the results of the experimental measurements used to characterise the broadening in $GaAs_{1-x}Bi_x$ QW samples are presented. Polarisation-resolved PV spectroscopy is a method whereby the laser facet is illuminated with spectrally-resolved light as described in chapter 3. As the energy of the incident light is varied, phase-sensitive techniques are used to measure the voltage associated with the photocurrent generated by the absorption of this incident light within the active region of the laser structure. The spectra collected in this manner are corrected to account for the spectral and polarisation dependence of the experimental setup, so that the spectra they represent are the measured setup-independent carrier generation rates in the structure [71]. Furthermore, the orthogonal nature of the p-like states at the VB edge in QW structures means that the use of polarisation-resolved measurements allows separate access to transitions related to light- and heavy-hole (LH and HH) states, so that the QW band structure can be probed in detail. The broadening of each observed transition is extracted by fitting a Gaussian lineshape function to the corresponding feature in the measured spectra. The Gaussian lineshape implies that the alloy band edge has undergone inhomogeneous broadening.

PVS measurements of four QW laser structures are shown in Fig. 5.2. The structure shown on top (sample 1) has a pure GaAs QW while the sample below this (sample 2) has a $GaAs_{1-x}Bi_x$ well with $x = 1.7\%$; both structures have the same $Al_{0.14}Ga_{0.86}As$ barriers. The two samples below these (samples 3 and 4), both have pure GaAs barriers. Sample 3 has a composition of $x = 4.4\%$ while sample 4 has a composition of $x = 6.6\%$. The quantum well thicknesses are

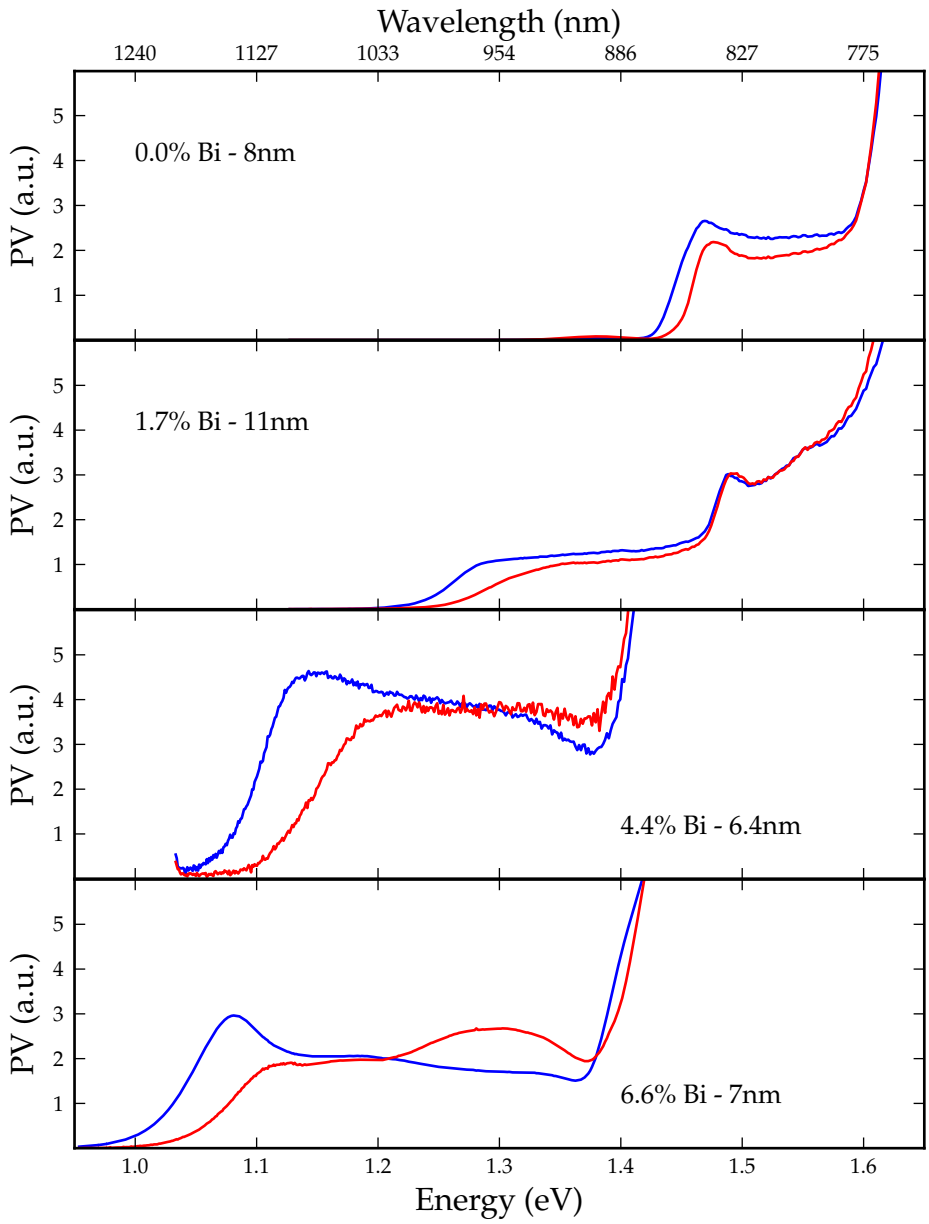


Figure 5.2: Measured TE and TM polarised (blue and red lines respectively) room temperature photovoltage spectra of $GaAs_{1-x}Bi_x$/(Al)GaAs single quantum well laser structures. For each structure the nominal Bi composition x and quantum well thickness are indicated on the plots.

indicated on the plots along with the estimated Bi composition. By comparing the TE and TM polarised spectra in Fig. 5.2, it is seen that all of the structures display a splitting of the HH and LH band edges. Samples 1 and 2 show a transition at $\approx$ 1.6 eV, corresponding to the band gap of the barrier material; equivalent transitions can be seen at $\approx$ 1.42 eV in samples 3 and 4, which have pure GaAs barriers. Sample 2 shows an additional polarisation-insensitive feature at $\approx$ 1.48 eV, which we attribute to transitions from the first bound electron state in the QW ($e1$) to the continuum of VB barrier states (BVB) [18]. These transitions are visualised in Fig. 5.3, where 1 and 2 represent the split e1 to HH and LH transitions and 3 represents the polarisation insensitive e1-BVB feature in sample 2. The transition energy and broadening determined from each of the features in the photovoltage spectra of Fig. 5.2 are listed in Table 5.1. Full details of the analysis of the measured $GaAs_{1-x}Bi_x$ photovoltage spectra can be found in Ref. [18] and in chapter 6 of this thesis.

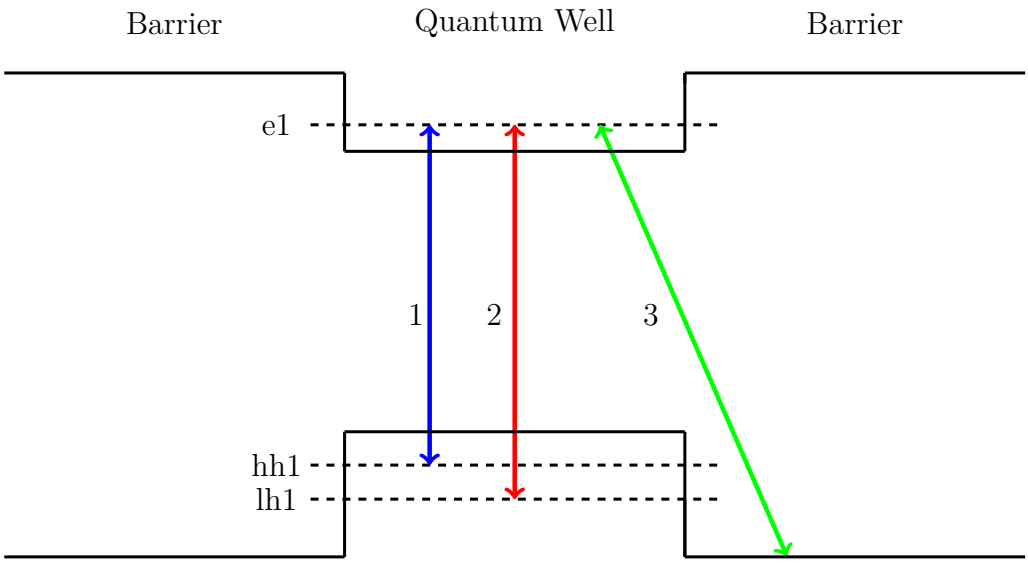


Figure 5.3: Real-space illustration of transitions between bound-to-bound (1 & 2) and bound to continuum (3) states in quantum well structures

Fig. 5.4 shows the measured temperature-dependent SE and PL spectra from 100 K to 350 K for the first ever electrically injected $GaAs_{1-x}Bi_x$ single QW laser of Ref. [66]. The SE spectra were measured at the lasing threshold through a window in the GaAs substrate [34] while the laser underwent pulsed electrical injection with a 1% duty cycle. The PL spectra were measured by exciting the bare wafer with continuous-wave laser emission from a 640 nm laser diode

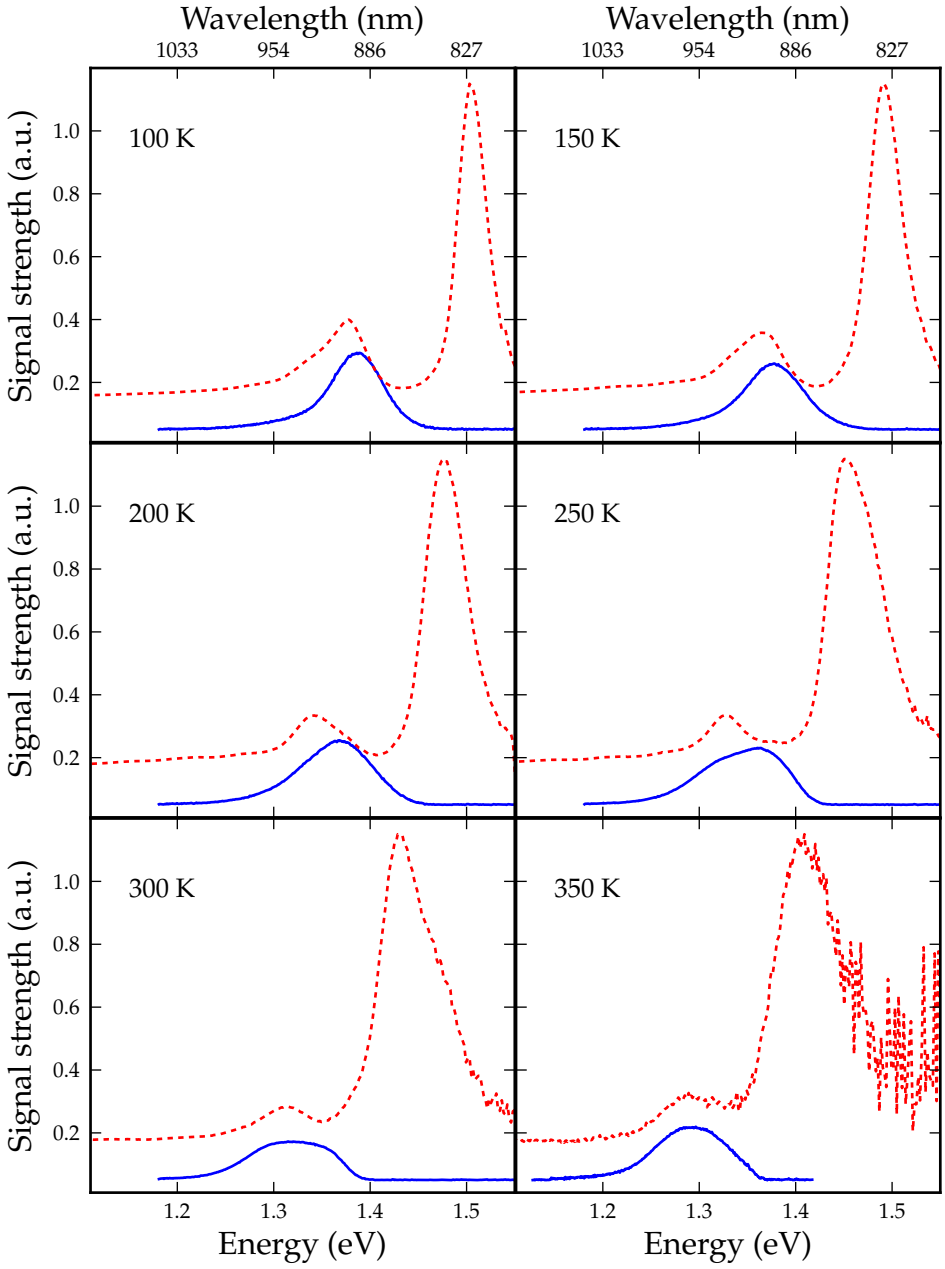


Figure 5.4: Measured spontaneous emission (blue lines) and photoluminescence (red dashed lines) spectra, for temperatures ranging from 100 to 350 K. The spontaneous emission measurements were performed under electrical injection at the lasing threshold, while the photoluminescence spectra were measured with 70 mW continuous-wave pump power at a wavelength of 640 nm. PL has been offset in the y-direction for clarity.

Table 5.1: Transition energies and broadening extracted from the room temperature photovoltage spectra of samples 1, 2, 3 and 4 shown in Fig. 5.2.

Sample	Transition	Energy (eV)	Broadening (meV)
1	$e1$-$hh1$	1.449	16
1	$e1$-$lh1$	1.459	12
2	$e1$-$hh1$	1.264	29
2	$e1$-$lh1$	1.292	48
2	$e1$-BVB	1.477	11
3	$e1$-$hh1$	1.107	31
3	$e1$-$lh1$	1.147	48
4	$e1$-$hh1$	1.051	29
4	$e1$-$lh1$	1.082	38

and spectrally resolving the resulting emission from the wafer. Details of the experimental methods can be found in chapter 3. A discrepancy is seen between the SE and PL peak emission energies below room temperature.

5.4 Theoretical interpretation of results

In this section a theoretical interpretation of the measured material properties is presented. Considering the PVS measurements, due to the fact that the $e1$-BVB transition in sample 2 shows broadening comparable to the bound-to-bound transitions in the Bi-free QW of sample 1, and that this $e1$-BVB transition does not involve the $GaAs_{1-x}Bi_x$ VB, it is concluded that the broadening of the band edges in $GaAs_{1-x}Bi_x$ comes about from alloy disorder which almost exclusively affects the VB, as indicated by previous theoretical analysis carried out by Dr. Muhammad Usman and Christopher A. Broderick [99]. In Table 5.1 it is seen that, somewhat counter-intuitively, the inhomogeneous broadening of the alloy band edge, brought about as a result of the alloy disorder, does not vary significantly with increasing Bi composition x. It is further noted that the linewidth of the LH band edge feature is larger than that associated with the HH feature. This is in accordance with the previously mentioned theoretical work in Ref. [99], in which it was shown that the enhanced inhomogeneous broadening of the LH band edge in $GaAs_{1-x}Bi_x$ epilayers is a result of a combination of the biaxial strain present in the material, as well as the strong hybridisation of the LH band edge states with a series of highly localised Bi-related states associated with Bi-Bi pairs and higher order clusters of Bi atoms.

The results of the temperature dependent PL and SE measurements of the

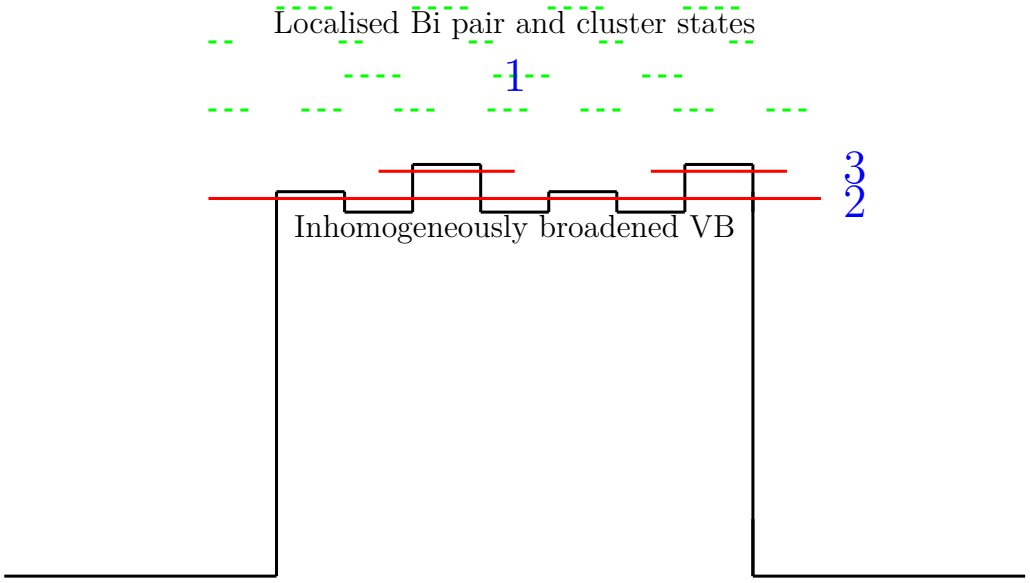


Figure 5.5: Illustration of different carrier localisation mechanisms discussed. Bi pair and cluster localised states lying above the band edge shown by green dashed lines and represented by 1. The inhomogeneously broadened VB edge is represented by 2 & 3.

$GaAs_{1-x}Bi_x$ single QW laser of Ref. [66] will now be discussed.

A discrepancy is seen between the SE and PL peak emission energies below room temperature. It has previously been shown that PL in $GaAs_{1-x}Bi_x$ at low temperatures is dominated by the recombination of excitons in Bi-related localised states lying in the tail of the emission spectrum, as seen in Fig. 5.5, represented by 1. These states have radiative lifetimes $\sim 10^3$ times longer than the timescale associated with the relaxation of carriers into localised states from the band edge [49, 50]. Detailed tight-binding supercell calculations by Christopher A. Broderick on disordered $GaAs_{1-x}Bi_x$ alloys, have explicitly demonstrated that the formation of these tail states is due to the presence of Bi-Bi pairs and larger clusters of Bi atoms [100]. Furthermore, it has recently been shown that increased excitation power leads, at fixed temperature, to a blue-shift of the PL peak as these tail states become saturated [63, 73].

Based on these observations, the measured discrepancy between the peaks of the SE and PL spectra at low temperature are attributed to the saturation of localised states due to the strong electrical pumping present in the SE measurements. The measured SE then comes predominantly from $GaAs_{1-x}Bi_x$ band edge at all temperatures [19], whereas the lower carrier density of the PL experiment results in emission from the localised states at low temperature. However, while these Bi-related lower energy localised states contribute only in part to

the measured SE, carrier trapping in these states at low temperature prevents the establishment of a thermal distribution of carriers in the QW. The effects of this can be seen in the strong dependence of the measured SE linewidth on temperature, as shown in Fig. 5.7. The SE linewidth is seen to increase strongly with temperature up to approximately 240 K, above which it strongly decreases. Part of this linewidth behaviour is expected to arise from thermalisation effects although, as we discuss further below, the strong increase in linewidth near 250 K includes a contribution from carriers thermalising into the first light hole band, while the decrease in linewidth at higher temperatures is partly due to absorption of the SE as it passes through the GaAs substrate. The PL spectra in Fig. 5.4 show a GaAs-related emission at higher energy. This GaAs-related emission is well separated from the GaAsBi PL and SE spectra at low temperature; it can be observed however that as the temperature increases, the PL peaks start to overlap. The GaAs substrate can then act as an absorbing layer for the higher energy GaAsBi emission; thereby reducing the width of the measured SE emission spectrum.

Given the broadening present at the GaBiAs VB edge, it can be expected that there will be a mobility edge in the VB states in the vicinity of 2 in Fig. 5.5, with all states above the schematic line at 2 being localised in character. At low temperatures holes will tend to be trapped at local maxima in the VB state distribution, weighted towards the states labelled 1. As temperature is increased, holes can gain sufficient energy to start to move towards a thermal distribution with carriers now recombining from states labelled 1, 2, and 3. The linewidth of the SE then increases due to the emission of light across a wide range of states. Then as the temperature increases beyond 240 K, the low density of Bi-related tail states become depleted of carriers and we begin to see the establishment of a thermal distribution of carriers in the QW. At these higher temperatures, carriers gain sufficient energy to start to form a thermal equilibrium.

The measured temperature dependence of the SE and PL spectra therefore demonstrates the absence of a thermal distribution of carriers below room temperature, and additionally shows the move towards a thermal distribution of carriers above room temperature, at which point the peaks of the SE and PL spectra come into coincidence. Additionally, the analysis indicates that this behaviour is a direct result of the effects of alloy disorder, which are manifested through the effects of Bi-related localised states, and through larger scale spatial fluctuations of the Bi composition, which generate spatial variations of the VB edge energy within the QW. Also visible in Fig. 5.6 is the characteristic “S-shape" in the tem-

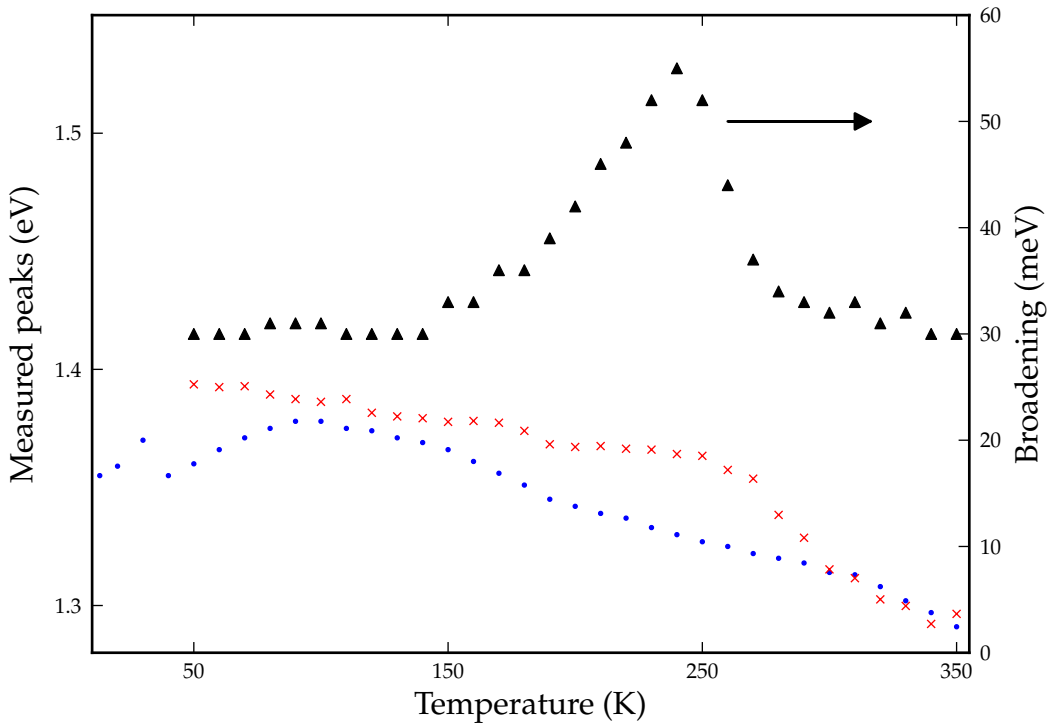


Figure 5.6: Measured temperature dependent spontaneous emission (crosses) and photoluminescence (filled circles) peak emission energies, as well as the broadening of the spontaneous emission spectra (filled triangles)

perature dependence of the PL emission peak. This S-shape comes about as a result of the aforementioned localised Bi pair and cluster tail states lying below the band edge, in which carriers become localised at low temperature [49, 50, 73].

Fig. 5.7 shows the measured variation of the SE spectrum with current density at 250 K. As the injection level is increased we see a weak S-shape in the SE peak, which is followed by an abrupt blue-shift of the SE peak at higher current densities. The broad low-energy emission (below 1.3 eV) is attributed to the $GaAs_{1-x}Bi_x$ localised states. The abrupt blue-shift in the SE peak by about 25 meV is attributed to carriers occupying the first light-hole band in the quantum well, as discussed further in Section 5.5. Although spontaneous emission starts to be observed from the light-hole band, the peak gain is nevertheless still associated with transitions from heavy-hole states, as indicted by the observation for the highest drive currents of a lasing peak in the emission spectrum above 1.3 eV. This peak is attributed to scattered laser light being captured by the fibre collecting the spontaneous emission spectrum through the window in the laser substrate. It can also be observed that the spontaneous emission does not pin, but rather

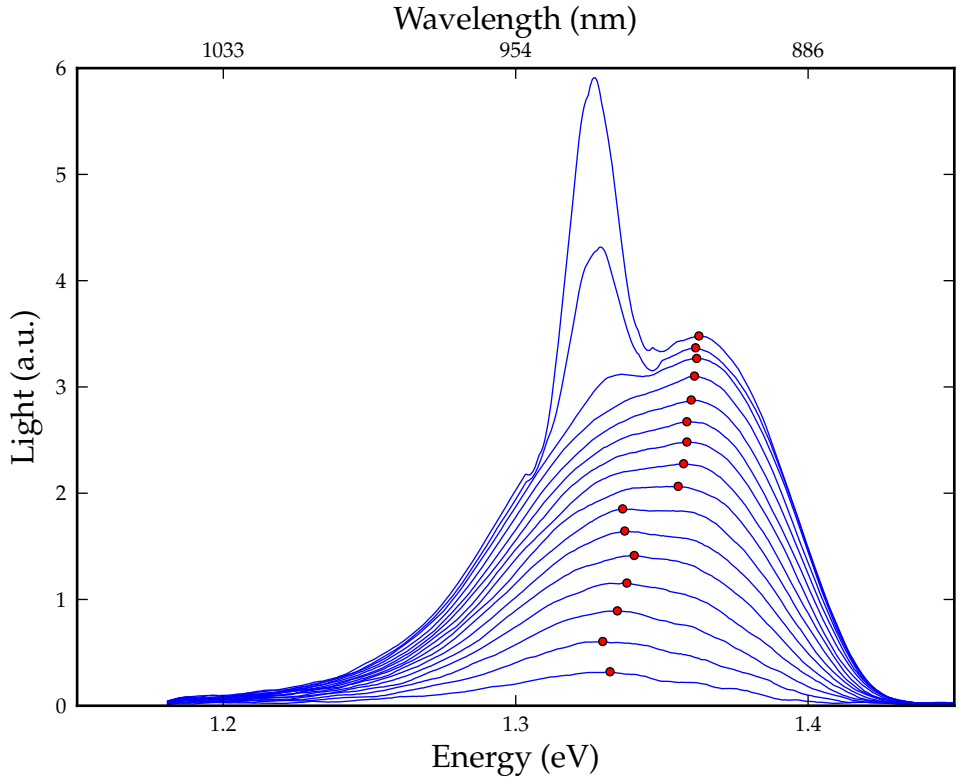


Figure 5.7: Measured injection level dependent spontaneous emission measurements up to threshold carrier density at 250 K, the peaks of each spectrum is indicated by a closed circle

continues to increase in magnitude above threshold (three highest drive currents in Fig 5.7). This is to be expected from a semiconductor laser structure in which the carriers are not in thermal equilibrium. The shift in the SE peak to the light hole peak around 250 K may also account for the unusual temperature dependence of the SE peak energy observed in Fig 5.6. It can be seen that the SE peak has an anomalously low temperature dependence between 170 K and 250 K, reflecting the shift to LH states, followed by a rapid reduction in energy above 270 K, as the measured peak appears to shift back towards the HH states.

It is possible that excitation power plays a role in the discrepency between the two datasets. As pump power is increased, the emission wavelength will naturally undergo a blueshift as low lying states become saturated and carriers begin to occupy higher lying states in the bandstructure. The SE measurement was collected under electrical injection at the threshold current density. Threshold current density in this material is quite high and its temperature dependence can be seen in Fig. 5.8. The current density for this measurement ranges from 3 $kAcm^{-2}$ at 50 K to 30 $kAcm^{-2}$ at room temperature. This means that the

injection strength for the electrically pumped measurement is increasing with increasing temperature. For the PL measurement, the excitation power is kept constant at 70 mW at all temperatures with a pumped area of ≈ 1 mm^2 and a pump wavelength of 640 nm. This corresponds to an optical power density of 0.7 mWcm^{-2}. Presuming each incident photon of energy 1.94 eV creates one electron-hole pair, this is then equivalent to a current density of order 0.35 mAcm^{-2}. Comparing this to the minimum electrical power density of 3 kAcm^{-2} in the spontaneous emission data presented, we see that the electrical injection rate is then over six orders of magnitude larger than the optical injection rate. This then justifies the assumption in our earlier discussion that there should be a much higher carrier density present for the spontaneous emission measurements compared to that which is present for the photoluminescence measurements.

5.4.1 Lasing characteristics of 2.2 % GaBiAs QW structure

In this section, the temperature dependent lasing characteristics of the first ever electrical injection $GaAs_{1-x}Bi_x$ laser of Ref. [66] are presented. The laser material is electrically pumped with a pulsed current source at 10 kHz, with 1% duty cycle, while the temperature is varied in the closed cycle helium cryostat. The facet light-current characteristic is measured from a window in the cryostat cold-head, and spontaneous emission is collected as a function of current and energy through a window milled in the laser substrate as described in chapter 3. Threshold current as a function of temperature is extracted from this data, and I_{th}^{rad} and z $_{th}$ [82] are extracted from this data. In Fig 5.8, $T_0(I_{th})$ is ≈ 100 K at low temperature and ≈ 170 K at 250 K. This is an excellent value for T_0, but is accompanied by a large threshold current density, suggesting that there are significant loss mechanisms in the laser. This is confirmed by comparison of the total threshold current density J_{th}, and its radiative component J_{rad} in Fig 5.8. The graph is plotted with the radiative current normalised to the total current at 50 K, i.e. assuming that there are no non-radiative losses at 50 K. It can be seen that even after the inclusion of this assumption, the radiative current (neglecting TM emission) is only 25% of the total current at 250 K. Hence we can estimate that non-radiative recombination pathways account for at least 75% of the total current at 250 K. The non-radiative losses are likely to be at least as high or higher than this value, as there is no evidence to suggest that non-radiative losses are negligible at 50 K.

In Fig 5.8, a small dip in the temperature dependence of J_{th}^{rad} and a corre-

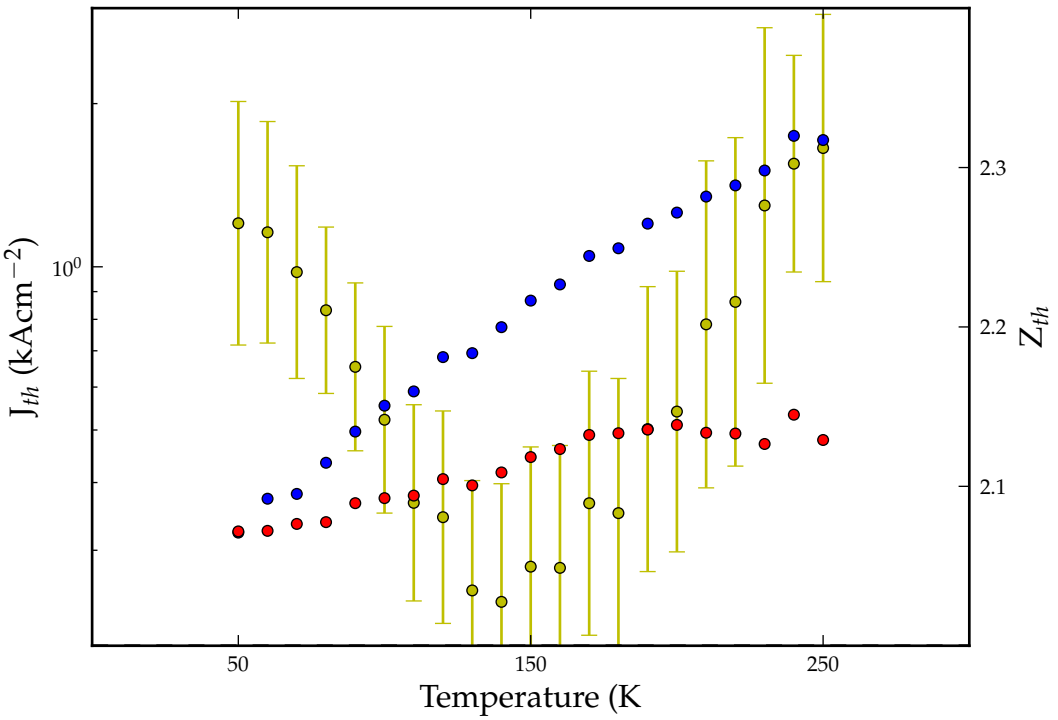


Figure 5.8: Variation of threshold current density (closed blue circles), J_{th}, and its radiative component (closed red circles), J_{th}^{rad}, with temperature, and the variation of z (closed yellow circles), the power of the carrier density, with temperature

sponding dip in J_{th} is seen, which strengthens the case for localisation / thermalisation effects in this material. Fig 5.8 shows that I_{th}^{rad} is relatively temperature insensitive (310 K $\leq T_0(I_{Rad}^{th}) \leq$ -3000 K). Similar behaviour has been observed in quantum dot and in dilute nitride semiconductor lasers, where the temperature insensitive nature of I_{rad}^{th} is attributed to a combination of carrier localisation and thermalisation effects, with the thermalisation effects leading to the observed negative values of T_0 in the previous devices studied.

It is noted that $z^{th} \approx 2$ across the temperature range as evidenced on the right y-axis of Fig 5.8. This would usually correspond to recombination dominated by radiative transitions. However, in this case it is suggested that $z^{th} \approx 2$ is a result of a loss mechanism with a carrier density power dependence similar to that of radiative recombination, due to the enhanced threshold current density and localisation effects in this material.

5.5 Calculations by Christopher A. Broderick

In this section a brief overview of some relevant calculations of temperature dependent SE by Christopher A. Broderick, using the $\mathbf{k} \cdot \mathbf{p}$ method is presented. The band structure of the $GaAs_{1-x}Bi_x$/(Al)GaAs QWs are calculated using a 12-band $\mathbf{k} \cdot \mathbf{p}$ model, which has recently been derived based on the results of detailed tight-binding supercell calculations of ordered $GaAs_{1-x}Bi_x$ alloys. In Ref. [21] it is demonstrated that the $GaAs_{1-x}Bi_x$ band structure can be accurately described in terms of a valence band anti-crossing (VBAC) interaction between the extended states of the GaAs host matrix and highly localised impurity states associated with substitutional Bi atoms. The 12-band model includes the extended, spin-degenerate conduction, light-hole, heavy-hole and spin-split-off bands of the GaAs host matrix, as well as VBAC interactions between the host matrix light- and heavy-hole bands and localised Bi related states that are resonant with the host matrix VB. The Bi-related parameters of the 12-band model have been constrained by comparing the band offsets and transition energies calculated using the model to the results of polarisation-resolved photovoltage measurements on a series of $GaAs_{1-x}Bi_x$/(Al)GaAs QW laser structures [18]. This means that the model will predict the temperature dependence of the average material bandgap; this model does not take account of localisation effects. Inhomogeneous broadening is added to the calculated spectra as a post processing procedure, with the inhomogeneous linewidth extracted from Gaussian fitting to the aforementioned PV measurements. The value of inhomogeneous broadening used at each temperature is indicated on Fig. 5.9. Following Ref. [42], the QW electronic structure is calculated using a semi-analytical plane wave expansion method, which accounts self-consistently for the effects of electrostatic confinement by solving Poisson's equation for the carrier-induced electrostatic potential. The spontaneous emission and radiative losses are calculated using a density matrix formalism, in which the transition matrix elements are evaluated explicitly from the QW eigenstates. This approach therefore includes the crucial effects of VBAC-induced state mixing and epitaxial strain on the calculated electronic and optical properties [19]. As can be seen from Fig. 5.9, the 12-band model describes the temperature dependence of the SE peak very well up over the full temperature range. In addition, we note two features of the spectra consistent with our earlier analysis. It can be seen that the calculated high temperature theoretical spectra are much broader than the experimental ones, consistent with the likely absorption in the substrate of the high-energy side of the experimental curves. In addition, the 250 K theoretical curve broadly follows the experimental one, with the peak emis-

sion energy being well above the calculated band edge energy, and including a significant contribution due to recombination associated with confined LH states.

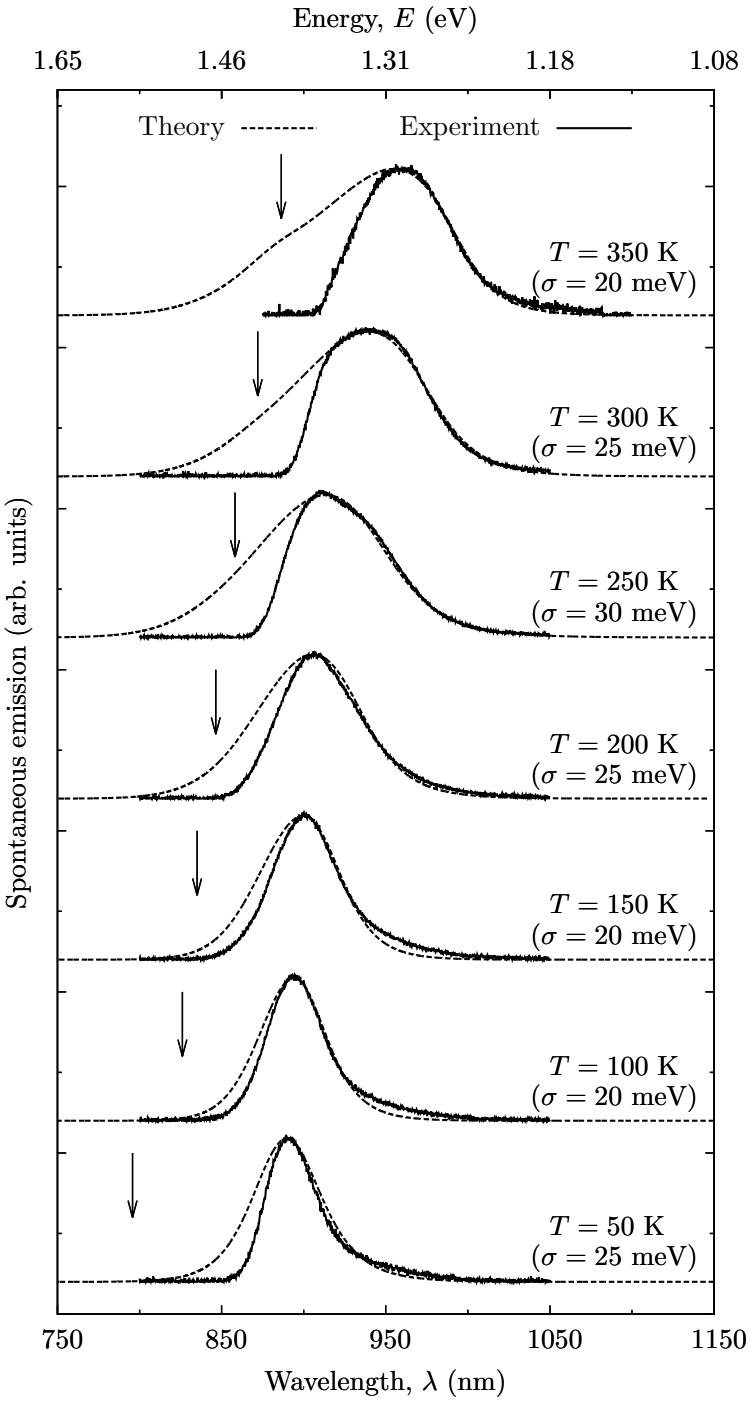


Figure 5.9: Comparison of measured and calculated SE for the 2.2 % $GaAs_{1-x}Bi_x$ QW laser structure of Ref. [66]. The calculated spectra at 300 K and 350 K have undergone a red shift of 12 nm to compare the shape of the band edge transition.

5.6 Summary

Section 5.2 provided an overview of the materials studied in this chapter. In section 5.3 the use of photovoltage spectroscopy to probe the band structure of $GaAs_{1-x}Bi_x$/(Al)GaAs QW laser structures was described, with Bi compositions of up to $x = 6.6\%$. Following this, temperature dependent measurements of photoluminescence and spontaneous emission from the first ever electrically injected $GaAs_{1-x}Bi_x$ single QW laser structure with $x = 2.2\%$ were described. In section 5.4, it was shown how the use of polarisation-resolved photovoltage measurements verify earlier theoretical predictions [99] that the light-hole band edge states in $GaAs_{1-x}Bi_x$ should undergo enhanced inhomogeneous broadening compared to that associated with heavy-hole states. Additionally, it was shown that the variation of the inhomogeneous broadening of the band edge transitions in $GaAs_{1-x}Bi_x$ alloys depends only weakly on the Bi composition x. It was determined that Bi-related localised states contribute to the spontaneous emission in electrically pumped $GaAs_{1-x}Bi_x$ QWs, with these localised states preventing the formation of a thermal carrier distribution. Additionally, measurements show that the spontaneous emission linewidth is strongly dependent upon temperature, obtaining a maximum value at close to 250 K before strongly decreasing with increasing temperature. This unusual material behaviour was explained by considering three effects, (i) the temperature-dependent dynamics of carriers at the band edge, using a combination of theoretical calculations[100, 19] and the results of previous studies [49, 50] of the luminescence dynamics in $GaAs_{1-x}Bi_x$ materials as well as also considering (ii) the contribution of LH states to the SE spectra and (iii) absorption by the substrate of the high energy part of the SE spectra at higher temperatures. In section 5.4.1 the temperature dependent lasing characteristics of the 2.2 % laser structure were presented, showing large values for I_{th} and T_0 and a value for $z \approx 2$. In section 5.5, calculations of temperature dependent SE by Christopher A. Broderick and a comparative analysis with the relevant experimental data was presented. This analysis confirmed the likely contribution of LH states and of substrate absorption to the measured temperature dependence of the SE linewidth.

Chapter 6

Experimental determination of the $GaAs_{1-x}Bi_x$/GaAs band offset, and $\mathbf{k} \cdot \mathbf{p}$ paramterisation

6.1 Introduction

In this chapter, following on from chapter 5, the first ever experimental analysis leading to the determination of the band offset at the $GaBi_xAs_{1-x}$/GaAs heterointerface is outlined. This experimentally determined band offset is used to constrain and parametrise a 12 band $\mathbf{k} \cdot \mathbf{p}$ model. The work undertaken in this chapter was a collaborative study with Christopher A. Broderick, who was responsible for all of the calculations and modelling mentioned in the chapter.

Dilute bismide alloys are naturally complementary to well-studied dilute nitride alloys such as GaN_xAs_{1-x}, [79] with the formation of Bi-related localised states and their interaction with the extended valence band (VB) edge states of the host matrix semiconductor determining the details of the electronic structure [100]. In particular, the replacement of As by Bi to form $GaBi_xAs_{1-x}$ has been observed experimentally and demonstrated theoretically to cause a rapid reduction of the fundamental band gap E_g by approximately 90 meV when 1% of the As atoms in GaAs are replaced by Bi, [97, 6] as well as a strong increase in the spin-orbit-splitting energy (Δ_{SO}) with increasing Bi composition x [36, 15].

Amongst the possible technological applications of dilute bismide alloys are in GaAs- and InP-based thermoelectric [32] and spintronic [68] devices, but the most promising application is the possible use of Bi to engineer the band structure of the quantum wells (QWs) forming the active region of semiconductor lasers operating at telecommunication wavelengths [94, 22]. The incorporation

of Bi in GaAs to form $GaBi_xAs_{1-x}$ with $x \gtrsim 10\%$ leads to a band structure in which the magnitude of the spin-orbit-splitting energy exceeds the band gap ($E_g < \Delta_{SO}$). This band structure condition offers the possibility of supression of the hot-hole-producing non-radiative CHSH Auger recombination pathway, a loss mechanism that strongly increases the threshold current and temperature sensitivity in conventional InP-based QW lasers operating at telecommunication wavelengths [94, 22, 92, 93].

The causes and effects of the strong modification of the $GaBi_xAs_{1-x}$ VB structure compared to that of GaAs have been studied theoretically by several authors [52, 108, 31, 100]. Despite a degree of controversy, [31] the general consensus is that Bi acts as an isovalent impurity, introducing highly localised states which are resonant with the extended states of the GaAs VB [108, 21]. It has been suggested [6] that the strong composition-dependent bowing and reduction (increase) in E_g (Δ_{SO}) with increasing x can be understood in terms of a valence band anti-crossing (VBAC) interaction. In the VBAC model, localised states associated with substitutional Bi atoms interact strongly with the extended states of the GaAs host matrix VB maximum. This results in an upward shift in energy of the alloy VB edge with increasing x, leading to the observed strong, composition-dependent bowing of E_g and Δ_{SO}.

The applicability of the VBAC model in $GaBi_xAs_{1-x}$ has previously been validated using an atomistic tight-binding model [21]. By using detailed tight-binding supercell calculations it has been confirmed explicitly that the strong composition-dependent bowing of E_g and Δ_{SO} with increasing x can be understood in terms of a VBAC interaction, and that this picture provides an accurate description of the main features of the $GaBi_xAs_{1-x}$ band structure, in agreement with a wide range of spectroscopic measurements across the full composition range for which experimental data is available [100, 99].

The growth of dilute bismide alloys represents a difficult challenge, and only recently has the growth of device-quality materials become possible. Advances in the understanding of optimised growth conditions for $GaBi_xAs_{1-x}$ have resulted in the realisation of the first electrically pumped dilute bismide QW laser [65]. This important milestone has signalled, from a theoretical perspective, the need to develop models of the $GaBi_xAs_{1-x}$ band structure which are appropriate for the description of the electronic and optical properties of nanostructures based on $GaBi_xAs_{1-x}$ and related materials.

This chapter begins with the use of photovoltage (PV) spectroscopy to identify and assign energies to the observed transitions in a series of

$GaBi_xAs_{1-x}$/(Al)GaAs QW laser structures. The use of polarisation-resolved PV spectroscopy allows explicit identification of transitions involving light and heavy holes by separately measuring the TM and TE polarised PV spectra. Using this information the band structure of these dilute bismide QW structures is compared with theoretical calculations based on a 12-band $\mathbf{k}\cdot\mathbf{p}$ model to directly determine the band offsets at $GaBi_xAs_{1-x}$/(Al)GaAs heterointerfaces.

In order to determine the band offsets in the QW samples, analysis of a Bi-free GaAs/AlGaAs single QW structure is carried out which leads to constraint of the band offset of the GaAs/AlGaAs alloy. This is achieved through the use of the results of calculations based on an 8-band $\mathbf{k}\cdot\mathbf{p}$ model which are compared with the transition energies extracted from the measured PV spectra. This fixes the GaAs/AlGaAs band offsets which are then used as the input to the 12-band $\mathbf{k}\cdot\mathbf{p}$ calculations for the Bi-containing samples. The incorporation of Bi introduces seven Bi-related parameters which are not known from the 8-band $\mathbf{k}\cdot\mathbf{p}$ model, which describes the GaAs host matrix. These parameters must be determined accurately in order to provide a reliable description of the $GaBi_xAs_{1-x}$ band structure using the 12-band model. These parameters are: (i – iii) the virtual crystal contributions to the energies of the conduction band minimum (α), valence band maximum (κ) and spin-split-off band (γ) at the Γ-point, (iv) the energy of the Bi-related impurity states relative to the unstrained GaAs VB maximum (ΔE_{Bi}), (v) the VBAC coupling strength (β), and (vi, vii) the hydrostatic and axial deformation potentials of the Bi-related impurity states (a_{Bi} and b_{Bi}). The theory of the effects of Bi on the band edge energies in $GaBi_xAs_{1-x}$ as described by these parameters, is outlined in Section 6.4 below.

As a result of this large number of Bi-related parameters it would appear that the task of fitting a suitable set of band structure parameters to the experimentally measured transition energies is a highly ambiguous one. This issue is circumvented by determining five of the seven Bi-related parameters directly from detailed tight-binding supercell calculations [21], leaving only two of the parameters (α, which determines the conduction band offset, and β, which is the dominant contribution to the light and heavy hole band offsets) free to fit to the measured transition energies. Since the PV spectra of one of the Bi-containing samples investigated shows clear transitions from bound electron states in the QW to the barrier VB, it is possible to examine the conduction band (CB) offset independently of that of the VB. This allows α and β to be fitted to the experimental data independently of one another, by comparing the results of the theoretical calculations with the experimentally measured transition energies. By

following this approach it is demonstrated explicitly for the first time that the band offsets at $GaBi_xAs_{1-x}$/GaAs heterointerfaces are type-I. Furthermore, based on the 12-band $\mathbf{k}\cdot\mathbf{p}$ model, a straightforward analytical procedure for calculating these band offsets is provided. When combined with the Bi-related band structure parameters systematically extracted from a combination of PV measurements and tight-binding supercell calculations, this unambiguously determines the $GaBi_xAs_{1-x}$/(Al)GaAs band offsets.

Through this analysis the set of parameters we arrive at for the 12-band dilute bismide $\mathbf{k}\cdot\mathbf{p}$ Hamiltonian is shown to be capable of describing the measured transition energies in additional single and triple quantum well (SQW and TQW) structures, verifying the robustness of the 12-band model. In particular, it is noted that the calculated energy differences between the first bound light- and heavy-hole states in the QWs ($lh1$ and $hh1$) are in good agreement with the experimentally determined values. This is noteworthy since accurate reproduction of the $hh1$–$lh1$ splitting is an important feature of any model which aims to describe QW band structure, since the optical properties of a QW are strongly influenced by the density of states at the VB edge [77, 78]. In particular, the VB edge density of states has a strong effect on the hole quasi-Fermi level when the QW is under injection and is therefore of particular significance for QW laser action [2]. The analysis confirms the validity of the 12-band $\mathbf{k}\cdot\mathbf{p}$ model as an appropriate starting point from which to calculate the electronic and optical properties of dilute bismide-based nanostructures.

The remainder of the chapter is organised as follows. In Section 6.2, the growth and characterisation of the QW laser structures studied in this chapter is outlined. This is followed in Section 6.3 by a brief discussion of polarisation-resolved PV spectroscopy. In Section 6.4 the general theory for calculating the band offsets at $GaBi_xAs_{1-x}$/(Al)GaAs heterointerfaces is presented, including the effects of Bi-induced biaxial compressive strain. Section 6.5.1 then, by the comparison of theory and experiment, arrives at a parametrisation of the 12 band Hamiltonian. Having parametrised the 12-band model, the predicted transition energies of the model are compared to those extracted from the experimental data for additional SQW and TQW structures in Section 6.5.2. Finally, in Section 6.6 the chapter is summarised.

6.2 Materials studied

In this section a brief description of the materials studied in this chapter will be given. All of the devices studied in this chapter are broad-area SCH single quantum well laser structures with either 50 μm or 100 μm stripe width, 1 mm long cavities and as-cleaved facets as described in Ref. [65]. All of the samples studied are grown at Philipps-Universität Marburg by Peter Ludewig.

The structural details of the QW laser structures investigated are described in Table 6.1. The samples were grown by metal organic vapor phase epitaxy in an AIX 200-GFR reactor system at a reactor pressure of 50 mbar and using Pd-purified H_2 as the carrier gas. Tertiarybutylarsine (TBAs), trimethylbismuth (TMBi) and triethylgallium (TEGa) were chosen as precursors, since they decompose sufficiently at the low temperatures of 400 – 425 °C required for $GaBi_xAs_{1-x}$ growth [67]. In addition, trimethylaluminum (TMAl) and diethyltellurium (DETe) were used for the deposition of the undoped and doped AlGaAs layers, as well as diethylzinc (DEZn) for the growth of the highly p-doped GaAs:Zn contact layer.

A GaAs:Te buffer was grown on an exact GaAs:Si (001) substrate at 625 °C followed by a 1.2 – 1.4 μm AlGaAs:Te cladding layer (containing 40 – 45% Al) and the lower AlGaAs barrier. Following this, the temperature was lowered during a TBAs stabilised growth interruption for the QW deposition (apart from the GaAs QW of sample 1, which was grown at 625 °C). The $GaBi_xAs_{1-x}$ QWs of samples 3 and 4 were grown in a pulsed mode at 400 °C as described in Ref. [65], whereas the QW of sample 2 was grown under continuous precursor supply at 425 °C [64]. After the QW growth the temperature was again raised to 625 °C at a TBAs stabilised growth interruption in order to deposit the upper AlGaAs barrier, a 1.2 – 1.4 μm AlGaAs:C cladding layer (again containing 40 – 45% Al), and a 170 nm GaAs:Zn p-contact layer. The C-doping in the cladding layer was achieved by a reduced V/III-ratio.

To determine layer thicknesses and compositions, high resolution x-ray diffraction (HR-XRD) $\omega - 2\theta$ scans around the GaAs (004) reflection were performed in combination with dynamical modelling by Peter Ludewig. As an example, the measured and simulated HR-XRD patterns for sample 4 are shown in Fig. 6.1, where good agreement is noted between the measured and simulated diffraction patterns. Since the signal of a $GaBi_xAs_{1-x}$ SQW layer is very weak in HR-XRD, test structures for samples 2 and 3 containing 5 QWs each were grown in order to analyse the samples. The results of these measurements are summarised in Table 6.1, where the listed uncertainties in the structural parameters were obtained as

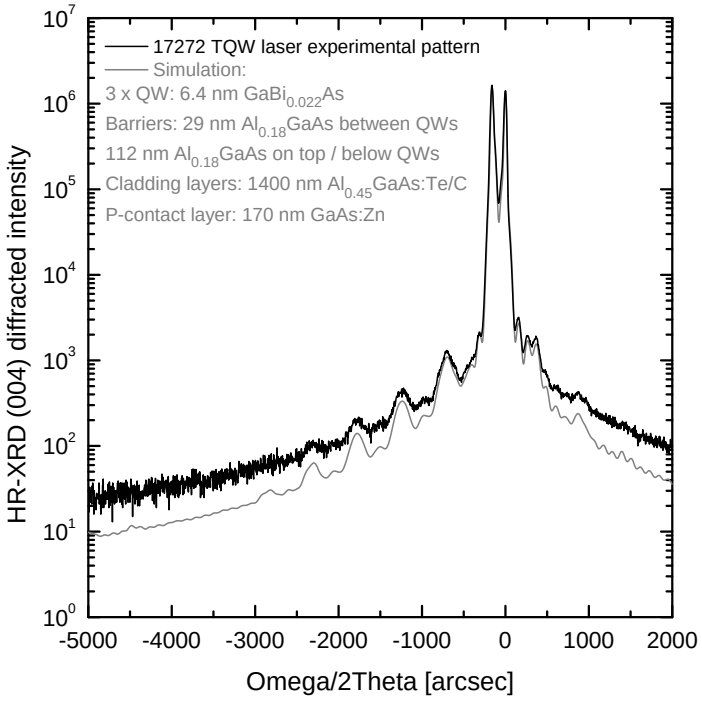


Figure 6.1: Black (Grey) solid line: Measured (Simulated) high-resolution x-ray diffraction pattern about the GaAs (004) reflection, for sample 4 of Table 6.1.

the extrema of values which produce reasonable agreement between the measured and simulated HR-XRD patterns.

6.3 Experimental measurements

Polarisation-resolved photovoltage spectroscopy is a technique which has previously been used to probe the energy and character of inter-band optical transitions in quantum well and dot heterostructures [72, 87, 28]. Typically, TE polarised excitation, where the light incident on the sample is polarised parallel to the QW epitaxial layer, results in interaction between the applied optical field, the *s*-like CB states and *p*-like VB states having both light and heavy hole (LH and HH) character. When the light incident on the sample is TM-polarised, the electric field vector of the light is perpendicular to the QW epitaxial layer, and the applied optical field can interact with CB states and also VB states with LH character only.

The orthogonal nature of the *p*-like states at the VB maximum in tetrahedrally bonded semiconductor materials allows independent probing of CB to LH and

Table 6.1: Structural parameters for the $GaBi_xAs_{1-x}$/(Al)GaAs QW structures investigated including nominal well thicknesses and well and barrier material compositions, as well as the expected growth uncertainties in these quantities. The QWs in sample 4 are separated by barriers of thickness 29 nm. The values in brackets are the best fit values used in the theoretical calculations of Section 6.5.

Sample number	Number of QWs	QW thickness (nm)	Barrier Al composition (%)	QW Bi composition (%)
1, 17275	1	8.0 ± 0.5 (8.0)	18.0 ± 2.0 (13.6)	0.0 (0.0)
2, 17150	1	11.0 ± 0.5 (11.0)	18.0 ± 2.0 (14.2)	1.7 ± 0.2 (1.7)
3, 17273	1	6.4 ± 0.5 (6.9)	12.0 ± 2.0 (7.4)	2.2 ± 0.2 (2.1)
4, 17272	3	6.4 ± 0.5 (5.9)	18.0 ± 2.0 (13.7)	2.2 ± 0.2 (2.5)
5, 17152	1	6.4 ± 0.5 (6.9)	18.0 ± 2.0 (14.1)	2.2 ± 0.2 (2.1)
6, 17392	1	6.4 ± 0.5 (6.9)	0.0 (0.0)	2.2 ± 0.2 (1.8)

HH transitions in QW structures in order to gain detailed insight into the band structure [71]. Using this technique, accurate measurement of the character and energies of the fundamental transitions involving the lowest energy electron states in the CB and the highest energy LH and HH states, and the energy splitting between the highest energy LH and HH states is achieved. This is generally not possible using non-polarisation-resolved measurements [86]. This technique also allows access to the the degree of broadening of transitions at the band edge, as well as the barrier band gap energy. In some samples it is also possible to resolve features related to transitions between excited bound states, as well as between bound states and the continuum states of the barrier material. Previous work has shown that polarisation-resolved PV spectroscopy, when used in conjunction with $\mathbf{k}\cdot\mathbf{p}$ modelling, can be highly successful at elucidating the band structure in edge-emitting laser structures [44, 28].

In the experiment, light from a broadband tungsten light source is focused onto the input slit of a grating monochromator. A narrow range of photon energies is selected by the monochromator before being polarised, chopped (typically at a frequency of the order of 1 kHz) and passed through an order-sorting filter. This

spectrally resolved light is then focused onto the facet of the laser device using a microscope objective. This incident light generates electron-hole pairs which are swept out of the active region by the built-in field, creating a photocurrent. The voltage induced by this photocurrent is measured using phase sensitive techniques. The desired range of excitation energies is swept through and a PV spectrum is collected at each possible orthogonal combination of the sample and polariser, following the procedure described in Ref. [71]. The PV spectra measured in this manner are then corrected in order to account for the wavelength and polarisation dependence of the experimental setup. Further detail regarding the experimental technique is available in chapter 3.

Transition energies for the observed features in each of the TE and TM polarised spectra are extracted by examining the first derivative of the measured PV multiplied by the photon energy. Transitions energies are systematically assigned using the peaks in these first derivatives, which correspond to the points of inflection located at the local maxima of the optical absorption edges. This method for determining the transition energies has been shown [86] for materials with inhomogeneously broadened band edge transitions to give results in good agreement with those determined using photo-modulated reflectance, a differential technique which is highly sensitive to critical points in the band structure [47, 39], .

Due to the symmetry present in an (001) grown QW the TE polarised optical transitions involve both LH and HH states, while the TM-polarised transitions involve LH states only. Therefore, in order to accurately determine the energy splitting between the highest LH and HH states in the QW, the measured TE polarised PV spectra are corrected in order to remove the LH contributions and obtain the PV generated by heavy-holes only. For LH states in an ideal QW the TM polarised optical transition strength is four times that associated with TE polarised transitions [25]. Assuming that this relationship holds in the QW laser devices studied here, the measured TE polarised PV spectra are corrected at a given photon energy by subtracting one quarter of the TM polarised PV measured at that energy. Since the LH related transitions occur at higher energies than those related to HH states in the compressively strained QWs studied here, this correction has the effect of decreasing the magnitude of the TE polarised PV signal as the photon energy increases above the band edge. This then leads to an increase in the measured splitting between the highest energy LH and HH states, compared to that obtained using the uncorrected TE-polarised spectra. This increase is found to be $\lesssim 4$ meV in the QW structures studied.

6.4 Determination of the bulk $GaBi_xAs_{1-x}/GaAs$ band offset

In this section the procedure for calculating the $GaBi_xAs_{1-x}/GaAs$ bulk band offsets in the presence of biaxial compressive strain is presented. For the Bi-free QW (sample 1) the 8-band $\mathbf{k}\cdot\mathbf{p}$ model of Ref. [70] is used, and for the Bi-containing QWs (samples 2 – 6) the 12-band $\mathbf{k}\cdot\mathbf{p}$ model of Refs. [20, 21] is used.

The calculation of the band offsets for the case of pure GaAs QW and AlGaAs barriers is straightforward, with the barrier to QW GaAs host matrix band offsets first determined in the usual way using, e.g., the model solid theory, [103, 57] and then the band edge energies in the QW calculated following the procedure to be outlined. The calculation of the $GaBi_xAs_{1-x}/GaAs$ band offsets is illustrated schematically in Fig. 6.2.

Firstly, on the left of Fig. 6.2 in the section labelled “Host" a GaAs host matrix is illustrated, with the zero of energy taken to lie at the unstrained VB maximum. Secondly, in the section labelled “Effect of Bi" the virtual crystal contributions to the Bi-induced band edge shifts are included (ignoring the effects of strain) for a given Bi concentration x as [21]

$$\widetilde{E}_{\mathrm{CB}}(x) = E_{\mathrm{CB}} - \alpha x \equiv E_g - \alpha x \tag{6.1}$$

$$\widetilde{E}_{\mathrm{LH/HH}}(x) = E_{\mathrm{LH/HH}} + \kappa x \equiv \kappa x \tag{6.2}$$

$$\widetilde{E}_{\mathrm{SO}}(x) = E_{\mathrm{SO}} - \gamma x \equiv -\Delta_{\mathrm{SO}} - \gamma x \tag{6.3}$$

The inclusion of Bi also introduces a set of degenerate impurity levels at an energy ΔE_{Bi} relative to the host matrix VB maximum [100].

Thirdly, in the section labelled “Effect of strain" the fact that a $GaBi_xAs_{1-x}$ QW grown on a GaAs substrate will be in a state of biaxial compressive strain is used to calculate the strain-induced shifts to the band edge energies. Following the conventions of Krijn [57] these strain-induced shifts to the band edge energies are calculated using the virtual crystal approximation, as

$$\widetilde{E}_{\mathrm{CB}}(x,\epsilon) = \widetilde{E}_{\mathrm{CB}}(x) + \delta E^{\mathrm{hy}}_{\mathrm{CB}} \tag{6.4}$$
$$\widetilde{E}_{\mathrm{LH}}(x,\epsilon) = \widetilde{E}_{\mathrm{LH}}(x) + \delta E^{\mathrm{hy}}_{\mathrm{VB}} + \delta E^{\mathrm{ax}}_{\mathrm{VB}} \tag{6.5}$$
$$\widetilde{E}_{\mathrm{HH}}(x,\epsilon) = \widetilde{E}_{\mathrm{HH}}(x) + \delta E^{\mathrm{hy}}_{\mathrm{VB}} - \delta E^{\mathrm{ax}}_{\mathrm{VB}} \tag{6.6}$$
$$\widetilde{E}_{\mathrm{SO}}(x,\epsilon) = \widetilde{E}_{\mathrm{SO}}(x) + \delta E^{\mathrm{hy}}_{\mathrm{VB}} \tag{6.7}$$

where the energy shifts resulting from the hydrostatic and axial components of the strain are

$$\delta E^{\mathrm{hy}}_{\mathrm{CB}} = a_c\left(\epsilon_{xx}+\epsilon_{yy}+\epsilon_{zz}\right) \tag{6.8}$$
$$\delta E^{\mathrm{hy}}_{\mathrm{VB}} = a_v\left(\epsilon_{xx}+\epsilon_{yy}+\epsilon_{zz}\right) \tag{6.9}$$
$$\delta E^{\mathrm{ax}}_{\mathrm{VB}} = -\frac{b}{2}\left(\epsilon_{xx}+\epsilon_{yy}-2\epsilon_{zz}\right) \tag{6.10}$$

and with the non-zero components of the strain tensor given by [57]

$$\epsilon_{xx} = \epsilon_{yy} = \frac{a(\mathrm{GaAs}) - a(x)}{a(x)} \tag{6.11}$$
$$\epsilon_{zz} = -\frac{2c_{12}(x)}{c_{11}(x)}\,\epsilon_{xx}\,. \tag{6.12}$$

In order to obtain the lattice and elastic constants for GaBi$_x$As$_{1-x}$ a linear interpolation between those of the endpoint binary compounds is applied. For example, the GaBi$_x$As$_{1-x}$ lattice constant is given by

$$a(x) = (1-x)a(\mathrm{GaAs}) + xa(\mathrm{GaBi}). \tag{6.13}$$

The (Al)GaAs lattice and elastic constants recommended by Vurgaftman et al. in Ref. [105] are used, and for GaBi the values calculated ab initio by Ferhat and Zaoui [35] are used. Due to a lack of sufficient information in the literature regarding the hydrostatic and axial deformation potentials of GaBi, a_c, a_v and b for GaBi$_x$As$_{1-x}$ are taken to be equal to those of the GaAs host matrix, which is expected to be a good approximation due to the dilute Bi compositions x considered in this work.

Due to the symmetry of the p-like Bi-related impurity states there is a lifting of the degeneracy of the LH and HH-like impurity states in the presence of bi-axial strain. Based on the results of tight-binding calculations on large, ordered

supercells it is found that $E_{\mathrm{Bi}}^{\mathrm{LH}}$ and $E_{\mathrm{Bi}}^{\mathrm{HH}}$ vary with strain as

$$E_{\mathrm{Bi}}^{\mathrm{LH}} = \Delta E_{\mathrm{Bi}} + \delta E_{\mathrm{Bi}}^{\mathrm{hy}} + \delta E_{\mathrm{Bi}}^{\mathrm{ax}} \tag{6.14}$$

$$E_{\mathrm{Bi}}^{\mathrm{HH}} = \Delta E_{\mathrm{Bi}} + \delta E_{\mathrm{Bi}}^{\mathrm{hy}} - \delta E_{\mathrm{Bi}}^{\mathrm{ax}} \tag{6.15}$$

with $\delta E_{\mathrm{Bi}}^{\mathrm{hy}}$ and $\delta E_{\mathrm{Bi}}^{\mathrm{ax}}$ given by

$$\delta E_{\mathrm{Bi}}^{\mathrm{hy}} = a_{\mathrm{Bi}} \left(\epsilon_{xx} + \epsilon_{yy} + \epsilon_{zz}\right) \tag{6.16}$$

$$\delta E_{\mathrm{Bi}}^{\mathrm{ax}} = -\frac{b_{\mathrm{Bi}}}{2} \left(\epsilon_{xx} + \epsilon_{yy} - 2\epsilon_{zz}\right). \tag{6.17}$$

The Bi impurity state hydrostatic and axial deformation potentials a_{Bi} and b_{Bi} have been determined by using large tight-binding supercell calculations to track the evolution of the Bi-related localised states as functions of hydrostatic and axial strain respectively. The calculated values of a_{Bi} and b_{Bi} are given in Table 6.2.

Finally, in the section labelled "E_+ (VBAC)" the valence band anti-crossing interaction between the virtual crystal band edges and the Bi-related states is included to calculate the final values of the band offsets. The CB is decoupled from the Bi-related states, and the host matrix HH band couples directly to $E_{\mathrm{Bi}}^{\mathrm{HH}}$ giving

$$E_{\mathrm{CB}}(x,\epsilon) = \widetilde{E}_{\mathrm{CB}}(x,\epsilon) \tag{6.18}$$

$$E_{\pm}^{\mathrm{HH}}(x,\epsilon) = \frac{\widetilde{E}_{\mathrm{HH}}(x,\epsilon) + E_{\mathrm{Bi}}^{\mathrm{HH}}}{2} \pm \sqrt{\left(\frac{\widetilde{E}_{\mathrm{HH}}(x,\epsilon) - E_{\mathrm{Bi}}^{\mathrm{HH}}}{2}\right)^2 + V_{\mathrm{Bi}}^2}\,. \tag{6.19}$$

Since biaxial strain couples the host matrix LH and SO bands, there exists a strain-induced second order coupling between the LH-like Bi-related impurity states and the host matrix SO band. As a result, the SO band cannot be treated independently and the LH, SO and lower LH-like VBAC band edges in the strained alloy are given as the eigenvalues $E_{\pm}^{\mathrm{LH}}(x,\epsilon)$ and $E_{\mathrm{SO}}(x,\epsilon)$ of the 3×3 Hermitian matrix

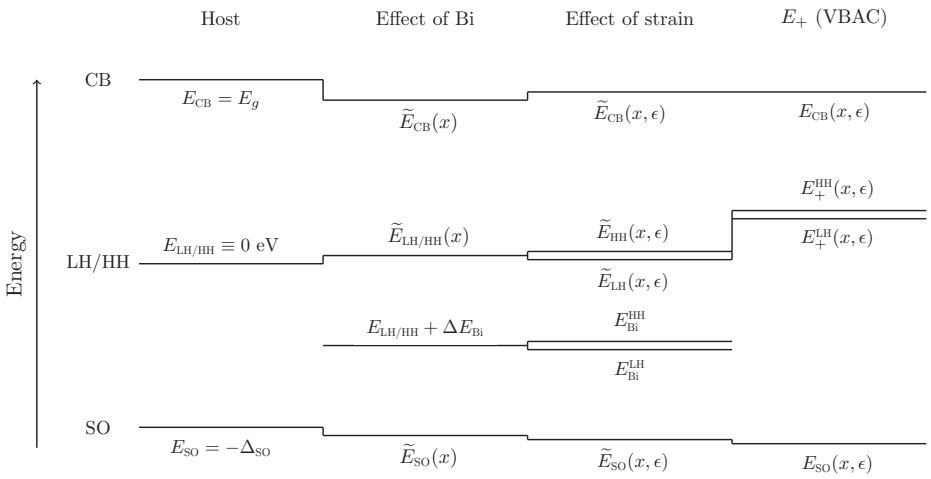


Figure 6.2: Schematic illustration of the calculation of the bulk GaBi$_x$As$_{1-x}$/GaAs band offsets for the lowest conduction band (CB), light- and heavy-hole (LH and HH) bands, and the spin-split-off (SO) band in the presence of biaxial strain. The full details of each step in the calculation are outlined in Section 6.4.

$$\begin{pmatrix} \widetilde{E}_{\mathrm{LH}}(x,\epsilon) & -\sqrt{2}\,\delta E_{\mathrm{VB}}^{\mathrm{ax}} & V_{\mathrm{Bi}} \\ & \widetilde{E}_{\mathrm{SO}}(x,\epsilon) & 0 \\ & & E_{\mathrm{Bi}}^{\mathrm{LH}} \end{pmatrix} \tag{6.20}$$

which completes the calculation. The values of the Bi-related parameters ΔE_{Bi}, α, β, γ, κ, a_{Bi} and b_{Bi} used in the calculations are given in Table 6.2.

6.5 Results

In this section the procedure undertaken to constrain the 12-band $\mathbf{k}\cdot\mathbf{p}$ model against the transition energies extracted from the measured polarisation-resolved PV spectra is presented. Firstly, an 8-band $\mathbf{k}\cdot\mathbf{p}$ model is used to determine the GaAs/AlGaAs band offsets in sample 1 by constraining the calculated transition energies against experiment in the Bi-free case. Then, beginning from this 8-band model, the CB and VB offsets in the dilute bismide case are determined by comparing the calculated transition energies for sample 2 against experiment.

With this parametrisation it is possible to calculate the band offsets for arbitrary composition GaBi$_x$As$_{1-x}$/(Al)GaAs QW structures following the procedure outlined in Section 6.4. The 12-band model is then applied to calculate the transi-

tion energies in additional SQW and TQW structures, and compare the measured and calculated transition energies. The results of this analysis are summarised in Tables 6.1 and 6.2.

6.5.1 Parameterisation of the 12-band model: samples 1 & 2

The first sample considered is an 8 nm GaAs/AlGaAs SQW structure, in which the barrier layers have a nominal Al composition of 20%. The measured TE and TM polarised PV spectra, as well as the first derivative with respect to energy of the product of the energy and the measured PV, are shown in Figs. 6.3 (a) and 6.4 (a) respectively.

The first step in the process of analysing the device is constraining the barrier Al composition theoretically, by comparing the measured barrier transition energy to a calculation of the bulk AlGaAs room temperature band gap. A polarisation-insensitive feature associated with transitions from the barrier conduction band to barrier valence band (BCB–BVB) is clearly visible at high energy in the measured TE and TM spectra. The transition energy associated with this feature is determined from the peak of the first derivative of the measured spectra to be 1.625 eV, which, according to the well-accepted AlGaAs parameters of Vurgaftman et al. [105], corresponds at room temperature to an Al composition in the barrier layers of 13.6%. This is a significant deviation from the nominal value of 20% but is plausible due to the near-vanishing strain present in a GaAs/AlGaAs QW, which makes the determination of the Al composition by HR-XRD difficult.

In order to calculate the transition energies and fit the GaAs/AlGaAs band offsets to the measured first electron to first heavy and light hole transition energies ($e1$–$hh1$ and $e1$–$lh1$) an Al composition in the barrier layers of 13.6% is assumed. The 8-band $\mathbf{k}\cdot\mathbf{p}$ Hamiltonian of Ref. [70] is used to calculate the transition energies. The $\mathbf{k}\cdot\mathbf{p}$ parameters of Ref. [105] are used for GaAs and AlAs, interpolating to calculate the parameters in the barrier layers. All parameters are as in Ref. [105] and the GaAs/AlGaAs band offsets are calculated using the model solid theory [103, 57] for which the calculated offset ratio ΔE_c:ΔE_v = 59:41. Using this parameter set the $e1$–$hh1$ and $e1$–$lh1$ transition energies are calculated as 1.461 eV and 1.470 eV respectively. Comparing these with the measured values listed in Table 6.3 it is seen that, without any adjustment, this parameter set overestimates the fundamental $e1$–$hh1$ QW band gap.

To constrain the GaAs/AlGaAs band offsets against the experimental data, the CB to VB offset ratio $\Delta E_c : \Delta E_v$ is adjusted and the calculated and measured

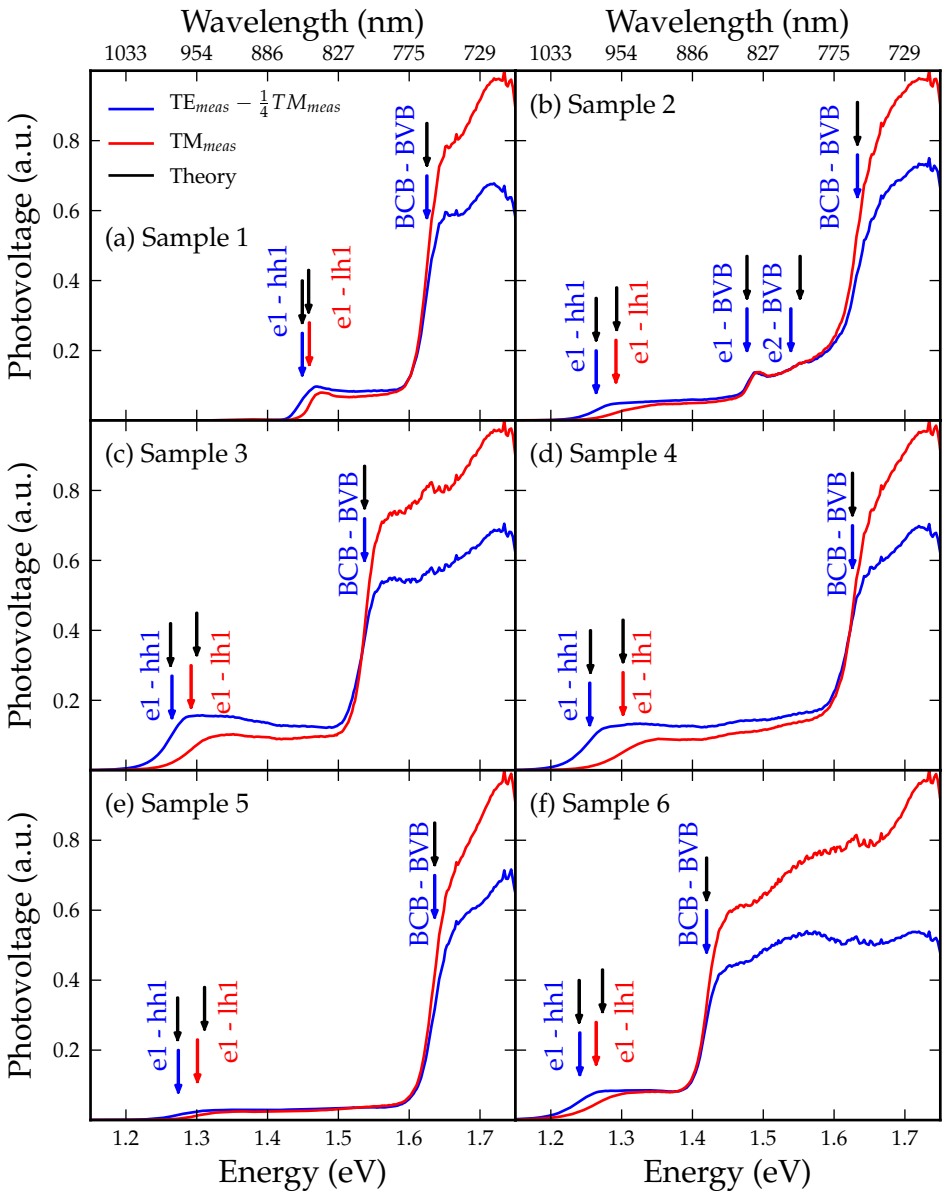


Figure 6.3: Measured polarisation-resolved photovoltage spectra of samples 1 – 6 of Table 6.1. Blue lines: TE polarised photovoltage. Red lines: TM-polarised photovoltage. Blue (Red) arrows denote transition energies extracted from TE (TM) polarised photovoltage spectra. Blue arrows are also used to denote the transition energies for polarisation-insensitive features, which are extracted from both the TE and TM polarised spectra. Black arrows: Transition energies calculated using either an 8-band $\mathbf{k}\cdot\mathbf{p}$ model (for sample 1) or a 12-band $\mathbf{k}\cdot\mathbf{p}$ model (for samples 2 – 6).

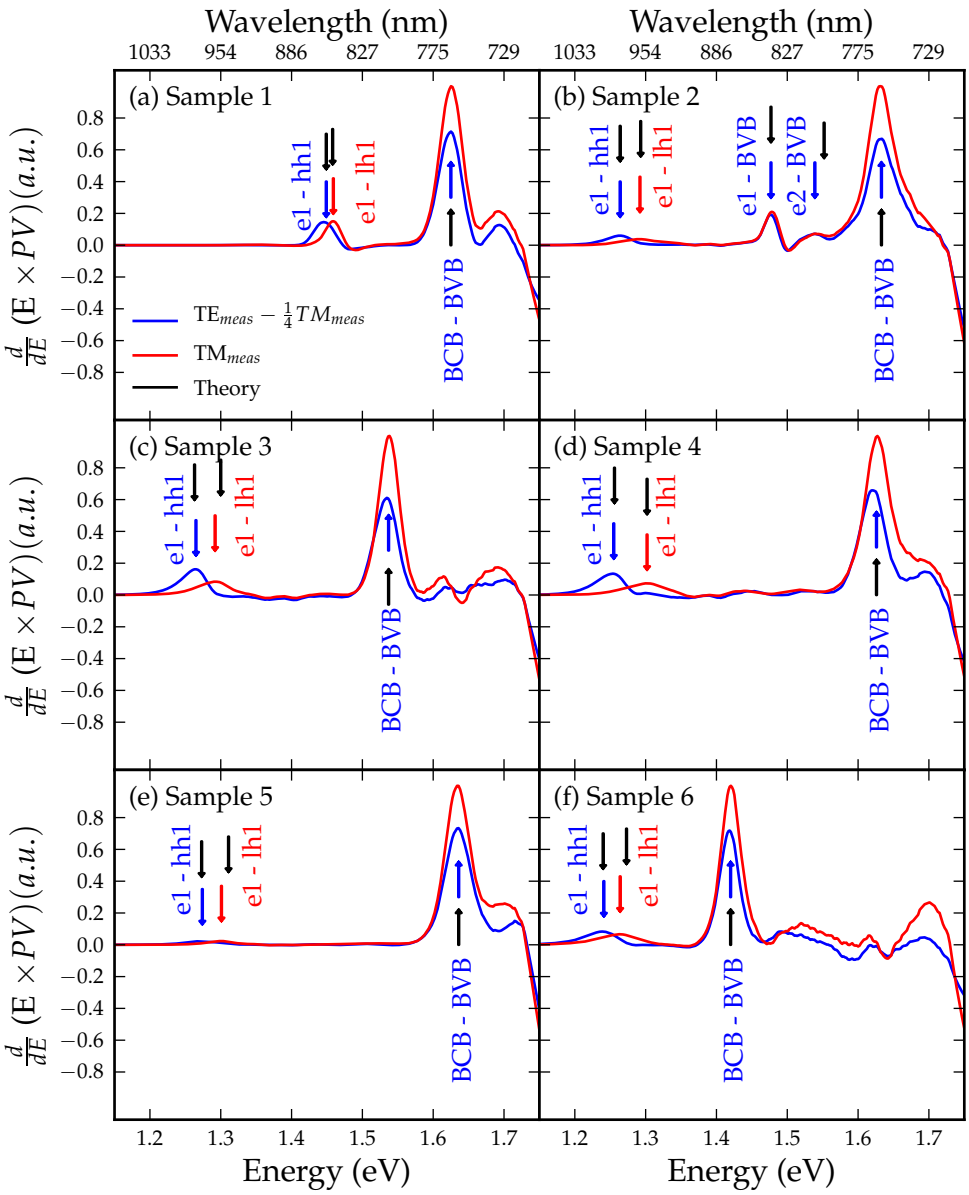


Figure 6.4: First derivative with respect to energy of the product of the photon energy and the measured polarisation-resolved photovoltage for samples 1 – 6 of Table 6.1. Blue (Red) lines denote the derivatives obtained from the TE (TM) polarised spectra. Blue (Red) arrows denote transition energies extracted from the TE (TM) polarised photovoltage spectra. Blue arrows are also used to denote the transition energies for polarisation-insensitive features, which are extracted from both the TE- and TM-polarised spectra. Black arrows: Transition energies calculated using 8- and 12-band $\mathbf{k}\cdot\mathbf{p}$ models for sample 1 and samples 2 – 6 respectively.

$e1$–$hh1$ and $e1$–$lh1$ transition energies are compared. As a result of the near-vanishing strain in a GaAs/AlGaAs QW the LH and HH bulk band edges lie within 1 meV of one another, so that light and heavy holes in the QW experience close to identical confining potentials. The majority contribution to the $hh1$–$lh1$ splitting therefore comes from the differences in the GaAs confinement of the highest energy LH and HH states in the QW, as determined by the LH and HH effective masses along the transverse (growth) direction, and the size of the VB offset ΔE_v between the QW and barrier materials.

By varying $\Delta E_c : \Delta E_v$ while keeping all other parameters fixed, a best fit to the measured transition energies is found with $\Delta E_c : \Delta E_v = 70 : 30$. With this 70 : 30 band offset ratio the calculated CB and VB offsets are 145 and 60 meV respectively, and the calculated $e1$–$hh1$ and $e1$–$lh1$ transition energies are both within 1 meV of the measured values. In particular, the calculated $hh1$–$lh1$ splitting of 9.4 meV is in excellent agreement with the measured value of 10 meV.

This completes the fitting of the GaAs/AlGaAs band offsets, which are used as input to the 12-band calculations for samples 2 – 6. In the remaining calculations the barrier Al composition is again determined by fitting to the measured barrier band gap at room temperature, and the GaAs/AlGaAs band offsets are fixed to maintain $\Delta E_c : \Delta E_v = 70 : 30$ in all cases. The first Bi-containing sample, sample 2, is now examined in detail. Beginning with the 8-band model from this section the Bi-related parameters α and β are fit to the measured transition energies in order to fully parametrise the 12-band model of Refs. [20, 21].

This sample is an 11 nm $GaBi_{0.017}As_{0.983}$/AlGaAs SQW structure, in which the barrier layers again have a nominal Al composition of 20%. The measured TE and TM polarised PV spectra, as well as the first derivative with respect to energy of the product of the energy and the measured PV, are shown in Figs. 6.3 (b) and 6.4 (b) respectively. Based on the measured BCB–BVB transition energy of 1.633 eV a barrier Al composition of 14.2% is inferred, which is used as input to the theoretical calculations.

Examining the TE and TM polarised spectra of Fig. 6.3 (b) two features are observed which have transition energies intermediate between those of the bound-to-bound $e1$–$hh1$ and $e1$–$lh1$ transitions and the continuum BCB–BVB transition. As a result of the measured transition energies associated with these features, as well as the fact that these two features are polarisation-insensitive, the conclusion is reached that they correspond to transitions from the first two bound electron states in the QW ($e1$ and $e2$) to the BVB. The interpretation of this pair of features as being associated with transitions from bound electron

states in the QW to continuum BVB states is reinforced by noting that these features have a significantly smaller linewidth than the lower energy $e1$–$hh1$ and $e1$–$lh1$ transitions, as can clearly be seen in Fig. 6.4 (b), and their transition energies are not split with respect to energy, which means that there are no confined hole states involved in the transition. This is consistent with previous calculations by M. Usman and C.A. Broderick of the $GaBi_xAs_{1-x}$ electronic structure [100] , which indicated that the incorporation of Bi results in a strong inhomogeneous broadening of states in the proximity of the VB edge, suggesting that transitions involving the $GaBi_xAs_{1-x}$ VB should have increased linewidths compared to transitions involving the $GaBi_xAs_{1-x}$ CB. This broadening of the band edge transition due to the effects of Bi on the $GaBi_xAs_{1-x}$ VB structure is clearly visible in the measured PV spectra, as can be seen by comparing Fig. 6.4 (a) to Figs. 6.4 (b) – 6.4 (f).

Starting with the GaAs/AlGaAs band offsets determined for sample 1, all seven of the Bi-related parameters of the 12-band model of Section 6.4 are assigned their values as determined by large supercell tight-binding calculations [21]. Since the $e1$–BVB transition does not involve the $GaBi_xAs_{1-x}$ VB, this transition can be used to directly determine the effect of Bi on the CB offset. The value of α is varied in the 12 band $\mathbf{k}\cdot\mathbf{p}$ model in order to fit to the $e1$–BVB transition energy extracted from the first derivatives of the TE and TM polarised PV spectra shown in Fig. 6.4 (b). With a calculated compressive strain of 0.2% the strain-induced shift to the conduction band edge is +17.8 meV. Taking the QW to have a thickness of 11 nm and a Bi composition of 1.7% (their nominal values) a best fit value of $\alpha = 2.63$ eV is found, to match the measured $e1$–BVB transition energy of 1.477 eV. This value of α generates a $GaBi_{0.017}As_{0.983}/Al_{0.142}Ga_{0.858}As$ CB offset of 195.8 meV, of which, when strain is taken into account, 26.9 meV is due to the incorporation of 1.7% Bi in the QW. This value of α is close to the value of 2.82 eV obtained from the tight-binding calculations [21].

Examining the calculated CB offsets and bound state energies for samples 1 and 2, the calculated energy separation between the $e1$ bound state and the BCB in sample 2 is seen to be 156 meV, with a total bulk CB offset of 178 meV. The calculated $e1$–BCB separation for sample 2 exceeds the *total* bulk CB offset of 145 meV calculated for sample 1, and so we conclude that a type-I CB line-up is present at the $GaBi_xAs_{1-x}/GaAs$ interface (i.e. $\alpha > 0$). This is the first experimental determination of the band offsets at the $GaBi_xAs_{1-x}/GaAs$

Table 6.2: Bi-related parameters for the 12-band $\mathbf{k}\cdot\mathbf{p}$ Hamiltonian of Refs. [20, 21]. The parameters α and β were determined as the best fit to the measured transition energies in sample 2, with the remaining parameters determined by detailed tight-binding supercell calculations.

Parameter	Value (eV)
ΔE_{Bi}	-0.183
α	2.63
β	1.45
γ	0.55
κ	1.01
a_{Bi}	-1.11
b_{Bi}	-1.71

interface. This type-I band offset sets a lower bound on the bulk CB offset in $GaBi_xAs_{1-x}/GaAs$ due to the 70 % CB offset determined in sample 1 equalling the largest CB offset reported in the literature for this material system. This supports the conclusions of the previous calculations, as well as those of the pressure-dependent measurements of Ref. [48], which suggested the presence of a type-I band offset for electrons in a $GaBi_xAs_{1-x}$ LED structure. A visualisation of the method employed to extract the band offsets can be seen in Fig. 6.5.

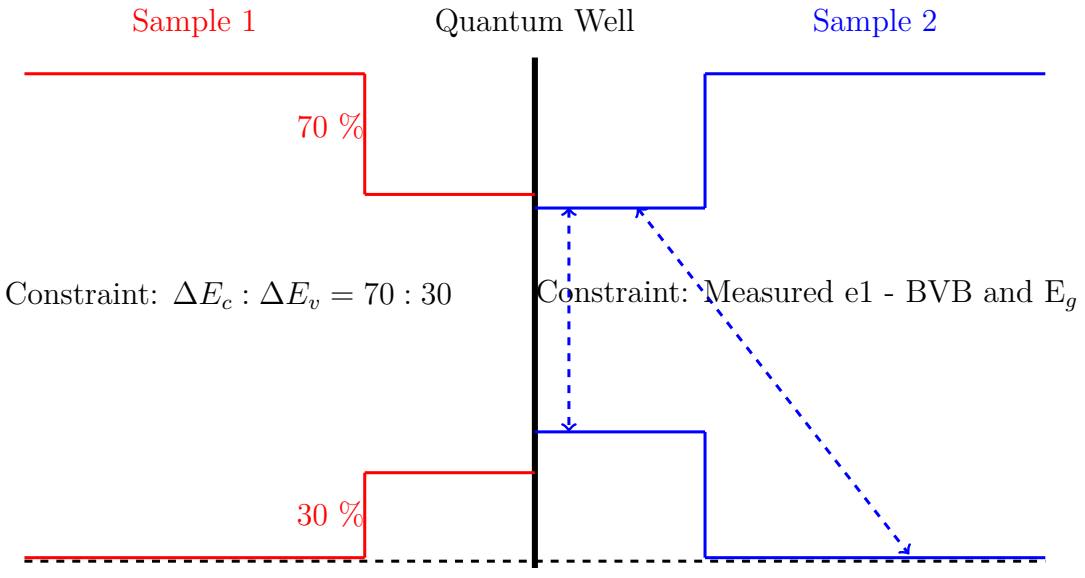


Figure 6.5: Real-space schematic of type-I band offset for $GaBi_xAs_{1-x}/GaAs$ bulk interfaces illustrating the use of samples 1 (red) & 2 (blue) for offset determination. Note the almost identical barrier material in both samples.

Next, the LH and HH band offsets are determined independently from the CB

offset by fixing α at its best fit value of 2.63 eV and varying the strength of the VBAC interaction β to fit to the measured $e1$–$hh1$ transition energy.

The value of $\beta = 1.13$ eV determined from large supercell tight-binding calculations underestimates the Bi-induced band gap reduction compared to the PV measurements. A value of $\beta = 1.45$ eV is found to give a calculated $e1$–$lh1$ transition energy which is within 1 meV of the measured value, and produces a $hh1$–$lh1$ splitting of 28.6 meV, in excellent agreement with the experimentally determined value of 29.2 meV. The measured transition energies for this sample, as well as those calculated using the 12-band $\mathbf{k}\cdot\mathbf{p}$ model are listed in Table 6.3.

It is seen that despite the fact that a large number of parameters contribute to determining the $hh1$–$lh1$ splitting in the Bi-containing case, the best fit value of β combined with the tight-binding calculated hydrostatic and axial deformation potentials for the Bi-impurity states is able to reproduce the measured $hh1$–$lh1$ splitting to within experimental error. This suggests that it is possible to obtain an accurate description of the VB edge density of states in $GaBi_xAs_{1-x}$ using the 12-band $\mathbf{k}\cdot\mathbf{p}$ model, and shows that the model is promising for the investigation of the optical properties of nanostructures based on $GaBi_xAs_{1-x}$ and related materials.

Having used the observed features in the measured TE- and TM-polarised PV spectra for this sample to determine the CB and VB offsets independently by fitting to the measured transition energies, in Table 6.2 a complete set of Bi-related parameters for the 12-band $\mathbf{k}\cdot\mathbf{p}$ model of Section 6.4 is presented.

6.5.2 Verification of parameterised model: samples 3 – 6

With the 12-band $\mathbf{k}\cdot\mathbf{p}$ Hamiltonian having been fully parametrised by a combination of tight-binding supercell calculation and systematic fitting to the transition energies in samples 1 and 2, the 12-band model is now applied to study four additional QW structures in order to test the accuracy and transferability of the experimentally inferred parameter set.

Samples 3 – 6 contain nominally identical 6.4 nm $GaBi_xAs_{1-x}$ QWs with $x = 2.2\%$. Samples 3, 5 and 6 are SQW structures, while sample 4 is a TQW structure with 29 nm barriers separating the $GaBi_xAs_{1-x}$ QWs. The barriers in sample 3 have a nominal Al composition of 12%, while those in samples 4 and 5 have nominal Al compositions of 20%; sample 6 has GaAs barriers. The measured TE- and TM-polarised PV spectra, as well as the first derivative with respect to energy of the product of the energy and the measured PV, for samples 3 – 6 are shown in Figs. 6.3 (c) – 6.3 (f) and 6.4 (c) – 6.4 (f) respectively. The measured

barrier band gaps for each of these samples are shown in Table 6.3, from which barrier Al compositions of 7.4, 13.7 and 14.1% are inferred for samples 3, 4 and 5 respectively. These material compositions are used as input to the theoretical calculations for each of the samples.

Table 6.3: Details of the measured and calculated transition energies in the QW samples investigated. Transitions labelled as "insensitive" are those for which the measured energies were equal (to within 5 meV) in the TE and TM polarised PV spectra. The associated designations were assigned based on the energies obtained from the 8 and 12-band $\mathbf{k}\cdot\mathbf{p}$ calculations, as well as symmetry considerations based on the character of the measured PV spectra. The structural parameters used as input to the theoretical calculations for each sample are given in parentheses in Table 6.1. The abbreviation BCB (BVB) denotes the barrier conduction (valence) band.

Sample number	Polarisation	Designation	Energy, meas. (eV)	Energy, calc. (eV)
1	TE	$e1$–$hh1$	1.449	1.449
1	TM	$e1$–$lh1$	1.459	1.458
1	Insensitive	BCB–BVB	1.625	1.625
2	TE	$e1$–$hh1$	1.264	1.264
2	TM	$e1$–$lh1$	1.292	1.293
2	Insensitive	$e1$–BVB	1.477	1.477
2	Insensitive	$e2$–BVB	1.539	1.552
2	Insensitive	BCB–BVB	1.633	1.633
3	TE	$e1$–$hh1$	1.265	1.263
3	TM	$e1$–$lh1$	1.292	1.300
3	Insensitive	BCB–BVB	1.537	1.537
4	TE	$e1$–$hh1$	1.255	1.256
4	TM	$e1$–$lh1$	1.302	1.302
4	Insensitive	BCB–BVB	1.626	1.626
5	TE	$e1$–$hh1$	1.274	1.273
5	TM	$e1$–$lh1$	1.301	1.311
5	Insensitive	BCB–BVB	1.636	1.636
6	TE	$e1$–$hh1$	1.241	1.240
6	TM	$e1$–$lh1$	1.264	1.273
6	Insensitive	BCB–BVB	1.420	1.420

Examining the first derivative of the TE-polarised PV spectrum for sample 3, the $e1$–$hh1$ transition is identified at an energy of 1.265 eV. Comparing this to the calculated transition energy using the parameters of Table 6.2 and taking the nominal QW composition and thickness, the calculated value of 1.263 eV is seen to be in good agreement with the experimentally determined value. It is noted, however, that the calculation overestimates the $hh1$–$lh1$ splitting by 12.3 meV

compared to the measured value. By varying the QW composition and thickness within the range of growth uncertainties stated in Table 6.1 a best fit to the $hh1$–$lh1$ splitting of 37.1 meV is obtained, which still overestimates the measured value of 27 meV by 10.1 meV.

Further insight into the discrepancy between the measured and calculated $e1$–$lh1$ transition energies in sample 3 is gained by comparison with sample 4. This is possible since both samples nominally contain the same 6.4 nm thick, $x = 2.2\%$ QWs, and so there should be very little difference between the energies of the $e1$–$lh1$ transitions between the two samples. This is expected because the calculated 6.3% difference in Al composition between the barrier layers in samples 3 and 4 mainly impacts the CB, causing an increase of 69 meV in the bulk CB offset, with an accompanying reduction of only 1.5 meV in the confinement energy of the $e1$ state due to the enhanced confinement it experiences in sample 4.

For sample 4, again the QW compositions and thicknesses are varied in the theoretical calculations, and good agreement is found between theory and experiment for the energies of the $e1$–$hh1$ and $e1$–$lh1$ transitions in an ideal TQW structure having 5.9 nm thick QWs with a Bi composition of $x = 2.5\%$. Specifically, the calculated value of 45.5 meV for the $hh1$–$lh1$ splitting agrees well with the measured value of 47 meV. The deviations from the nominal values of the QW compositions and thicknesses required to obtain good fits to the measured transition energies suggests that material inhomogeneities in the $GaBi_xAs_{1-x}$ layers play a strong role in determining the details of the VB structure and that compositional fluctuations within the $GaBi_xAs_{1-x}$ layers have strong effects on the material properties.

6.6 Summary

Using a combination of experimental measurements and theoretical calculations the band offsets in $GaBi_xAs_{1-x}$/(Al)GaAs quantum wells have been directly determined. The use of polariation-resolved photovoltage spectroscopy has enabled probing of transitions related separately to light and heavy holes in the laser structures studied, and hence given information regarding the band structure of the quantum wells in the devices. By combining a 12-band $\mathbf{k}\cdot\mathbf{p}$ Hamiltonian for $GaBi_xAs_{1-x}$, which has previously been derived from detailed tight-binding supercell calculations, with experimental results, a general procedure for calculating the band offsets in GaAs-based dilute bismide quantum well structures at arbitrary Bi composition x has been developed.

The 12-band $\mathbf{k}\cdot\mathbf{p}$ model for $GaBi_xAs_{1-x}$/(Al)GaAs has been parameterised in such a way that the calculated transition energies are in good agreement with experiment for a number of different laser structures. This combined experimental and theoretical approach has enabled verification for the first time the presence of a type-I band offset at the $GaBi_xAs_{1-x}$/GaAs heterointerface, in agreement with the previous calculations for bulk $GaBi_xAs_{1-x}$, as well as with pressure-dependent measurements which have been performed on a $GaBi_xAs_{1-x}$-based LED structure [48]. The type-I band offset extracted provides a lower bound on the bulk CB offset in $GaBi_xAs_{1-x}$/GaAs due to the 70 % GaAs/AlGaAs CB offset determined in sample 1 equalling the largest CB offset reported in the literature for this material system. Furthermore, by applying the 12-band $\mathbf{k}\cdot\mathbf{p}$ model to calculate the band structure of additional laser structures the validity of the model has been displayed by showing that it is capable of describing the main features of the band structure in $GaBi_xAs_{1-x}$/(Al)GaAs laser structures with varying Bi composition, as well as with varying quantum well thickness and number.

The experimental and theoretical work which has been presented therefore represents the first direct investigation of the band offsets in heterostructures based upon this highly-mismatched III-V alloy.

Chapter 7

Experimental investigation of optical lifetimes in $GaAs_{1-x}Bi_x$ quantum wells using TRPL

7.1 Introduction

This chapter is concerned with low temperature **T**ime **R**esolved **P**hoto **L**uminescence (TRPL) measurements of the $GaAs_{1-x}Bi_x$ material. This material has been sufficiently introduced in chapters 5 and 6 to not have an in depth review in this chapter.

TRPL is a tool used to uncover the temporal response of the optical transitions in the material after a very short optical excitation pulse has been applied. In section 7.2 a brief description of the materials studied is presented. This is followed by a description of the experimental method used to make the measurements. The format employed here differs from the rest of the thesis as this experimental method is used only once, and so will be described here and not in chapter 3. In section 7.4 the results of the measurements are shown and discussed. Evidence of localisation effects in the $GaAs_{1-x}Bi_x$ layer are found over a wide energy range , with the extracted carrier lifetime exceeding 10ns over a wide wavelength range. It is described how these lifetimes are generally longer than those observed in bulk $GaAs_{1-x}Bi_x$ layers with similar energy-gap and composition. In section 7.5 the work which has been presented as part of this chapter will be summarised.

7.2 Materials studied

In this section a brief description of the materials studied in this chapter will be given. In this chapter only one sample is studied. This is the 2.2 % laser of Ref. [66]. Fig. 7.1 shows the structure of the material which is measured in this experiment. PL measurements are carried out on bare wafer samples of the laser structure and so there are no processed devices examined in this chapter. The material investigated is studied using TRPL measurement. This

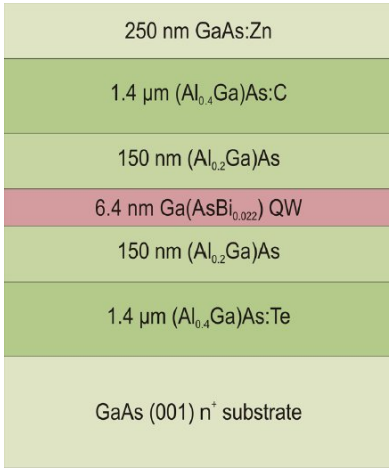


Figure 7.1: Device stack from Philipps-Universität Marburg

allows investigation of the extent of the recombination rate as a function of energy as the carriers relax following high energy excitation. The material is grown at Philipps-Universität Marburg by Peter Ludewig by metal organic vapour phase epitaxy (MOVPE). This material has 20 % nominal AlGaAs barriers, which have previously in this thesis been shown to actually contain ≈ 14 % Al, and Bi composition 2.2 %. An anomalous peak was observed in the TRPL traces of this material which did not correspond to any of the peaks seen in the CW PL of chapter 5. This was investigated and found to be luminescence from the heavily doped GaAs:Zn contact layer. Consequently, this layer was removed using reactive ion etching techniques, and the TRPL and CW PL traces came into coincidence.

7.3 Experimental method

As was previously described in chapter 3, photo-luminescence (PL) spectroscopy is a measurement which is generallly not carried out on a processed laser device, but rather on a bare wafer sample. A TRPL measurement is achieved by illumi-

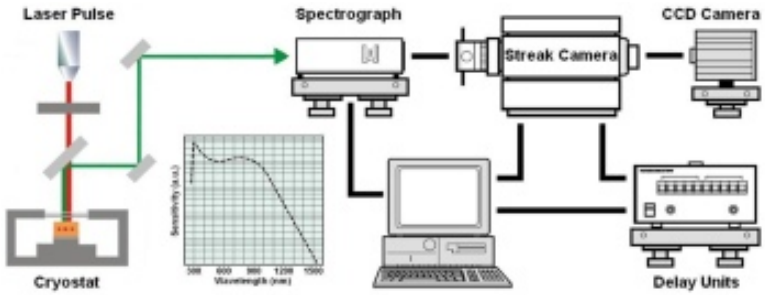


Figure 7.2: Schematic of the TRPL setup used

nating the bare wafer sample with emission from a 650 nm mode locked diode laser. This incident radiation creates electron-hole pairs within the material under test, and because the photons in the 650 nm pump pulses are much more energetic than the bandgap of the material which is being investigated, these carriers are promoted to levels high in the conduction band and low in the valence band. The choice of 650 nm excitation allows investigation of both the GaAs and GaBiAs layers within the material. Following excitation the carriers decay towards the conduction and valence band edges and, depending on the carrier lifetimes in each region can emit photons or decay to a lower energy state within the bandstructure, from which radiative or non-radiative recombination occurs. The radiative transitions are measured and both spectrally and temporally resolved to gain insight into material bandstructure and carrier lifetimes. The temporal evolution of the spectrum is recorded using a Hamamatsu streak camera system equipped with an infrared-enhanced thermoelectrically chilled photocathode. The experimental setup is depicted in Fig. 7.2. This measurement is carried out under phase sensitive conditions similar to the lock in amplifier and chopper discussed previously, except in the nano-second regime. Data collected in this way are spectrally corrected in the usual manner to account for instrument response. The wafer is clamped on a vertical flat mount in the cryostat and measured at 10 K. All of the TRPL work was carried out in the specialist TRPL lab of Dr. Tomasz Oschalski for which we graciously acknowledge his assistance here.

7.4 Results

The results of the TRPL measurements are presented in Fig. 7.3 where the colour scale depicts the logarithm of the intensity of the emission as a function of both wavelength and time. In this figure areas shaded red are areas of strong emission and blue shaded regions represent zero emission. Emission can clearly

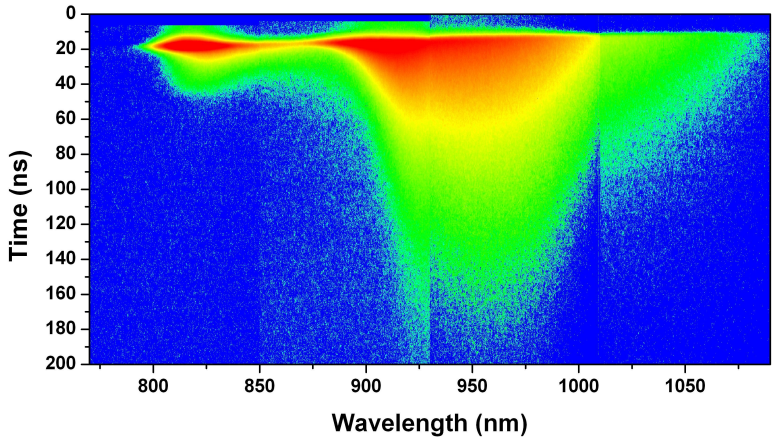


Figure 7.3: TRPL streak camera image showing the energy and temporal character of the emission from both the GaAs and $GaAs_{1-x}Bi_x$ layers. Red represents strong emission and blue represents zero emission.

be seen from both the 2.2 % $GaAs_{1-x}Bi_x$ layer, in the 900 nm to 1050 nm spectral region, and from the pure GaAs layers with an emission peak $\approx$ 815 nm. The discontinuities observed in the spectra close to 930 nm and 1010 nm are due to scale changes in the detection system and do not affect the lifetimes extracted from the measurements. It is clear to see that the GaAs emission, as well as undergoing less broadening, has very much faster emission dynamics than the $GaAs_{1-x}Bi_x$ layer. This is consistent with the radiative recombination rate in GaAs being, as expected, of the order of a nanosecond, due to the good electron-hole overlap in this material. The longer carrier lifetimes at longer wavelengths suggest a reduced electron-hole overlap in the $GaAs_{1-x}Bi_x$ layers. This result agrees with the determinations of chapters 5 and 6 where the broad and disordered nature of the $GaAs_{1-x}Bi_x$ bandstructure is discussed in detail.

In Fig. 7.4, the temporal behaviour of the optical emission at certain wavelengths extracted from Fig. 7.3 are presented. These are plotted on a logarithmic scale for ease of analysis. The top left and right panel of this figure contain plots which clearly show evidence of a two (or multi) component decay for some spectral regions on the low energy side of the GaAs peak. This two component decay reflects the interplaying processes present at this excited energy within the material. The initial decay rate is comparable to that observed above the GaAs band edge, and therefore may be associated with recombination to defect-related states in the GaAs layer. The slower process is on a timescale comparable to that observed in the $GaAs_{1-x}Bi_x$ layer. If it is due to recombination in this layer, then it suggests a very broad energy distribution of localised states in the $GaAs_{1-x}Bi_x$ layer.

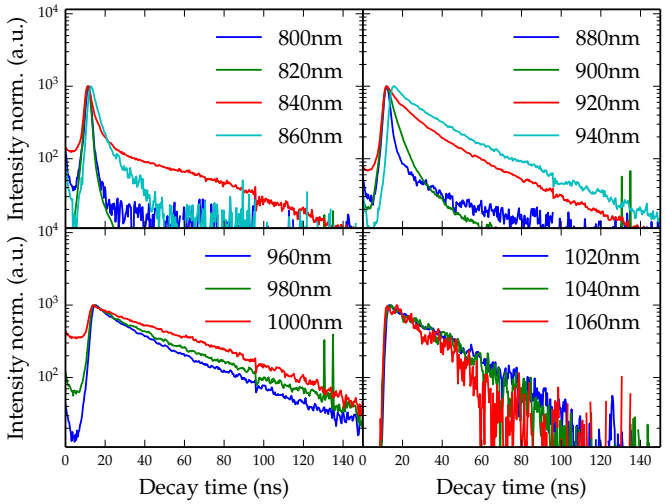


Figure 7.4: Temporal decay of the TRPL streak image integrated at a range of wavelengths. Note the two component decay clearly visible in some of the plots in the region of the GaAs peak.

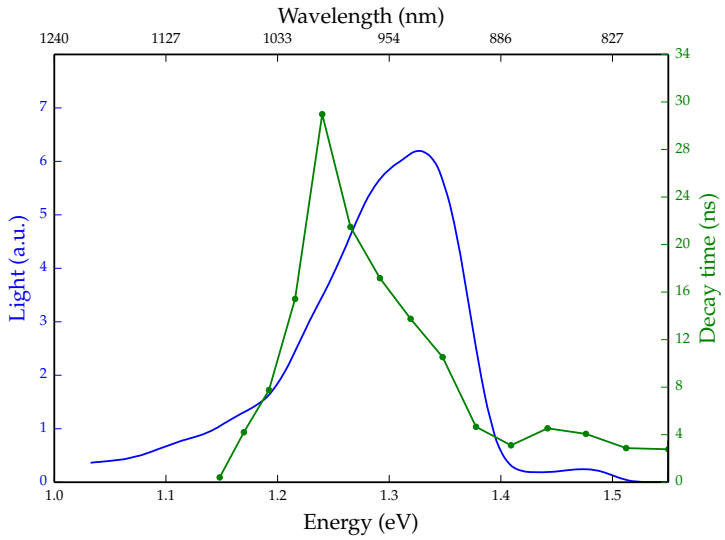


Figure 7.5: Integrated PL just after excitation shown in blue with extracted lifetimes plotted in green (line with circles).

Fig. 7.5 shows the integrated PL and the lifetimes extracted just after the excitation pulse. In this figure it is seen that the lifetime in the GaAs layers is small, ≈ 3 ns, and that this increases to a maximum of ≈ 35 ns on the low energy side of the $GaAs_{1-x}Bi_x$ emission peak. The lifetime then decreases with decreasing energy in the low-energy tail of the PL spectrum.

This is the first measurement of lifetimes in $GaAs_{1-x}Bi_x$ quantum well structures. There have, however, been measurements and theoretical predictions of TRPL in bulk $GaAs_{1-x}Bi_x$ epilayers which will now be discussed.

Simone Mazzucato and colleagues have carried out extensive time resolved studies of $GaAs_{1-x}Bi_x$ material [69]. When the work in this chapter is compared to the work of Mazzucato et al, some interesting insights become clear. A similar emission energy to the material studied here is achieved in bulk layers at a lower composition. This can be understood as a result of confinement within the quantum well layer making the lowest lying transition energy higher than for a bulk material of the same composition. Interestingly, the bulk samples seem to undergo less broadening than that experienced by the quantum well layers. Mazzucato's work also shows a similar S-like character in the temperature dependent peak PL emission as reported in chapter 5 of this thesis for quantum wells. Mazzucato reports lifetimes (≈ 1-2 ns) which are much shorter than those measured here, and also describes the large variation of the lifetime in the $GaAs_{1-x}Bi_x$ layer in terms of localised and delocalised exciton states. These faster dynamics may be as a result of better electron-hole interaction in the bulk material,reflecting that carriers, in particular electrons can propagate more easily in the bulk compared to the quantum well samples studied here. It may also be due to better material quality in the quantum well structures, so that the competing non-radiative recombination rates are reduced in these structures.

Sebastian Imhof and colleagues have undertaken time resolved measurements of $GaAs_{1-x}Bi_x$ bulk epilayers, as well as extensive kinetic Monte Carlo simulations of the material [50]. This work again shows agreement with the measurements carried out in this thesis with short lifetimes on the high energy side of the PL peak, referred to as delocalised exciton recombination by Mazzucato, and longer lifetimes on the low energy side, referred to as localised exciton recombination by Mazzucato. This work also shows that the bulk lifetimes are much shorter (< 10 ns) than that of the quantum wells measured here, but are however longer than the lifetimes measured in the Mazzucato work.

This shows that even amongst the bulk samples there is variability of the lifetime, most likely driven by material quality. The lifetimes extracted from

the measurements on the quantum well samples here are over three times as long as the longest lifetime reported for bulk material. Further theoretical and experimental analysis would be required to understand the relative importance of improved material quality and of modified carrier dynamics in explaining the enhanced lifetimes observed in the quantum well system.

7.5 Summary

Section 7.2 provided an overview of the materials studied in this chapter. It was found that due to the doping concentration of the p-contact layer, an anomalous peak was present in the PL spectra. This peak was removed by an etch of the surface removing the GaAs:Zn layer. In section 7.3 an overview of the experimental method employed to extract the time and spectral dependence of the PL spectra was presented. In this section it was seen that a 650 nm mode locked diode laser and a Hamamatsu streak camera can be combined to provide time resolved PL measurements. In section 7.4, the results of the TRPL measurements were shown and discussed. These results were also compared to similar measurements carried out on bulk epilayers. It was seen that $GaAs_{1-x}Bi_x$ quantum well layers show an optical bandgap which is larger than that of bulk epitaxial films for the same composition. This bandgap enlargement is understood through the quantum well bound states sitting above the unstrained bulk material bandgap in energy. This result is noteworthy as it, along with the heavy-hole light-hole splitting shown in the photovoltage measurements of chapter 6, reinforces the fact that the material is in fact behaving as would be expected of a quantum well. It was observed that the broadening of the quantum well band edge transitions is larger than that observed for bulk films of similar composition [69]. The optical lifetimes in the $GaAs_{1-x}Bi_x$ layers were shown to be larger than the corresponding lifetimes of the bulk films. The enhanced lifetimes could be due to improved material quality or modified carrier dynamics in the QW sample; further theoretical and experimental analysis would be required to confirm the primary cause of the observed behaviour.

Chapter 8

Conclusions

8.1 Summary

In the following sub-sections the main results of this thesis this thesis are summarised. This is followed in section 8.2 by overall conclusions and an overview of potential future work.

8.1.1 Experimental analysis and rate equation modelling of an InP based quantum dash laser showing bistable threshold

In chapter 4 an experimental analysis was carried out on two similar InP-based quantum dash lasers, one of which showed bistable threshold behaviour at low temperature. It was concluded that passive saturable absorption caused a bistability in the laser due to impeded interwell transport at low temperature. It was also seen that the bistability was followed at higher temperatures by a giant, and sometimes negative, value of T_0. A modified 11 dimensional rate equation model which incorporated carrier transport effects was used to qualitatively test the proposed mechanism for bistability and very good qualitative agreement between theory and experiment was found.

8.1.2 Experimental study of bismuth-induced broadening in $GaAs_{1-x}Bi_x$ quantum well laser structures

In chapter 5 an experimental study of bismuth-induced broadening in $GaAs_{1-x}Bi_x$ quantum well laser structures was carried out. Photovoltage spectroscopy was used to probe the band structure of $GaAs_{1-x}Bi_x$/(Al)GaAs QW laser structures,

with Bi compositions of up to $x = 6.6\%$. Following this, temperature dependent measurements of photoluminescence and spontaneous emission from the first ever electrically injected $GaAs_{1-x}Bi_x$ single QW laser structure with $x = 2.2\%$ were described. It was subsequently shown that the use of polarisation-resolved photovoltage measurements verify earlier theoretical predictions [99] that the light-hole band edge states in $GaAs_{1-x}Bi_x$ should undergo enhanced inhomogeneous broadening compared to that associated with heavy-hole states. Additionally, it was shown that the variation of the inhomogeneous broadening of the band edge transitions in $GaAs_{1-x}Bi_x$ alloys depends only weakly on the Bi composition x. It was determined that Bi-related localised states prevent the formation of a thermal distribution of carriers at low temperature in electrically pumped $GaAs_{1-x}Bi_x$ QWs. Additionally, measurements showed that the spontaneous emission linewidth is strongly dependent upon temperature, with a maximum value obtained at close to 250 K before strongly decreasing with increasing temperature. This unusual material behaviour was explained by considering the temperature-dependent dynamics of carriers at the band edge, using a combination of theoretical calculations[100, 19] and consideration of the results of previous studies [49, 50] of the luminescence dynamics in $GaAs_{1-x}Bi_x$ materials. The temperature dependent lasing characteristics of the 2.2 % laser structure were presented, showing large values for I_{th} and T_0. Further analysis of the radiative and non-radiative processes in this material showed that at least 75% of the total threshold current density at 250 K was non-radiative in nature. Calculations of temperature dependent SE by Christopher A. Broderick and a comparative analysis with the relevant experimental data was presented, showing that the average band edge approximation of the model holds up well at low temperature and up to the thermalisation event which occurs at T $\approx$ 300 K.

8.1.3 Experimental determination of the $GaBi_xAs_{1-x}$/GaAs band offset, and $\mathbf{k} \cdot \mathbf{p}$ parameterisation

In chapter 6, using a combination of experimental measurements and theoretical calculations, the band offsets in $GaBi_xAs_{1-x}$/(Al)GaAs quantum wells were directly determined. The use of polarisation-resolved photovoltage spectroscopy enabled probing of transitions relating separately to light and heavy holes in the laser structures studied, and hence the band structure of the quantum wells in the devices. By using a 12-band $\mathbf{k} \cdot \mathbf{p}$ Hamiltonian for $GaBi_xAs_{1-x}$, which had previously been derived from detailed tight-binding supercell calculations, identification of the key contributions to the conduction and valence band offsets in

$GaBi_xAs_{1-x}$, and a general procedure for calculating the band offsets in GaAs-based dilute bismide quantum well structures at arbitrary Bi composition x have been developed.

The 12-band $\mathbf{k} \cdot \mathbf{p}$ model for $GaBi_xAs_{1-x}$/(Al)GaAs has been parameterised in such a way that the calculated transition energies are in good agreement with experiment for a number of different laser structures. This combined experimental and theoretical approach has enabled verification for the first time of a type-I band offset at the $GaBi_xAs_{1-x}$/GaAs heterointerface, in agreement with previous calculations for bulk $GaBi_xAs_{1-x}$, as well as with pressure-dependent measurements which have been performed on a $GaBi_xAs_{1-x}$-based LED structure [48]. This type-I band offset is seen to be a lower bound on the bulk conduction band (CB) offset in $GaBi_xAs_{1-x}$/GaAs due to the 70 % GaAs/AlGaAs CB offset used in the analysis equalling the largest CB offset reported in the literature for this material system. Furthermore, by applying the 12-band $\mathbf{k} \cdot \mathbf{p}$ model to calculate the band structure of additional laser structures the validity of the model has been displayed by showing that it is capable of describing the main features of the band structure in $GaBi_xAs_{1-x}$/(Al)GaAs laser structures with varying Bi composition, as well as with varying quantum well thickness and number.

8.1.4 Experimental investigation of optical lifetimes in $GaAs_{1-x}Bi_x$ quantum wells using TRPL

In chapter 7, using a 650 nm mode locked laser for excitation, and a Hamamatsu streak camera for temporal resolution of the luminescence, the spectral dependence of the recombination lifetime was measured in $GaAs_{1-x}Bi_x$ quantum wells for the first time. The results of the TRPL measurements were shown and discussed. These results were then compared to previous measurements carried out on bulk epilayers. It was seen that $GaAs_{1-x}Bi_x$ quantum well layers show an optical bandgap which is larger than that of bulk epitaxial films for the same composition. This bandgap enlargement is understood through the quantum well bound states sitting above the unstrained bulk material bandgap in energy. This result is noteworthy as it, along with the heavy-hole light-hole splitting shown in the photovoltage measurements of chapter 6, reinforces the fact that the material is in fact behaving as would be expected of a quantum well. It was observed that the broadening of the quantum well material is larger than that of the bulk films for similar composition [69]. The recombination lifetimes in the $GaAs_{1-x}Bi_x$ layers were shown to be larger than the corresponding lifetimes of the bulk films. The enhanced lifetimes could be due to improved material quality or modified

carrier dynamics in the QW sample; further theoretical and experimental analysis would be required to confirm the primary cause of the observed behaviour.

8.2 Conclusions

This thesis has been concerned primarily with optical absorption and emission measurements of telecommunication wavelength lasers, and of materials in the process of being developed for high efficiency telecommunication wavelength emission. Chapter 4 provided an experimental analysis of an InP based quantum dash laser emitting at 1.55 μm, which showed bistability of the threshold current. In this chapter it was shown that optical bistability can be achieved within materials without the need for complex multi section devices. This allows for the design of all optical switches through bandstructure engineering.

In chapter 5 a study of the broadening present in $GaAs_{1-x}Bi_x$ was undertaken and the first spontaneous emission measurements on this material were presented. This work provides detailed insight into the novel $GaAs_{1-x}Bi_x$ material bandstructure, and more importantly, the electronic and optical characteristics of device quality quantum wells. This work is not breakthrough in the sense that it does not confirm $GaAs_{1-x}Bi_x$ as the next big player in telecommunications. However, this work shows that $GaAs_{1-x}Bi_x$ is still a candidate for optical telecommunications due to the confirmation that the observed band edge inhomogeneous broadening, which degrades laser characteristics, is independent of composition and may even marginally decrease with increasing Bi composition.

In chapter 6 the results of a collaborative project undertaken with Christopher A. Broderick were presented. In this chapter the first ever determination of band offsets at the $GaAs/GaAs_{1-x}Bi_x$ heterointerface were presented. This determination of the band offset between GaAs and $GaAs_{1-x}Bi_x$ has been key to the development of better quality devices. This was achieved through the design of devices with enough conduction band offset to allow electron confinement while maintaining wave-guide performance. The importance of this was seen within the BIANCHO project with the reduction of threshold by a factor of two for a 2.2 % Bi laser through optimisation of the barrier material and also through identification that GaAs barriers provide sufficient electron confinement at higher Bi compositions, x, in the quantum well($x \approx 5$ %). This determination of band offsets will continue to be of use in the design of devices based on $GaAs_{1-x}Bi_x$ active regions into the future.

Chapter 7 gave an overview of the process of obtaining time resolved band edge

photo-emission from the $GaAs_{1-x}Bi_x$ material. This was the first time band edge emission was time resolved in this material. The TRPL measurements provided the first ever measure of optical lifetimes at the $GaAs_{1-x}Bi_x$ band edge.

8.2.1 Future work

The incorporation of Bi into semiconductor materials to favourably influence the bandstructure is essentially in its infancy. For this reason future work has a huge scope. I will focus on the incremental progress which can be made on the work presented here in this section.

More work is required to adequately understand the recombination dynamics in the GaBiAs material. This would involve both experimental measurements of TRPL and numerical analysis of material properties.

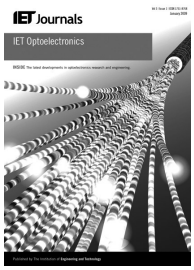
An avenue sure to be explored in the near future is the processing of these GaBiAs laser materials into buried heterostructure or ridge waveguide laser structures with the aim to measure the material gain, and then compare to the theoretical models of the material for benchmarking purposes.

Turning to the InP quantum dash structures of chapter 4, an interesting project would be to explore the possibility of growing quantum dashes with a slightly higher barrier than the lasers studied in this work with the aim of extending the bistable regime and thus the high T_0 regime to higher temperatures, with the ultimate aim of infinite or negative T_0 above room temperature.

Appendix A

Bistable Q-Dash laser

Published in IET Optoelectronics
Received on 27th June 2013
Revised on 30th August 2013
Accepted on 23rd September 2013
doi: 10.1049/iet-opt.2013.0083



ISSN 1751-8768

Bistability of threshold in quantum dash-in-a-well lasers

Patrick E. Harnedy[1,2], Simon Osborne[1], Siddharth Joshi[3], François Lelarge[3], Eoin P. O'Reilly[1,2]

[1]*Photonics Theory Group, Tyndall National Institute, Lee Maltings, Dyke Parade, Cork, Ireland*
[2]*Department of Physics, University College Cork, Cork, Ireland*
[3]*III-V Lab, a joint Laboratory of Alcatel Lucent Bell Labs, Thales Research & Technology and CEA-LETI Route de Nozay, 91460 Marcoussis, France*
E-mail: patrick.harnedy@tyndall.ie

Abstract: The authors observe a bistability of threshold in a quantum dash ridge-waveguide laser diode at temperatures below 230 K. A giant and sometimes negative characteristic temperature, T_0, is measured at temperatures between 230 K and 320 K. They analyse the temperature dependent light-current characteristics of this device, and a similar device with lower barriers, to gain an insight into the mechanism causing bistable behaviour. A rate equation model shows localisation and passive saturable absorption as the causes of the bistable behaviour in the higher barrier laser at low temperature. They find good qualitative agreement between the experimental and the theoretical results.

1 Introduction

InAs grown on the commercially favoured (100) InP substrate orientation can, under appropriate growth conditions, form quantum dots elongated along the (1–10) axis, known as quantum dashes [1]. Quantum dash lasers have shown many impressive attributes including low threshold current, high characteristic temperature, T_0, low chirp and in some cases spontaneous mode-locking [2].

Quantum dash lasers offer improved optical bandwidth over quantum well lasers because of inhomogeneous broadening caused by the dash size distribution. This offers the possibility of extremely short pulses from these lasers [3]. The InAs/InP quantum dash material system is a very exciting prospect for the next generation optical networks, because of the high temperature stability and large bitrates which have been associated with it [4].

We study these devices to investigate the possibilities as well as constraints offered by increasing the confinement of the carriers within quantum confined structures. We investigate the temperature dependent gain and loss mechanisms of these lasers.

In this paper, we examine two devices emitting at 1.55 μm at room temperature, which are nominally identical except for barrier height, as seen in Fig. 1. From here on, the high barrier device will be referred to as DW_H and the lower barrier device will be called DW_L. Both devices are processed as ridge-waveguide lasers with as cleaved facets. We measure the temperature dependent characteristics of these devices and uncover a temperature dependent bistability of threshold in DW_H. We put forward a theory based on carrier localisation and impeded interwell transport at lower temperatures to explain this bistable behaviour and use a simple rate equation model to test this theory. We find good qualitative agreement between the measured and calculated data.

Section 2 presents a comparison of the experimental measurements which have been made on DW_H and DW_L, including a temperature dependent bistability at threshold in DW_H. In Section 3, we present the proposed mechanism for the bistable behaviour in DW_H, and introduce a simple rate equation model which we have used to successfully model this behaviour. Section 4 details the results of the modelling and compares the calculated and experimental data. Finally, we summarise our conclusions in Section 5.

2 Experimental

For each of the two materials, eight lasers were tested from four laser bars; these bars were cleaved from one quarter of their respective wafers. We found consistent results for the different devices from each material. The devices studied in this paper are grown by gas-source molecular beam epitaxy. They consist of six stacks of InAs quantum dashes surrounded by quantum wells of the quaternary alloy $Ga_xIn_{1-x}As_yP_{1-y}$. The wells are bounded by barriers, also of $Ga_xIn_{1-x}As_yP_{1-y}$. This active region is grown in a P–N junction lattice-matched to the InP substrate and to the cladding layers. The growth of these materials is reported in [2]. The thickness of the InAs quantum dash embedded within the QW is slightly larger for the DW_H in order to keep the same emission wavelength ($\simeq$10% increase). The

© The Institution of Engineering and Technology 2014

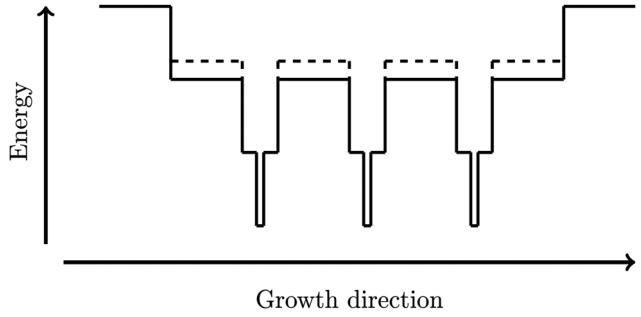


Fig. 1 *Flat band approximation showing the DWELL structure of the two devices considered, one with a high barrier (dashed), and the other with a lower barrier*

quantum well region of both devices is of $Ga_{0.36}In_{0.64}As_{0.78}P_{0.22}$ and is 3.5 nm thick on each side of the quantum dash layer. Both designs are based on 20 nm-thick barriers with a 140 nm-thick separate confinement heterostructure. The difference between the materials is that the barrier in the DW_L is comprised of $Ga_{0.20}In_{0.80}As_{0.43}P_{0.57}$, whereas the barrier of the DW_H is comprised of $Ga_{0.15}In_{0.85}As_{0.32}P_{0.68}$, leading to a greater confinement for the carriers in the DW_H.

The bare laser chips are mounted on the cold finger of a closed cycle helium cryostat and contacted using a clip system. The temperature dependence of the threshold current of the lasers is measured from the temperature dependent facet light-current curves. Lasing is observed from the quantum dash states at all the temperatures. The threshold current is taken as the value of the current that corresponds to the positive peak in the second derivative of the light-current curve. This is the inflection point of the first derivative and consequently a good measure of the threshold current. The temperature dependence of the radiative current of the lasers is extracted from the spontaneous emission measurements made from a window in the laser substrate, as in [5], and normalised to J_{th} at a low temperature.

As can be seen from Fig. 2, the threshold current of DW_L increases exponentially from the low temperature to 148 K. This is followed by a region of slightly increased T_0 up to 235 K. This is attributed to the formation of a thermal

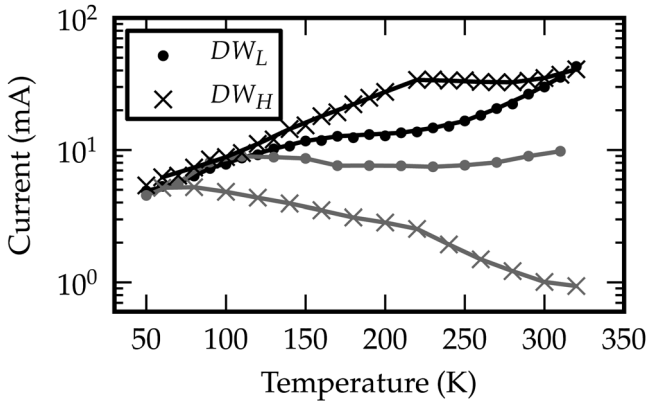


Fig. 2 *Temperature dependence of the threshold (black) and the radiative (grey) currents for the DW_L (filled circles) and the DW_H (crosses)*

DW_H has a bistable threshold below 220 K

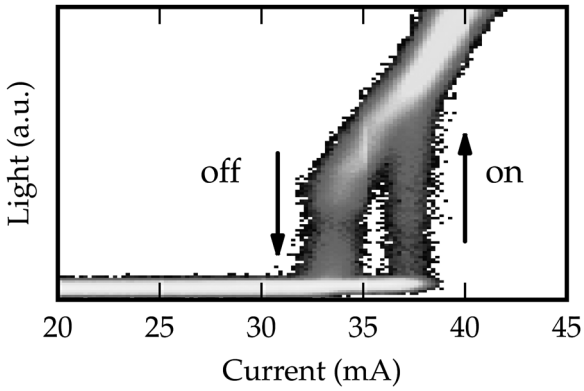


Fig. 3 *Three hundred overlayed light-current measurements of the high barrier laser at 190 K, clearly showing an abrupt switch to the lasing at 37.5 mA and an equally abrupt switch from the lasing at 33.3 mA*

equilibrium of the carriers in the dashes, resulting in a slight decrease in the rate of increase of the threshold current. This is then followed by a region of exponentially increasing threshold current, with $T_0 = 61$ K. In this laser, the radiative current increases with the threshold current up to 150 K and then decreases up to 230 K before recovering and increasing again above this temperature. DW_L exhibits behaviour which is typical of previous quantum dash lasers which have been measured [6].

In the DW_H, the threshold current at which lasing commences increases exponentially up to 230 K; between 230 K and 310 K there is a reduction in the threshold current accompanied by a giant (and negative over a small interval) T_0 value. Above 310 K, the threshold current once again increases exponentially. The radiative current of this device is decreasing over the entire temperature range, showing only slight signs of increasing above 320 K. Similar characteristics have previously been observed in 1.3 μm quantum dot in a well lasers [7].

At temperatures lower than 220 K, DW_H shows the bistability of threshold, as seen in Fig. 3, with lasing switching off at a lower current than it switches on. There is an increased threshold current compared with DW_L and an abrupt switch to and from lasing seen in DW_H at these temperatures.

In Fig. 4, the temperature dependence of the measured switch points of the bistability can be seen. It is noted that the size of the bistability grows from low temperature to a maximum size at 190 K and from there diminishes very strongly with increasing temperature, before disappearing at 230 K.

Fig. 5 shows ASE spectra above and below threshold at 190 and 300 K. At room temperature (stable region) the lasing transition occurs on the low energy side of the gain spectrum, as is typical in a semiconductor laser. In the bistable region (190 K), the lasing transition occurs on the high energy side of the gain spectrum and is considerably narrowed. We speculate that this high energy lasing is a result of the preferential absorption of spontaneous emission at the band edge because of saturable absorption, thus pushing the lasing transition to higher energies than it would otherwise occur. This saturable absorption effect could be achieved if the energy gap of the first well was slightly larger than that of the later wells. We do not need to include such a bandgap shift in the theoretical model presented below in order to demonstrate the transition to

© The Institution of Engineering and Technology 2014

doi: 10.1049/iet-opt.2013.0083

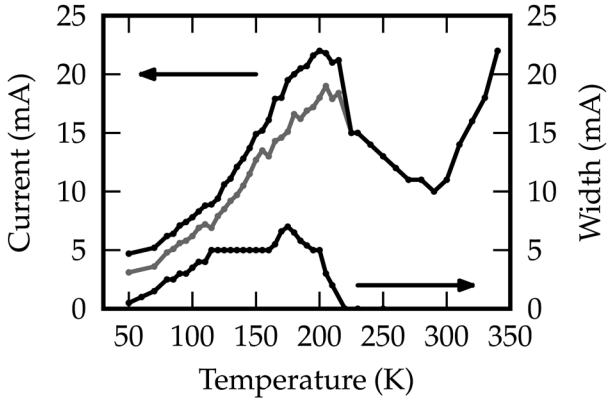


Fig. 4 *Left y-axis plot shows the temperature dependence of the experimentally determined threshold current including the switch on/off points in the bistable region*

Right *y*-axis plot shows the temperature dependence of the size of the bistability, which is seen to grow in size from 50 K to about 200 K, above which it diminishes strongly with increasing temperature

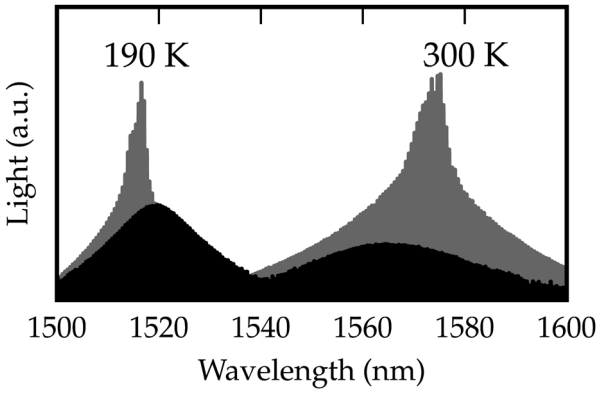


Fig. 5 *Amplified spontaneous emission (black) (at 80% of I_{th}) and lasing spectra (grey) at 190 K (left) and 300 K (right)*

Note that the lasing transition is at the high energy side of the gain peak in the bistable region and at the low energy side at 300 K

bistable behaviour at lower temperatures. Overall, the narrowing of the 190 K spectrum is also at least in part a thermal effect, with the carriers being distributed over a decreased energy range at lower temperature, leading to increasing carrier localisation, consistent with the sharp roll off observed at the short wavelength end of the gain spectrum at lower temperature.

3 Model

We propose passive saturable absorption as a result of carrier localisation at low temperature as the mechanism supporting the bistable behaviour in DW_{H}.

It is well established that InGaAsP alloys grown on InP have a small conduction band offset, and that there is a large valence band offset, in particular for unstrained barriers [8–10] such as are considered here [11]. Owing to this and the low hole mobility, the carrier distribution can become localised, and so the holes get trapped in the quantum wells near the p-doped side of the device at lower temperatures. This leads to large changes in the carrier density in successive layers, with the holes in particular being preferentially trapped in the upper layers, on the p-doped side. Some layers which are less populated act as absorbers, whereas the others produce gain. This can lead to saturable absorption in the temperature range where the carrier densities vary strongly from layer to layer. Extra gain is then required in the first (p-side) well so that the net gain can equal the cavity and mirror losses plus the extra absorption from the n-side layers in order to achieve lasing. Once enough gain is produced to saturate the absorbing regions, and they become transparent, an abrupt switch to lasing occurs. At this point the absorbing wells should clamp at or near transparency, supported by the formation of a photon-mediated carrier equilibrium. As the current is reduced from this state of lasing, stimulated emission keeps this photon-mediated carrier equilibrium active to a current less than the original abrupt switch on, leading to the bistability seen in Fig. 3.

As the temperature rises, the escape rate increases for the carriers trapped in a given (p-side) well, and so a thermal distribution of carriers begins to form. This leads above 230 K for DW_{H} to a region of decreasing threshold current and giant T_0 as the losses due to the absorbing layers decrease and as these layers become populated with carriers. Previous analysis has shown that the Auger recombination provides an increasingly significant recombination pathway with increasing temperature in 1.5 μm quantum dash lasers [6], consistent with the reduced T_0 then observed at higher temperatures both in DW_{H} and in DW_{L}.

Based on the above analysis, we conclude that the bistable effect is most probably caused by transport issues between the quantum well regions of DW_{H} at low temperatures. To test this hypothesis, a simplified quantum well structure is modelled to investigate how transport within the structure influences the light output as the temperature changes. In this model, we presume that the transport between the quantum well layers is the limiting factor at low temperatures. Although the gain in the actual devices is due to recombination in the six quantum dash layers, we find that the main physical effects can be understood by using a simple system of rate equations incorporating carrier transport effects to model a three quantum well device [12]

$$\dot{n}_1^{\mathrm{b}} = \frac{\eta_i I}{qV} - \frac{n_1^{\mathrm{b}}}{\tau_{\mathrm{d}}} + \frac{n_1^{w_{\mathrm{u}}}}{\tau_{\mathrm{d}}} - \frac{n_1^{\mathrm{b}}}{\tau_n} \tag{1}$$

$$\dot{n}_i^{\mathrm{b}} = \frac{n_{i-1}^{w_{\mathrm{u}}}}{\tau_{\mathrm{d}}} - \frac{2n_i^{\mathrm{b}}}{\tau_{\mathrm{d}}} + \frac{n_i^{w_{\mathrm{u}}}}{\tau_{\mathrm{d}}} - \frac{n_i^{\mathrm{b}}}{\tau_n} \tag{2}$$

$$\dot{n}_4^{\mathrm{b}} = \frac{n_3^{w_{\mathrm{u}}}}{\tau_{\mathrm{d}}} - \frac{n_4^{\mathrm{b}}}{\tau_{\mathrm{d}}} - \frac{n_4^{\mathrm{b}}}{\tau_n} \tag{3}$$

$$\dot{n}_i^{w_{\mathrm{u}}} = \frac{n_i^{\mathrm{b}}}{\tau_{\mathrm{d}}} - \frac{2n_i^{w_{\mathrm{u}}}}{\tau_{\mathrm{d}}} + \frac{n_{i+1}^{\mathrm{b}}}{\tau_{\mathrm{d}}} - \frac{n_i^{w}}{\tau_{\mathrm{c}}} + \frac{n_i^{w}}{\tau_{\mathrm{e}}} - \frac{n_i^{w_{\mathrm{u}}}}{\tau_n} \tag{4}$$

$$\dot{n}_i^{w} = \frac{n_i^{w_{\mathrm{u}}}}{\tau_{\mathrm{c}}} - \frac{n_2^{w}}{\tau_{\mathrm{e}}} - \frac{n_i^{w}}{\tau_n} - G_i S \tag{5}$$

$$G_i = G_0 S \ln\left(\frac{n_i^{w}}{n_{\mathrm{tr}}}\right) \tag{6}$$

$$\dot{S} = \Gamma v_g \sum_{i=0}^{m} G_i S - \frac{S}{\tau_{\mathrm{p}}} + \beta \sum_{i=0}^{m} \frac{n_i^{w}}{\tau_n} \tag{7}$$

Here η_{i} is the injection efficiency, I is the current, q is the

© The Institution of Engineering and Technology 2014

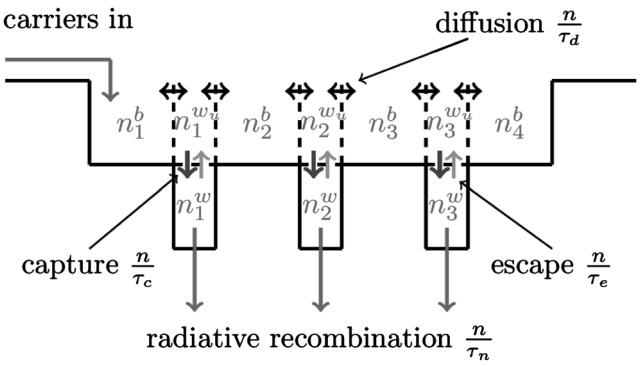


Fig. 6 *Flow diagram of the rate equation system showing how the diffusion time, the capture time, the escape time and the recombination time influence the carrier distribution through the system*

elementary charge and V is the volume of the active region, respectively. $\dot{n}_i^{\mathrm{b}}$, $\dot{n}_i^{w_{\mathrm{u}}}$ and $\dot{n}_i^{w}$ are the rate of change of carrier population in the barriers, the unconfined quantum well regions and the confined quantum well regions, with respect to time. n_{tr} is the transparency carrier density. τ_{c}, τ_{e}, τ_{d}, τ_n, and τ_{p} are the capture, escape, diffusion, recombination and photon lifetimes. $\dot{S}$ is the rate of change of photon density with respect to time and G_i is the gain calculated by using the logarithmic gain approximation of (6) in each of the quantum wells. Layer indexing starts on the p-side of the device.

The dynamic flow of carriers through the equation system is depicted in Fig. 6. The capture, escape, diffusion and recombination time constants are used to distribute the carriers through the system.

All the carrier lifetimes used in the model are assumed to be independent of temperature and carrier density, except for the carrier escape time. This is justified by τ_{e} having a much larger temperature dependence than the other processes. Inclusion of carrier density dependent lifetimes is possible, but would not qualitatively change the overall behaviour observed. We include a temperature dependence for the transparency carrier density, N_{tr}, in order to account for the temperature dependence of the gain in (6). The escape time is calculated from

$$\tau_{\mathrm{e}} = \tau_{\mathrm{c}} * \exp^{(E_{\mathrm{b}}/k_{\mathrm{b}}T)} \tag{8}$$

where k_{b} is the Boltzmann constant, E_{b} is the energy difference from the band edge of the well to the band edge of the barrier and T is the temperature [13], respectively. The temperature dependence of the transparency carrier density is included through the relation [14]

$$N_{\mathrm{tr}}(T) = N_{\mathrm{tr}}(300) * \frac{T}{300} \tag{9}$$

At low temperatures, the calculated escape time is large enough to result in the carriers becoming localised in the upper layers because of the large ratio of the capture and the escape times; this causes saturable absorption.

As the temperature approaches 230 K, and the ratio of the escape time to the capture time decreases, a more uniform distribution of carriers across the wells begins to form, removing the saturable absorption process so that the bistability is eliminated and the threshold current reduces with increasing temperature. At higher temperatures, τ_{e} approaches τ_{c}, because of the thermal broadening of the carrier distribution and higher energy states being populated with carriers. This makes it more difficult to achieve transparency carrier density at the lasing energy, as described by (9), which contributes to the increasing threshold current with increasing temperature in this region.

4 Results

We integrate the system of equations by using a fourth-order Runga-Kutta method to determine the device characteristics as a function of the drive current and of temperature. The right panels in Fig. 7 show the calculated photon density (top) and the carrier density in the quantum wells (bottom) against the applied current for an escape time which corresponds to room temperature. As can be seen the light output shows lasing with no sign of bistability and the carrier densities all clamp at threshold, as expected.

The left panels show the same calculation for an escape time which corresponds to a temperature of 150 K. We now

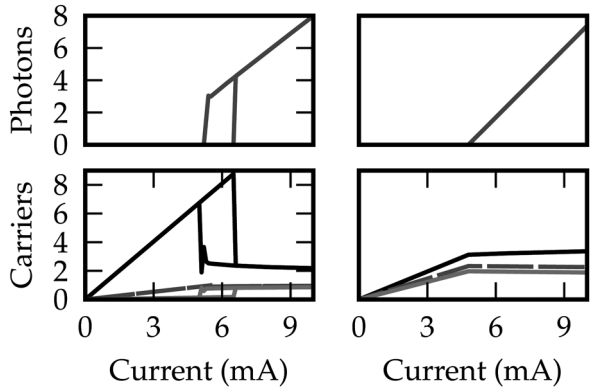


Fig. 7 *Top panels show the calculated light (arb. units)-current characteristics for two different escape times, representing the stable and the bistable regimes*

Bottom panels show the calculated carrier densities (arb. units) for each confined region (well1 = black; well2 = grey, dashed; and well3 = light grey), for the same escape times as the top panels

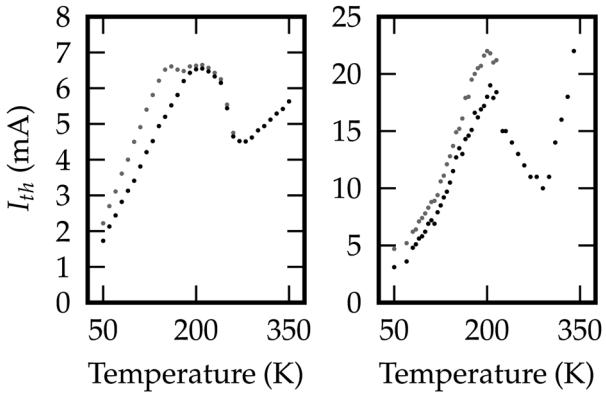


Fig. 8 *Calculated temperature dependence of the threshold current (left panel) and the measured temperature dependence of the threshold current (right panel)*

Switch on points grey and switch off points black in the bistable regime

© The Institution of Engineering and Technology 2014

doi: 10.1049/iet-opt.2013.0083

see a bistability of the light current characteristic and of the carrier density.

We vary the escape time according to (8) and the transparency carrier density according to (9) in the temperature range from 50 to 350 K and compare the resulting threshold currents with the measured values in Fig. 8.

From 50 to 230 K in both cases there is a bistable, increasing threshold current. From 230 to 280 K there is a decreasing threshold current, and negative T_0. Both the measured and the calculated values of the threshold current begin to increase above 300 K.

Despite the fact that the model presented here includes only two temperature dependent parameters; the transparency carrier density N_{tr} and the carrier escape time from the quantum wells, τ_e, it still provides very good qualitative agreement between the measured and calculated threshold currents. Overall, we conclude that the simple model presented here therefore confirms that carrier localisation and a non-uniform spatial carrier distribution can lead to bistable behaviour of the threshold current at low temperatures in the DW_H device considered here.

5 Conclusions

We have observed a bistability of threshold in a DWELL laser at low temperatures. We examined the experimental data, and from this proposed that passive saturable absorption causes this bistability. We saw that this bistability was followed at higher temperatures by a large, and sometimes negative, value of T_0. We modified a simple rate equation model by incorporating carrier transport effects to qualitatively test the proposed mechanism and found good agreement between theory and experiment.

This effect has the potential to be exploited in several areas. Modelocking, where decoupled carrier states are required to achieve transform limited pulses, and where a wide gain bandwidth provides the possibility of very short pulses, could be achieved by making a two section device from the DW_H material. In addition, if the barrier could be raised slightly more it would offer the possibility of bistable behaviour at room temperature, allowing applications such as passive optical switching using either injected light or current to switch between the two stable output powers.

6 Acknowledgment

This work was partly supported by the European Union Seventh Framework Programme (BIANCHO; FP7-257974) and by the Science Foundation Ireland (10/IN.1/I299).

7 References

1 Alghoraibi, I., Jouland, L., Paranthoen, C., *et al*.: 'InAs self-assembled quantum dot and quantum dash lasers on InP for 1.55 μm optical telecommunications'. Proc. IEEE Information and Communication Technologies 2006 (ICTTA '06), 2006

2 Lelarge, F., Dagens, B., Renaudier, J., *et al*.: 'Recent advances on InAs/InP quantum dash based semiconductor lasers and optical amplifiers operating at 1.55 μM', *IEEE J. Selected Topics in Quantum Electronics*, 2007, **13**, (January-February), p. 111

3 Latkowski, S., Maldonado-Basilio, R., Landais, P.: 'Sub-picosecond pulse generation by 40-GHz passively mode-locked quantum-dash 1-mm-long Fabry-Perot laser diode', *Opt. Express*, 2009, **17**, p. 19166

4 Duan, G.-H., Shen, A., Akrout, A., *et al*.: 'High performance InP-based quantum dash semiconductor mode-locked lasers for optical communications', *Bell Labs Tech. J.*, 2009, **14**, p. 63

5 Phillips, A.F., Sweeney, S.J., Adams, A.R., Thijs, P.J.A.: 'The temperature dependence of 1.3- And 1.5-μm compressively strained InGaAs(P) MQW semiconductor lasers', *IEEE J. Selected Topics in Quantum Electronics*, 1999, **5**, p. 401

6 Heck, S.C., Healy, S.B., Osborne, S., *et al*.: 'An analysis of 1.55 μm InAs/lnP quantum dash lasers', *Appl. Phys. Lett.*, 2008, **92** p. 251105

7 Crowley, M.T., Marko, I.P., Masse, N.F., *et al*.: 'The importance of recombination via excited states in InAs/GaAs 1.3 μm quantum-dot lasers', *IEEE J. Selected Topics in Quantum Electronics*, 2009, **15**, p. 799

8 Krijn, M.P.C.M.: 'Heterojunction band offsets and effective masses in lll-V quaternary alloys', *Semiconductor Sci. Technol.*, 1991, **6**, p. 27

9 Barrau, J., Amand, T., Brousseau, M., Simes, R.J., Goldstein, L.: 'Induced electrostatic confinement of the electron gas in tensile strained InGaAs/lnGaAsP quantum well lasers', *J. Appl. Phys.*, 1992, **71**, p. 5768

10 Silver, M., O'Reilly, E.: 'Gain and radiative current density in InGaAs/lnGaAsP lasers with electrostatically confined electron states', *IEEE J. Quantum Electronics*, 1994, **30**, p. 547

11 Heck, S.C., Osborne, S., Healy, S.B., *et al*.: 'Experimental and theoretical study of InAs/lnGaAsP/lnP quantum dash lasers', *IEEE J. Quantum Electronics*, 2009, **45**, p. 1508

12 Vandermeer, A.D., Cassidy, D.T.: 'A rate equation model of asymmetric multiple quantum- well lasers', *IEEE J. Quantum Electronics*, 2005, **41** (July) p. 917

13 Crowley, M.T., Houlihan, J., Piwonski, T., *et al*.: 'Refractive index dynamics of InAs/GaAs quantum dots', *Appl. Phys. Lett.*, 2013, **103**, p. 021114 (pages 4)

14 OReilly, E., Silver, M.: 'Temperature sensitivity and high temperature operation of long wavelength semiconductor lasers', *Appl. Phys. Lett.*, 1993, **63**, p. 3318

© The Institution of Engineering and Technology 2014

Appendix B

Determination of GaAs/GaBiAs band offsets

Determination of type-I band offsets in $GaBi_xAs_{1-x}$ quantum wells using polarisation-resolved photovoltage spectroscopy and 12-band $\mathbf{k}\cdot\mathbf{p}$ calculations

Christopher A. Broderick,[1,2,*] Patrick E. Harnedy,[1,2] Peter Ludewig,[3] Zoe L. Bushell,[3,4] Robert J. Manning,[1,2] Kerstin Volz,[3] and Eoin P. O'Reilly[1,2,†]

[1] *Tyndall National Institute, Lee Maltings, Dyke Parade, Cork, Ireland*
[2] *Department of Physics, University College Cork, Cork, Ireland*
[3] *Material Science Center and Faculty of Physics, Philipps-Universität Marburg, 35032 Marburg, Germany*
[4] *Advanced Technology Institute and Department of Physics, University of Surrey, Guildford, Surrey GU2 7XH, United Kingdom*

(Dated: March 5, 2015)

Using photovoltage (PV) spectroscopy we analyse the electronic structure of a series of $GaBi_xAs_{1-x}$/(Al)GaAs dilute bismide quantum well (QW) laser structures. The use of polarisation-resolved PV measurements allows us to separately identify transitions involving bound light- and heavy-hole states in the QWs, as well as bound-to-continuum transitions from the QWs to the barriers. Analysis of these transitions enables us to probe the $GaBi_xAs_{1-x}$/(Al)GaAs conduction and valence band offsets, thereby quantifying the band offsets. Using a 12-band $\mathbf{k}\cdot\mathbf{p}$ Hamiltonian, we extract the band offsets in the QWs explicitly by constraining the Bi-related parameters of the model against the experimentally measured transition energies. The PV measurements and $\mathbf{k}\cdot\mathbf{p}$ calculations we present provide the first explicit confirmation of a type-I band offset at the $GaBi_xAs_{1-x}$/GaAs heterointerface near $x = 2\%$. This result, combined with the theory we present for calculating the band offsets at $GaBi_xAs_{1-x}$/(Al)GaAs heterointerfaces, can be used to determine the band offsets at arbitrary Bi composition x.

I. INTRODUCTION

Research interest in dilute bismide alloys, in which a small fraction of the group-V atoms in a conventional III-V semiconductor such as GaAs are replaced by bismuth (Bi) to form, e.g., $GaBi_xAs_{1-x}$, has been steadily increasing in recent years. This increased interest is due to fundamental interest in the unique electronic properties of dilute bismide alloys, as well as a recognition of the potential of dilute bismide alloys for specific device applications.[1]

Dilute bismide alloys are naturally complementary to well-studied dilute nitride alloys such as GaN_xAs_{1-x}, where replacing As atoms by nitrogen (N) is known to introduce a resonant impurity level lying above the conduction band (CB) edge in energy.[2] The formation of Bi-related localised states and their interaction with the extended valence band (VB) edge states of the host matrix semiconductor determine the details of the electronic structure of $GaBi_xAs_{1-x}$ and related alloys.[3] In particular, the replacement of As by Bi has been observed experimentally and demonstrated theoretically to cause a rapid reduction of the $GaBi_xAs_{1-x}$ band gap (E_g) by up to 90 meV when 1% of the As atoms in GaAs are replaced by Bi.[4,5] There is also a strong increase in the $GaBi_xAs_{1-x}$ spin-orbit-splitting energy ($\Delta_{\rm SO}$) with increasing Bi composition x.[6,7]

The incorporation of Bi in GaAs to form $GaBi_xAs_{1-x}$ with $x \gtrsim 10\%$ leads to a band structure in which the magnitude of the spin-orbit-splitting exceeds the band gap ($\Delta_{\rm SO} > E_g$). This band structure condition offers the possibility to suppress the hot-hole-producing non-radiative CHSH Auger recombination pathway, a loss mechanism that strongly increases the threshold current and temperature sensitivity in conventional InP-based quantum well (QW) lasers operating at telecommunication wavelengths.[8–11]

The causes and effects of the strong modification of the $GaBi_xAs_{1-x}$ VB structure compared to that of GaAs have been studied theoretically by several authors.[3,12–14] Despite a degree of controversy,[14] the general consensus is that Bi acts as an isovalent impurity, introducing highly localised states which are resonant with the extended states of the GaAs VB.[13,15,16] It has been suggested[5] that the strong, composition-dependent bowing and reduction (increase) in E_g ($\Delta_{\rm SO}$) with increasing x can be understood in terms of a valence band-anticrossing (VBAC) interaction. In the VBAC model localised states associated with substitutional Bi atoms interact strongly with the extended states of the GaAs host matrix VB maximum. This results in an upward shift in energy of the alloy VB edge with increasing x, leading to the observed strong, composition-dependent bowing of E_g and $\Delta_{\rm SO}$.[5,15]

We have previously demonstrated[15] the validity of the VBAC model in $GaBi_xAs_{1-x}$ using an atomistic tight-binding approach, which we have applied successfully to the study of the electronic,[3,17] optical[18] and spin[19] properties of $GaBi_xAs_{1-x}$ alloys. By using detailed tight-binding supercell calculations we have confirmed explicitly that the strong composition-dependent bowing of E_g and $\Delta_{\rm SO}$ with increasing x can be understood in terms of a VBAC interaction. Based on this approach we have derived a 12-band $\mathbf{k}\cdot\mathbf{p}$ Hamiltonian for (In)$GaBi_xAs_{1-x}$ alloys.[15,20] While this model ignores more detailed features of the band structure due, e.g., to the effects of alloy disorder, overall it provides a reli-

able description of the main features of the band structure in the vicinity of the band edges, and is in excellent agreement with a range of experimental measurements of E_g and Δ_{SO} in both GaAs-[15] and InP-based[20] dilute bismide alloys.

Here, we use photovoltage (PV) spectroscopy, in conjunction with the 12-band model, to determine the band offsets in strained $GaBi_xAs_{1-x}$ QW structures. The use of polarisation-resolved PV measurements allows us to explicitly identify transitions involving light- and heavy-holes by separately measuring the TM- and TE-polarised PV spectra in a series of $GaBi_xAs_{1-x}$/(Al)GaAs QW laser structures. Using this information we are then able to probe the band structure of these dilute bismide QW structures using theoretical calculations based on the 12-band $\mathbf{k}\cdot\mathbf{p}$ model and directly determine the band offsets in a series of $GaBi_xAs_{1-x}$/(Al)GaAs single and triple QW (SQW and TQW) laser structures. Through a systematic fit to the results of PV measurements and atomistic supercell calculations, we directly analyse the band offsets in these QW structures and constrain the Bi-related parameters of the 12-band model. By following this approach we (i) demonstrate directly for the first time that the band offsets at $GaBi_xAs_{1-x}$/GaAs heterointerfaces are of type-I close to $x = 2\%$, and (ii) show that the 12-band model is promising for application to the calculation of the electronic and optical properties of emerging $GaBi_xAs_{1-x}$ -based optoelectronic devices. Despite the fact that the 12-band model does not explicitly treat the effects of compositional inhomogeneity and short-range alloy disorder on the $GaBi_xAs_{1-x}$ band structure, we show that our theoretical analysis provides a constrained $\mathbf{k}\cdot\mathbf{p}$ parameter set which accurately describes the electronic properties of real dilute bismide QW laser structures. As such, the constrained theoretical model developed in this paper can be applied to investigate the electronic and optical properties of real $GaBi_xAs_{1-x}$ QW lasers. Such investigations are beyond the scope of the present paper, and will be presented elsewhere.[21]

The remainder of this paper is organised as follows. In Section II we outline the growth and characterisation of the QW laser structures. This is followed in Section III by a brief discussion of polarisation-resolved PV spectroscopy, including details of the experimental setup, measurement procedure and data analysis. In Section IV we outline first in Section IV A the 12-band $\mathbf{k}\cdot\mathbf{p}$ Hamiltonian we use to calculate the QW band structure, before presenting in Section IV B the general theory for calculating the band offsets at $GaBi_xAs_{1-x}$/(Al)GaAs heterointerfaces, including the effects of pseudomorphic strain. Sections V A and V B then focus on the comparison between theory and experiment for the QW structures under investigation. Having parametrised the 12-band model in response to the experimental data we then compare the transition energies predicted by the model to those extracted from the experimental data for additional SQW and TQW structures in Section V C. Finally, in Section VI we conclude.

II. SAMPLE GROWTH AND CHARACTERISATION

The structural details of the QW laser structures investigated are described in Table I. The samples were grown by metal-organic vapor phase epitaxy in an AIX 200-GFR reactor system, at a reactor pressure of 50 mbar and using Pd-purified H_2 as the carrier gas. Tertiarybutylarsine (TBAs), trimethylbismuth (TMBi) and triethylgallium (TEGa) were chosen as precursors, since they decompose sufficiently at the low temperatures of 400 – 425°C required for $GaBi_xAs_{1-x}$ growth.[22] In addition, trimethylaluminum (TMAl) and diethyltellurium (DETe) were used for the deposition of the undoped and doped (Al)GaAs layers, as well as diethylzinc (DEZn) for the growth of the highly p-doped GaAs:Zn contact layer.

A GaAs:Te buffer was grown on an exact GaAs:Si (001) substrate at 625°C followed by a 1.2 – 1.4 μm AlGaAs:Te cladding layer (containing 40 – 45% Al) and the lower (Al)GaAs barrier. Following this, the temperature was lowered during a TBAs stabilised growth interruption for the QW deposition (apart from the GaAs QW of sample 1, which was grown at 625°C). The $GaBi_xAs_{1-x}$ QWs of samples 3 and 4 were grown in a pulsed mode at 400°C as described in Ref. 23, whereas the QW of sample 2 was grown under continuous precursor supply at 425°C.[24] After the QW growth the temperature was again raised to 625°C at a TBAs stabilised growth interruption in order to deposit (i) the upper (Al)GaAs barrier, (ii) a 1.2

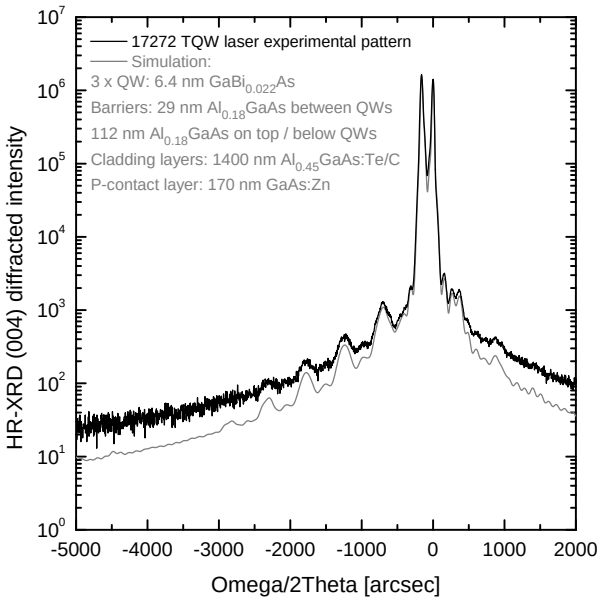


FIG. 1: Black (Grey) solid line: measured (simulated) high-resolution x-ray diffraction pattern about the GaAs (004) reflection, for sample 4 of Table I.

– 1.4 μm AlGaAs:C cladding layer (again containing 40 – 45% Al), and (iii) a 170nm GaAs:Zn p-contact layer. The C-doping in the cladding layer was achieved by a reduced V/III ratio.

To determine layer widths and compositions, high-resolution x-ray diffraction (HR-XRD) $\omega - 2\theta$ scans around the GaAs (004) reflection were performed in combination with dynamical modelling. As an example, the measured and simulated HR-XRD patterns for sample 4 are shown in Fig. 1, where we note good agreement between the measured and simulated diffraction patterns. Since the signal of a $GaBi_xAs_{1-x}$ SQW layer is very weak in HR-XRD, test structures for samples 2 and 3 containing 5 QWs each were grown in order to analyse the samples. The results of these measurements are summarised in Table I, where the listed uncertainties in the structural parameters were obtained as the extrema of the values which were found to produce reasonable agreement between the measured and simulated HR-XRD patterns. For the PV measurements broad area laser structures were fabricated, as described in Ref. 23.

III. POLARISATION-RESOLVED PHOTOVOLTAGE MEASUREMENTS

Polarisation-resolved photovoltage spectroscopy is a technique which has been used to probe the energy and character of interband optical transitions in edge-emitting quantum well and dot laser structures.[25–27] Typically, TE-polarised excitation, where the light incident on the laser end facet is polarised parallel to the QW epitaxial layer, results in interaction between the applied optical field, the s-like CB states and p-like VB states having both light- and heavy-hole (LH and HH) character. When the light incident on the laser end facet is TM-polarised, and the electric field vector of the light is perpendicular to the QW epitaxial layer, the applied optical field can interact with CB states and VB states with LH character only.

The orthogonal nature of the p-like states at the VB maximum in tetrahedrally bonded semiconductor materials allows one to independently probe CB to LH and CB to HH transitions in QW structures in order to gain detailed insight into the band structure.[28] Using this technique one can accurately measure the character and energies of (i) the fundamental transitions involving the lowest energy electron states in the CB and the highest energy LH and HH states, (ii) the energy splitting between the highest energy LH and HH states, which is not in general possible using non-polarisation-resolved measurements,[29] (iii) the degree of broadening of transitions at the band edge, as well as (iv) the barrier band gap energy. In some samples it is also possible to resolve features related to transitions between excited bound states, as well as between bound states and the continuum states of the barrier material. Previous work has shown that polarisation-resolved PV spectroscopy, when used in conjunction with $\mathbf{k}\cdot\mathbf{p}$ modelling, can be highly successful at elucidating the band structure in edge-emitting laser structures.[27,30]

In the experiment, light from a broadband tungsten source is focused onto the input slit of a grating monochromator. A narrow range of photon energies is selected by the monochromator before being polarised, chopped (typically at a frequency $\sim$ 1 kHz) and passed through an order-sorting filter. This spectrally resolved light is then focused onto the facet of the laser device using a microscope objective. This incident light generates electron-hole pairs which are swept out of the active region by the built-in field, creating a photocurrent. We measure the voltage induced by this photocurrent using phase sensitive techniques. We sweep through the desired range of excitation energies and collect a PV spectrum at each possible orthogonal combination of the sample and polariser, following the procedure described in Ref. 28. The PV spectra measured in this manner are then corrected in order to account for the wavelength and polarisation dependence of the experimental setup, so that the measured spectra represent the true polarisation-dependent carrier generation and extraction rates in the laser structure.

Transition energies for the observed features in each of the TE- and TM-polarised spectra are extracted by examining the first derivative with respect to energy of the product of the measured PV and the photon energy. We systematically assign transition energies using the peaks in these first derivatives, which correspond to the points of inflection located at the local maxima of the optical absorption edges. This method for determining the transition energies has been shown[29] to be in good agreement with those determined using photo-modulated reflectance, a differential technique which is highly sensitive to critical points in the band structure.[31,32]

Due to the symmetry present in an (001)-grown QW the TE-polarised optical transitions involve both LH and HH states, while the TM-polarised transitions involve LH states only. Therefore, in order to accurately determine the energy splitting between the highest energy LH and HH states ($lh1$ and $hh1$) in the QW, we correct the measured TE-polarised PV spectra in order to remove the LH contributions and obtain the PV generated by carriers in HH states only. For LH states in an ideal QW the TM-polarised optical transition strength is four times that associated with TE-polarised transitions.[33] Assuming that this relationship holds in the QW laser devices studied here, we correct the measured TE-polarised PV spectra at a given photon energy by subtracting one-quarter of the TM-polarised PV measured at that energy. Since the LH-related transitions occur at higher energies than those related to HH states in the compressively strained QWs studied here, this correction has the effect of decreasing the magnitude of the TE-polarised PV signal as the photon energy increases above the LH band edge. Correcting the TE-polarised PV spectra in this manner leads to an increase in the measured $hh1$–$lh1$ splitting

TABLE I: Structural parameters for the $GaBi_xAs_{1-x}$/(Al)GaAs quantum well (QW) laser structures investigated, including nominal QW widths and QW material compositions, as well as the expected growth uncertainties in these quantities. The (Al)GaAs barrier compositions were determined directly by fitting to the band gaps obtained from the photovoltage measurements (as described in Section V). The QWs in sample 4 are separated by barriers of width 29 nm. The values in brackets are the best fit values used in the theoretical calculations of Section V.

Sample no.	Number of QWs	QW width (nm)	QW Bi composition, x (%)	Barrier Al composition (%)
1	1	8.0 ± 0.5 (8.0)	0.0 ± 0.0 (0.0)	13.6
2	1	11.0 ± 0.5 (11.0)	1.7 ± 0.2 (1.7)	14.2
3	1	6.4 ± 0.5 (6.9)	2.2 ± 0.2 (2.1)	7.4
4	3	6.4 ± 0.5 (6.2)	2.2 ± 0.2 (2.5)	13.7
5	1	6.4 ± 0.5 (6.9)	2.2 ± 0.2 (2.1)	14.4
6	1	6.4 ± 0.5 (6.9)	2.2 ± 0.2 (1.8)	0.0

compared to that obtained using the uncorrected spectra. This correction to the measured TE-polarised PV spectra becomes an important consideration primarily due to the large spectral linewidth of the LH-related PV features in $GaBi_xAs_{1-x}$, the magnitude of which exceeds the measured $hh1$–$lh1$ splitting in all of the laser structures studied. The corrected TE-polarised spectra lead to an increase of up to 4 meV in the $hh1$–$lh1$ splitting for the laser structures studied here, which represents up to 25% of the measured $hh1$–$lh1$ splitting. As such, this correction becomes an important consideration when comparing the results of the theoretical calculations to the measured transition energies, and we note that the effect of this correction becomes more pronounced in structures having small $hh1$–$lh1$ splitting and/or spectrally broad band edge PV features.

IV. THEORETICAL MODEL

In this section we outline the theoretical model used to calculate the electronic structure of the QW laser structures. For the Bi-free QW (sample 1) we use the 8-band $\mathbf{k}\cdot\mathbf{p}$ model of Ref. 34 and for the Bi-containing QWs (samples 2 – 6) we use a 12-band $\mathbf{k}\cdot\mathbf{p}$ Hamiltonian that we have recently presented for dilute bismide alloys.[15,20] We begin by outlining the 12-band model in Section IV A, and then provide a general procedure for calculating the strained $GaBi_xAs_{1-x}$/(Al)GaAs QW band offsets in Section IV B.

A. 12-band $\mathbf{k}\cdot\mathbf{p}$ Hamiltonian

In order to calculate the QW transition energies in the Bi-containing samples we use a 12-band $\mathbf{k}\cdot\mathbf{p}$ Hamiltonian that we have recently derived for $GaBi_xAs_{1-x}$.[15] The 12-band model includes the extended, spin-degenerate conduction, light-hole, heavy-hole and spin-split-off (SO) bands of the GaAs host matrix, as well as the VBAC interaction between the host matrix LH and HH states and localised, Bi-related states which are resonant with the host matrix VB. This 12-band Hamiltonian has been derived on the basis of detailed tight-binding supercell calculations and has been shown to be in excellent agreement with tight-binding calculations of ordered $GaBi_xAs_{1-x}$ supercell band structures, as well as with spectroscopic measurements of the variation of the band gap and spin-orbit-splitting energies with Bi composition in $GaBi_xAs_{1-x}$/GaAs and $In_{0.53}Ga_{0.47}Bi_xAs_{1-x}$/InP materials.[15,20]

We consider pseudomorphically strained $GaBi_xAs_{1-x}$ QW structures grown along the (001) direction. At the centre of the QW Brillouin zone, where $k_x = k_y = 0$, the 12-band Hamiltonian block-diagonalises into two identical 6×6 sub-matrices given by[15]

$$H = \begin{pmatrix} E_{\rm CB} & 0 & \sqrt{2}U & -U & 0 & 0 \\ & E_{\rm HH} & 0 & 0 & V_{\rm Bi} & 0 \\ & & E_{\rm LH} & Q & 0 & V_{\rm Bi} \\ & & & E_{\rm SO} & 0 & 0 \\ & & & & E_{\rm Bi}^{\rm HH} & 0 \\ & & & & & E_{\rm Bi}^{\rm LH} \end{pmatrix}, \qquad (1)$$

where we have neglected to show the below-diagonal matrix elements since the Hamiltonian is a Hermitian matrix – the below-diagonals can be obtained from the above-diagonals by complex conjugation. The matrix elements of Eq. (1) are given at the QW Brillouin zone centre by

$$E_{\rm CB} = E_g - \alpha x + \delta E_{\rm CB}^{\rm hy} + \frac{\hbar^2}{2m_0} s_c k_z^2 \,, \quad (2)$$

$$E_{\rm HH} = \kappa x + \delta E_{\rm VB}^{\rm hy} - \delta E_{\rm VB}^{\rm ax} - \frac{\hbar^2}{2m_0} (\gamma_1 - 2\gamma_2) k_z^2 \,, \quad (3)$$

$$E_{\rm LH} = \kappa x + \delta E_{\rm VB}^{\rm hy} + \delta E_{\rm VB}^{\rm ax} - \frac{\hbar^2}{2m_0} (\gamma_1 + 2\gamma_2) k_z^2 \,, \quad (4)$$

$$E_{\rm SO} = -\Delta_{\rm SO} - \gamma x + \delta E_{\rm VB}^{\rm hy} - \frac{\hbar^2}{2m_0} \gamma_1 k_z^2 \,, \quad (5)$$

$$Q = -\sqrt{2}\, \delta E_{\rm VB}^{\rm ax} + \sqrt{2} \frac{\hbar^2}{m_0} \gamma_2 k_z^2 \,, \quad (6)$$

$$U = \frac{P}{\sqrt{3}} k_z \,, \quad (7)$$

$$V_{\rm Bi} = \beta \sqrt{x} \,, \quad (8)$$

where $V_{\rm Bi}$ is the Bi composition-dependent interaction matrix element between the Bi-related impurity states and the extended states of the host matrix VB maximum. E_g and $\Delta_{\rm SO}$ are, respectively, the band gap and spin-orbit-splitting energy of the (Al)GaAs host matrix, and the zero of energy has been taken at the GaAs VB maximum. The Bi composition-dependent terms depending upon α, κ and γ describe, respectively, the virtual crystal contributions to the Bi-induced changes to the CB, LH/HH and SO band edge energies.[15] The terms corresponding to the hydrostatic ($\delta E_{\rm CB}^{\rm hy}$, $\delta E_{\rm VB}^{\rm hy}$) and axial ($\delta E_{\rm VB}^{\rm ax}$) strain-induced shifts to the band edge energies will be defined in Section IV B. The definitions of the parameters s_c, γ_1, γ_2 and P, which are related to the GaAs host matrix, can be found in Refs. 34 and 35.

In Eq. (1), $E_{\rm Bi}^{\rm LH}$ and $E_{\rm Bi}^{\rm HH}$ are, respectively, the energies of the LH- and HH-like Bi-related impurity states, which are degenerate in unstrained, ordered $GaBi_xAs_{1-x}$.[3,15] However, this degeneracy is lifted in the QWs considered here since the incorporation of Bi increases the $GaBi_xAs_{1-x}$ lattice constant above that of GaAs, so that the QWs are grown in a state of pseudomorphic compressive strain. The procedure for calculating these impurity state energies in the presence of pseudomorphic strain will be outlined in Section IV B.

The Hamiltonian of Eq. (1) is quantised along the growth (z) direction by making the replacement $k_z \rightarrow -i\frac{\rm d}{{\rm d}z}$ and symmetrising the resulting differential operators with respect to the position-dependent material parameters in order to conserve the flow of probability current density across the QW-barrier interfaces. We then calculate the QW electronic structure in the envelope function approximation, using a numerically efficienct semi-analytical plane wave expansion method.[36,37] All calculations were performed at room temperature and the plane wave basis sets were chosen for each QW structure so that the calculated bound state energies in the QW had converged to within 0.1 meV. The numerical calculations also take account of the built-in field across the QWs, which is included explicitly in the band structure calculations and which produces a red-shift of the QW band gap due to the quantum-confined Stark effect.[33] The calculated transition energies for bound-to-bound transitions additionally include a red-shift corresponding to the exciton binding energy, calculated independently for each transition using a fractional dimensional approach based on that of Ref. 38, which we have modified to take account of the VBAC-induced enhancement of the LH and HH effective masses. This approach to calculating the $GaBi_xAs_{1-x}$ QW band structure has been verified by further analysis, including in particular comparison between the calculated and measured spontaneous emission spectra over a wide temperature range for the $GaBi_xAs_{1-x}$ QW laser of Ref. 23.[21]

B. Calculation of the $GaBi_xAs_{1-x}$/(Al)GaAs QW band offsets

We describe here the procedure for calculating the $GaBi_xAs_{1-x}$/GaAs QW band offsets in the presence of pseudomorphic strain using the 12-band $\mathbf{k}\cdot\mathbf{p}$ model. The calculation is illustrated schematically in Fig. 2.

Firstly, on the left of Fig. 2 in the section labelled "Host" we begin with a GaAs host matrix, taking the zero of energy to lie at the unstrained VB maximum. Secondly, in the section labelled "Effect of Bi" we include the virtual crystal contributions to the Bi-induced band edge shifts (ignoring for now the effects of strain) for a given Bi concentration x as[15]

$$\widetilde{E}_{\rm CB}(x) = E_{\rm CB} - \alpha x \equiv E_g - \alpha x \,, \quad (9)$$

$$\widetilde{E}_{\rm LH/HH}(x) = E_{\rm LH/HH} + \kappa x \equiv \kappa x \,, \quad (10)$$

$$\widetilde{E}_{\rm SO}(x) = E_{\rm SO} - \gamma x \equiv -\Delta_{\rm SO} - \gamma x \,. \quad (11)$$

The incorporation of Bi has in addition introduced a set of degenerate resonant impurity levels at an energy $\Delta E_{\rm Bi}$ relative to the host matrix VB maximum.[3,15,16]

Thirdly, in the section labelled "Effect of strain" we calculate the strain-induced shifts to the band edge energies, due to the fact that a $GaBi_xAs_{1-x}$ QW grown on a GaAs substrate will be in a state of pseudomorphic compressive strain. Following the conventions of Krijn[39] we calculate these strain-induced shifts to the band edge energies as

$$\widetilde{E}_{\rm CB}(x,\epsilon) = \widetilde{E}_{\rm CB}(x) + \delta E_{\rm CB}^{\rm hy} \,, \quad (12)$$

$$\widetilde{E}_{\rm LH}(x,\epsilon) = \widetilde{E}_{\rm LH}(x) + \delta E_{\rm VB}^{\rm hy} + \delta E_{\rm VB}^{\rm ax} \,, \quad (13)$$

$$\widetilde{E}_{\rm HH}(x,\epsilon) = \widetilde{E}_{\rm HH}(x) + \delta E_{\rm VB}^{\rm hy} - \delta E_{\rm VB}^{\rm ax} \,, \quad (14)$$

$$\widetilde{E}_{\rm SO}(x,\epsilon) = \widetilde{E}_{\rm SO}(x) + \delta E_{\rm VB}^{\rm hy} \,, \quad (15)$$

where the energy shifts resulting from the hydrostatic and axial components of the strain are[40]

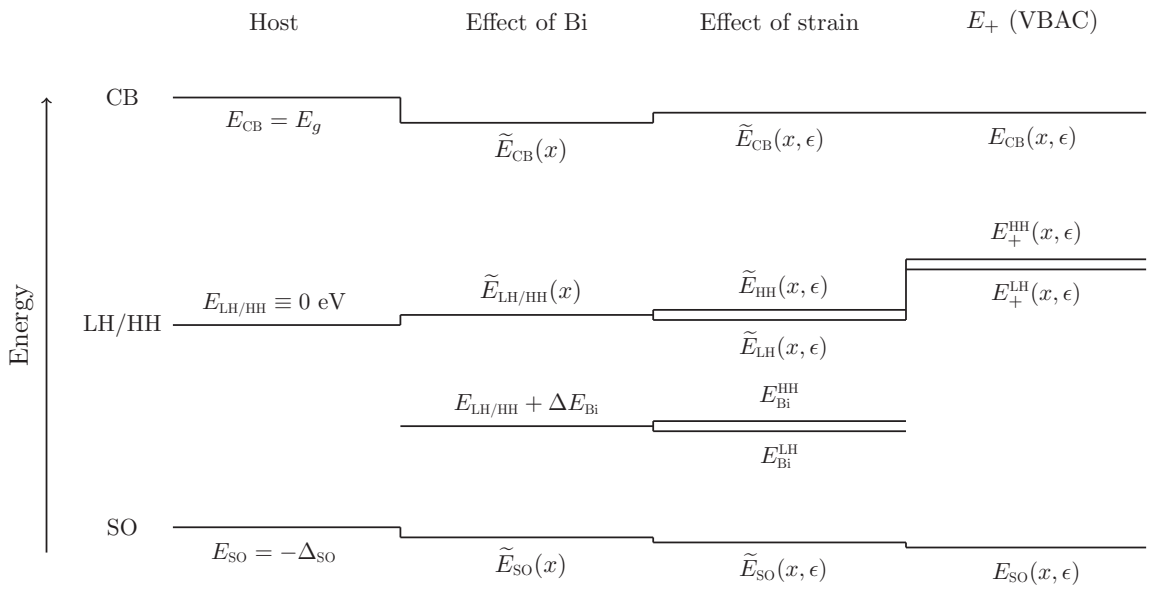


FIG. 2: Schematic illustration of the calculation of the bulk $GaBi_xAs_{1-x}$/GaAs band offsets for the lowest conduction band (CB), light- and heavy-hole (LH and HH) bands, and the spin-split-off (SO) band, using the 12-band $\mathbf{k}\cdot\mathbf{p}$ model[15] in the presence of pseudomorphic strain. The zero of energy is taken at the valence band maximum of the unstrained GaAs host matrix. The full details of each step in the calculation are outlined in Section IV B.

$$\delta E_{\rm CB}^{\rm hy} = a_c\left(\epsilon_{xx}+\epsilon_{yy}+\epsilon_{zz}\right), \quad (16)$$

$$\delta E_{\rm VB}^{\rm hy} = a_v\left(\epsilon_{xx}+\epsilon_{yy}+\epsilon_{zz}\right), \quad (17)$$

$$\delta E_{\rm VB}^{\rm ax} = -\frac{b}{2}\left(\epsilon_{xx}+\epsilon_{yy}-2\epsilon_{zz}\right), \quad (18)$$

and with the non-zero components of the strain tensor given by[39]

$$\epsilon_{xx} = \epsilon_{yy} = \frac{a({\rm GaAs})-a(x)}{a(x)}, \quad (19)$$

$$\epsilon_{zz} = -\frac{2c_{12}(x)}{c_{11}(x)}\,\epsilon_{xx}. \quad (20)$$

In order to obtain the lattice and elastic constants for $GaBi_xAs_{1-x}$ we interpolate linearly between those of the endpoint binary compounds. For example, the $GaBi_xAs_{1-x}$ lattice constant is given by

$$a(x) = (1-x)a({\rm GaAs}) + xa({\rm GaBi}). \quad (21)$$

We use the (Al)GaAs lattice and elastic constants recommended by Vurgaftman et al. in Ref. 41, and for GaBi we use those calculated ab initio by Ferhat and Zaoui.[42] Due to a lack of information in the literature regarding the hydrostatic and axial deformation potentials of GaBi, we take a_c, a_v and b for $GaBi_xAs_{1-x}$ to be equal to those of the GaAs host matrix, which is expected to be a good approximation for low Bi compositions x.

Due to the symmetry of the p-like Bi-related impurity states there is a lifting of the degeneracy of the LH- and HH-like impurity states in the presence of pseudomorphic strain. Based on the results of tight-binding calculations on large, ordered supercells we find that $E_{\rm Bi}^{\rm LH}$ and $E_{\rm Bi}^{\rm HH}$ vary with strain as

$$E_{\rm Bi}^{\rm LH} = \Delta E_{\rm Bi} + \delta E_{\rm Bi}^{\rm hy} + \delta E_{\rm Bi}^{\rm ax}, \quad (22)$$

$$E_{\rm Bi}^{\rm HH} = \Delta E_{\rm Bi} + \delta E_{\rm Bi}^{\rm hy} - \delta E_{\rm Bi}^{\rm ax}, \quad (23)$$

with $\delta E_{\rm Bi}^{\rm hy}$ and $\delta E_{\rm Bi}^{\rm ax}$ given by

$$\delta E_{\rm Bi}^{\rm hy} = a_{\rm Bi}\left(\epsilon_{xx}+\epsilon_{yy}+\epsilon_{zz}\right), \quad (24)$$

$$\delta E_{\rm Bi}^{\rm ax} = -\frac{b_{\rm Bi}}{2}\left(\epsilon_{xx}+\epsilon_{yy}-2\epsilon_{zz}\right). \quad (25)$$

We have determined the Bi-impurity state hydrostatic and axial deformation potentials $a_{\rm Bi}$ and $b_{\rm Bi}$ by using large

tight-binding supercell calculations to track the evolution of the Bi-related localised states as functions of hydrostatic and axial strain respectively. Our calculated values of $a_{\rm Bi}$ and $b_{\rm Bi}$ are given in Table II.

Finally, in the section labelled "E_+ (VBAC)" we include the VBAC interactions between the strained virtual crystal band edges and the Bi-related localised states to finally determine the band offsets. Examining the Hamiltonian of Eq. (1) we see that in bulk (with $k_z = 0$) the CB is decoupled from the Bi-related states, while the host matrix HH-band couples directly to $E_{\rm Bi}^{\rm HH}$, giving

$$E_{\rm CB}(x,\epsilon) = \widetilde{E}_{\rm CB}(x,\epsilon)\,, \tag{26}$$

$$E_{\pm}^{\rm HH}(x,\epsilon) = \frac{\widetilde{E}_{\rm HH}(x,\epsilon)+E_{\rm Bi}^{\rm HH}}{2} \pm \sqrt{\left(\frac{\widetilde{E}_{\rm HH}(x,\epsilon)-E_{\rm Bi}^{\rm HH}}{2}\right)^2+|V_{\rm Bi}|^2}\,. \tag{27}$$

Since the axial component of the pseudomorphic strain couples the host matrix LH and SO bands,[39] there exists a strain-induced second order coupling between the LH-like Bi-related localised states and the host matrix SO band. As a result, the SO band cannot be treated independently and the LH, SO and lower energy LH-like VBAC band edges in the strained alloy are obtained as the eigenvalues $E_{\pm}^{\rm LH}(x,\epsilon)$ and $E_{\rm SO}(x,\epsilon)$ of the 3×3 Hermitian matrix (cf. Eq. (1))

$$\begin{pmatrix} \widetilde{E}_{\rm LH}(x,\epsilon) & -\sqrt{2}\,\delta E_{\rm VB}^{\rm ax} & V_{\rm Bi} \\ & \widetilde{E}_{\rm SO}(x,\epsilon) & 0 \\ & & E_{\rm Bi}^{\rm LH} \end{pmatrix}, \tag{28}$$

which completes the calculation.

We note from the above discussion that the incorporation of Bi introduces seven Bi-related parameters, which are not known from the 8-band $\mathbf{k}\cdot\mathbf{p}$ Hamiltonian that describes the GaAs host matrix. All seven of these parameters are required to provide a reliable description of the strained $GaBi_xAs_{1-x}$ band structure using the 12-band model. These parameters are: (i – iii) the virtual crystal contributions to the energies of the CB minimum (α), VB maximum (κ) and SO band (γ) at the Γ-point, (iv) the energy of the Bi-related localised states relative to the unstrained GaAs VB maximum ($\Delta E_{\rm Bi}$), (v) the VBAC coupling strength (β), and (vi, vii) the hydrostatic and axial deformation potentials of the Bi-related localised states ($a_{\rm Bi}$ and $b_{\rm Bi}$). As a result of this large number of Bi-related parameters it would appear that the task of fitting a suitable set of band structure parameters to the experimentally measured transition energies is an ambiguous one. We circumvent this issue by determining five of the seven Bi-related parameters directly from detailed tight-binding supercell calculations,[15] leaving only two of the parameters (α and β, which respectively determine the dominant contributions to the CB and VB offsets) free to fit to the measured transition energies. We find that the fitted values are in both cases very close to the values derived using the tight-binding method.

We now turn our attention to the determination of the $GaBi_xAs_{1-x}$/GaAs band offsets by constraining the Bi-related parameters of the 12-band model against the transition energies measured for the QW structures listed in Table I. The values of the Bi-related parameters determined by this analysis are listed in Table II.

V. RESULTS

In this section we (i) outline the procedure employed to constrain the 12-band $\mathbf{k}\cdot\mathbf{p}$ model against the transition energies extracted from the measured polarisation-resolved PV spectra, and (ii) use theoretical calculations based on the 12-band model to extract the $GaBi_xAs_{1-x}$/GaAs band offsets through systematic comparison to the results of the experimental measurements. The band offsets are first determined experimentally for a $GaBi_xAs_{1-x}$/AlGaAs sample. In order to extract the $GaBi_xAs_{1-x}$/GaAs offset, we therefore also need as input a value for the GaAs/AlGaAs CB to VB offset ratio. We therefore firstly use an 8-band $\mathbf{k}\cdot\mathbf{p}$ model to investigate the GaAs/AlGaAs band offsets in the Bi-free sample 1. Then, beginning from this 8-band model for the GaAs/AlGaAs QW host matrix, the CB and VB offsets in the dilute bismide case are determined by comparing the transition energies calculated for sample 2 using the 12-band model of Section IV against experiment. We use the band offsets constrained in this manner to then calculate the transition energies in four additional $GaBi_xAs_{1-x}$ SQW and TQW structures, and compare the measured and calculated transition energies in each case in order to verify the theoretical model. The results of this analysis, for the laser structures listed in Table I, are summarised in Tables I – IV.

A. Sample 1

The first sample we consider is an 8 nm wide GaAs/AlGaAs SQW. Since our goal is to determine the $GaBi_xAs_{1-x}$/GaAs band offsets, we must employ assumed values of the band offsets between the GaAs QW host matrix and the AlGaAs barrier layers in order to extract the $GaBi_xAs_{1-x}$/GaAs band offsets from the theoretical calculations. We note that the band offsets extracted from the theoretical calculations will depend upon the assumed GaAs/AlGaAs CB to VB offset ratio $\Delta E_c : \Delta E_v$ in the theoretical calculations. Previous work places this ratio in the range of $60:40$ to $70:30$.[43] The $GaBi_xAs_{1-x}$/GaAs type-I band offsets extracted from the theoretical calculations will decrease as the assumed GaAs/AlGaAs CB to VB ratio increases. We choose for the calculations below a GaAs/AlGaAs CB to VB offset ratio of $\Delta E_c : \Delta E_v = 70:30$ at the upper end of the

reported range; this assumed value then provides a lower limit for the extracted value of the $GaBi_xAs_{1-x}$/GaAs type-I CB offset.

The measured TE- and TM-polarised PV spectra for sample 1, as well as the first derivative with respect to energy of the product of the energy and the measured PV, are shown in Figs. 3(a) and 4(a) respectively. A strong, polarisation-insensitive feature associated with transitions from the barrier conduction band to barrier valence band (BCB–BVB) is clearly visible at high energy in the measured TE and TM spectra. The transition energy associated with this feature is determined from the peak of the first derivative of the measured spectra to be 1.625 eV, which, according to the widely-used AlGaAs parameters of Vurgaftman et al.,[41] corresponds at room temperature to an Al composition in the barrier layers of 13.6%. This barrier Al composition, as well as that for the other laser structures considered, was verified via photoluminescence measurements. For all of the laser structure listed in Table I the energy of the emission peak corresponding to the barrier band gap was found to be in good agreement with that determined from the PV spectra.[44]

We therefore assume an Al composition in the barrier layers of 13.6%, and use the 8-band $\mathbf{k}\cdot\mathbf{p}$ Hamiltonian of Ref. 34, parametrised according to Ref. 41, to calculate the measured first electron to first HH and LH bound state transition energies ($e1$–$hh1$ and $e1$–$lh1$). Using this parameter set, as well as the aforementioned 70 : 30 CB to VB offset ratio, we calculate that the $e1$–$hh1$ and $e1$–$lh1$ transition energies are 1.449 and 1.458 eV respectively for the nominal QW width of 8 nm. Comparing these calculated transition energies with the measured values listed in Table IV, we see that this parameter set for the GaAs/AlGaAs QW host matrix is in excellent agreement with experiment. With this 70 : 30 band offset ratio the calculated CB and VB offsets are 145 and 60 meV respectively, and the calculated $e1$–$hh1$ and $e1$–$lh1$ transition energies are both within 1 meV of the measured values. In particular, the calculated $hh1$–$lh1$ splitting of 9.4 meV is in excellent agreement with the measured value of 10 meV.

By comparison, if we take the value $\Delta E_c : \Delta E_v = 61 : 39$ calculated using the model solid theory,[39,45] this gives $e1$–$hh1$ and $e1$–$lh1$ transition energies of 1.448 and 1.463 eV respectively, which exceeds the measured $hh1$–$lh1$ splitting by 5 meV (due to a reversal of the ordering of the $lh1$ and $hh2$ states). The theoretical results presented below therefore use the offset value of 70 : 30, both because it gives a slightly better fit to the GaAs/AlGaAs QW sample, and also because this will provide a lower limit for the $GaBi_xAs_{1-x}$/GaAs type-I CB offset. We now look to the first Bi-containing laser structure, sample 2, and beginning with the 8-band model we fit the Bi-related parameters α and β of Section IV to the measured transition energies. As well as fully parametrising the 12-band model of Section IV, we will also see that this analysis confirms the presence of a type-I $GaBi_xAs_{1-x}$/GaAs band offset near $x = 2\%$, a conclusion which will be further supported by our analysis of samples 3 – 6 in Section V C.

B. Sample 2

The second sample we consider is an 11 nm wide $GaBi_{0.017}As_{0.983}$/AlGaAs SQW structure. The measured TE- and TM-polarised PV spectra, as well as the first derivative with respect to energy of the product of the energy and the measured PV, are shown in Figs. 3(b) and 4(b) respectively. Based on the measured BCB–BVB transition energy of 1.633 eV we infer a barrier Al composition of 14.2% in the barrier layers, which we use as input to the theoretical calculations.

Examining the TE- and TM-polarised spectra of Fig. 3(b) we observe two features which have transition energies intermediate between those of the bound-to-bound $e1$–$hh1$ and $e1$–$lh1$ transitions and the continuum BCB–BVB transition. As a result of the measured transition energies associated with these features, as well as the fact that these two features are polarisation-insensitive, we conclude that they correspond to transitions from the first two bound electron states in the QW ($e1$ and $e2$) to the BVB. The interpretation of this pair of features as being associated with transtions from bound electron states in the QW to continuum BVB states is reinforced by noting that these features have a significantly smaller linewidth than the lower energy $e1$–$hh1$ and $e1$–$lh1$ transitions, as can clearly be seen in Fig. 4(b). This is consistent with our previous calculations of the $GaBi_xAs_{1-x}$ electronic structure,[3,17–19] which indicated that the incorporation of Bi results in strong inhomogenous broadening of states in the proximity of the VB edge in energy, suggesting that transitions involving $GaBi_xAs_{1-x}$ VB states should have increased spectral linewidths compared to transitions involving $GaBi_xAs_{1-x}$ CB states. This broadening of the band edge transitions due to the effects of Bi on the $GaBi_xAs_{1-x}$ VB structure is clearly visible in the measured PV spectra, as can be seen by comparing Fig. 4(a) to Figs. 4(b) – 4(f). This is quantified by the linewidth associated with each observed PV feature (listed in Table IV), which was obtained for each observed transition as the best-fit standard deviation of a Gaussian lineshape.

We begin by assigning all seven of the Bi-related parameters of the 12-band model of Section IV their values as determined by large supercell tight-binding calculations.[15] Since the $e1$–BVB transition does not involve the $GaBi_xAs_{1-x}$ VB, we can then use this transition to directly determine the effect of Bi incorporation on the CB offset. We vary the value of α in Eqs. (2) and (9) in order to fit to the $e1$–BVB transition energy extracted from the first derivatives of the TE- and TM- polarised PV spectra shown in Fig. 4(b), taking the GaAs/AlGaAs CB to VB offset ratio to be 70:30, as discussed above. With a calculated com-

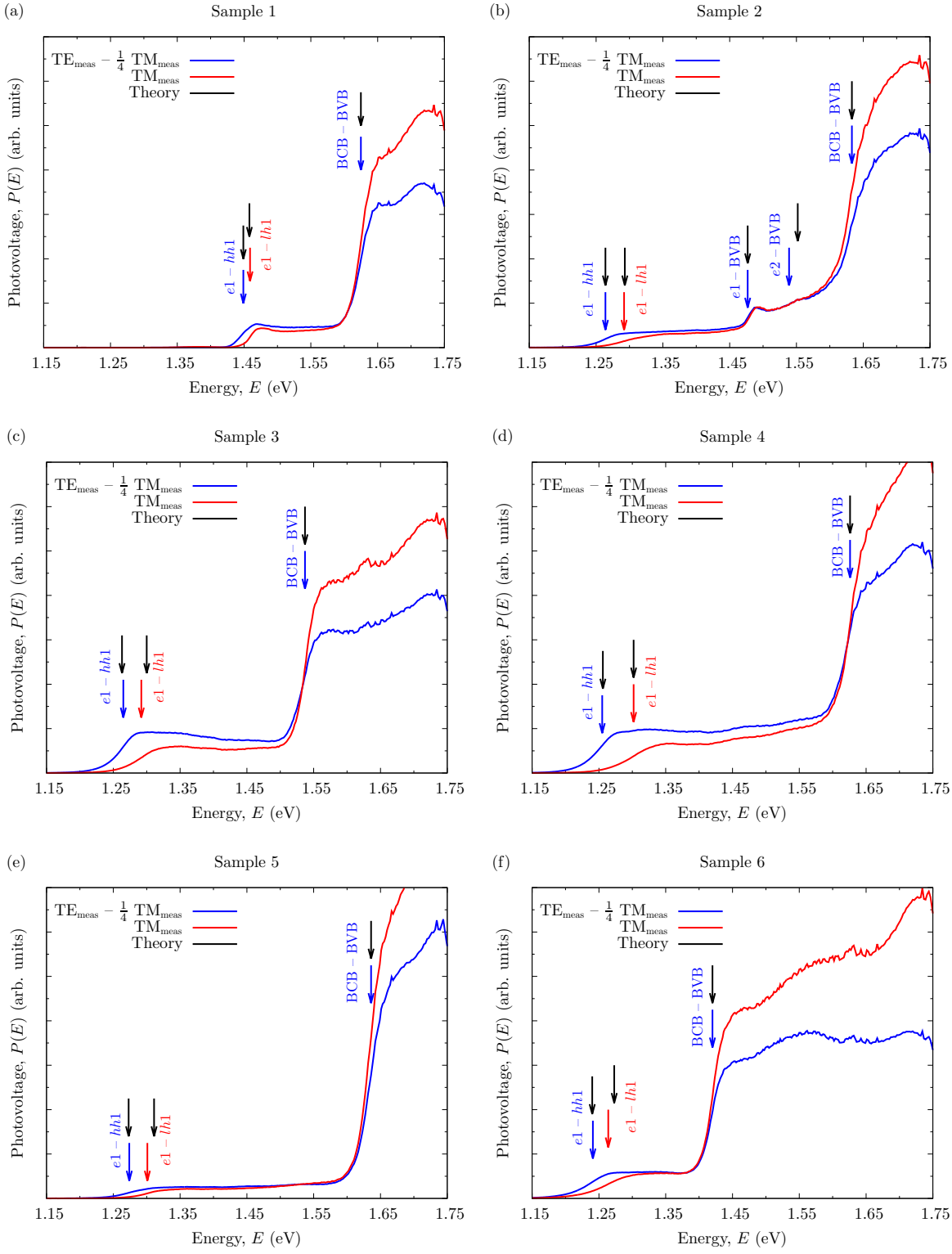


FIG. 3: Measured polarisation-resolved photovoltage spectra of samples 1 – 6 of Table I ((a) – (f), respectively). Blue lines: TE-polarised photovoltage. Red lines: TM-polarised photovoltage. Blue (Red) arrows denote transition energies extracted from TE- (TM-) polarised photovoltage spectra. Blue arrows are also used to denote the transition energies for polarisation-insensitive features, which are extracted from both the TE- and TM-polarised spectra. The extracted transition energies for each sample are listed in Table IV. The linewidth of the feature associated with each transition is also listed in Table IV. Black arrows: Transition energies calculated using either an 8-band $\mathbf{k}\cdot\mathbf{p}$ model (for sample 1) or a 12-band $\mathbf{k}\cdot\mathbf{p}$ model (for samples 2 – 6).

pressive strain of 0.2% the strain-induced shift to the $GaBi_xAs_{1-x}$ conduction band edge is +17.8 meV. Taking

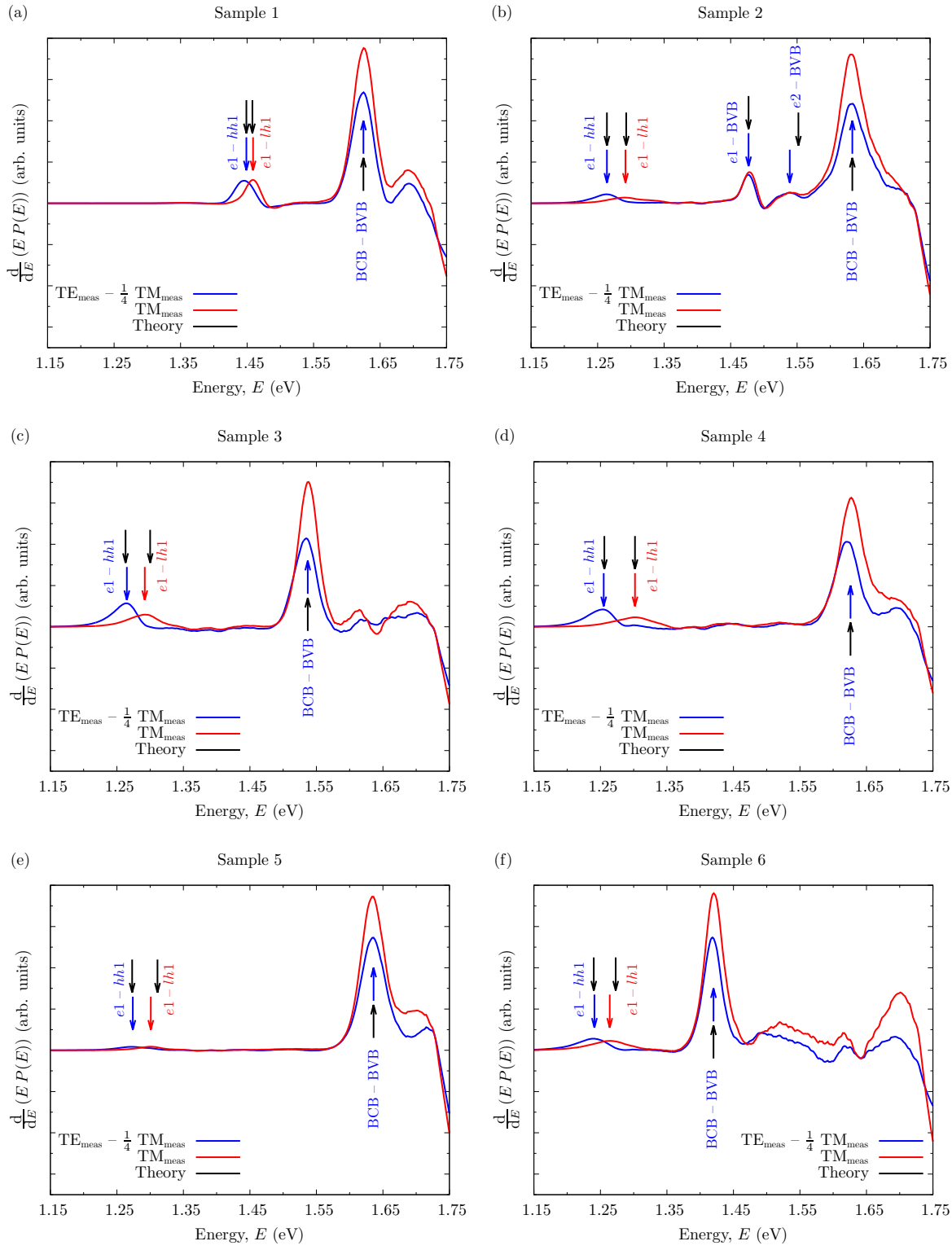


FIG. 4: First derivative with respect to energy of the product of the photon energy and the measured polarisation-resolved photovoltage for samples 1 – 6 of Table I ((a) – (f), respectively). Blue (Red) lines denote the derivatives obtained from the TE- (TM-) polarised spectra. Blue (Red) arrows denote transition energies extracted from the TE- (TM-) polarised photovoltage spectra. Blue arrows are also used to denote the transition energies for polarisation-insensitive features, which are extracted from both the TE- and TM-polarised spectra. The extracted transition energies for each sample are listed in Table IV. Black arrows: Transition energies calculated using 8- and 12-band $\mathbf{k}\cdot\mathbf{p}$ models for sample 1 and samples 2 – 6 respectively.

the QW to have a width of 11 nm and a Bi composition of 1.7% (their nominal values) we find a best fit value

TABLE II: Bi-related parameters for the 12-band $\mathbf{k}\cdot\mathbf{p}$ Hamiltonian of Section IV A. The parameters α and β were determined as the best fit to the measured transition energies in sample 2 (as described in the text), with the remaining parameters determined by detailed tight-binding (TB) supercell calculations.[15]

Parameter	TB calculation (eV)	Experimental fit (eV)
$\Delta E_{\rm Bi}$	−0.183	−0.183
α	2.82	2.63
β	1.13	1.45
γ	0.55	0.55
κ	1.01	1.01
$a_{\rm Bi}$	−1.11	−1.11
$b_{\rm Bi}$	−1.71	−1.71

TABLE III: Calculated type-I band offsets between the quantum well and barrier layers for the conduction ($\Delta E_{\rm CB}$), light-hole ($\Delta E_{\rm LH}$) and heavy-hole ($\Delta E_{\rm HH}$) bands, for the six structures of Table I. The calculated in-plane strain (ϵ_{xx}) in the quantum well layer of each structure is also shown. The band offsets were calculated following the procedure outlined in Section IV B using the constrained quantum well structural parameters shown in parentheses in Table I, as well as the constrained Bi-related parameters listed in Table II.

Sample no.	ϵ_{xx} (%)	$\Delta E_{\rm CB}$ (meV)	$\Delta E_{\rm LH}$ (meV)	$\Delta E_{\rm HH}$ (meV)
1	—	145	60	60
2	−0.20	178	187	200
3	−0.25	118	178	194
4	−0.30	188	225	245
5	−0.25	186	208	224
6	−0.21	31	129	142

of $\alpha = 2.63$ eV, which matches the measured $e1$–BVB transition energy of 1.477 eV. This value of α generates a $GaBi_{0.017}As_{0.983}/Al_{0.142}Ga_{0.858}As$ CB offset of 195.8 meV, of which, when strain is taken into account, 26.9 meV is due to the incorporation of 1.7% Bi in the QW. We note that this value of α is close to the value of 2.82 eV obtained from the tight-binding calculations.[15]

Examining the calculated CB offsets and bound state energies for samples 1 and 2, we observe that the calculated energy separation between the $e1$ bound state and the BCB in sample 2 is 156 meV, with a total bulk CB offset of 178 meV. The calculated $e1$–BCB separation for sample 2 exceeds the total bulk CB offset of 145 meV calculated for sample 1, and so we conclude that a type-I CB line-up is present at the $GaBi_xAs_{1-x}$/GaAs interface (i.e. $\alpha > 0$, and sufficiently large to overcome to strain-induced upward shift in the CB edge energy). This then supports the results of our previous calculations[3,15,17] as well as the conclusions of Ref. 46, which suggested the presence of a type-I band offset for electrons in a $GaBi_xAs_{1-x}$ LED structure on the basis of pressure-dependent measurements.

Next, we determine the LH and HH band offsets independently from the CB offset while keeping α fixed at its best fit value of 2.63 eV. The alloy VB edge energy, given by $E_+^{\rm HH}$ in Eq. (27), depends on a combination of the parameters β (cf. Eq. (8)) and κ (cf. Eq. (27)). We fit to the measured $e1$–$hh1$ transition energy by keeping κ fixed to the value obtained from the tight-binding calculations, while varying β. Other combinations of κ and β could also be chosen. However, the choice to vary only β is justified since the VBAC interactions, as opposed to virtual crystal contributions, contribute the majority of the upwards shift in the $GaBi_xAs_{1-x}$ VB edge energy at low x, so that the exact combination of β and κ chosen will only weakly affect the calculated VB offset for the range of Bi compositions under consideration.

The value of $\beta = 1.13$ eV determined from tight-binding supercell calculations underestimates the Bi-induced band gap reduction compared to the PV measurements. We find that a value of $\beta = 1.45$ eV reproduces the calculated $e1$–$hh1$ and $e1$–$lh1$ transition energies to within 1 meV of the measured values. To produce the same Bi-induced reduction in the QW band gap by varying κ while instead keeping $\beta = 1.13$ eV requires that κ be increased from 1.01 to 3.49 eV. We note that the variation of the $GaBi_xAs_{1-x}$ VB edge energy as a function of x calculated using these two combinations of β and κ agree to within 25 meV up to $x \approx 5\%$, beyond which composition contributions from the virtual crystal term κx begin to have a larger proportional impact in determining the $GaBi_xAs_{1-x}$ VB edge energy than the VBAC term $\beta\sqrt{x}$. This is more than double the largest Bi composition under consideration in the present work, thereby justifying our choice to fix κ and vary β for the fit at $x \approx 2\%$.

With 0.2% compressive strain in the QW there is: (i) a hydrostatic strain-induced shift to the GaAs host matrix VB maximum of −2.6 meV, (ii) axial strain-induced shifts to the host matrix LH and HH band edges of −6.6 and +6.6 meV respectively, (iii) a hydrostatic strain-induced shift to the Bi-localised state energies of −2.4 meV, and (iv) axial-strain induced shifts to the LH and HH-like Bi-localised state energies of −6.6 and +6.6 meV respectively. These splittings of the host matrix and Bi-impurity state LH and HH band edges combined with a value of $\beta = 1.45$ eV lead to a splitting of the bulk LH and HH band edges in the $GaBi_{0.017}As_{0.983}$ layer of the QW of 16.2 meV, which, when combined with confinement effects, produces a $hh1$–$lh1$ splitting of 28.6 meV, in excellent agreement with the experimentally measured value of 29.2 meV. The measured transition energies for this sample, as well as those calculated using the 12-band $\mathbf{k}\cdot\mathbf{p}$ model, are listed in Table IV.

Having used the observed features in the measured TE- and TM-polarised PV spectra for this sample to determine the CB and VB offsets independently by fitting to the measured transition energies, we present in Table II a complete set of constrained Bi-related parameters for the 12-band $\mathbf{k}\cdot\mathbf{p}$ model of Section IV. The band offsets in all

six QW structures, calculated using the best fit parameters of Table II, are listed in Table III. We now turn our attention to four additional SQW and TQW structures and compare the measured transition energies to those calculated using the constrained 12-band model.

C. Samples 3 – 6

With the 12-band $\mathbf{k}\cdot\mathbf{p}$ Hamiltonian having been fully parametrised by a combination of tight-binding supercell calculations and systematic fitting to the transition energies in samples 1 and 2, we now apply the 12-band model to study four additional QW structures in order to test the accuracy and transferability of the parameter set.

Samples 3 – 6 contain nominally identical 6.4 nm wide $GaBi_xAs_{1-x}$ QWs with $x = 2.2\%$. Samples 3, 5 and 6 are SQW structures, while sample 4 is a TQW structure with 29 nm wide barriers separating the $GaBi_xAs_{1-x}$ QWs. Samples 3 – 6 have AlGaAs barriers, while sample 6 has GaAs barriers. While the wide barriers in the TQW laser structure ensure that the QWs are effectively decoupled from one another, we have included sample 4 in our analysis in order to investigate as many laser structures having identical nominal Bi compositions as possible. The measured TE- and TM-polarised PV spectra, as well as the first derivative with respect to energy of the product of the energy and the measured PV, for samples 3 – 6 are shown in Figs. 3(c) – 3(f) and 4(c) – 4(f) respectively. The measured barrier band gaps for each of these samples are shown in Table IV, from which we infer barrier Al compositions of 7.4, 13.7 and 14.4% for samples 3, 4 and 5 respectively. We use these material compositions as input to the theoretical calculations for each of the samples.

Examining the first derivative of the TE-polarised PV spectrum for sample 3 (shown in Fig. 4(c)), we identify the $e1$–$hh1$ transition at an energy of 1.265 eV. Comparing this to the calculated transition energy using the parameters of Table II and taking the nominal QW composition and width we see that the calculated value of 1.263 eV for a 6.9 nm QW having $x = 2.1\%$ is in good agreement with experiment. We note, however, that the calculation overestimates the $hh1$–$lh1$ splitting by 12.3 meV compared to the measured value. By varying the QW composition and width within the range of growth uncertainties stated in Table I we obtain a best fit to the $hh1$–$lh1$ splitting of 37.1 meV (using the values shown in parentheses in Table I), which still overestimates the measured value of 27 meV by 10.1 meV.

We can gain further insight into the discrepancy between the measured and calculated $e1$–$lh1$ transition energies in sample 3 by comparison with sample 4. This is possible since both samples nominally contain the same 6.4 nm wide, $x = 2.2\%$ QWs, and so there should be very little difference between the energies of the $e1$–$lh1$ transitions between the two samples. This is expected because the calculated 6.3% difference in Al composition between the barrier layers in samples 3 and 4 mainly impacts the CB, causing an increase of 70 meV in the bulk CB offset (cf. Table III), with an accompanying reduction of only 1.5 meV in the confinement energy of the $e1$ state due to the enhanced confinement it experiences in sample 4.

For sample 4 we again vary the QW composition and width in the theoretical calculations and find good agreement between theory and experiment for the energies of the $e1$–$hh1$ and $e1$–$lh1$ transitions in an ideal TQW structure having 5.9 nm wide QWs with a Bi composition of $x = 2.5\%$. Specifically, the calculated value of 45.5 meV for the $hh1$–$lh1$ splitting agrees well with the measured value of 47 meV. The deviations from the nominal values of the QW compositions and widths required to obtain good fits to the measured transition energies confirms that material inhomogeneities in the $GaBi_xAs_{1-x}$ layers play a strong role in determining the details of the VB structure, and that compositional fluctuations within the $GaBi_xAs_{1-x}$ layers have strong effects on the material properties. The best fit QW widths and Bi compositions are given in parentheses in Table I. However, due to the strong Bi-induced inhomogenous broadening of the LH band edge, we can see in Figs. 4(e) and 4(f) that $hh1$–$lh1$ is also overestimated in samples 5 and 6, so that this splitting is overestimated for three of the four 6.4 nm wide QW structures considered. Further analysis is required to confirm the origin of this behaviour which may reflect, e.g., the effects of compositional inhomogeneities along the growth direction (so that the LH states "see" a wider QW), or intrinsic disorder effects.[18]

Nevertheless, we note that the overall agreement between the measured and calculated transition energies in Table IV is good. We additionally note that the agreement between theory and experiment is very good for the wide 11 nm SQW (sample 1), as well as the TQW structure (sample 4). This shows that the 12-band model is well-suited to analyse the electronic properties of QW and laser structures. Finally, we note that the good agreement between theory and experiment for the $e1$–$hh1$ transition in sample 6, which has a GaAs barrier and a calculated 31 meV type-I CB offset, confirms that the constrained theoretical model and extracted type-I $GaBi_xAs_{1-x}$/(Al)GaAs band offsets describe the QW electronic structure accurately.

Overall, we conclude that the 12-band $\mathbf{k}\cdot\mathbf{p}$ model of Section IV A, parametrised by fitting to the observed bound-to-bound and bound-to-continuum transitions in samples 1 and 2, is transferrable in the sense that it can be used to describe the main features of the band structure of $GaBi_xAs_{1-x}$ QW structures with varying Bi composition, QW width and QW number.

TABLE IV: Details of the measured and calculated transition energies for the quantum well samples of Table I. Transitions labelled as "Insensitive" are those for which the measured energies were equal (to within 5 meV) in the TE- and TM-polarised photovoltage spectra. The associated designations were assigned based on the transition energies obtained from the 8- and 12-band $\mathbf{k}\cdot\mathbf{p}$ calculations, as well as symmetry considerations based on the character of the measured photovoltage spectra. The structural parameters used as input to the theoretical calculations for each sample are given in parentheses in Table I. The abbreviation BCB (BVB) denotes the barrier conduction (valence) band. The linewidths of the photovoltage features associated with the observed transitions (determined in each case by fitting a Gaussian lineshape function to the corresponding features shown in Figs. 3(a)– 3(f)) are also listed, and demonstrate the strong inhomogeneous broadening associated with transitions involving the $GaBi_xAs_{1-x}$ valence band edge.

Sample no.	Polarisation	Designation	Energy, meas. (eV)	Energy, calc. (eV)	Linewidth (meV)
1	TE	$e1$–$hh1$	1.449	1.449	16
1	TM	$e1$–$lh1$	1.459	1.458	12
1	Insensitive	BCB–BVB	1.625	1.625	—
2	TE	$e1$–$hh1$	1.264	1.264	29
2	TM	$e1$–$lh1$	1.292	1.293	48
2	Insensitive	$e1$–BVB	1.477	1.477	11
2	Insensitive	$e2$–BVB	1.539	1.552	—
2	Insensitive	BCB–BVB	1.633	1.633	—
3	TE	$e1$–$hh1$	1.265	1.263	37
3	TM	$e1$–$lh1$	1.292	1.300	36
3	Insensitive	BCB–BVB	1.537	1.537	—
4	TE	$e1$–$hh1$	1.255	1.256	33
4	TM	$e1$–$lh1$	1.302	1.302	42
4	Insensitive	BCB–BVB	1.626	1.626	—
5	TE	$e1$–$hh1$	1.274	1.273	41
5	TM	$e1$–$lh1$	1.301	1.311	32
5	Insensitive	BCB–BVB	1.636	1.636	—
6	TE	$e1$–$hh1$	1.241	1.240	38
6	TM	$e1$–$lh1$	1.264	1.273	45
6	Insensitive	BCB–BVB	1.420	1.420	—

VI. CONCLUSIONS

Using a combination of experimental measurements and theoretical calculations we have directly determined the presence of type-I band offsets in a series of $GaBi_xAs_{1-x}$/(Al)GaAs quantum well structures. The use of polarisation-resolved photovoltage spectroscopy has enabled us to probe transitions related separately to light- and heavy-holes in the laser structures studied, and hence the band structure of the quantum wells. By using a 12-band $\mathbf{k}\cdot\mathbf{p}$ Hamiltonian for $GaBi_xAs_{1-x}$, which we have previously derived from detailed tight-binding supercell calculations, we have (i) identified the key contributions to the conduction and valence band offsets in $GaBi_xAs_{1-x}$, and (ii) develop the theory of the band offsets in dilute bismide quantum well structures at arbitrary Bi composition x.

Via a systematic fitting procedure involving tight-binding supercell calculations and polarisation-resolved photovoltage measurements we have constrained the 12-band $\mathbf{k}\cdot\mathbf{p}$ model for $GaBi_xAs_{1-x}$/(Al)GaAs in such a way that the calculated transition energies are in good agreement with experiment for a number of different quantum well structures. This combined experimental and theoretical approach confirms the presence of a type-I band offset at the $GaBi_xAs_{1-x}$/GaAs heterointerface, in agreement with our previous calculations for bulk $GaBi_xAs_{1-x}$ as well as with pressure-dependent measurements which have been performed on a $GaBi_xAs_{1-x}$-based LED structure.[46] Furthermore, by applying the 12-band $\mathbf{k}\cdot\mathbf{p}$ model to calculate the band structure of additional quantum well structures we have shown that it is capable of describing the main features of the band structure in $GaBi_xAs_{1-x}$/(Al)GaAs laser structures with varying Bi composition, as well as with varying quantum well width and number.

The experimental and theoretical work we have presented represents the first direct investigation of the band offsets in dilute bismide alloys, and the first detailed analysis of the electronic properties of dilute bismide semiconductor laser structures. In addition, our analysis also highlights that the observed strong broadening of the band edge absorption features in $GaBi_xAs_{1-x}$ alloys is primarily due to Bi-induced inhomogeneous broadening of the valence band edge states, with only relatively small spectral broadening of the conduction band edge states, in agreement with previous theoretical analyses we have undertaken.[17,18]

The parametrisation of an appropriate $\mathbf{k}\cdot\mathbf{p}$ Hamiltonian for dilute bismide alloys in a manner that is constrained by both theory and experiment opens up the possibility of using the model to investigate the elec-

tronic and optical properties of dilute bismide-based nanostructures,[21] a key requirement in order to theoretically evaluate the promise of this emerging material system for optoelectronic device applications.

Acknowledgements

This work was supported by the European Union Seventh Framework Programme (BIANCHO; project no. FP7-257974). CB acknowledges support from the Irish Research Council (EMBARK Postgraduate Scholarship no. RS/2010/2766). CB, PH and EOR acknowledge additional support from Science Foundation Ireland (project no. 10/IN.1/I299).

* Electronic address: c.broderick@umail.ucc.ie
† Electronic address: eoin.oreilly@tyndall.ie

[1] H. Li and Z. M. Wang, eds., *Bismuth-Containing Compounds (Springer Series in Materials Science, Vol. 186)* (Springer, 2013).
[2] E. P. O'Reilly, A. Lindsay, P. J. Klar, A. Polimeni, and M. Capizzi, Semicond. Sci. Technol. **24**, 033001 (2009).
[3] M. Usman, C. A. Broderick, A. Lindsay, and E. P. O'Reilly, Phys. Rev. B **84**, 245202 (2011).
[4] S. Tixier, S. E. Webster, E. C. Young, T. Tiedje, S. Francoeur, A. Mascarenhas, P. Wei, and F. Schiettekatte, Appl. Phys. Lett. **86**, 112113 (2005).
[5] K. Alberi, J. Wu, W. Walukiewicz, K. M. Yu, O. D. Dubon, S. P. Watkinsa, C. X. Wang, X. Liu, Y.-J. Cho, and J. Furdyna, Phys. Rev. B **75**, 045203 (2007).
[6] B. Fluegel, S. Francoeur, A. Mascarenhas, S. Tixier, E. C. Young, and T. Tiedje, Phys. Rev. Lett. **97**, 067205 (2006).
[7] Z. Batool, K. Hild, T. J. C. Hosea, X. Lu, T. Tiedje, and S. J. Sweeney, J. Appl. Phys. **111**, 113108 (2012).
[8] S. J. Sweeney, Z. Batool, K. Hild, S. R. Jin, and T. J. C. Hosea, in Proceedings of the 13$^{\text{th}}$ International Conference on Transparent Optical Networks (ICTON), Stockholm (2011).
[9] C. A. Broderick, M. Usman, S. J. Sweeney, and E. P. O'Reilly, Semicond. Sci. Technol. **27**, 094011 (2012).
[10] S. J. Sweeney, A. R. Adams, M. Silver, E. P. O'Reilly, J. R. Watling, A. B. Walker, and P. J. A. Thijs, IEEE Photon. Tech. Lett. **10**, 1076 (1998).
[11] S. J. Sweeney, A. R. Adams, M. Silver, E. P. O'Reilly, J. R. Watling, A. B. Walker, and P. J. A. Thijs, Phys. Stat. Sol. B **211**, 525 (1999).
[12] A. Janotti, S.-H. Wei, and S. B. Zhang, Phys. Rev. B **65**, 115203 (2002).
[13] Y. Zhang, A. Mascarenhas, and L.-W. Wang, Phys. Rev. B **71**, 155201 (2005).
[14] H.-X. Deng, J. Li, S.-S. Li, H. Peng, J.-B. Xia, L.-W. Wang, and S.-H. Wei, Phys. Rev. B **82**, 193204 (2010).
[15] C. A. Broderick, M. Usman, and E. P. O'Reilly, Semicond. Sci. Technol. **28**, 125025 (2013).
[16] R. S. Joshya, A. J. Ptak, R. France, A. Mascarenhas, and R. N. Kini, Phys. Rev. B **90**, 165203 (2014).
[17] M. Usman, C. A. Broderick, Z. Batool, K. Hild, T. J. C. Hosea, S. J. Sweeney, and E. P. O'Reilly, Phys. Rev. B **87**, 115104 (2013).
[18] M. Usman and E. P. O'Reilly, Appl. Phys. Lett. **104**, 071103 (2014).
[19] C. A. Broderick, S. Mazzucato, H. Carrère, T. Amand, H. Makhloufi, A. Arnoult, C. Fontaine, O. Donmez, A. Erol, M. Usman, et al., Phys. Rev. B **90**, 195301 (2014).
[20] C. A. Broderick, M. Usman, and E. P. O'Reilly, Phys. Stat. Sol. B **250**, 773 (2013).
[21] C. A. Broderick, P. E. Harnedy, and E. P. O'Reilly, submitted (2015).
[22] P. Ludewig, N. Knaub, W. Stolz, and K. Volz, J. Cryst. Growth **370**, 186 (2013).
[23] P. Ludewig, N. Knaub, N. Hossain, S. Reinhard, I. P. Marko, S. R. Jin, K. Hild, S. Chatterjee, W. Stolz, S. J. Sweeney, et al., Appl. Phys. Lett. **102**, 242115 (2013).
[24] P. Ludewig, Z. L. Bushell, L. Natterman, N. Knaub, W. Stolz, and K. Volz, J. Cryst. Growth **396**, 95 (2014).
[25] P. C. Mogensen, S. A. Hall, P. M. Smowton, U. Bangert, P. Blood, and P. Dawson, IEEE J. Quant. Electron. **34**, 1652 (1998).
[26] I. C. Sandall, P. M. Smowton, C. L. Walker, H.-Y. Liu, M. Hopkinson, and D. J. Mowbray, IEEE Photon. Tech. Lett. **18**, 965 (2006).
[27] M. T. Crowley, S. C. Heck, S. B. Healy, S. Osborne, D. P. Williams, S. Schulz, and E. P. O'Reilly, Semicond. Sci. Technol. **28**, 15012 (2013).
[28] M. Mexis, P. Blood, and P. M. Smowton, Semicond. Sci. Technol. **22**, 1298 (2007).
[29] K. Ryczko, G. Sek, P. Sitarek, A. Mika, J. Misiewicz, F. Langer, S. Höfling, A. Forchel, and M. Kamp, J. Appl. Phys. **113**, 233508 (2013).
[30] S. C. Heck, S. Osborne, S. B. Healy, E. P. O'Reilly, F. Lelarge, F. Poingt, O. L. Gouezigou, and A. Accard, IEEE J. Quant. Electron. **45**, 1508 (2009).
[31] J. Misiewicz, P. Sitarek, and G. Sek, Opto-Electron. Rev. **8**, 1 (2000).
[32] O. J. Glembocki and B. V. Shanabrook, Semicond. Semimet. **36**, 221 (1992).
[33] S. L. Chuang, *Physics of Photonic Devices* (Wiley, 2009).
[34] A. T. Meney, B. Gonul, and E. P. O'Reilly, Phys. Rev. B **50**, 10893 (1994).
[35] S. Tomić, E. P. O'Reilly, R. Fehse, S. J. Sweeney, A. R. Adams, A. D. Andreev, S. A. Choulis, T. J. C. Hosea, and H. Riechert, IEEE J. Sel. Top. Quant. Electron. **9**, 1228 (2003).
[36] S. B. Healy and E. P. O'Reilly, IEEE J. Quant. Electron. **42**, 608 (2006).
[37] M. Ehrhardt and T. Koprucki, eds., *Multiband Effective Mass Approximations: Advanced Mathematical Models and Numerical Techniques* (Springer, 2014).
[38] H. Mathieu, P. Lefebvre, and P. Christol, Phys. Rev. B **46**, 4092 (1992).
[39] M. P. C. M. Krijn, Semicond. Sci. Technol. **6**, 27 (1991).

Appendix C

Spontaneous emission measurements

Theory of the electronic and optical properties of dilute bismide quantum well lasers

Christopher A. Broderick, Patrick E. Harnedy, and Eoin P. O'Reilly, *Member, IEEE*

(Invited Paper)

***Abstract*—We present a theoretical study of the gain characteristics of $GaBi_xAs_{1-x}$/(Al)GaAs dilute bismide quantum well (QW) lasers. After providing a brief overview of the current state of development of dilute bismide alloys for semiconductor laser applications, we introduce the 12-band k·p Hamiltonian we have developed for the description of the band structure of $GaBi_xAs_{1-x}$ and related alloys. Using a theoretical approach based on the 12-band model we then undertake a detailed analysis of the electronic and optical properties of a series of ideal and real $GaBi_xAs_{1-x}$/(Al)GaAs QW laser structures as a function of Bi composition x. We theoretically optimize the gain characteristics of an existing low x device by varying the Al composition in the barrier layers, which governs a trade-off between the electronic and optical confinement. The theoretical results are compared to temperature-dependent spontaneous emission measurements at low x, which reveals the presence of significant Bi-induced inhomogeneous broadening of the optical spectra. We also investigate the gain characteristics of $GaBi_xAs_{1-x}$/(Al)GaAs QW lasers at higher values of x, including a QW designed to emit at 1.55 μm. Our theoretical results elucidate the impact of Bi incorporation on the electronic and optical properties of GaAs-based QW lasers, and reveal several general trends in the gain characteristics as a function of x. Overall, our analysis confirms that dilute bismide alloys are a promising candidate material system for the development of highly efficient, uncooled GaAs-based QW lasers operating at telecomunication wavelengths.**

***Keywords*—Dilute bismide alloys, semiconductor lasers, 1.55-μm laser emission, semiconductor device modeling**

I. Introduction

THE highly mismatched semiconductor alloy (In)$GaBi_xAs_{1-x}$ has several novel electronic properties, including both a rapid reduction in band gap (E_g) and a strong increase in spin-orbit-splitting energy (Δ_{SO}) with increasing Bi composition x. This has stimulated significant interest in the use of bismuth-containing alloys for a range of applications [1], including semiconductor lasers [2], [3], [4] and photodiodes [5], [6], [7], as well as photovoltaics [8], spintronics [9], [10] and thermoelectrics [11].

A critical issue with existing 1.3 and 1.55 μm semiconductor lasers is that their threshold current and optical cavity losses tend to increase strongly with increasing temperature, due largely to a combination of two intrinsic loss mechanisms, Auger recombination [12], [13] and intervalence band absorption [14]. $GaBi_xAs_{1-x}$ alloys having Bi compositions $x \gtrsim 10\%$ have been demonstrated to have a band structure in which the spin-orbit-splitting energy is larger than the band gap ($\Delta_{SO} > E_g$), and a band gap close to 0.8 eV (1.55 μm). It has been proposed that this large spin-orbit-splitting energy could lead to the suppression of the dominant Auger recombination loss mechanism in 1.55 μm semiconductor lasers [2], finally opening the route to efficient, temperature-stable telecom lasers with significantly reduced power consumption. This possibility has led to significant interest in the development of dilute bismide semiconductor lasers. Considerable progress has been made since the first demonstration of an optically pumped dilute bismide laser by Yoshimoto *et al.* in 2010 [15], with room temperature electrically pumped $GaBi_xAs_{1-x}$ lasing first demonstrated for $x = 2.1\%$ by Volz *et al.* in 2013 [16], and since extended up to $x = 6.5\%$ by Krotkus *et al.* [17]. The challenge now is to push the Bi composition above 10 – 12% in $GaBi_xAs_{1-x}$/GaAs laser structures and/or to demonstrate a laser based on, e.g., $In_{1-y}Ga_yBi_xAs_{1-x}$ alloys grown on InP, for which the condition $\Delta_{SO} > E_g$ can be achieved at lower Bi compositions, $x \gtrsim 4\%$ [4], [18].

We begin in this paper by presenting an overview of the progress that has been achieved to date in the growth of dilute bismide materials and laser structures. In order to address the potential for further development, we then introduce a theoretical model to describe the impact that Bi has on the band structure and gain characteristics of existing devices. The theoretical model has been benchmarked against experiment, where it has already contributed to the optimisation of the current generation of devices [19], [17], and is used here to address the potential of $GaBi_xAs_{1-x}$ quantum well (QW) laser structures with higher Bi compositions. We present band structure and gain calculations for a $GaBi_xAs_{1-x}$/GaAs laser structure with high Bi composition ($x \sim 14\%$) – chosen to give peak gain close to 1550 nm and to have $\Delta_{SO} > E_g$ in order to suppress the dominant Auger recombination pathway. We show that the material and modal gain at this composition is significantly higher than that at lower x, due to the combined effects of the increased conduction band offset and strain in the QW at larger x. We describe that the photoluminescence efficiency of recently studied dilute bismide QW structures containing up to $x = 11.5\%$ was close to that obtained in the materials used to achieve lasing with $x = 6\%$ [17]. Overall, we conclude that these combined theoretical and experimental results confirm the potential of ideal dilute bismide QW structures for use as highly efficient telecom lasers.

The remainder of this paper is organized as follows. In

Manuscript received XXX, 2015; revised XXX, 2015.

The authors are with the Photonics Theory Group, Tyndall National Institute, Dyke Parade, Cork, Ireland and the Department of Physics, University College Cork, Cork, Ireland. (e-mail: c.broderick@umail.ucc.ie, eoin.oreilly@tyndall.ie.)

Section II we provide a brief overview of the progress that has been made in developing dilute bismide materials and devices for semiconductor laser applications. This is followed in Section III by an outline of our theoretical model for dilute bismide QW lasers. We then present our results in Section IV, beginning in Section IV-A by considering the competing effects of carrier and optical confinement on the performance of $GaBi_xAs_{1-x}$ QWs as a function of the composition of the (Al)GaAs barrier materials. We identify optimized laser structures at $x = 2.1\%$ and provide general guidelines for the optimum choice of barrier materials as a function of x. Next, in Section IV-B, we present a detailed analysis of the first-generation $GaBi_xAs_{1-x}$ QW laser of Ref. [16] and explicitly quantify the effects of Bi incorporation on the electronic and optical properties. This is followed by a comparison between theoretical calculations of the temperature dependent spontaneous emission spectra and the results of experimental measurements. In Section IV-C we turn our attention to $GaBi_xAs_{1-x}$ QW lasers operating at 1.55 μm and quantify the expected performance of an ideal device at high Bi composition x. Finally, we present our conclusions in Section V.

II. Development of dilute bismide materials and devices

Growth of dilute bismide alloys has primarily been achieved using molecular beam epitaxy (MBE) [20], [21] and metal-organic vapor phase epitaxy (MOVPE) [22], [23], [24]. Using both approaches it has been established that reduced growth temperatures are generally required to promote Bi incorporation in $GaBi_xAs_{1-x}$ and related alloys. Bi compositions up to $x = 7\%$ have been achieved in $GaBi_xAs_{1-x}$ using MOVPE [24], while the ability to further lower the growth temperature using MBE means that larger Bi compositions can typically be achieved. $GaBi_xAs_{1-x}$ alloys have recently been grown with Bi compositions as high as $x = 17.8\%$ using MBE [25].

The reduced growth temperatures required to incorporate Bi present significant practical difficulties for the realization of dilute bismide semiconductor lasers, since lower growth temperatures also lead to a degradation in material quality. While low-temperature optically pumped lasing was demonstrated in 2010 in an MBE-grown $GaBi_xAs_{1-x}$ bulk-like device [15], the first electrically pumped dilute bismide QW laser was demonstrated in 2013 using MOVPE growth, with a Bi composition of $x = 2.1\%$ [16]. This was followed in 2014 by the demonstration of the first electrically pumped MBE-grown $GaBi_xAs_{1-x}$ bulk-like laser [26]. Continued refinement of MOVPE growth of dilute bismide alloys has led to the development of $GaBi_xAs_{1-x}$ QW lasers with Bi compositions up to $x = 4.4\%$ [19]. The highest Bi composition, $x = 6.5\%$, achieved to date in a $GaBi_xAs_{1-x}$ QW laser was presented recently in Ref. [17], where electrically pumped lasing at a wavelength of 1060 nm was demonstrated at room temperature. This laser structure was fabricated using a hybrid approach in which the active region was grown using MBE, with the remainder of the laser structure grown using MOVPE.

Existing dilute bismide QW lasers suffer strongly from defect-related recombination leading to high threshold current densities [19], so that further work is required to develop optimized devices for practical applications. However, while no $GaBi_xAs_{1-x}$ QW lasers have yet been developed with sufficiently high Bi compositions to suppress the dominant CHSH Auger recombination mechanism, progress on dilute bismide QW lasers has been rapid and efforts to reach this important milestone are ongoing. For example, recent investigations of $GaBi_xP_yAs_{1-x-y}$ alloys have shown that incorporation of a small amount of phosphorus enhances Bi incorporation during MOVPE growth [27], but the precise mechanism by which this occurs has yet to be determined.

While the majority of research on dilute bismide alloys has centered on $GaBi_xAs_{1-x}$ materials and devices, there is also interest in alternative Bi-containing material systems. One noteable example is the growth of $In_{1-y}Ga_yBi_xAs_{1-x}$ alloys on InP [4]. Experimental measurements [28] and theoretical calculations [29] have verified that a band structure satisfying $\Delta_{SO} > E_g$ can be achieved in $In_{0.53}Ga_{0.47}Bi_xAs_{1-x}$/InP alloys for Bi compositions as low as $x = 4\%$. Such alloys have recently been grown with Bi compositions up to $x = 5.8\%$, and it has been confirmed by theory and experiment that $\Delta_{SO} > E_g$ at all temperatures [30]. Due to the fact that the $\Delta_{SO} > E_g$ band structure condition can be achieved at much lower Bi compositions in these InP-based materials as compared to $GaBi_xAs_{1-x}$ alloys, the development of InP-based semiconductor lasers could provide important proof of principle for the suppression of CHSH Auger recombination in GaAs-based dilute bismide devices. However, since $GaBi_xAs_{1-x}$ is at present the only dilute bismide alloy from which semiconductor lasers have been developed, we restrict our attention in this paper to $GaBi_xAs_{1-x}$ QW lasers.

III. Theoretical model

When a small fraction x of the As atoms in GaAs are substituted by Bi to form the $GaBi_xAs_{1-x}$ alloy, the large differences in size and electronegativity between the Bi atoms and the As atoms they replace mean that Bi acts as an isovalent impurity. Theoretical calculations have identified that the observed trends in the $GaBi_xAs_{1-x}$ electronic structure arise primarily due to the formation of Bi-related localized states in the valence band (VB) [31], [32], [33], a conclusion which has been supported by recent experimental measurements [34]. We have shown using a combined tight-binding and $\mathbf{k}\cdot\mathbf{p}$ analysis that the interaction of these localized states with the extended VB edge states of the host matrix can account successfully for the observed rapid decrease in E_g and increase in Δ_{SO} in $GaBi_xAs_{1-x}$ with increasing Bi composition x.

In order to calculate the band structure of the $GaBi_xAs_{1-x}$-based QW laser structures we have introduced a 12-band $\mathbf{k}\cdot\mathbf{p}$ Hamiltonian for $GaBi_xAs_{1-x}$ and related alloys [18], [29]. The 12-band model was derived on the basis of a tight-binding supercell model that has been successfully applied to study the electronic, optical and spin properties of $GaBi_xAs_{1-x}$ alloys [32], [40], [41], [42]. The basis set explicitly includes the extended, spin-degenerate zone-center Bloch states related to the lowest conduction band (CB), as well as the light-hole (LH), heavy-hole (HH) and spin-split-off (SO) bands of the

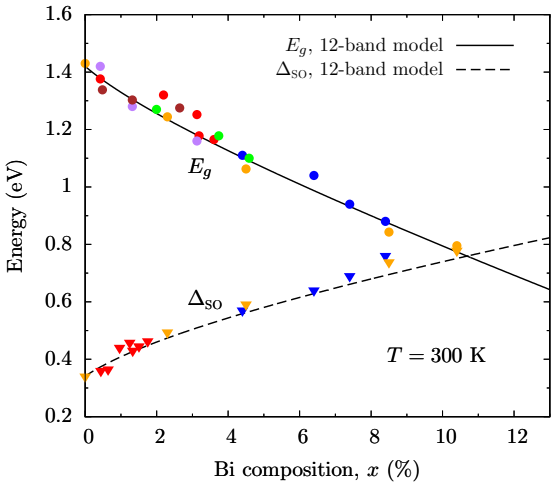


Fig. 1. Comparison between theory and experiment for the variation of the band gap (E_g) and spin-orbit-splitting energy (Δ_{SO}) as a function of Bi composition x in $GaBi_xAs_{1-x}$ at 300 K. Experimental measurements of E_g are depicted by closed circles; the data are from Refs. [35], [36], [37], [20], [38], and [39] and are shown using blue, red, green, purple, brown, and orange closed circles respectively. Experimental measurements of Δ_{SO} are depicted by closed triangles; the data are from Refs. [35], [9], and [39] and are shown using blue, red, and orange closed triangles respectively. Solid (dashed) black lines show the variation of E_g (Δ_{SO}) calculated using the 12-band **k·p** model of Ref. [18].

GaAs host matrix. To obtain a suitable description of the $GaBi_xAs_{1-x}$ band structure this set of unperturbed Bloch states for the GaAs host matrix is augmented by a set of spin-degenerate LH- and HH-like Bi-related localized states which are resonant with the host matrix VB, leading to a 12-band Hamiltonian for the $GaBi_xAs_{1-x}$ alloy in which the Bi-related localized states couple to the extended states at the GaAs VB edge through a composition-dependent VBAC interaction [18], [29]. This model is closely related to the well-established band-anticrossing model which has previously been used to describe the electronic properties of dilute nitride alloys such as GaN_xAs_{1-x} [43], [44]. Because N atoms are significantly smaller and more electronegative than As, they introduce defect states which are resonant with the GaAs CB [45], [46]; in $GaBi_xAs_{1-x}$ the large, electropositive Bi atoms introduce resonant localized defect states in a similar manner below the GaAs VB maximum. Figure 1 shows the variation of E_g (solid black line) and Δ_{SO} (dashed black line) as a function of Bi composition x at 300 K in $GaBi_xAs_{1-x}$, calculated using the 12-band model of Ref. [18]. By comparing the results of these calculations to a range of experimental data from the literature we see that the 12-band model produces a highly accurate description of the main features of the $GaBi_xAs_{1-x}$ band structure, and does so across a wide composition range.

The $GaBi_xAs_{1-x}$ band structure parameters used in our calculations were initially obtained from the theoretical analysis presented in Ref. [18], and have subsequently been refined for low Bi compositions by a systematic comparison between theory and polarization-resolved photovoltage measurements for a series of $GaBi_xAs_{1-x}$/(Al)GaAs QW samples with $x \approx 2\%$ [47]. Both the theoretical and experimental analysis show a type-I band offset at the $GaBi_xAs_{1-x}$/GaAs heterointerface, with the strained QW CB offset increasing by approximately 25 meV per % Bi. Ref. [47] also contains a theoretical analysis of the QW band offsets within the context of the 12-band model; we apply the theory of the $GaBi_xAs_{1-x}$/(Al)GaAs bulk band offsets developed therein to calculate the band offsets in the laser structures studied here. For our calculations of the electronic and optical properties of devices containing QWs with $x < 3\%$ we employ the material parameters and band offsets derived for real devices in Ref. [47], while for higher Bi compositions we use those derived in Ref. [18]. The hydrostatic and axial deformation potentials describing the effect of pseudomorphic strain on the energies of the Bi-related localized states taken from Ref. [47] for all calculations.

The numerical calculation of the QW band structure and eigenstates is based on the semi-analytical plane wave expansion method outlined in Refs. [48] and [49]. The QW band structure and eigenstates, calculated in the axial approximation [50], are then used directly to compute the laser optical properties. For the calculation of the optical spectra the interband transition matrix elements were calculated directly from the QW eigenstates using the general formalism of Szmulowicz [51], and the electron and hole populations were assumed to be individually in thermal equilibrium, with each described using a separate quasi-Fermi distribution function. Since the transition matrix elements were calculated directly from the QW eigenstates the calculated optical spectra incorporate important band structure effects, including (i) Bi-induced hybridization and localization of hole states, (ii) strain-induced VB non-parabolicity and mixing, and (iii) temperature- and carrier density-dependent spillout of carriers from the QWs. The spontaneous emission (SE) and material gain spectra were calculated following the procedure outlined in Refs. [52] and [53], with the homogeneous linewidth broadening described using a hyperbolic secant lineshape and an interband relaxation time of $\tau_{in} = 100$ fs [44], [54]. It is well established that the optical spectra of dilute bismide alloys have relatively large spectral linewidths, which are dominated by inhomogeneous broadening related to the effects of Bi clustering and alloy disorder on the electronic properties of the VB states [55], [40]. In order to take these effects into account we have included inhomogeneous broadening in our theoretical calculations by convolving the calculated optical spectra with a Gaussian lineshape (the linewidth of which we denote by σ below).

Our analysis in Ref. [47] suggests that the small offset at the CB edge should lead to very weak electron confinement in $GaBi_xAs_{1-x}$/GaAs QWs at low Bi compositions x. As such, hole-induced electrostatic confinement of electron states plays an important role in determining the electronic and optical properties of $GaBi_xAs_{1-x}$/GaAs QW lasers at low x. The electron confinement can be improved by introducing AlGaAs barriers, but at the cost of then degrading the optical confinement factor for the overall laser structure. For selected laser structures we have therefore performed self-consistent calculations of the electronic and optical properties, in which the 12-band Schrödinger equation for the laser structure is

solved self-consistently with Poisson's equation in order to determine the net carrier-induced electrostatic potential and its influence on the calculated modal gain as a function of the Al composition in the barrier layers. For the self-consistent calculations we solve Poisson's equation in reciprocal space, using the technique outlined in Ref. [48]. Unless specified otherwise, all calculations were performed at 300 K and the plane wave basis set for each laser structure was chosen to ensure that both the electron and hole quasi-Fermi levels had converged to within 0.1 meV with respect to further increases in the size of the basis set.

For the calculation of the threshold gain we assume internal cavity losses of 4 cm^{-1}, choose an unstrained $Al_{0.4}Ga_{0.6}As$ seperate confinement heterostructure (SCH), and take an overall cavity length of 1 mm for all of the devices considered [16]. The confinement factor Γ of the fundamental (TE-polarized) optical mode was calculated for each laser structure using an effective index approach [56]. By varying the thickness of the barrier layers it was found for all structures considered that Γ is maximized for 130 – 180 nm thick (Al)GaAs barriers. As such, all calculations presented below were performed for laser structures having 150 nm thick barriers between the $GaBi_xAs_{1-x}$ QW and $Al_{0.4}Ga_{0.6}As$ cladding layers.

IV. Results

The ultimate goal in the development of dilute bismide lasers is to achieve an Auger-free device with $\Delta_{SO} > E_g$. The initial $GaBi_xAs_{1-x}$ devices demonstrated had relatively low Bi composition, $x \approx 2\%$ [16], with more recent devices extending the Bi composition to $x = 6.5\%$ [17]. We first present in Section IV-A an overview of the dependence of the gain characteristics of $x = 2.1\%$ QW laser characteristics on the Al composition in the surrounding barrier (Al)GaAs layers, and use the results of our theoretical calculations to identify optimized barrier materials as a function of x. We show that Al-containing barriers are required to optimise the threshold characteristics of an $x = 2.1\%$ structure, but that GaAs barriers can provide optimum characteristics for structures with $x \gtrsim 6\%$.

Then, in Section IV-B, we explicitly investigate the impact of Bi incorporation on the device characteristics at low x by comparing the gain characteristics of the $GaBi_{0.021}As_{0.979}$/AlGaAs device of Ref. [16] with those of a GaAs/AlGaAs QW laser structure. We show that incorporating a small amount of Bi brings little benefit to the overall device characteristics. In addition, experimental measurements of the temperature-dependent SE at threshold shows that there is a strong inhomogeneous broadening of the interband transitions in the bismide-containing laser structures, which further degrades the calculated device characteristics.

Theoretical results are then presented in Section IV-C for the predicted gain characteristics of a $GaBi_{0.13}As_{0.87}$/GaAs QW laser structure, for which the peak material gain is close to 1.55 μm, and in which the band structure of the $GaBi_{0.13}As_{0.87}$ layer satisfies the $\Delta_{SO} > E_g$ band structure condition. Our calculations, which include band edge inhomogneous broadening consistent with experiment, show reduced transparency and threshold carrier densities compared to the $x = 2.1\%$ laser structures, as well as significantly enhanced differential gain, due primarily to the increased strain in the QW at higher x. We conclude therefore that it should be possible to achieve efficient 1.55 μm emission from a $GaBi_xAs_{1-x}$/GaAs QW laser structure, so long as $GaBi_xAs_{1-x}$ layers with sufficient optical quality can be grown at higher Bi compositions $x \gtrsim 10\%$.

A. Optimization of $GaBi_xAs_{1-x}$/(Al)GaAs lasers at $x = 2.1\%$

Theoretical and experimental analysis has shown that $GaBi_xAs_{1-x}$/GaAs QWs have a very small CB offset at low Bi compositions x, estimated at only 55 meV for a QW with $x = 2.1\%$ [47]. Such a low CB offset is detrimental to laser operation, leading to strong electron spillout from the QW at high temperatures and carrier densities, and is therefore a major factor limiting the material gain at low Bi compositions. Electron confinement can be improved by growing $GaBi_xAs_{1-x}$/AlGaAs QW structures, but at the cost of reduced optical confinement in a laser structure with a fixed Al composition in the cladding layers.

We therefore first investigate the optimum Al composition in the barrier layers to achieve good electronic and optical confinement in a 6.9 nm wide $GaBi_{0.021}As_{0.979}/Al_yGa_{1-y}As$ QW laser structure, and through this analysis we optimize the modal gain from the device as a function of injected carrier density, while minimizing the carrier density required to reach threshold. This $x = 2.1\%$ QW was chosen based on the $GaBi_xAs_{1-x}$ QW laser presented in Ref. [16], with the structural and calculational parameters having been extracted for this specific device from a systematic comparison between the results of theoretical calculations and polarization-resolved photovoltage measurements performed on the laser structure [47]. Based on measurements of the SE at threshold for the device of Ref. [16], to be considered in Section IV-B below, the gain calculations include inhomogeneous broadening which is taken into account by convolving the calculated spectra with a Gaussian lineshape of linewidth $\sigma = 25$ meV at 300 K. We present here an overview of the dependence of the gain characteristics of $x = 2.1\%$ $GaBi_xAs_{1-x}$ QW laser characteristics on the assumed Al composition y in the surrounding barrier layers. We show that $Al_yGa_{1-y}As$ barriers are required to optimize the threshold characteristics of an $x = 2.1\%$ structure and identify the range of Al compositions y for which the threshold carrier density can be minimized.

Figure 2 shows the calculated peak TE-polarized modal gain as a function of carrier density for a series of $GaBi_{0.021}As_{0.979}/Al_yGa_{1-y}As$ QW structures having barrier Al compositions $0 < y < 25\%$. Our theoretical calculations suggest that QWs having barrier Al compositions $y = 10 - 15\%$ (green and blue lines) offer enhanced modal gain at fixed carrier density as compared to a QW having GaAs barriers (black line). Barrier Al compositions $y \lesssim 10\%$ provide insufficient electron confinement to produce good levels of material gain, while for $y \gtrsim 15\%$ refractive index contrast between the barrier and cladding layers is reduced, eroding the optical confinement and hence the modal gain. These results confirm the importance of AlGaAs barriers for the design and realisation of $GaBi_xAs_{1-x}$ QW lasers at low x.

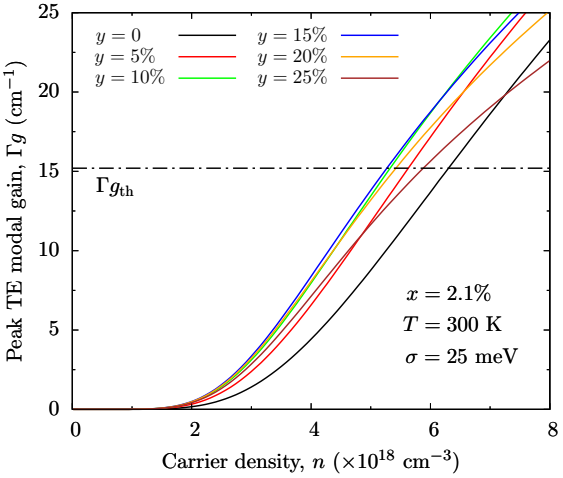


Fig. 2. Calculated variation of the peak TE-polarized modal gain as a function of carrier density at 300 K for a series of 6.9 nm wide $GaBi_{0.021}As_{0.979}$ quantum wells having $Al_yGa_{1-y}As$ barriers. Quantum wells having barrier Al compositions of $y = 0$, 5, 10, 15, 20 and 25% are denoted using black, red, green, blue, orange and brown solid lines respectively. The calculated gain spectra include an inhomogeneous broadening of 25 meV. The horizontal dash-dotted line denotes the calculated threshold modal gain, $\Gamma g_{\rm th} = 15.2$ cm^{-1}.

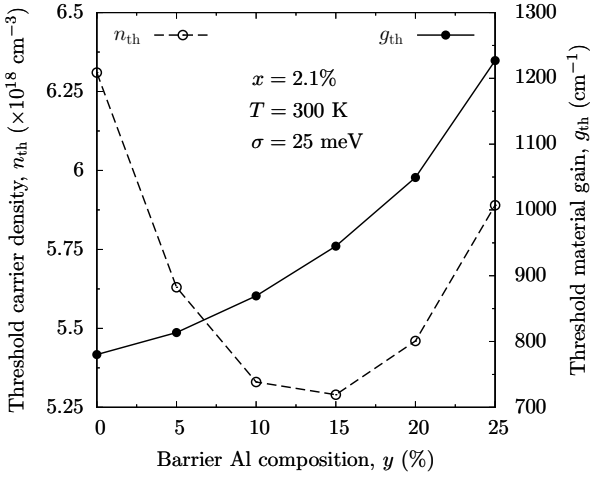


Fig. 3. Calculated variation of the threshold carrier density at 300 K ($n_{\rm th}$; open circles, dashed lines) and threshold material gain ($g_{\rm th}$; closed circles, solid lines) as a function of the barrier Al composition y for a series of 6.9 nm wide $GaBi_{0.021}As_{0.979}$ quantum wells having $Al_yGa_{1-y}As$ barriers. The calculated gain spectra, from which the values of $n_{\rm th}$ were obtained, include an inhomogeneous broadening of 25 meV.

In order to confirm these conclusions we have also calculated the variation of the threshold carrier density $n_{\rm th}$ and material gain at threshold $g_{\rm th}$ as a function of y for the same series of laser structures. The results of these calculations are shown in Fig. 3. Examining first the variation of $g_{\rm th}$ with y (closed circles, solid line) we see that the degradation in the optical confinement when Al is incorporated in the barrier layers leads to an increase in $g_{\rm th}$ with increasing y. This increase in $g_{\rm th}$ is modest at low Al compositions $y \lesssim 10\%$, with the optical confinement factor $\Gamma = 1.75\%$ at $y = 10\%$ being 90% of its calculated value of 1.95% at $y = 0$. For $y \gtrsim 10\%$ the optical confinement degrades rapidly with increasing y, with Γ reaching values as low as 1.24% at $y = 25\%$. This results in a large increase in the material gain at threshold, since $g_{\rm th} \propto \Gamma^{-1}$. The net effect of this behaviour on the laser performance can be seen clearly by considering the variation of the threshold carrier density $n_{\rm th}$ with y (open circles, dashed line). Beginning with a QW having GaAs barriers ($y = 0$) we calculate a large threshold carrier density of $n_{\rm th} = 6.3 \times 10^{18}$ cm^{-3}. When Al is incorporated into the barrier layers $n_{\rm th}$ decreases rapidly with increasing y, reaching a minimum value of approximately $n_{\rm th} = 5.3 \times 10^{18}$ cm^{-3} for $10\% < y < 15\%$. For $y \lesssim 10\%$ we therefore conclude that the increase in the material gain at fixed carrier density arising from the enhanced electron confinement is sufficient to overcome the associated reduction in optical confinement, leading to a reduction in $n_{\rm th}$. For $y > 15\%$ we calculate that $n_{\rm th}$ increases rapidly with increasing y, reflecting that any further improvement in the material gain is insufficient to overcome the degradation in optical confinement and associated increase in $g_{\rm th}$.

Since the ultimate goal is to grow dilute bismide lasers with higher Bi compositions, we have repeated this analysis for a series of $GaBi_xAs_{1-x}$/(Al)GaAs laser structures as a function of x. In general we find that Al incorporation in the barrier layers is required to enhance the otherwise weak electron confinement for $x \lesssim 5\%$. For $x = 6\%$ we calculate that the $GaBi_xAs_{1-x}$/GaAs CB offset is sufficiently large that incorporating Al in the barrier layers has a negligible impact on the material gain. We therefore conclude that Al incorporation is not required in the barrier layers for $GaBi_xAs_{1-x}$ QWs with $x \gtrsim 6\%$. GaAs barriers should suffice to provide modal gain which slightly exceeds that observed in the $x = 2.1\%$ Bi-containing devices at fixed carrier density, provided that QWs with $x \gtrsim 6\%$ can be grown with sufficiently high quality.

This conclusion has proved useful, particularly for the growth of hybrid laser structures such as those presented in Ref. [17], where the cladding and part of the barrier layers are grown by MOVPE, and the active region by MBE. Our analysis suggests that, for sufficiently large Bi compositions in the QW(s), GaAs can be used as the final layer grown before a laser sub-structure is transferred in either direction between MOVPE and MBE growth chambers, thereby minimising the impact of AlGaAs-related degradation during transport and storage of partly grown laser structures.

B. Electronic and optical properties of ideal $GaBi_xAs_{1-x}$/AlGaAs lasers at $x = 2.1\%$

In order to identify and quantify the effects of Bi incorporation on the electronic and optical properties of laser structures having low Bi composition, we now compare the calculated gain characteristics of a 6.9 nm wide $GaBi_{0.021}As_{0.979}/Al_{0.144}Ga_{0.856}As$ laser structure with those of an equivalent Bi-free ($x = 0$) $GaAs/Al_{0.144}Ga_{0.856}As$ QW laser structure. The QW width and Bi composition for the

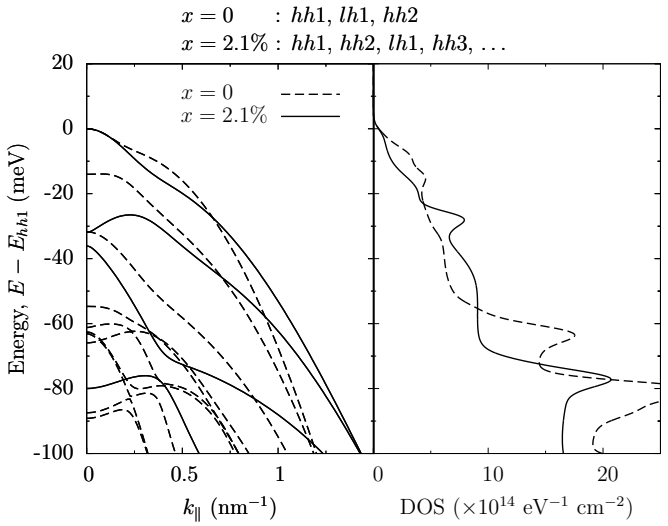


Fig. 4. Calculated band structure (left panel) and density of states (DOS; right panel) in the vicinity of the valence band edge for 6.9 nm wide GaAs ($x = 0$; dashed lines) and $GaBi_{0.021}As_{0.979}$ ($x = 2.1\%$; solid lines) quantum wells with $Al_{0.144}Ga_{0.856}As$ barriers. Note that the zero of energy has been taken in each case at the energy of the highest bound hole state ($hh1$) in order to facilitate comparison between the two quantum wells.

theoretical calculations are chosen following the analysis of Ref. [47], in order to model the device presented in Ref. [16].

Based on our analysis in Ref. [47] we assume a 70:30 CB to VB offset ratio between GaAs and AlGaAs, giving calculated CB and VB offsets of 150 meV and 65 meV, respectively, in the Bi-free QW structure. The incorporation of 2.1% Bi introduces a compressive pseudomorphic strain of 0.25% relative to the GaAs substrate, which lifts the degeneracy of the HH and LH states at the VB edge in the $GaBi_xAs_{1-x}$ layer. When both strain and VBAC effects are taken into account, this leads to calculated HH and LH band offsets of 224 and 208 meV respectively (HH-LH bulk band splitting of 16 meV), and a calculated CB offset of 185 meV between the strained QW and $Al_{0.144}Ga_{0.856}As$ barrier. The calculated transition energy between the lowest energy bound electron state ($e1$) and the highest energy hole state ($hh1$) is 1.480 eV in the Bi-free QW, and 1.289 eV in the 2.1% Bi QW. Of this 191 meV reduction in the QW band gap, 160 meV is due to the VBAC-induced upward shift in the VB edge energy, while the remaining 31 meV is due to the Bi-induced downward shift in the CB edge energy.

Figure 4 shows the calculated VB structure and density of states (DOS) for the $x = 0$ and 2.1% QWs. The zero of energy is taken at the energy of the first bound hole state in each case, in order to facilitate a direct comparison of the DOS in the two QWs. Three factors lead to differences in the band structure and density of states for the 2 structures considered: (i) the small compressive strain in the 2.1% Bi-containing sample leads to a small increase in the splitting between the highest heavy-hole state ($hh1$) and the highest light-hole state ($lh1$), leading to a small reduction in the calculated DOS for the 2.1% structure over the first 20 meV below the VB edge energy; (ii) the VBAC interaction tends to push the dispersion of the highest valence band upwards with increasing in-plane wave vector $k_\parallel$, thereby increasing the DOS in the $x = 2.1\%$ structure relative to the Bi-free structure for energies between 20 and 60 meV below the VB edge; (iii) the $Al_{0.144}Ga_{0.856}As$ barrier VB edge is calculated to be about 60 meV (> 200 meV) below the highest VB state in the 0% (2.1%) sample, so that the calculated VB density of states in the Bi-free structure, including barrier states, again increases above the $x = 2.1\%$ case for energies between 60 and 100 meV below the VB edge. Overall, when these three effects are taken into account, we conclude that the calculated differences between the VB DOS of the two structures are relatively small. This leads, as we see below, to only a small change in the calculated transparency carrier density in the 2.1% structure compared to the Bi-free case.

Having considered the electronic structure of the Bi-containing QW, we now turn our attention to the optical properties. We first consider the effects of strain and Bi-induced hybridization on the interband transition strengths, and then use the calculated band structure and matrix elements to investigate the effect of Bi incorporation on the SE and material gain. Figures 5(a) and 5(b) show respectively the squared TE- and TM-polarized interband momentum matrix elements, calculated as a function of the in-plane wave vector $k_\parallel$ for transitions between the lowest energy bound electron state ($e1$) and the highest energy HH- and LH-like bound states ($hh1$ and $lh1$), for the Bi-free (dashed lines) and Bi-containing (solid lines) QWs. We see both for the TE- and TM-polarized matrix elements in Figs. 5(a) and 5(b) that the incorporation of Bi reduces the magnitude of the transition strength at $k_\parallel = 0$ for transitions between the $e1$ and $hh1$/$lh1$ states. For example, the $e1$–$hh1$ TE-polarized transition strength at $k_\parallel = 0$ in the Bi-containing QW (18.42 eV) is 66.6% of that in the Bi-free QW (27.65 eV). The majority of the Bi-induced reduction in the transition strengths is due to the VBAC effect, which accounts for all but 1.1% of the calculated 33.4% reduction of the transition strength for the $e1$–$hh1$ transition in the strained QW. This is due to the fact that the hybridization of the bound hole states in the QW with the Bi-related localized states leads to hole states with reduced GaAs host matrix character. This in turn leads to a reduced inner product between the bound electron and hole eigenstates due to the fact that a portion of the hole states is now made up Bi-related localized states, which do not couple to the s-like states at the CB minimum [18].

Using the calculated band dispersion and $k_\parallel$-dependent matrix elements, we next investigate the variation of the peak material gain as a function of the carrier density n, and of the radiative current density J_{rad} for temperatures $T = 100$, 200 and 300 K. The results of these calculations are shown by the solid and dashed lines in Figs. 6(a) and 6(b) respectively, where we show only the TE-polarized material gain, which is of larger magnitude in both the Bi-free and Bi-containing QWs. The material gain at fixed carrier density is inversely proportional to the photon energy. In order to facilitate a direct comparison of the gain characteristics of the two QWs we have therefore shifted all CB states in the $x = 0$ calculation

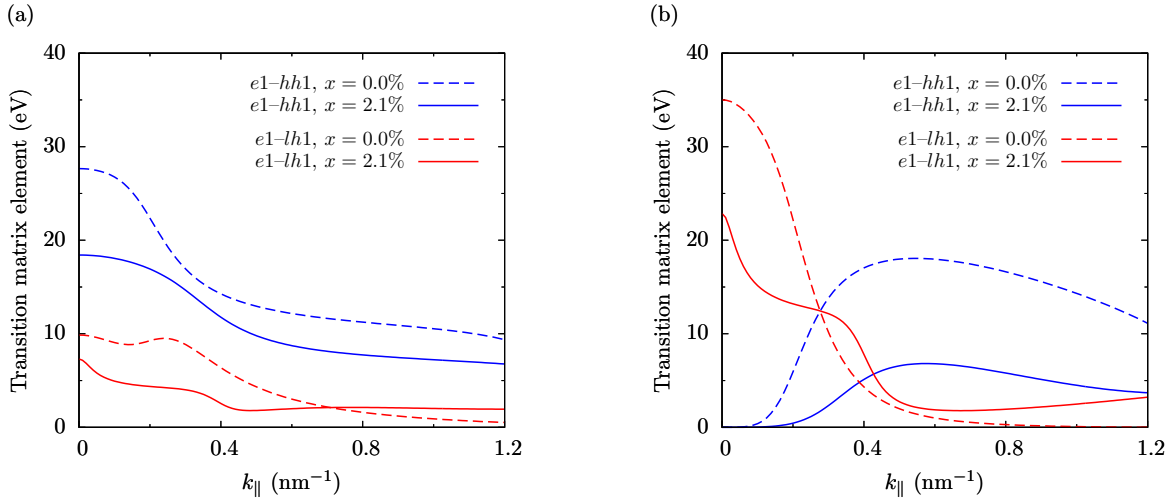


Fig. 5. Calculated (a) TE-polarized, and (b) TM-polarized transition matrix elements, as a function of the in-plane wave vector ($k_\parallel$), for optical transitions between the lowest electron and highest light- and heavy-hole states (denoted respectively by red and blue lines) for 6.9 nm wide GaAs ($x = 0$; dashed lines) and $GaBi_{0.021}As_{0.979}$ ($x = 2.1\%$; solid lines) quantum wells with $Al_{0.144}Ga_{0.856}As$ barriers.

downwards in energy by 191 meV to bring the ground state $e1$–$hh1$ transition energy of the Bi-free QW into coincidence with that of the Bi-containing QW. Therefore, the differences between the calculated gain characteristics of the $x = 0$ and 2.1% QWs presented in Figs. 6(a) and 6(b) arise purely due to the effects of Bi incorporation on the QW electronic structure. A threshold gain of $g_{\text{th}} = 919$ cm^{-1} – denoted by a horizontal dash-dotted line in each of Figs. 6(a) and 6(b) – was calculated for the Bi-containing laser structure, corresponding to an optical confinement factor for the fundamental TE-polarized optical mode of $\Gamma = 1.66\%$.

It can be seen that there is little change between the calculated transparency carrier density, n_{tr}, for the $x = 0$ and 2.1% structures for all temperatures considered. This reflects that there were only small differences between the calculated DOS for the two structures, as seen above in Fig. 4. However, we find that above transparency (i) the gain saturates at a lower level with increasing carrier density in the Bi-containing QW, and (ii) the carrier density required to reach threshold n_{th} is higher at $x = 2.1\%$ than in the Bi-free QW. Both of these features arise due to the general reduction in the magnitude of the interband transition matrix elements in the Bi-containing QW.

The role of the reduced interband transition matrix elements is confirmed in Fig. 6(b), which shows the calculated variation of the peak TE-polarized material gain as a function of the radiative current density J_{rad}, where J_{rad} has been determined directly for each QW by integrating over the SE spectrum at each combination of temperature and carrier density [57]. The reduction in the calculated radiative current density at transparency, $J_{\text{rad}}^{\text{tr}}$ arises directly from the reduced magnitude of the interband transition matrix elements. In the Boltzmann approximation, $J_{\text{rad}}^{\text{tr}}$ should vary as Bn_{tr}^2, with the radiative recombination coefficient B being directly proportional to the average value of the interband transition matrix elements [58], [59], [60]. Because of the reduction in the magnitude of the optical matrix elements, we calculate a lower value of $J_{\text{rad}}^{\text{tr}}$ over the full temperature range investigated in the Bi-containing QW, as well as larger peak gain at low and intermediate values of J_{rad} compared to the Bi-free QW. This trend then reverses at higher values of material gain, since much larger carrier densities are required to produce the same level of material gain in the Bi-containing QW, thereby ensuring that J_{rad} is larger at higher gain values than in the Bi-free QW. We note however that the impact of Bi incorporation on the differential gain with respect to J_{rad} is minimal in the vicinity of threshold, and the calculated values are comparable for both QWs.

Having considered in detail the effect of Bi incorporation on the electronic and optical properties of this $GaBi_xAs_{1-x}$ laser structure, we now compare the results of our theoretical calculations to experimental measurements performed on the device of Ref. [16]. In the experiment the SE spectrum was measured at the lasing threshold for temperatures between 50 and 300 K. The measurements were performed by collecting the SE from the QW through a small aperture milled in the laser substrate [19], [61]. This technique ensures that the light collected from the device is only that which propagates perpendicular to the laser cavity. In addition to ensuring that only the pure (unamplified) SE is collected, this technique also ensures that only the TE-polarized component of the SE is observed. For the comparison between the calculated and measured spectra the TM-polarized transition matrix elements were therefore set equal to zero, so that the calculated SE spectra are purely TE-polarized. The results of this analysis are shown in Fig. 7 where the calculated (measured) spectra are shown using dashed (solid) lines. At each temperature the theoretical spectra were normalized at the SE peak. Following this the calculated spectra were inhomogeneously broadened

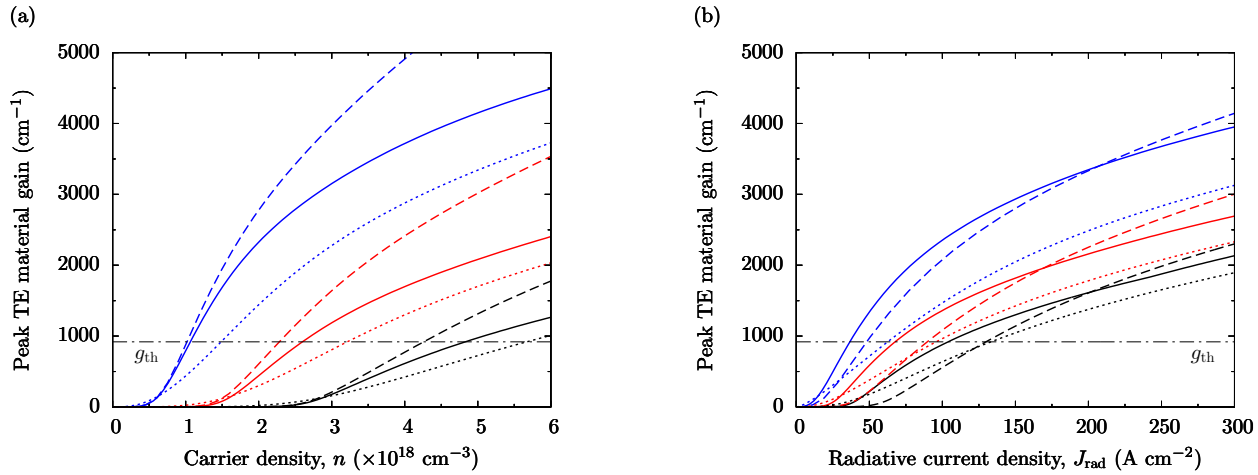


Fig. 6. Calculated variation of the peak TE-polarized material gain as a function of (a) carrier density, and (b) radiative current density, at temperatures of 100, 200 and 300 K (blue, red and black lines, respectively) for 6.9 nm thick $GaBi_{0.021}As_{0.979}$ ($x = 2.1\%$; solid lines) and GaAs ($x = 0$; dashed lines) quantum wells with $Al_{0.144}Ga_{0.856}As$ barriers. In (a) and (b) the horizontal dash-dotted lines denote the threshold material gain, $g_{\rm th} = 919$ cm^{-1}.

as described above, with the inhomogeneous linewidth σ chosen to produce the best fit to the measured SE on the low energy side of the SE peak. The values of σ obtained at each temperature are given in parentheses in Fig. 7.

It can be seen that the calculated value of the inhomogeneous linewidth σ varies little with temperature (20 meV $\leq \sigma \leq$ 30 meV over the full temperature range). We note that the agreement between the theoretical and experimental data is generally poor at higher energies (shorter wavelengths), with the calculated spectra being generally wider than the measured ones. We attribute the discrepancy at lower temperatures to the broadening model used. We are fitting an inhomogeneous broadening of the band edge states by inhomogeneously broadening the full SE spectrum. However, we note that if the carriers were in thermal equilibrium, then the decrease in the magnitude of the SE spectrum at higher energies should be related to a product of the (broadened) density of states times the carrier quasi-Fermi functions. Convoluting the calculated SE spectrum with an inhomogeneous broadening function will then overestimate the width of the spectrum at higher energies, as observed in Fig. 7.

As the temperature increases we see that the measured and calculated spectra are in better agreement up to 150 K, as thermal broadening effects become more important on the higher energy side of the spectrum. For higher temperatures $\geq$ 200 K we again note a large descrepancy between the theoretical and experimental spectra on the high energy side of the SE peak. This is attributed to absorption of a portion of the high energy SE from the QW as it travels through the GaAs substrate before being collected in the experiment [19]. The vertical arrows in Fig. 7 denote the band gap of the GaAs substrate at each temperature, and show that absorption from the substrate begins to encroach heavily on the measured SE spectra for temperatures $>$ 250 K. This intepretation is further supported by the variation of the measured SE linewidth with increasing temperature. As the temperature increases the linewidth of the SE spectra increases monotonically up to approximately 250 K, above which temperature it begins to decrease again with further increases in temperature. Overall, the theoretical model provides a reasonably accurate description of the band edge emission from the $GaBi_xAs_{1-x}$ QW, in particular capturing the evolution of the band edge emission SE peak over a wide range of temperatures. As lasing is primarily determined by the state and carrier distributions near the band edge, we conclude that our model should therefore be appropriate to analyse the gain characteristics of the different device structures considered in this paper.

Figure 8 show the TE- and TM-polarized material gain spectra for the laser structure (solid and dashed lines, respectively), calculated at 300 K for carrier densities of 5, 7 and 9 $\times 10^{18}$ cm^{-3} (blue, red and black lines, respectively). These material gain spectra include an inhomogeneous broadening of $\sigma = 25$ meV, as identified from Fig. 7. We note that ridge-waveguide dilute bismide laser structures have not to date been fabricated, so that it is not currently possible to compare the calculated gain spectra directly to experiment. However, for injection levels above the threshold carrier density $n_{\rm th} = 6.12 \times 10^{18}$ cm^{-3} we calculate that the peak material gain lies close to the measured room temperature emission wavelength of 947 nm [16]. We further calculate that $n_{\rm th}$ increases strongly with temperature, reaching values in excess of 8×10^{18} cm^{-3} above 350 K. We note that these large calculated values of $n_{\rm th}$ are consistent with the fact that no lasing was observed in the device for temperatures $>$ 350 K.

Based on these calculations we have also estimated the radiative recombination coefficient B for the laser structure. In the Boltzmann approximation the radiative current density at threshold is given by $J_{\rm rad}^{\rm th} = eBn_{\rm th}^2$. Evaluating $J_{\rm rad}^{\rm th}$ directly by integrating over the calculated SE spectrum at threshold we calculate B in the Boltzmann approximation, where $n_{\rm th}$

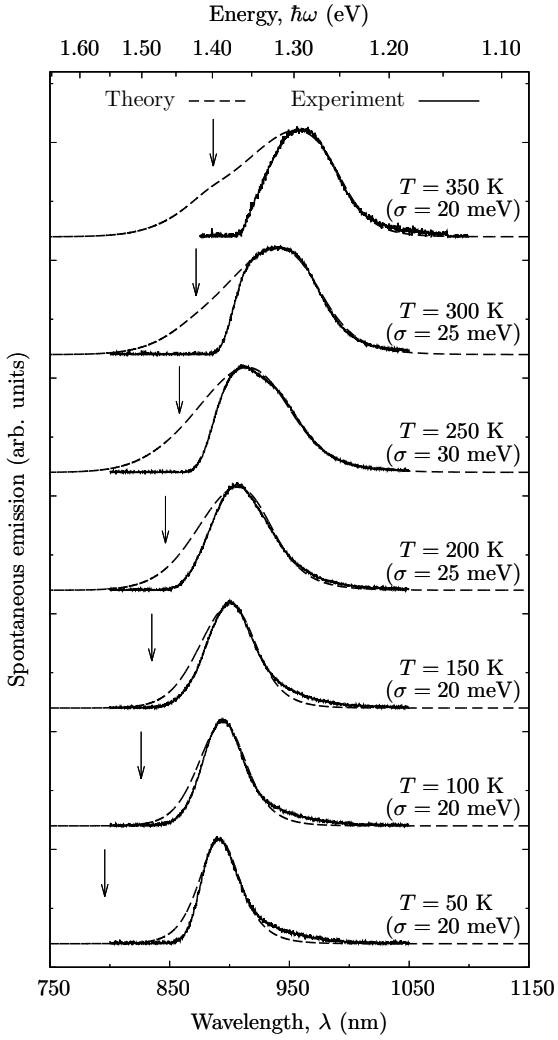


Fig. 7. Comparison between the measured (solid lines) and calculated (dashed lines) spontaneous emission spectra at threshold for a 6.9 nm wide $GaBi_{0.021}As_{0.979}/Al_{0.144}Ga_{0.856}As$ single quantum well laser, for temperatures between 50 and 350 K. At each temperature the calculated spectrum has been normalized to the measured spectrum at the peak spontaneous emission, and has been inhomogeneously broadened using a Gaussian lineshape to produce the best fit to experiment on the low-energy side of the peak. The best fit value of the inhomogeneous linewidth σ of the Gaussian lineshape is shown in parentheses at each temperature. The calculated spectra at 300 and 350 K have been redshifted by $\Delta\lambda = 12$ nm. The vertical arrow at each temperature denotes the band gap of the (GaAs) substrate material, through which the spontaneous emission from the quantum well must pass before being collected in the experiment.

is determined directly for each structure from the calculated gain spectra. We estimate a value of $B = 3.6 \times 10^{-11}$ cm^3 s^{-1} at 300 K . We further note that the calculated values of B between 50 and 350 K follow the $B(T) \propto T^{-1}$ temperature dependence expected for an ideal QW [59].

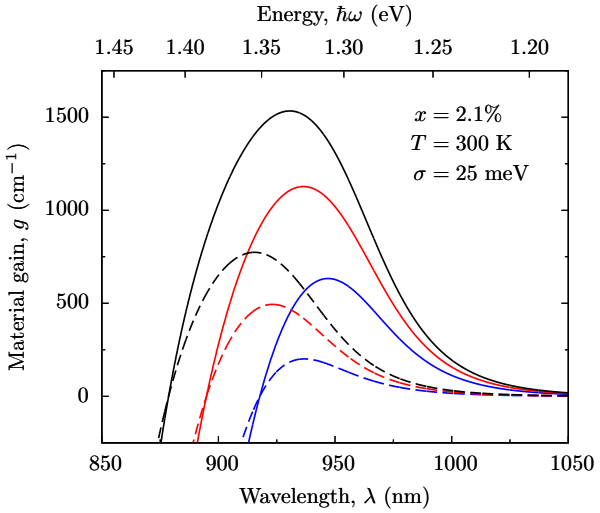


Fig. 8. Inhomogeneously broadened TE-polarized (solid lines) and TM-polarized (dashed lines) material gain spectra, calculated at 300 K for carrier densities of 5, 7 and 9 $\times 10^{18}$ cm^{-3} (blue, red and black lines, respectively) for a 6.9 nm wide $GaBi_{0.021}As_{0.979}/Al_{0.144}Ga_{0.906}As$ quantum well.

C. Gain characteristics of 1.55 μm $GaBi_xAs_{1-x}$/GaAs lasers

Having elucidated the consequences of Bi incorporation on the gain characteristics and performance of real $GaBi_xAs_{1-x}$ QW lasers at low x, we now turn our attention to an ideal 1550 nm device at higher Bi composition. We choose a $GaBi_xAs_{1-x}$ QW of width 6.9 nm, in order to compare the calculated modal gain directly to that calculated for the $x = 2.1\%$ QW of Sections IV-A and IV-B, and, in light of the analysis presented in Section IV-A, we choose GaAs as the barrier material. For this 6.9 nm wide $GaBi_xAs_{1-x}$/GaAs QW we calculate that a Bi composition of $x = 13\%$ produces an emission wavelength close to 1550 nm. We note that the bulk band structure of $GaBi_{0.13}As_{0.87}$ QW satisfies the $\Delta_{SO} > E_g$ condition (cf. Fig. 1), so that it should be possible to use $GaBi_xAs_{1-x}$ alloys to develop a 1.55 μm laser structure in which the dominant CHSH Auger recombination mechanism is suppressed.

Figure 9 shows the calculated VB structure (left panel) and DOS (right panel) in the vicinity of the VB edge for this $GaBi_{0.13}As_{0.87}$/GaAs QW (dashed lines). The calculated VB structure and DOS for the $GaBi_{0.021}As_{0.979}/Al_{0.144}Ga_{0.856}As$ QW of Section IV-B are included from Fig. 4 for comparative purposes (solid lines). Incorporation of 13% Bi in the QW produces an in-plane compressive strain of 1.53%, as compared to 0.25% in the QW with $x = 2.1\%$. We calculate that, despite the tendency of the VBAC interaction to increase the effective masses of the bound hole states in the QW, the increased compressive strain at larger values of x is sufficient to overcome this effect and lead to a significant reduction of the DOS in the vicinity of the VB edge (see Fig. 9). We observe that while the separation in energy between the two highest energy hole subbands (which are heavy-hole like at $k_{\|} = 0$ for $x = 2.1$ and 13%) is virtually unchanged in the $GaBi_{0.13}As_{0.87}$ QW as compared to the $x = 2.1\%$ structure,

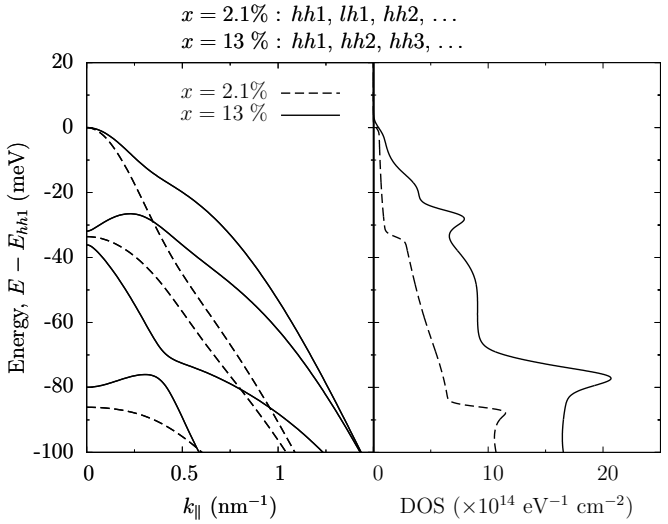


Fig. 9. Calculated band structure (left panel) and density of states (DOS; right panel) in the vicinity of the valence band edge for 6.9 nm wide $GaBi_{0.021}As_{0.979}/Al_{0.144}Ga_{0.856}As$ (solid lines, as in Fig. 4) and $GaBi_{0.13}As_{0.87}$/GaAs (dashed lines) quantum wells. The Bi composition x of the $GaBi_{0.13}As_{0.87}$ quantum well was chosen to produce an emission wavelength close to 1550 nm. Note that the zero of energy has been taken in each case at the energy of the highest bound hole state ($hh1$) in order to facilitate comparison between the two quantum wells.

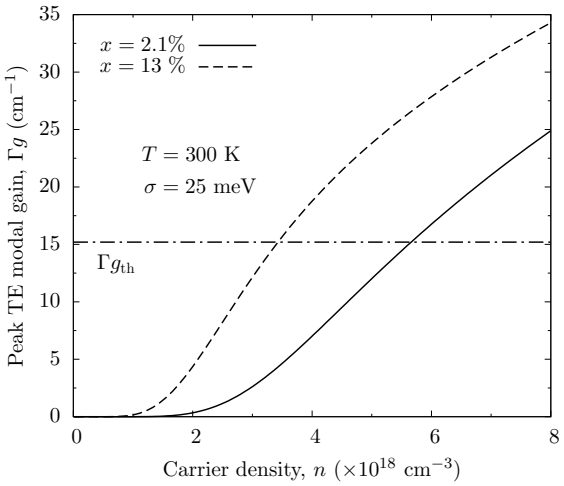


Fig. 10. Calculated variation of the peak TE-polarized modal gain as a function of carrier density at 300 K for the $GaBi_{0.021}As_{0.979}/Al_{0.144}Ga_{0.856}As$ (solid line) and $GaBi_{0.13}As_{0.87}$/GaAs (dashed line) quantum wells of Fig. 9. The calculated gain spectra include an inhomogeneous broadening of 25 meV. The horizontal dash-dotted line denotes the calculated threshold modal gain, $\Gamma g_{\rm th} = 15.2$ cm^{-1}.

the increased compressive strain at $x = 13\%$ gives rise to a strong reduction of the in-plane hole effective masses. The strong reduction of the DOS at energies close to the QW VB edge (right panel), should then enhance the performance of this high Bi composition QW compared to the low x devices studied above [62].

Compared to the value of $\Gamma = 1.66\%$ calculated for the optical confinement factor $x = 2.1\%$ device of Section IV-B, we calculate $\Gamma = 1.26\%$ in the $x = 13\%$ QW. The reduction in Γ occurs because of the longer emission wavelength of the $x = 13\%$ structure. This decrease in Γ leads to an increase in the material gain at threshold $g_{\rm th}$. Based on the calculated difference in Γ between the two laser structures we calculate $g_{\rm th} = 1208$ cm^{-1} at $x = 13\%$, which is 32% higher than the value of 919 cm^{-1} calculated above for the $x = 2.1\%$ device. However, the calculated CB offset of 245 meV in the $GaBi_{0.13}As_{0.87}$/GaAs QW is 60 meV larger than that calculated at $x = 2.1\%$, leading to enhanced electron confinement in the 1550 nm QW. The calculated interband transition matrix element at $k_\parallel = 0$ for the $e1$–$hh1$ optical transition in the $x = 13\%$ QW (16.54 eV) is approximately 90% of that calculated at $x = 2.1\%$ (18.42 eV). When combined with the favourable effects of strain on the VB structure and DOS at larger values of x, these effects ensure that the material gain at fixed carrier density is significantly improved in the $x = 13\%$ QW than in the $x = 2.1\%$ device studied above.

Spectroscopic analysis of a series of $GaBi_xAs_{1-x}$ alloys suggests that the inhomogeneous linewidth of the HH band edge optical transitions remains approximately constant for Bi compositions up to $x = 10.4\%$ [32]. In order to compare the gain characteristics of the $x = 2.1$ and 13% laser structures we therefore take the same inhomogeneous linewidth of $\sigma = 25$ meV for the calculation of the gain spectra at $x = 13\%$. Specifically, we calculate that the $x = 13\%$ laser structure has a threshold carrier density of $n_{\rm th} = 3.42 \times 10^{18}$ cm^{-3} at 300 K, which is close to 60% of the value of 5.72×10^{18} cm^{-3} calculated above for the $x = 2.1\%$ device of Ref. [16]. Additionally, for the $x = 13\%$ laser structure we calculate a value of $\frac{{\rm d}g}{{\rm d}n} = 2.76 \times 10^{-16}$ cm^2 for the differential material gain at threshold, which is increased by a factor of approximately two compared to the value of 1.32×10^{-16} cm^2 calculated above for the $x = 2.1\%$ device. Overall, our analysis suggests that this strong improvement in the threshold characteristics of the device at high x results primarily from the effects of the increased compressive strain in the QW. Firstly, the strain-induced reduction in the DOS at the VB edge leads to an increase in the quasi-Fermi level separation at fixed carrier density, meaning that population inversion can be achieved at lower carrier densities. Secondly, the reduced in-plane hole effective masses ensure that holes occupy VB states over a smaller spread of in-plane wave vectors at $x = 13\%$ than at $x = 2.1\%$, meaning that more carriers are available to contribute to the lasing mode. These factors ensure that a larger increase in material gain can be obtained for a given change in carrier density at $x = 13\%$, leading to the calculated improvement in $\frac{{\rm d}g}{{\rm d}n}$.

Figure 10 shows the calculated variation of the modal gain Γg as a function of carrier density for the $x = 2.1\%$ (solid line) and $x = 13\%$ (dashed lines) laser structures at 300 K. The horizontal dash-dotted line denotes the calculated threshold modal gain, $\Gamma g_{\rm th} = 15.2$ cm^{-1}. We see that the enhancement

of the material gain described above is sufficient to overcome the reduction in optical confinement factor between $x = 2.1$ and 13%, leading to significantly improved modal gain at fixed carrier density. Additionally, we also note that the differential modal gain at threshold is also significantly improved at $x = 13\%$, due to the fact that the calculated increase in the differential material gain at threshold is sufficient to overcome the reduction in Γ between $x = 2.1$ and 13%.

We therefore conclude that the performance of ideal $GaBi_xAs_{1-x}$ QW lasers at high Bi compositions ($x \gtrsim 10\%$) should be significantly improved compared to that of shorter wavelength devices at lower x. The calculated improvement in the laser gain characteristics with increasing x is primarily attributable to the increased compressive strain in the at larger values of x. We also note that the presence of a QW band structure in which $\Delta_{SO} > E_g$ promises to deliver even greater benefit for the laser operation, due to the elimination of the dominant non-radiative and absorptive losses.

V. Conclusions

We have presented a theoretical investigation of dilute bismide quantum well lasers. Beginning from a 12-band **k·p** Hamiltonian that we have previously derived for dilute bismide alloys we have calculated the electronic and optical properties of a series of $GaBi_xAs_{1-x}$ quantum well laser structures as a function of Bi composition x.

We began with a consideration of the effects of electrostatic confinement of electron states by highly-localized, Bi-hybridized hole states in $GaBi_xAs_{1-x}$/(Al)GaAs quantum wells at low x, where the band offsets are significantly larger in the valence band than in the conduction band. Through systematic theoretical optimization of the barrier Al composition in a series of $GaBi_xAs_{1-x}$/(Al)GaAs quantum wells at $x = 2.1\%$ we showed that the trade-off between the electronic and optical confinement at low x can be engineered in such a way as to minimize the carrier density at threshold, as well as to maximize the modal and differential gain at fixed carrier density. Recent growth and experimental investigations have confirmed that this approach to optimizing the active region of $GaBi_xAs_{1-x}$ devices at low x has significant benefits for the laser performance, leading in particular to significantly reduced threshold current densities compared to those observed in first-generation $GaBi_xAs_{1-x}$ laser structures. We further considered the evolution of the gain characteristics of $GaBi_xAs_{1-x}$ quantum well laser structures as the Bi composition x is increased, and showed that the $GaBi_xAs_{1-x}$/GaAs conduction band offset is sufficiently large to remove the requirement for Al incorporation in the barrier layers for Bi compositions $x \gtrsim 6\%$.

This was followed by a detailed analysis of first-generation $GaBi_xAs_{1-x}$ laser structures at $x = 2.1\%$, where we identified and quantified the effects of Bi incorporation on the electronic and optical properties. Specifically, we showed that Bi-induced hybridization and anticrossing of valence states leads at low Bi compositions $x \lesssim 6\%$ to (i) a reduction of the optical transition strengths, (ii) strong spatial localization of hole states, (iii) an increase in the carrier density at threshold, and (iv) a decrease in the material and differential gain at fixed carrier density. Having identified general trends in the electronic and optical properties of $GaBi_xAs_{1-x}$ quantum well lasers at $x = 2.1\%$, we then compared the results of our theoretical calculations to temperature-dependent experimental measurements of the spontaneous emission at threshold for the device of Ref. [16]. We showed that our theoretical model accurately describes the evolution of the band edge optical emission and emission peak as a function of temperature. Furthermore, our analysis confirmed the presence of large inhomogeneous broadening of the optical spectra, as well as a non-thermal distribution of carriers in $GaBi_xAs_{1-x}$ quantum wells at low temperatures $\lesssim 200$ K, with the latter arising primarily due to the presence of a range of localized states (associated with pairs and larger clusters of Bi atoms) in the vinicity of the valence band edge.

Finally, we considered a $GaBi_xAs_{1-x}$/GaAs laser structure designed to emit at 1.55 μm, and having a band structure in which the spin-orbit-splitting energy exceeds the band gap (a condition which must be satisfied to suppress the dominant hot-hole-producing CHSH Auger recombination mechanism). We showed that the gain characteristics of an ideal $GaBi_xAs_{1-x}$ quantum well laser can be expected to improve significantly with increasing Bi composition for $x \gtrsim 10\%$. This improvement is primarily a result of the increased compressive strain in the quantum well, which gives rise to a low density of states in the vicinity of the valence band edge and leads to a reduction of the carrier density at threshold, as well as an increase in the modal and differential gain at fixed carrier density.

Overall, our theoretical calculations have elucidated the evolution of the gain characteristics of $GaBi_xAs_{1-x}$ dilute bismide quantum well lasers as a function of Bi composition x. We conclude that our theoretical approach provides a good general understanding of semiconductor lasers based on this novel III-V material system. Furthermore, our theoretical analysis has confirmed the promise of dilute bismide alloys for the development of highly efficient, uncooled GaAs-based quantum well lasers operating at 1.55 μm, provided current difficulties associated with material growth can be overcome.

Acknowledgment

The authors acknowledge support from the European Union Seventh Framework Programme (BIANCHO, project no. FP7-257974) and from Science Foundation Ireland (project no. 10/IN.1/I299). CB acknowledges support from the Irish Research Council (EMBARK Postgraduate Scholarship no. RS/2010/2766). The authors thank Peter Ludewig, Kerstin Volz and colleagues at Philipps-Universität Marburg, Germany, Arūnas Krotkus and colleagues at the Center for Physical Sciences and Technology, Lithuania, and Igor P. Marko, Shirong Jin, Stephen J. Sweeney and colleagues at the University of Surrey, U.K., for material and device fabrication, for valuable discussions, and for providing windowed laser devices to facilitate the spontaneous emission measurements.

References

[1] H. Li and Z. M. Wang, Eds., *Bismuth-Containing Compounds (Springer Series in Materials Science, Vol. 186).* Springer, 2013.

[2] S. J. Sweeney, "Bismide-alloys for higher efficiency infrared semiconductor lasers," *in proceedings of the 22nd IEEE International Semiconductor Laser Conference*, p. 111, 2010.

[3] C. A. Broderick, M. Usman, and E. P. O'Reilly, "Band engineering in dilute nitride and bismide semiconductor lasers," *Semicond. Sci. Technol.*, vol. 27, p. 094011, 2012.

[4] S. R. Jin and S. J. Sweeney, "InGaAsBi alloys on InP for efficient near-and mid-infrared light emitting devices," *J. Appl. Phys.*, vol. 114, p. 213103, 2013.

[5] A. Geižutisa, V. Pačebutas, R. Butkutė, P. Svidovskya, V. Strazdienėa, and A. Krotkus, "Growth and characterization of UTC photo-diodes containing $GaAs_{1-x}Bi_x$ absorber layer," *Solid State Electron.*, vol. 99, p. 101, 2014.

[6] J. J. Lee, J. D. Kim, and M. Razeghi, "Growth and characterization of InSbBi for long wavelength infrared photodetectors," *Appl. Phys. Lett.*, vol. 70, p. 3266, 1997.

[7] I. C. Sandall, F. Bastiman, B. White, R. Richards, D. Mendes, J. P. R. David, and C. H. Tan, "Demonstration of InAsBi photoresponse beyond 3.5 μm," *Appl. Phys. Lett.*, vol. 104, p. 171109, 2014.

[8] C. J. Hunter, F. Bastiman, A. R. Mohmad, R. Richards, J. S. Ng, S. J. Sweeney, and J. P. R. David, "Absorption characteristics of $GaAs_{1-x}Bi_x$/GaAs diodes in the near-infrared," *IEEE Photon. Tech. Lett.*, vol. 24, p. 2191, 2012.

[9] B. Fluegel, S. Francoeur, A. Mascarenhas, S. Tixier, E. C. Young, and T. Tiedje, "Giant spin-orbit bowing in $GaAs_{1-x}Bi_x$," *Phys. Rev. Lett.*, vol. 97, p. 067205, 2006.

[10] S. Mazzucato, T. T. Zhang, H. Carrère, D. Lagarde, P. Boonpeng, A. Arnoult, G. Lacoste, A. Balocchi, T. Amand, C. Fontaine, and X. Marie, "Electron spin dynamics and g-factor in GaAsBi," *Appl. Phys. Lett.*, vol. 102, p. 252107, 2013.

[11] P. Dongmo, Y. Zhong, P. Attia, C. Bomberger, R. Cheaito, J. F. Ihlefeld, P. E. Hopkins, and J. Zide, "Enhanced room temperature electronic and thermoelectric properties of the dilute bismuthide InGaBiAs," *J. Appl. Phys.*, vol. 112, p. 093710, 2012.

[12] S. J. Sweeney, A. F. Phillips, A. R. Adams, E. P. O'Reilly, and P. J. A. Thijs, "The effect of temperature dependent processes on the performance of 1.5 μm compressively strained InGaAs(P) MQW semiconductor diode lasers," *IEEE Photon. Tech. Lett.*, vol. 10, p. 1076, 1998.

[13] S. J. Sweeney, A. R. Adams, M. Silver, E. P. O'Reilly, J. R. Watling, A. B. Walker, and P. J. A. Thijs, "Dependence of threshold current on QW position and on pressure in 1.5 μm InGaAs(P) lasers," *Phys. Stat. Sol. B*, vol. 211, p. 525, 1999.

[14] A. R. Adams, "Band-structure engineering for low-threshold high-efficiency semiconductor lasers," *Electron. Lett.*, vol. 22, p. 249, 1986.

[15] Y. Tominaga, K. Oe, and M. Yoshimoto, "Low temperature dependence of oscillation wavelength in $GaAs_xBi_{1-x}$ laser by photo-pumping," *Appl. Phys. Express*, vol. 3, p. 062201, 2010.

[16] P. Ludewig, N. Knaub, N. Hossain, S. Reinhard, L. Natterman, I. P. Marko, S. R. Jin, K. Hild, S. Chatterjee, W. Stolz, S. J. Sweeney, and K. Volz, "Electrical injection Ga(AsBi)/(AlGa)As single quantum well laser," *Appl. Phys. Lett.*, vol. 102, p. 242115, 2013.

[17] R. Butkutė, A. Geižutis, V. Pačebutas, B. Čechavičius, V. Bukauskas, R. Kundrotas, P. Ludewig, K. Volz, and A. Krotkus, "Multi-quantum well Ga(AsBi)/GaAs laser diodes with more than 6% of bismuth," *Electron. Lett.*, vol. 50, p. 1155, 2014.

[18] C. A. Broderick, M. Usman, and E. P. O'Reilly, "Derivation of 12- and 14-band **k·p** Hamiltonians for dilute bismide and bismide-nitride semiconductors," *Semicond. Sci. Technol.*, vol. 28, p. 125025, 2013.

[19] I. P. Marko, P. Ludewig, Z. L. Bushell, S. R. Jin, K. Hild, Z. Batool, S. Reinhard, L. Natterman, W. Stolz, K. Volz, and S. J. Sweeney, "Physical properties and optimization of GaBiAs/(Al)GaAs based near-infrared laser diodes grown by MOVPE with up to 4.4% Bi," *J. Phys. D: Appl. Phys.*, vol. 47, p. 345103, 2014.

[20] S. Tixier, M. Adamcyk, T. Tiedje, S. Francoeur, A. Mascarenhas, P. Wei, and F. Schiettekatte, "Molecular beam epitaxy growth of $GaAs_{1-x}Bi_x$," *Appl. Phys. Lett.*, vol. 82, p. 2245, 2003.

[21] M. Yoshimoto, S. Murata, A. Chayahara, Y. Horino, J. Saraie, and K. Oe, "Metastable GaAsBi alloy grown by molecular beam epitaxy," *Jpn. J. Appl. Phys.*, vol. 42, p. L1235, 2003.

[22] Z. Chine, H. Fitouri, I. Zaied, A. Rebey, and B. E. Jani, "Growth of GaAsBi alloy under alternated bismuth flows by metalorganic vapor phase epitaxy," *J. Cryst. Growth*, vol. 330, p. 35, 2011.

[23] P. Ludewig, N. Knaub, W. Stolz, and K. Volz, "MOVPE growth of Ga(AsBi)/GaAs multi quantum well structures," *J. Cryst. Growth*, vol. 370, p. 186, 2013.

[24] P. Ludewig, Z. L. Bushell, L. Natterman, N. Knaub, W. Stolz, and K. Volz, "Growth of Ga(AsBi) on GaAs by continuous flow MOVPE," *J. Cryst. Growth*, vol. 396, p. 95, 2014.

[25] M. Masnadi-Shirazi, R. B. Lewis, V. Bahrami-Yekta, T. Tiedje, M. Chicoine, and P. Servati, "Bandgap and optical absorption edge of $GaAs_{1-x}Bi_x$ alloys with $0 < x < 17.8\%$," *J. Appl. Phys.*, vol. 116, p. 223506, 2014.

[26] T. Fuyuki, K. Yoshida, R. Yoshioka, and M. Yoshimoto, "Electrically pumped room-temperature operation of $GaAs_{1-x}Bi_x$ laser diodes with low-temperature dependence of oscillation wavelength," *Appl. Phys. Express*, vol. 7, p. 082101, 2014.

[27] K. Forghani, Y. Guan, M. Losurdo, G. Luo, D. Morgan, S. E. Babcock, A. S. Brown, L. J. Mawst, and T. F. Kuech, "$GaAs_{1-y-z}P_yBi_z$, an alternative reduced band gap alloy system lattice-matched to GaAs," *Appl. Phys. Lett.*, vol. 105, p. 111101, 2014.

[28] I. P. Marko, Z. Batool, K. Hild, S. R. Jin, N. Hossain, T. J. C. Hosea, J. P. Petropoulos, Y. Zhong, P. B. Dongmo, J. M. O. Zide, and S. J. Sweeney, "Temperature and Bi-concentration dependence of the bandgap and spin-orbit splitting in InGaBiAs/InP semiconductors for mid-infrared applications," *Appl. Phys. Lett.*, vol. 101, p. 221108, 2012.

[29] C. A. Broderick, M. Usman, and E. P. O'Reilly, "12-band **k·p** Hamiltonian for dilute bismide alloys of (In)GaAs derived from supercell calculations," *Phys. Stat. Sol. B*, vol. 250, p. 773, 2013.

[30] G. M. T. Chai, C. A. Broderick, S. R. Jin, J. P. Petropoulous, Y. Zong, P. B. Dongmo, J. M. O. Zide, E. P. O'Reilly, S. J. Sweeney, and T. J. C. Hosea, "Experimental and modelling study of InGaBiAs/InP alloys with up to 5.8% Bi and with $\Delta_{SO} > E_g$," *submitted*, 2015.

[31] Y. Zhang, A. Mascarenhas, and L.-W. Wang, "Similar and dissimilar aspects of III-V semiconductors containing Bi versus N," *Phys. Rev. B*, vol. 71, p. 155201, 2005.

[32] M. Usman, C. A. Broderick, A. Lindsay, and E. P. O'Reilly, "Tight-binding analysis of the electronic structure of dilute bismide alloys of GaP and GaAs," *Phys. Rev. B*, vol. 84, p. 245202, 2011.

[33] O. Rubel, A. Bokhanchuk, S. J. Ahmed, and E. Assmann, "Unfolding the band structure of disordered solids: From bound states to high-mobility Kane fermions," *Phys. Rev. B*, vol. 90, p. 115202, 2014.

[34] R. S. Joshya, A. J. Ptak, R. France, A. Mascarenhas, and R. N. Kini, "Resonant state due to Bi in the dilute bismide alloy $GaAs_{1-x}Bi_x$," *Phys. Rev. B*, vol. 90, p. 165203, 2014.

[35] K. Alberi, J. Wu, W. Walukiewicz, K. M. Yu, O. D. Dubon, S. P. Watkinsa, C. X. Wang, X. Liu, Y.-J. Cho, and J. Furdyna, "Valence-band anticrossing in mismatched III-V semiconductor alloys," *Phys. Rev. B*, vol. 75, p. 045203, 2007.

[36] S. Francoeur, M.-J. Seong, A. Mascarenhas, S. Tixier, M. Adamcyk, and T. Tiedje, "Band gap of $GaAs_{1-x}Bi_x$, $0 < x < 3.6\%$," *Appl. Phys. Lett.*, vol. 82, p. 3874, 2003.

[37] W. Huang, K. Oe, G. Feng, and M. Yoshimoto, "Molecular-beam epitaxy and characteristics of $GaN_yAs_{1-x-y}Bi_x$," *J. Appl. Phys.*, vol. 98, p. 053505, 2005.

[38] J. Yoshida, T. Kita, O. Wada, and K. Oe, "Temperature dependence of $GaAs_{1-x}Bi_x$ band gap studied by photoreflectance spectroscopy," *Jpn. J. Appl. Phys.*, vol. 42, p. 371, 2003.

[39] Z. Batool, K. Hild, T. J. C. Hosea, X. Lu, T. Tiedje, and S. J. Sweeney,

"The electronic band structure of GaBiAs/GaAs layers: Influence of strain and band anti-crossing," *J. Appl. Phys.*, vol. 111, p. 113108, 2012.

[40] M. Usman, C. A. Broderick, Z. Batool, K. Hild, T. J. C. Hosea, S. J. Sweeney, and E. P. O'Reilly, "Impact of alloy disorder on the band structure of compressively strained $GaBi_xAs_{1-x}$," *Phys. Rev. B*, vol. 87, p. 115104, 2013.

[41] M. Usman and E. P. O'Reilly, "Atomistic tight-binding study of the electronic structure and interband optical transitions in $GaBi_xAs_{1-x}$/GaAs quantum wells," *Appl. Phys. Lett.*, vol. 104, p. 071103, 2014.

[42] C. A. Broderick, S. Mazzucato, H. Carrère, T. Amand, H. Makhloufi, A. Arnoult, C. Fontaine, O. Donmez, A. Erol, M. Usman, E. P. O'Reilly, and X. Marie, "Anisotropic electron g factor as a probe of the electronic structure of $GaBi_xAs_{1-x}$/GaAs epilayers," *Phys. Rev. B*, vol. 90, p. 195301, 2014.

[43] A. Lindsay, S. Tomić, and E. P. O'Reilly, "Derivation of a 10-band $\mathbf{k}\cdot\mathbf{p}$ model for dilute nitride semiconductors," *Solid State Electron.*, vol. 47, p. 443, 2003.

[44] S. Tomić, E. P. O'Reilly, R. Fehse, S. J. Sweeney, A. R. Adams, A. D. Andreev, S. A. Choulis, T. J. C. Hosea, and H. Riechert, "Theoretical and experimental analysis of 1.3-μm InGaAsN/GaAs lasers," *IEEE J. Sel. Top. Quant. Electron.*, vol. 9, p. 1228, 2003.

[45] E. P. O'Reilly, A. Lindsay, S. Tomić, and M. Kamal-Saadi, "Tight-binding and $\mathbf{k}\cdot\mathbf{p}$ models for the electronic structure of Ga(In)NAs and related alloys," *Semicond. Sci. Technol.*, vol. 17, p. 870, 2002.

[46] E. P. O'Reilly, A. Lindsay, P. J. Klar, A. Polimeni, and M. Capizzi, "Trends in the electronic structure of dilute nitride alloys," *Semicond. Sci. Technol.*, vol. 24, p. 033001, 2009.

[47] C. A. Broderick, P. E. Harnedy, P. Ludewig, Z. L. Bushell, R. J. Manning, K. Volz, and E. P. O'Reilly, "Determination of type-I band offsets in $GaBi_xAs_{1-x}$ quantum wells using polarisation-resolved photovoltage spectroscopy and 12-band $\mathbf{k}\cdot\mathbf{p}$ calculations," *submitted*, 2015.

[48] S. B. Healy and E. P. O'Reilly, "Influence of electrostatic confinement on optical gain in GaInNAs quantum-well lasers," *IEEE J. Quant. Electron.*, vol. 42, p. 608, 2006.

[49] M. Ehrhardt and T. Koprucki, Eds., *Multiband Effective Mass Approximations: Advanced Mathematical Models and Numerical Techniques*. Springer, 2014.

[50] A. T. Meney, B. Gonul, and E. P. O'Reilly, "Evaluation of various approximations used in the envelope-function method," *Phys. Rev. B*, vol. 50, p. 10893, 1994.

[51] F. Szmulowicz, "Derivation of a general expression for the momentum matrix elements within the envelope-function approximation," *Phys. Rev. B*, vol. 51, p. 1613, 1995.

[52] S. L. Chuang, J. O'Gorman, and A. F. J. Levi, "Amplified spontaneous emission and carrier pinning in laser diodes," *IEEE J. Quant. Electron.*, vol. 29, p. 1631, 1993.

[53] C.-S. Chang, S. L. Chuang, J. R. Minch, W.-C. W. Fang, Y. K. Chen, and T. Tanbun-Ek, "Amplified spontaneous emission spectroscopy in strained quantum-well lasers," *IEEE J. Sel. Top. Quant. Electron.*, vol. 1, p. 1100, 1995.

[54] S. Tomić and E. P. O'Reilly, "Optimization of material parameters in 1.3-μm InGaAsN-GaAs lasers," *IEEE Photon. Tech. Lett.*, vol. 15, p. 6, 2003.

[55] S. Imhof, C. Wagner, A. Chernikov, M. Koch, K. Kolata, N. S. Köster, S. Chatterjee, S. W. Koch, X. Lu, S. R. Johnson, D. A. Beaton, T. Tiedje, O. Rubel, and A. Thränhart, "Evidence of two disorder scales in Ga(AsBi)," *Phys. Stat. Sol. B*, vol. 248, p. 851, 2011.

[56] K. Kawano and T. Kitoh, *Introduction to Optical Waveguide Analysis: Solving Maxwell's Equation and the Schrödinger Equation*. Wiley, 2001.

[57] C.-S. Chang and S. L. Chuang, "Modeling of strained quantum-well lasers with spin-orbit coupling," *IEEE J. Sel. Top. Quant. Electron.*, vol. 1, p. 218, 1995.

[58] G. Lasher and F. Stern, "Spontaneous and stimulated recombination radiation in semiconductors," *Phys. Rev.*, vol. 133, p. A 553, 1964.

[59] A. Haug, "Relations between the T_0 values of bulk and quantum well GaAs," *Appl. Phys. B*, vol. 44, p. 151, 1987.

[60] A. Ghiti, M. Silver, and E. P. O'Reilly, "Low threshold and high-differential gain in ideal tensile- and compressive-strained quantum-well lasers," *J. Appl. Phys.*, vol. 71, p. 4626, 1992.

[61] S. J. Sweeney, "Novel experimental techniques for semiconductor laser characterisation and optimisation," *Phys. Scr.*, vol. 152, p. 2004, 2004.

[62] E. P. O'Reilly and A. R. Adams, "Band-structure engineering in strained semiconductor lasers," *IEEE J. Quant. Electron.*, vol. 30, p. 366, 1994.



Christopher A. Broderick was born in London, England in 1988 and grew up in Cork, Ireland. He received the B.Sc. (Hons.) degree in physics from University College Cork in 2010. Following this he was awarded an EMBARK Postgraduate Scholarship by the Irish Research Council and began his doctoral studies in theoretical condensed matter physics with the Photonics Theory Group at Tyndall National Institute, Cork, Ireland in October 2010. His doctoral research focused on developing the theory of the electronic and optical properties of dilute bismide alloys. He received the Ph.D. degree from University College Cork in 2015.

Christopher's current research interests include condensed matter theory, photonic materials and devices, and computational physics.



Patrick E. Harnedy was born in Cork, Ireland in 1988. He received the B.Sc. (Hons.) degree in applied physics and instrumentation from Cork Institute of Technology in 2011. He began his doctoral studies with the Photonics Theory Group at Tyndall National Institute, Ireland in October 2011. His doctoral research, which he completed in 2015, focused on experimental studies of the electronic and optical properties of dilute bismide and InP-based materials and optoelectronic devices.

Patrick began working for an artisan distillery in West Cork, Ireland in 2015, where he currently holds the position of Process Innovation Manager with responsibility for mass-balance reconciliation and process improvement practices, as well as process innovation and automation.



Eoin P. O'Reilly (M'03) was born in Dublin, Ireland. He received the B.A. degree in theoretical physics from Trinity College, Dublin, in 1978, and the Ph.D. degree in theoretical condensed matter physics from the University of Cambridge, Cambridge, U.K., in 1982. From 1984 to 2001, he was a member of staff at the University of Surrey, Guildford, U.K., where he was Head of the Department of Physics from 1997 to 2001.

Since 2001 he has been at Tyndall National Institute, University College Cork, Ireland, where he is currently Chief Scientist, and also a member of the Department of Physics at University College Cork. O'Reilly's research seeks to improve the fundamental understanding of photonic materials and devices, to enable the design of structures for new capabilities and applications. He is an Associate Editor of Semiconductor Science and Technology. He was a co-recipient in 2014 of the Rank Prize for Optoelectronics for his pioneering work on strained-layer semiconductor lasers.

Bibliography

[1] *What is a Lock-in Amplifier? Technical note, PerkinElmer, TN1000.* 29

[2] A. R. Adams. Strained-layer quantum well lasers. *IEEE J. Sel. Top. Quant. Electron.*, 17:1364, 2011. 86

[3] Alf R Adams and Eoin P O'Reilly. Semiconductor lasers take the strain. *Physics World*, 5(10):43–7, 1992. 12

[4] GP Agrawal and NK Dutta. Long-Wavelength Semiconductor Lasers, Van Nostrand Reinhold. *New York*, page 367, 1986. 7

[5] K. Alberi, O. D. Dubon, W. Walukiewicz, K. M. Yu, K. Bertulis, and A. Krotkus. Valence band-anticrossing in $GaAs_{1-x}Bi_x$. *Appl Phys Lett*, 91:051909, 2007. 67

[6] K. Alberi, J. Wu, W. Walukiewicz, K. M. Yu, O. D. Dubon, S. P. Watkinsa, C. X. Wang, X. Liu, Y.-J. Cho, and J. Furdyna. Valence-band anticrossing in mismatched III-V semiconductor alloys. *Phys. Rev. B*, 75:045203, 2007. 83, 84

[7] Zh I Alferov, VM Andreev, DZ Garbuzov, Yu V Zhilyaev, EP Morozov, EL Portnoi, and VG Trofim. Investigation of the influence of the AlAs:GaAs heterostructure parameters on the laser threshold current and the realization of continuous emission at room temperature. *Sov. Phys. Semicond*, 4(9):1573–1575, 1971. 7

[8] Zh I Alferov, VM Andreev, EL Portnoi, and MK Trukan. AlAs:GaAs heterojunction injection lasers with a low room-temperature threshold. *Sov Phys Semiconductors*, 3(9):1107–1110, 1970. 7

[9] Zh.I. Alferov. The history and future of semiconductor heterostructures. *Semiconductors*, 32(1):1–14, 1998. 7

[10] I. Alghoraibi, L. Jouland, C. Paranthoen, A. Le Corre, O. Dehaese, N. Bertru, H. Folliot, P. Caroff, and S. Loualiche. InAs self-assembled quantum dot and quantum dash lasers on InP for 1.55 μm optical telecommunications. In *Information and Communication Technologies, 2006. ICTTA '06. 2nd*, volume 2, pages 2085 – 2090, 2006. 49

[11] Y. Arakawa and H. Sakaki. Multidimensional quantum well laser and temperature dependence of its threshold current. *Appl Phys Lett*, 40(11):939–941, 1982. 9, 49

[12] M. Asada, Y. Miyamoto, and Y. Suematsu. Gain and the threshold of three-dimensional quantum-box lasers. *Quantum Electronics, IEEE Journal of*, 22(9):1915 – 1921, September 1986. 49

[13] Seth R Bank, Mark A Wistey, Lynford L Goddard, Homan B Yuen, Vincenzo Lordi, and James S Harris. Low-threshold continuous-wave 1.5-μm GaInNAsSb lasers grown on GaAs. *Quantum Electronics, IEEE Journal of*, 40(6):656–664, 2004. 10

[14] J. Barrau, T. Amand, M. Brousseau, R. J. Simes, and L. Goldstein. Induced electrostatic confinement of the electron gas in tensile strained InGaAs/InGaAsP quantum well lasers. *J Appl Phys*, 71(12):5768–5771, 1992. 56

[15] Z. Batool, K. Hild, T. J. C. Hosea, X. Lu, T. Tiedje, and S. J. Sweeney. The electronic band structure of GaBiAs/GaAs layers: Influence of strain and band anti-crossing. *J Appl Phys*, 111:113108, 2012. 67, 83

[16] D. Bimberg, M. Grundmann, and N. N Ledentsov. *Quantum dot heterostructures*. Wiley, New Jersey, 2009. 49

[17] D. N. Bose. Advanced Technology Centre, I.I.T., KHARAGPUR, 721 302: http://www.cat.ernet.in/newsletter/news/lasernews/ln992/ln992a01.html, May 2014. v, 11

[18] C. A. Broderick, P. E. Harnedy, P. Ludewig, Z. L. Bushell, R. J. Manning, K. Volz, and E. P. O'Reilly. Determination of type-1 band offsets in $GaBi_xAs_{1-x}$ quantum wells using polarization-resolved photovoltage spectroscopy and 12-band $\mathbf{k}\cdot\mathbf{p}$ calculations. Submitted to SST. 71, 80

[19] C. A. Broderick, P. E. Harnedy, and E. P. O'Reilly. Theory of the electronic and optical properties of dilute bismide quantum well lasers. page in preparation, 2014. 74, 80, 82, 113

[20] C. A. Broderick, M. Usman, and E. P. O'Reilly. 12-band $\mathbf{k} \cdot \mathbf{p}$ model for dilute bismide alloys of (In)GaAs derived from supercell calculations. *Phys. Stat. Sol. B*, 250:773, 2013. ix, 91, 98, 100

[21] C. A. Broderick, M. Usman, and E. P. O'Reilly. Derivation of 12 and 14-band $\mathbf{k}\cdot\mathbf{p}$ Hamiltonians for dilute bismide and bismide-nitride alloys. *Semicond Sci Technol*, 28:125025, 2013. ix, 67, 80, 84, 85, 91, 98, 99, 100

[22] C. A. Broderick, M. Usman, S. J. Sweeney, and E. P. O'Reilly. Band engineering in dilute nitride and bismide semiconductor lasers. *Semicond Sci Technol*, 27:094011, 2012. 9, 10, 25, 83, 84

[23] Lin C. F. *Optical Components for Communication*. Springer, New York, 2004. 42

[24] Daniel T. Cassidy. Technique for measurement of the gain spectra of semiconductor diode lasers. *J Appl Phys*, 56(11):3096–3099, 1984. 39

[25] S. L. Chuang. *Physics of Photonic Devices*. Wiley, New Jersey, 2009. 46, 90

[26] Larry A. Coldren and Scott W. Carzine. *Diode Lasers and Photonic Integrated Circuits*. Wiley, New Jersey, 1995. v, 5, 7, 10, 11, 12, 20, 21, 22, 23

[27] J J Coleman. The development of the semiconductor laser diode after the first demonstration in 1962. *Semicond Sci Technol*, 27(9):090207, 2012. 7

[28] M. T. Crowley, S. C. Heck, S. B. Healy, S. Osborne, D. P. Williams, S. Schulz, and E. P. O'Reilly. Long wavelength transverse magnetic polarized absorption in 1.3 μm InAs/InGaAs dots-in-a-well type active regions. *Semicond Sci Technol*, 28:15012, 2013. 88, 89

[29] M. T. Crowley, J. Houlihan, T. Piwonski, I. O'Driscoll, D. P. Williams, E. P. O'Reilly, A. V. Uskov, and G. Huyet. Refractive index dynamics of InAs/GaAs quantum dots. *Appl Phys Lett*, 103(2):021114, 2013. 58

[30] M. T. Crowley, I. P. Marko, N. F. Masse, A. D. Andreev, S. Tomic, S. J. Sweeney, E. P. O'Reilly, and A. R. Adams. The Importance of Recombination via Excited States in InAs/GaAs 1.3 μm Quantum-Dot Lasers. *Selected Topics in Quantum Electronics, IEEE Journal of*, 15(3):799 – 807, 2009. 53

[31] H.-X. Deng, J. Li, S.-S. Li, H. Peng, J.-B. Xia, L.-W. Wang, and S.-H. Wei. Band crossing in isovalent semiconductor alloys with large size mismatch: First-principles calculations of the electronic structure of Bi and N incorporated GaAs. *Phys. Rev. B*, 82:193204, 2010. 84

[32] P. Dongmo, Y. Zhong, P. Attia, C. Bomberger, R. Cheaito, J. F. Ihlefeld, P. E. Hopkins, and J. Zide. Enhanced room temperature electronic and thermoelectric properties of the dilute bismuthide InGaBiAs. *J Appl Phys*, 112:093710, 2012. 83

[33] G.-H. Duan, A. Shen, A. Akrout, F. V. Dijk, F. Lelarge, F. Pommereau, O. LeGouezigou, J.-G. Provost, H. Gariah, F. Blache, F. Mallecot, K. Merghem, A. Martinez, and A. Ramdane. High performance InP-based quantum dash semiconductor mode-locked lasers for optical communications. *Bell Labs Technical Journal*, 14(3):63 – 84, 2009. 50

[34] R. Fehse, S. Tomic, A. R. Adams, S. J. Sweeney, E. P. O'Reilly, A. Andreev, and H. Riechert. A quantitative study of radiative, Auger, and defect related recombination processes in 1.3 μm GaInNAs-based quantum-well lasers. *Selected Topics in Quantum Electronics, IEEE Journal of*, 8(4):801 – 810, 2002. 71

[35] M. Ferhat and A. Zaoui. Structural and electronic properties of III-V bismuth compounds. *Phys. Rev. B*, 73:115107, 2006. 92

[36] B. Fluegel, S. Francoeur, A. Mascarenhas, S. Tixier, E. C. Young, and T. Tiedje. Giant Spin-Orbit Bowing in $GaAs_{1-x}Bi_x$. *Phys Rev Lett*, 97:067205, 2006. 83

[37] F. Girardin and G.-H. Duan. Characterization of semiconductor lasers by spontaneous emission measurements. *Selected Topics in Quantum Electronics, IEEE Journal of*, 3(2):461 – 470, April 1997. 32, 34

[38] Basil W. Hakki and Thomas L. Paoli. Gain spectra in GaAs double−heterostructure injection lasers. *J Appl Phys*, 46(3):1299–1306, 1975. 32, 39

[39] D. J. Hall, T. J. C. Hosea, and C. C. Button. Analysis of strained InGaAs/InGaAsP single quantum wells using room temperature photoreflectance. *Semicond Sci Technol*, 13:302, 1998. 46, 90

[40] I Hayashi, MB Panish, PW Foy, and S Sumski. Junction lasers which operate continuously at room temperature. *Appl Phys Lett*, 17(3):109–111, 1970. 7

[41] Jr. H.C. Casey and M.B. Panish. Heterostructure lasers, part A: fundamental principles: Academic Press, 1978. *Journal of Molecular Structure*, 70(0):318 –, 1981. 7

[42] S. B. Healy and E. P. O'Reilly. Influence of electrostatic confinement on optical gain in GaInNAs quantum-well lasers. *Quantum Electronics, IEEE Journal of*, 42(6):608 – 615, June 2006. 80

[43] S. C. Heck, S. B. Healy, S. Osborne, E. P. OReilly, F. Lelarge, F. Poingt, A. Accard, F. Pommereau, O. Le Gouezigou, and B. Dagens. An analysis of 1.55 μm InAs/InP quantum dash lasers. *Appl Phys Lett*, 92(25):251105 – 251105 – 3, June 2008. 53, 56

[44] S. C. Heck, S. Osborne, S. B. Healy, E. P. O'Reilly, F. Lelarge, F. Poingt, O. Le Gouezigou, and A. Accard. Experimental and Theoretical Study of InAs/InGaAsP/InP Quantum Dash Lasers. *Quantum Electronics, IEEE Journal of*, 45(12):1508 – 1516, 2009. 56, 89

[45] Susannah C. Heck. *Experimental study of quantum dot and dash lasers. PhD thesis, Department of Physics, University College Cork, 2009.* v, 8, 16, 33, 40, 43

[46] C. H. Henry, R. A. Logan, and K. A. Bertness. Measurement of spectrum, bias dependence, and intensity of spontaneous emission in GaAs lasers. *J Appl Phys*, 52(7):4453–4456, 1981. 32, 34

[47] T. J. C. Hosea, D. Lancefield, and N. S. Garawal. Detailed analysis of room-temperature photoreflectance of strained InGaAs/AlGaAs undoped single quantum wells. *J Appl Phys*, 79:4338, 1996. 46, 90

[48] N. Hossain, I. P. Marko, S. R. Jin, K. Hild, S. J. Sweeney, R. B. Lewis, D. A. Beaton, and T. Tiedje. Recombination mechanisms and band alignment of $GaAs_{1-x}Bi_x$/GaAs light emitting diodes. *Appl Phys Lett*, 100:051105, 2012. 100, 104, 114

[49] S. Imhof, C. Wagner, A. Chernikov, M. Koch, K. Kolata, N. S. Köster, S. Chatterjee, S. W. Koch, X. Lu, S. R. Johnson, D. A. Beaton, T. Tiedje, O. Rubel, and A. Thränhardt. Evidence of two disorder scales in Ga(AsBi). *Phys. Stat. Sol. B*, 248:851, 2011. 74, 76, 82, 113

[50] S. Imhof, C. Wagner, A. Thränhardt, A. Chernikov, M. Koch, N. S. Köster, S. Chatterjee, S. W. Koch, O. Rubel, X. Lu, S. R. Johnson, D. A. Beaton, and T. Tiedje. Luminescence dynamics in Ga(AsBi). *Appl Phys Lett*, 98:161104, 2011. 74, 76, 82, 110, 113

[51] Skulls in the stars. Skulls: http://skullsinthestars.com/2010/08/02/optics-basics-lasers/, May 2014. v, 19

[52] A. Janotti, S.-H. Wei, and S. B. Zhang. Theoretical study of the effects of isovalent coalloying of Bi and N in GaAs. *Phys. Rev. B*, 65:115203, 2002. 84

[53] L Ya Karachinsky, T Kettler, II Novikov, Yu M Shernyakov, N Yu Gordeev, MV Maximov, NV Kryzhanovskaya, AE Zhukov, ES Semenova, AP Vasil'Ev, et al. Metamorphic 1.5 μm-range quantum dot lasers on a GaAs substrate. *Semicond Sci Technol*, 21(5):691, 2006. 10

[54] M. P. Kesler and C. Harder. Spontaneous emission and gain in GaAlAs quantum well lasers. *Quantum Electronics, IEEE Journal of*, 27(6):1812 – 1816, June 1991. 34

[55] N Kirstaedter, NN Ledentsov, M Grundmann, D Bimberg, VM Ustinov, SS Ruvimov, MV Maximov, Ps S Kop'ev, Zh I Alferov, U Richter, et al. Low threshold, large T_0 injection laser emission from (InGa) As quantum dots. *Electronics Letters*, 30(17):1416–1417, 1994. 9

[56] Masahiko Kondow, Kazuhisa Uomi, Atsuko Niwa, Takeshi Kitatani, Seiji Watahiki, and Yoshiaki Yazawa. GaInNAs: a novel material for long-wavelength-range laser diodes with excellent high-temperature performance. *Japanese Journal of Applied Physics*, 35(2S):1273, 1996. 10

[57] M. P. C. M. Krijn. Heterojunction band offsets and effective masses in III-V quaternary alloys. *Semicond Sci Technol*, 6:27, 1991. 56, 91, 92, 95

[58] S. Latkowski, R. Maldonado-Basilio, and P. Landais. Sub-picosecond pulse generation by 40-GHz passively mode-locked quantum-dash 1-mm-long

Fabry-Pérot laser diode. *Opt Express*, 17(21):19166 – 19172, October 2009. 50

[59] NN Ledentsov, AR Kovsh, AE Zhukov, NA Maleev, SS Mikhrin, AP Vasil'ev, ES Semenova, MV Maximov, Yu M Shernyakov, NV Kryzhanovskaya, et al. High performance quantum dot lasers on GaAs substrates operating in 1.5 μm range. *Electronics Letters*, 39(15):1126–1128, 2003. 10

[60] F. Lelarge, B. Dagens, J. Renaudier, R. Brenot, A. Accard, F. Van Dijk, D. Make, O. Le Gouezigou, J. Provost, F. Poingt, J. Landreau, O. Drisse, E. Derouin, B. Rousseau, F. Pommereau, and D. Guang-Hua. Recent Advances on InAs/InP Quantum Dash Based Semiconductor Lasers and Optical Amplifiers Operating at 1.55 μm. *Selected Topics in Quantum Electronics, IEEE Journal of*, 13(1):111 – 124, Jan - feb. 10, 49, 51

[61] J. S. Liang, S. D. Wang, Y. S. Huang, C. W. Tien, Y. M. Chang, C. W. Chen, N. Y. Li, D. Y. Lin, and Fred H. Pollak. Polarized edge-incident photovoltage spectroscopy and reflectance characterization of a GaAs/GaAlAs vertical-cavity surface-emitting laser structure. *Appl Phys Lett*, 80(5):752–754, 2002. 44

[62] G.T. Liu, A. Stintz, H. Li, K.J. Malloy, and L.F. Lester. Extremely low room-temperature threshold current density diode lasers using InAs dots in $In_{0.15}Ga_{0.85}As$ quantum well. *Electronics Letters*, 35:1163–1165(2), July 1999. 49

[63] Xianfeng Lu, D. A. Beaton, R. B. Lewis, T. Tiedje, and Yong Zhang. Composition dependence of photoluminescence of GaBixAs1−x alloys. *Appl Phys Lett*, 95(4):–, 2009. 74

[64] P. Ludewig, Z. L. Bushell, L. Natterman, N. Knaub, W. Stolz, and K. Volz. Continuous growth of Ga(AsBi) on GaAs by MOVPE. *J Cryst Growth*, in press, 2014. 87

[65] P. Ludewig, N. Knaub, N. Hossain, S. Reinhard, I. P. Marko, S. R. Jin, K. Hild, S. Chatterjee, W. Stolz, S. J. Sweeney, and K. Volz. Electrical injection Ga(AsBi)/(AlGa)As single quantum well laser. *Appl Phys Lett*, 102:242115, 2013. 84, 87

[66] P. Ludewig, N. Knaub, N. Hossain, S. Reinhard, L. Nattermann, I. P. Marko, S. R. Jin, K. Hild, S. Chatterjee, W. Stolz, S. J. Sweeney, and

K. Volz. Electrical injection Ga(AsBi)/(AlGa)As single quantum well laser. *Appl Phys Lett*, 102(24), 2013. vii, 67, 68, 69, 71, 74, 78, 81, 106

[67] P. Ludewig, N. Knaub, W. Stolz, and K. Volz. MOVPE growth of Ga(AsBi)/GaAs multi quantum well structures. *J Cryst Growth*, 370:186, 2013. 87

[68] S. Mazzucato, T. T. Zhang, H. Carrère, D. Lagarde, P. Boonpeng, A. Arnoult, G. Lacoste, A. Balocchi, T. Amand, C. Fontaine, and X. Marie. Electron spin dynamics and g-factor in GaAsBi. *Appl Phys Lett*, 102:252107, 2013. 83

[69] Simone Mazzucato, Henri Lehec, Helene Carrere, Hajer Makhloufi, Alexandre Arnoult, Chantal Fontaine, Thierry Amand, and Xavier Marie. Low-temperature photoluminescence study of exciton recombination in bulk GaAsBi. *Nanoscale Research Letters*, 9(1):19, 2014. 110, 111, 114

[70] A. T. Meney, B. Gonul, and E. P. O'Reilly. Evaluation of various approximations used in the envelope-function method. *Phys. Rev. B*, 50:10893, 1994. 91, 95

[71] M. Mexis, P. Blood, and P. M. Smowton. Polarization response of quantum-confined structures using edge-photovoltage spectroscopy. *Semicond Sci Technol*, 22:1298, 2007. 44, 45, 69, 89, 90

[72] P. C. Mogensen, S. A. Hall, P. M. Smowton, U. Bangert, P. Blood, and P. Dawson. The effect of high compressive strain on the operation of AlGaInP quantum-well lasers. *IEEE J. Quant. Electron.*, 34:1652, 1998. 44, 88

[73] A. R. Mohmad, F. Bastiman, C. J. Hunter, R. D. Richards, S. J. Sweeney, J. S. Ng, J. P. R. David, and B. Y. Majlis. Localization effects and band gap of GaAsBi alloys. *Phys. Stat. Sol. B*, 2014. 74, 76

[74] L. V. T. Nguyen, A. J. Lowery, P. C. R. Gurney, and D. Novak. A time-domain model for high-speed quantum-well lasers including carrier transport effects. *Selected Topics in Quantum Electronics, IEEE Journal of*, 1(2):494 – 504, June 1995. 58

[75] University of Ulm. Compound semiconductors: Physics, technology and device concepts,http://www-opto.e-technik.uni-ulm.de/lehre/cs/, May 2014. v, 14

[76] Newport Optics. Newport: https://www.newport.com/Fiber-Optic-Basics/978863/1033/content.aspx, May 2014. v, 6

[77] E. P. O'Reilly. Valence band engineering in strained-layer structures. *Semicond Sci Technol*, 4:121, 1989. 86

[78] E. P. O'Reilly and A. R. Adams. Band-structure engineering in strained semiconductor lasers. *IEEE J. Quant. Electron.*, 30:366, 1994. 12, 86

[79] E. P. O'Reilly, A. Lindsay, P. J. Klar, A. Polimeni, and M. Capizzi. Trends in the electronic structure of dilute nitride alloys. *Semicond Sci Technol*, 24:033001, 2009. 83

[80] E.P. O'Reilly and M. Silver. Temperature sensitivity and high temperature operation of long wavelength semiconductor lasers. *Appl Phys Lett*, 63(24):3318–3320, 1993. 58

[81] Gyoungwon Park, Oleg B Shchekin, Diana L Huffaker, and Dennis G Deppe. Low-threshold oxide-confined 1.3-μm quantum-dot laser. *Photonics Technology Letters, IEEE*, 12(3):230–232, 2000. 9

[82] A. F. Phillips, S. J. Sweeney, A. R. Adams, and P. J. A. Thijs. The temperature dependence of 1.3- and 1.5- μm compressively strained InGaAs(P) MQW semiconductor lasers. *Selected Topics in Quantum Electronics, IEEE Journal of*, 5(3):401 – 412, May 1999. 24, 32, 36, 52, 67, 78

[83] P. A. Probst and B. Collet. Low-frequency digital lock-in amplifier. *Rev Sci Instrum*, 56(3):466 – 470, 1985. 29

[84] JP Reithmaier, A Somers, S Deubert, R Schwertberger, W Kaiser, A Forchel, M Calligaro, P Resneau, O Parillaud, S Bansropun, et al. InP based lasers and optical amplifiers with wire-/dot-like active regions. *J Phys D: Appl Phys*, 38(13):2088, 2005. 10

[85] S. Rubanov and P.R. Munroe. Damage in III-V Compounds during Focused Ion Beam Milling. *Microsc Microanal*, 11:446–455, 10 2005. 32

[86] K. Ryczko, G. Sek, P. Sitarek, A. Mika, J. Misiewicz, F. Langer, S. Höfling, A. Forchel, and M. Kamp. Verification of band offsets and electron effective masses in GaAsN/GaAs quantum wells: Spectroscopic experiment versus 10-band $\mathbf{k}\cdot\mathbf{p}$ modeling. *J Appl Phys*, 113:233508, 2013. 46, 89, 90

[87] I. C. Sandall, P. M. Smowton, C. L. Walker, H.-Y. Liu, M. Hopkinson, and D. J. Mowbray. Recombination mechanisms in 1.3 μm InAs quantum-dot lasers. *IEEE Photon. Tech. Lett.*, 18:965, 2006. 44, 88

[88] M. Silver, E. P. O'Reilly, and A. R. Adams. Determination of the wavelength dependence of Auger recombination in long-wavelength quantum-well semiconductor lasers using hydrostatic pressure. *Quantum Electronics, IEEE Journal of*, 33(9):1557 – 1566, September 1997. 24

[89] M. Silver and E.P. O'Reilly. Gain and radiative current density in InGaAs/lnGaAsP lasers with electrostatically confined electron states. *Quantum Electronics, IEEE Journal of*, 30(2):547–553, 1994. 56

[90] Yasuharu Suematsu and Kenichi Iga. Semiconductor Lasers in Photonics. *J. Lightwave Technol.*, 26(9):1132–1144, May 2008. 6, 7

[91] M. Sugiyama and G. Sigesato. A review of focused ion beam technology and its applications in transmission electron microscopy. *J. Electron Microsc.*, 53(5):527 – 536, 2004. 32

[92] S. J. Sweeney, A. R. Adams, M. Silver, E. P. O'Reilly, J. R. Watling, A. B. Walker, and P. J. A. Thijs. The effect of temperature dependent processes on the performance of 1.5 μm compressively strained InGaAs(P) MQW semiconductor diode lasers. *IEEE Photon. Tech. Lett.*, 10:1076, 1998. 9, 10, 25, 84

[93] S. J. Sweeney, A. R. Adams, M. Silver, E. P. O'Reilly, J. R. Watling, A. B. Walker, and P. J. A. Thijs. Dependence of threshold current on QW position and on pressure in 1.5 μm InGaAs(P) lasers. *Phys. Stat. Sol. B*, 211:525, 1999. 9, 10, 24, 25, 84

[94] S. J. Sweeney, Z. Batool, K. Hild, S. R. Jin, and T. J. C. Hosea. The potential role of bismide alloys in future photonic devices. *in Proceedings of the 13th International Conference on Transparent Optical Networks (ICTON), Stockholm*, 2011. 9, 10, 25, 67, 83, 84

[95] Advanced Research Systems. ARS Cryo principles of operation: http://www.arscryo.com/TechNotes/CryocoolerPrincipleofOperation.html, May 2014. v, 28, 29

[96] I Tangring, HQ Ni, BP Wu, DH Wu, YH Xiong, SS Huang, ZC Niu, SM Wang, ZH Lai, and A Larsson. 1.58 μm InGaAs quantum well laser on GaAs. *Appl Phys Lett*, 91(22):221101–221101, 2007. 10

[97] S. Tixier, S. E. Webster, E. C. Young, T. Tiedje, S. Francoeur, A. Mascarenhas, P. Wei, and F. Schiettekatte. Band gaps of the dilute quaternary alloys $GaN_xAs_{1-x-y}Bi_y$ and $Ga_{1-y}In_yN_xAs_{1-x}$. *Appl Phys Lett*, 86:112113, 2005. 83

[98] WT Tsang. Extremely low threshold (AlGa) As graded-index waveguide separate-confinement heterostructure lasers grown by molecular beam epitaxy. *Appl Phys Lett*, 40(3):217–219, 1982. 9

[99] M. Usman, C. A. Broderick, Z. Batool, K. Hild, T. J. C. Hosea, S. J. Sweeney, and E. P. O'Reilly. Impact of alloy disorder on the band structure of compressively strained $GaBi_xAs_{1-x}$. *Phys. Rev. B*, 87:115104, 2013. 73, 82, 84, 113

[100] M. Usman, C. A. Broderick, A. Lindsay, and E. P. O'Reilly. Tight-binding analysis of the electronic structure of dilute bismide alloys of GaP and GaAs. *Phys. Rev. B*, 84:245202, 2011. 67, 74, 82, 83, 84, 91, 99, 113

[101] JP Van der Ziel, R Dingle, RC Miller, W Wiegmann, and WA Nordland Jr. Laser oscillation from quantum states in very thin $GaAs/Al_{0.2}Ga_{0.8}As$ multilayer structures. *Appl Phys Lett*, 26(8):463–465, 1975. 9

[102] A. D. Vandermeer and D. T. Cassidy. A rate equation model of asymmetric multiple quantum-well lasers. *Quantum Electronics, IEEE Journal of*, 41(7):917 – 924, 2005. 57, 58

[103] C. G. Van de Walle. Band lineups and deformation potentials in the model-solid theory. *Phys. Rev. B*, 39:1871, 1989. 91, 95

[104] C. A. Volkert and A. M. Minor. Focused Ion Beam Microscopy and Micromachining. *MRS Bulletin*, 32:389–399, 5 2007. 32

[105] I. Vurgaftman, J. R. Meyer, and L. R. Ram-Mohan. Band parameters for III-V compound semiconductors and their alloys. *J Appl Phys*, 89:5815, 2001. 92, 95

[106] Eli Yablonovitch and EO Kane. Reduction of lasing threshold current density by the lowering of valence band effective mass. *Lightwave Technology, Journal of*, 4(5):504–506, 1986. 13

[107] M Yokozeki, J Mitomo, Y Sato, T Hino, and H Narui. 1.50 μm CW operation of GaInNAs/GaAs laser diodes grown by MOCVD. *Electronics Letters*, 40(17):1060–1061, 2004. 10

[108] Y. Zhang, A. Mascarenhas, and L.-W. Wang. Similar and dissimilar aspects of III-V semiconductors containing Bi versus N. *Phys. Rev. B*, 71:155201, 2005. 84

[109] AE Zhukov, AR Kovsh, SS Mikhrin, ES Semenova, NA Maleev, AP Vasil'ev, EV Nikitina, NV Kryzhanovskaya, AG Gladyshev, Yu M Shernyakov, et al. Metamorphic lasers for 1.3-μm spectral range grown on GaAs substrates by MBE. *Semiconductors*, 37(9):1119–1122, 2003. 10